

UNIVERSITY OF CALIFORNIA
SANTA BARBARA

High-Field EPR for Studies of Structure in
Biological Systems

A dissertation submitted in partial satisfaction
of the requirements for the degree of

Doctor of Philosophy

in

Physics

by

Devin Thomas Edwards

Committee in Charge:

Professor Mark S. Sherwin, Chair

Professor Songi Han

Professor Fyl Pincus

Professor Everett A. Lipman

September 2013

The dissertation of
Devin Thomas Edwards is approved:

Professor Songi Han

Professor Fyl Pincus

Professor Everett A. Lipman

Professor Mark S. Sherwin, Chair

May 2013

High-Field EPR for Studies of Structure in Biological Systems

Copyright © 2013

by

Devin Thomas Edwards

Acknowledgements

This work would have been impossible without the dedicated guidance, support and mentoring of my research advisers Prof. Songi Han and Prof. Mark Sherwin. Together they guided all of the work in this dissertation, pruning bad ideas from good ideas and displaying remarkable patience (and confidence) when things seemed stuck. Further, the assistance of my other committee members, Prof. Lipman and Prof. Pincus have been vital in completing my work, and in finding what to do next. Susumu Takahashi and Brandon Armstrong spent countless hours training me in the early years of graduate school, and without them I would never have gotten off the ground. Dr. Louis-Claude Brunel worked with me in lab every day for many years, and I was lucky to absorb both good spirits, and a great deal of knowledge and experience from him. I would like to thank our close collaborators Prof. Daniella Goldfarb, and Prof. Steffen Glaser. I was extremely fortunate to fall into collaborative projects with PIs who were willing to interact directly with a student from across the world. I would have never come to graduate school without the support and good example provided by Prof. Ken Segall who mentored me as an undergraduate. Ken, along with Professors Amato, Parks, Galvez, and Buboltz at Colgate University helped me realize that physics was something that I was both passionate about, and capable of pursuing.

A number of scientists, graduate students, and undergraduates contributed to the lab work, all of them brilliant and deserving far more mention than I can

provide here. Jerry Ramian and David Enyeart are responsible for maintaining the FEL, but also contribute immense technical skill and knowledge to everyone around them. Fellow graduate students Alicia Smith and Jessica Clayton have been excellent collaborators. They have learned quickly, been always helpful, and patient in helping solve the problems I created. Sunyia Hussain, Katherine Stone, and Anna Pavlova support me constantly, taught me all the biology I know, and contributed the expertise (and samples) to keep my work relevant for studying biological systems. Undergraduates Thor Visher, Sahar El Abbadi, Justin Bricker, Anjali Daniels, Mary Lou Bailey, Allegra Latimer, Andrew Pierce, and Maia Kinnebrew contributed immensely to this work, and also were close friends and allies in the lab. The entirety of the Han and Sherwin groups became a family to me, and their impact on my work and my mood can not be overstated.

I of course wish to acknowledge the support of family and close friends over this time. In particular my mother (Marge), father (Doug) and brother (Morgan) were constantly supportive, without ever becoming upset with my long work hours and too brief visits home. I was blessed to have a great number of friends in Santa Barbara and around the country who helped me stay sane, and I wish to thank them semi-anonymously. In no particular order: LM, ML, CB, KG, SDL, KSD, SH, AH, EvT, HB, BZ, CM, JF, MDL, RK, DM, MJ & KJ, IH, JH, BW, CT, KM, BB, ND, AY, DT, CY.

Department of Physics, University of California, Santa Barbara, CA 93106, (805) 893-3504,

dedwards@physics.ucsb.edu

Devin T. Edwards

Research Interests

Development and application of new methods to study biomolecular structure and assembly; novel applications of spectroscopic techniques including magnetic resonance.

Education

University of California, Santa Barbara, CA September
2007-Present

Ph. D. in Physics, Anticipated September 2013

Advisors: Prof. Mark Sherwin (Physics), Prof. Songi Han (Chem-
istry)

M.A. in Physics, December 2009 (GPA=4.0/4.0; 4.0=A)

Colgate University, Hamilton, NY September 2003-June 2007

B.A. in Physics, May 2003 (GPA=3.93/4.33; 4.33=A+)

Research Experience

Graduate Student Researcher June 2008-

Prof. M. Sherwin and Prof. S. Han: University of California,

Santa Barbara

- High-field (240 GHz) Electron Paramagnetic Resonance (EPR) measurements of spins labels, proteins, and biomolecules
- EPR structural studies of oligomerization in membrane proteins
- Modeling of EPR lineshapes and decay processes for new distance measurement methods
- High-powered EPR at 240 GHz powered by a Free Electron Laser

Undergraduate Student Researcher June 2005-May 2007

Prof. K. Segall: Colgate University

- Measurements and analysis of superconducting arrays below 1K
- Modeling non-linear dynamics in arrays of Josephson junctions

Publications

- 1 Walker, S; Edwards, D.T.; Siaw; T.-A., ; Armstrong, B.; Han, S. “Temperature dependence of high field ^{13}C dynamic nuclear polarization processes below 35 Kelvin” accepted on July 24 **2013** in *Physical Chemistry Chemical Physics*, DOI:10.1039/C3CP51628H.

- 2 Edwards, D.T.; Ma, Z.; Meade, T.; Goldfarb, D.; Han, S.; Sherwin, M.S. “Extending the distance range accessed with continuous wave EPR with Gd³⁺ spin probes at high magnetic fields” *Physical Chemistry Chemical Physics* **2013**, *15*,11313-11326.
- 3 Edwards, D.T.; Zhang, Y.; Glaser, S., Han, S.; Sherwin, M.S. “Phase Cycling with a 240 GHz, Free Electron Laser-powered Electron Paramagnetic Resonance Spectrometer” in *Physical Chemistry Chemical Physics* **2013**, *15*, 5707-206.
- 4 Edwards, D.T.; Takahashi, S.; Han, S.; Sherwin, M.S. “Distance measurements across randomly distributed nitroxide probes from the temperature dependence of the electron spin phase memory time at 240 GHz” in *Journal of Magnetic Resonance* **2012**, *223*, 198-206.
- 5 Takahashi, S.; Brunel, L.-C.; Edwards, D.T.; van Tol, J.; Ramian, G.; Han, S.; Sherwin, M.S. “Pulsed electron paramagnetic resonance spectroscopy powered by a free-electron laser” in *Nature* **2012**, *489*, 409-413.
- 6 Armstrong, B. D.; Edwards, D. T.; Wylde, R. J.; Walker, S. A.; Han, S. “A 200 GHz dynamic nuclear polarization spectrometer” in *Physical Chemistry Chemical Physics* **2010**, *12*, 5920-5926.

Manuscripts In Preparation

- 1 Edwards, D.T.; Stone, K.; Hussain, S.; Kinnebrew, M.; Sherwin, M.S.; Goldfarb, D.; Han, S. “Measurement of multiple distances in a proteorhodopsin oligomer utilizing Gd^{3+} spin probes.”

Invited Talks

Weizmann Institute of Science: Magnetic Resonance Seminar
May 2012

“High-Power, Pulsed EPR at 240 GHz using Free Electron Lasers”

Colgate University: Physics and Astronomy Seminar March 2012

“New Methods in High Frequency EPR for Biological Systems”

Institute for Terahertz Science and Technology Seminar October
2011

“ Gd^{3+} -Based Spin Probes for High Frequency Electron Paramagnetic Resonance”

Institute for Terahertz Science and Technology Seminar October
2009

“Pulsed Electron Paramagnetic Resonance at 240 GHz for Biological Studies”

Conference and Seminar Talks

American Physical Society March Meeting March 2012

“Nanometer Scale Distance Measurements for Biological Systems using Gd^{3+} based Spin Probes at High Magnetic Fields”

Rocky Mountain Conference on Analytical Chemistry July 2012

“ Gd^{3+} -Based Spin Probes for Enhanced EPR Distance Measurements in Complex Sample Environments and at Elevated Temperatures”

Rocky Mountain Conference on Analytical Chemistry July 2011

“Opportunities in High Field EPR: Extending the Distance Range with Gd^{3+} -based Probes”

Rocky Mountain Conference on Analytical Chemistry August 2010

“ T_2 Measurements at 240 GHz for Nuclear Spin Bath Effects and Biological Distance Measurement”

Rocky Mountain Conference on Analytical Chemistry July 2009

“Distance Measurement through Electron Spin Decoherence at 240 GHz”

American Physical Society March Meeting March 2007

“Interaction of breathers with moving vortices in a Josephson junction ladder”

Recognition

Student Travel Awards, Rocky Mountain Conference on Analytic Chemistry

Yearly 2009-2012

Doctoral Student Travel Grant, University of California, Santa Barbara June

2010

Physics Department TA Award, University of California, Santa Barbara June

2006

Sigma Xi Physics Honor Society

Inducted June 2008

Teaching and Mentoring

Acted as a teaching assistant for undergraduate lab courses for both honors physics students as well as students in biology programs.

Mentored undergraduate students from UCSB's EUREKA (Summer 2012) and INSET (Summer 2010) programs resulting in both students presenting their work at conferences.

Guided work by 4 undergraduate students and 2 graduate students in continuing the development and application of high-field, pulsed EPR.

Abstract

High-Field EPR for Studies of Structure in Biological Systems

Devin Thomas Edwards

Electron Paramagnetic Resonance is a powerful technique for studying the local environment near a paramagnetic species. When coupled with the ability to introduce stable paramagnetic labels in a variety of biological systems, EPR becomes an important tool to unravel questions of structure and dynamics in biological systems. Because these paramagnetic species are introduced site specifically, EPR offers unusual spatial precision to address specific questions that evade other techniques. As with other kinds of magnetic resonance, EPR becomes more powerful at higher magnetic fields. However, in EPR expansion to high fields has been slowed by technical challenges of working at hundreds of GHz. This work expands the capabilities of high-field EPR through dual approaches. The first approach is to develop new methods for biological studies exclusive to high magnetic fields. For instance, a distance measurement technique is developed based on the temperature dependence of electron-spin phase memory times at high fields. Further, Gd^{3+} is demonstrated as a spin-label exceptionally well-suited for use at high magnetic fields. In particular, cw EPR with Gd^{3+} allows measurements of interspin distances up to 4 nm under less severe conditions than are typically necessary for pulsed EPR distance measurements. Additionally, pulsed EPR dis-

tance measurements with Gd^{3+} are used to elucidate the oligomeric structure of a membrane protein. The results strengthen the case for Gd^{3+} as a particularly useful probe for targeting complex, oligomeric systems, which tend to be difficult to study in other ways. The second approach is to eliminate the power restrictions of high-field, pulsed EPR through the use of UCSB's Free Electron Lasers as a radiation source to enable the highest power, pulsed EPR at frequencies over 100 GHz. The ability to manipulate and measure spins 50-100x faster than with other sources is introduced and the technical approach described. The intrinsic phase instability of the FEL source can then be eliminated through a post-processing routine, which recovers the capability for phase cycling using the FEL. As phase cycling can be used to dramatically reduce artifacts, and is a common technique in both EPR and NMR, this greatly expands the detection capabilities of the spectrometer. Together these approaches have allowed new capabilities for studying biological systems, particularly the ability to measure more complex systems, and closer to physiological conditions than otherwise possible. Beyond this, it is hoped these developments continue to spur efforts to realize mature, high-field EPR techniques and technology.

Contents

List of Figures	xviii
List of Tables	xx
1 Introduction	1
1.1 Fundamentals of Electron Paramagnetic Resonance	7
1.1.1 Continuous Wave Magnetic Resonance	9
1.1.2 Pulsed EPR	14
1.1.3 Major Components of the Spin Hamiltonian	20
1.2 EPR Distance Measurements in Biological Systems	28
1.2.1 cw-lineshape Analysis	32
1.2.2 Double Electron-Electron Resonance	38
1.2.3 Comparing the Capabilities of cw and pulsed EPR for Distance Measurement	45
1.3 Opportunities and Challenges of High-Field EPR	48
I New Distance Measurement Techniques at High Fields	57
2 Probing Interspin Distances through Spin Bath Quenching	60
2.1 Exploiting High Polarizations at High Fields	60
2.2 Spin Bath Quenching(SBQ) and Distances	62
2.3 Spin Bath Quenching in Nitroxide Radicals and Spin-labeled Vesicles	67
2.3.1 Solution Study of Nitroxides	67
2.3.2 Residual Relaxation and Distance Limits	75
2.3.3 Application to A Model Membrane	80

2.3.4	Potential Distance Limits and Application for Studying Geometry and Clustering	83
2.4	Observing Long Distances by Decoherence in Gd^{3+}	86
2.4.1	The Gd^{3+} Ion as Suitable Probe for Pulsed, High Field EPR on Biological Systems	87
2.4.2	Measurements of the Temperature Dependence of T_M in Gd^{3+}	92
2.5	Studying Pairwise Systems and Clustering with Spin Bath Quenching	99
2.6	Impact of Spin Bath Quenching	104
3	Distance Measurements using Gd Lineshapes	108
3.1	Introduction	108
3.2	Spectroscopic Properties of Gd^{3+}	111
3.3	Dipolar Broadening in for Gd^{3+}	113
3.4	Dipolar Broadening in Test and Model Systems	117
3.4.1	Solutions of Gd^{3+}	117
3.4.2	Linewidths of Coordinating Complexes	125
3.4.3	EPR on a Bis- Gd^{3+} Complex	129
3.5	Refractive Broadening	132
3.6	The Limits for Gd^{3+} -based cw Distance Measurements	136
3.6.1	Temperature Effects	136
3.6.2	Distance Limits	138
3.7	Impact and Outlook	139
4	Double Electron-Electron Resonance (DEER) Studies of a Membrane Protein	142
4.1	Gd^{3+} as a Spin Probe for DEER of Oligomers	142
4.2	Pulsed EPR Measurements of Protein Oligomers	146
4.2.1	Field Swept Echo Measurements	149
4.2.2	Comparison of Phase Memory Times	149
4.2.3	DEER on the 58C Mutant	153
4.2.4	DEER on the 177C Mutant	155
4.3	Impact of Gd^{3+} and Nitroxide Studies in Oligomers	159
II Free Electron Laser-powered EPR (FELEPR) Spectroscopy		162
5	Development of a Free Electron Laser-powered EPR (FELEPR) Spectrometer	165
5.1	The Need for a High Power, 240 GHz Spectrometer	165

5.2	Spectrometer Design	167
5.2.1	Free Electron Laser	170
5.2.2	Injection Locking	172
5.2.3	Silicon Switches and Cavity Dump Coupling (CDC)	173
5.2.4	Pulse Slicer	175
5.2.5	Laser System	181
5.3	EPR Results	184
5.3.1	One Pulse Measurements: Simple Rabi Oscillations	185
5.3.2	Two Pulse	190
5.4	Transient Larmor Shifts due to Paramagnetic Demagnetization	195
5.5	Future of FELEPR	207
6	Phase Cycling the FELEPR	209
6.1	Introducing Phase to the FELEPR Experiment	209
6.2	Locking Detector Phase to FEL Pulse	212
6.2.1	Correction Procedure	214
6.2.2	Screening Pulse Quality from the FEL	218
6.2.3	Stochastic Phase Cycling	219
6.2.4	Expanding Spectrometer Sensitivity with Coherent Averaging	224
6.2.5	Impact of and Considerations for a Coherent Detector Phase	226
6.3	Measuring and Modifying Relative Phase in the Two Pulse Experiment	230
6.3.1	Combined Effects of Offset Frequency and Pulse Phase for 2-Pulse Excitation	231
6.3.2	Observation of Offset-dependent Modulations of the FID Magnitude	234
6.3.3	Modulating the Relative Phase with Dielectric Materials	237
6.3.4	Impact of Relative Phases in Two Pulse EPR	241
6.4	Impact of Phase Cycling for FELEPR	243
7	Conclusion	245
A	Experiments and Methods	248
A.1	EPR Spectrometers	248
A.2	Samples	251
A.3	Measurement and Calculation Details	257
B	Increased Rabi Frequency in Gd^{3+}	265
C	Evaluating the Gd^{3+} Hamiltonian with Perturbation Theory	268
D	Calculation of Refractive Broadening for Gd^{3+} Lineshapes	276

List of Figures

1.1	MTSL Spin Label.	29
1.2	S= $\frac{1}{2}$ Pake Pattern.	34
1.3	cw Distance Measurement using Nitroxides.	37
1.4	Four Pulse DEER Sequence.	40
2.1	240 GHz Nitroxide Spectrum and Echo Decays.	69
2.2	Spin Bath Quenching Affects T_M	71
2.3	Dipolar Coupling Rates in Nitroxide Solutions.	71
2.4	Determining Nearest-Neighbor Distances.	73
2.5	Effect of Solvent Deuteration of Residual Relaxation.	76
2.6	Effect of Deuterated TEMPO on Residual Relaxation.	77
2.7	Spin Bath Quenching in Spin-Labeled Vesicles.	79
2.8	The Gd ³⁺ Spectrum at 240 GHz.	90
2.9	The Gd ³⁺ Echo Decay in GdCl ₃	94
2.10	Temperature Dependence of the Phase Memory Time of GdCl ₃	95
2.11	Phase Memory Times During Spin Labeling.	97
2.12	Spin Bath Quenching in TOTAPOL.	99
2.13	Structure of Gd ³⁺ Coordinating Complexes.	102
2.14	Temperature Dependence of the Phase Memory Time of Complexed Gd ³⁺	103
3.1	High Spin Pake Patterns.	115
3.2	Broadening of the Central Transition of Gd ³⁺	118
3.3	Distance Limits of Dipolar Broadening in Random Solutions of GdCl ₃	122
3.4	Refractive Broadening at High Concentrations.	123
3.5	Dipolar Broadening at High Temperatures.	126
3.6	Intrinsic Linewidth of Gd ³⁺ Chelates.	126
3.7	Dipolar Broadening in Spin-Pair System.	129
3.8	Eliminating the Effects of Refractive Broadening.	132
3.9	Calculated Broadening from Dipolar Interactions.	137

4.1	Proteorhodopsin Hexamer.	147
4.2	Field Swept Echo Spectra of MTSL- and Gd ³⁺ -labeled Proteorhodopsin.	148
4.3	Phase Memory Times of Different Site in Proteorhodopsin.	150
4.4	DEER Results for Site 58 of Proteorhodopsin.	152
4.5	DEER Results for Site 177 of Proteorhodopsin.	156
5.1	Power Limitations of EPR at High Fields.	167
5.2	240 GHz Detection.	169
5.3	FELEPR Pulse Slicer.	176
5.4	FELEPR Timing Diagram.	182
5.5	Typical cw EPR Spectrum of a BDPA grain.	186
5.6	Rabi Oscillations with an FEL.	187
5.7	FELEPR Nitroxide Echo.	191
5.8	Fast Echo Sequence with FELEPR.	192
5.9	FELEPR Echo on Gd ³⁺	194
5.10	Off-Resonance Rabi Oscillations.	196
5.11	Reproduced Rabi Oscillations.	198
5.12	Dependence of Larmor Frequency on Pulse Length.	199
5.13	Calculated Rabi Oscillations.	206
6.1	Typical Time Domain Trace for Single Pulse FELEPR.	213
6.2	Retrospective Correction of Phase.	215
6.3	Eliminating Inconsistent FEL Pulses.	220
6.4	Phase Cycling to Eliminate Artifacts.	222
6.5	Improved Sensitivity with Phase Cycling.	225
6.6	Oscillations from Offset Frequency.	233
6.7	Effect of Interpulse Spacing on Oscillation Frequency.	236
6.8	Effect of Silicon Wafers on FELEPR Phase.	238
6.9	Effect of Wafer Incident Angle on Phase Shift.	239
6.10	Effect of Mirror Position on FELEPR Phase.	240
D.1	Reflection Sample Geometry.	277
D.2	Sample 1 Error Plots.	284
D.3	Sample 2 Error Plots.	285
D.4	Sample 3 Error Plots.	286
D.5	Sample 4 Error Plots.	288
D.6	Sample 5 Error Plots.	289

List of Tables

1.1	Common Spectrometer Fields and Frequencies.	10
2.1	Nitroxide Concentrations, Interspin Distances, and Residual Relaxation Rates.	68
2.2	Vesicle Compositions, Interspin Distances.	106
2.3	TOTAPOL and TEMPO Comparison.	107

Chapter 1

Introduction

As a spectroscopic tool Electron Paramagnetic Resonance (EPR; also called Electron Spin Resonance: ESR) is regularly considered as merely an esoteric cousin of Nuclear Magnetic Resonance (NMR), with a far narrower scope of application and potential. Indeed, the ability to manipulate the magnetic moment of nuclei through NMR has proven a critical tool in modern science, technology and medicine. Since 1945 when NMR was first observed in solids (independently by Bloch¹ and Purcell²) it has exploded and birthed new methods in analytical chemistry, medical imaging, and structural biology. NMR is responsible for 4 Nobel prizes since 1952: in Physics for Bloch & Purcell(1952), in Chemistry for Ernst's work on high-resolution NMR(1991), in Chemistry for Wüthrich's demonstration of 3D structural determination in biomacromolecules (2002), and most recently in Medicine for Lauterbur and Mansfield's discoveries in Magnetic Resonance Imaging (MRI) in 2003. Modern NMR is a tool of expansive potential that allows synthetic chemists to identify their products, has determined the 3D

structure of 8000 proteins³, is at the heart of the the powerful MRI medical diagnostics, and through functional MRI (fMRI) offers a noninvasive methods to probe neurological activity.⁴

By contrast, EPR was discovered by Zavoisky^{5,6} in the USSR in 1944, a year before the first reproducible observations of NMR(intriguingly, Zavoisky also likely observed NMR in 1941⁷, but was unable to reproduce the result). The development of microwave electronics for application in radar during the second World War provided the critical technology necessary for the development of EPR.⁷ However, while EPR has developed steadily and has emerged as an important technique in physics and physical chemistry, it has never become the pervasive and common spectroscopy tool which NMR has become. It is telling that throughout the last 65 years the fields of the Nobel Prizes recognizing NMR have moved from Physics to Chemistry and finally to Medicine. Outside of failing to garner Nobel prizes, EPR has failed to follow as grand a trajectory and become a science with as profound application in daily life, though it has, in the last decade, emerged as a tool for biochemists. Some of this discrepancy may be attributed to the fact that EPR targets unpaired electrons, which are less ubiquitous than nuclei. For instance, hydrogen atoms (a prime target for NMR studies) are a common constituent of biomacromolecules, and are highly concentrated in water. Similarly, carbon (a critical constituent of organic molecules) has a NMR active isotope (^{13}C). Despite the comparative scarcity of unpaired electrons, EPR is nearly 3

orders of magnitude more sensitive than NMR, making even single electron spin detection possible.⁸ Further, since unpaired electrons are not omnipresent like nuclei, it is far easier to probe a specific site, offering an advantage in selectivity over NMR.

In practice, many of challenges of EPR emerge from the comparative difficulty of the experiments. In EPR, the substantially faster relaxation times and stronger interactions with neighboring dipoles results in rapidly decaying signal and broad lines. NMR had been revolutionized by two steps, the emergence of Fourier Transform (FT) pulsed NMR, and the steady progress of NMR to higher magnetic fields. Even for EPR at fields below 1 T, where high power sources are available, it is still generally impossible to completely excite a typical EPR spectrum due to the limited spectral bandwidth of pulses. Further, the microwave technology necessary to carry out high-power, pulsed EPR has generally remained expensive and specialized. Though commercial options exist, they have only in the past decade become what could be considered “user” instruments that can be operated regularly in a lab that does not specialize in pulsed EPR. While this has resulted in pulsed EPR being utilized more regularly for structural biochemistry, these widely utilized commercial spectrometers operate only at low fields.

By comparison, NMR is regularly done at fields up to 20 Tesla, and would be carried out at higher fields if suitable magnets were developed. Moving to higher fields in either NMR or EPR requires increasing the frequency of the source.

Even at high fields, NMR frequencies are low enough (<1 GHz) to be easily generated, while the higher frequencies for EPR (>100 GHz) can be difficult to generate. Thus, in EPR, unlike NMR, operating at low fields remains the standard, as sources operating at frequencies above ~ 30 GHz are generally expensive, technically challenging to operate, and offer only limited power levels. This has long hindered the development of EPR at fields above the traditional X-Band spectrometer (operating at 0.35 T and 10 GHz). In particular, the limitations of source power have forced pulsed EPR at high fields to utilize long excitation pulses, which severely hampers the capabilities of the technique. Just as with NMR, EPR fundamentally becomes more powerful at higher magnetic fields due to increases in spectral resolution and sensitivity and so despite the technical limitations, high-field EPR is an important form of spectroscopy in physics, materials science, physical chemistry, and biochemistry.⁹⁻¹⁴

This dissertation details efforts to expand the impact of EPR spectroscopy by advancing the capabilities and effectiveness of high-field EPR. Though EPR is applied to a wide variety of systems, this work focuses on one of the most promising and powerful applications of EPR, which is to study structure in biological systems. EPR offers a method to probe biomacromolecules that resist other structural characterizations, in particular those that are large, complex or difficult to crystallize. EPR also acts as a superb complementary technique to address specific structural questions that may elude global structural characteri-

zation. Finally, some biological systems inherently include paramagnetic ions as part of their structure; the properties of these ions are important, and they can be used as internal probes of the biomolecules structure.

We find that the advantages of high-field EPR have been insufficiently leveraged for studying biology due to the lack of development of new techniques specialized for high fields, as well as the inability to perform high-powered EPR at these fields due to a lack of sources. We approach the first problem utilizing a home-built, pulsed and cw EPR spectrometers operating at 8.5 Tesla and 3.5 T to investigate novel methods that can be leveraged only at high magnetic fields. Low-power, high-field EPR is an important research tool across many scientific disciplines. However, its development is driven by a small group of researchers, typically by extending low field techniques (with modifications) to higher magnetic fields. We instead attempt to uncover new techniques and methods that can not be exploited at low magnetic fields but may offer advantages over existing techniques. This part of the dissertation includes measurements of interspin distances based on silencing fluctuations in the electron spin bath, and incorporates new applications of Gd^{3+} -based spin labels, which are ideally suited for high-field EPR applications.

The second component of this research seeks to overcome many of the limitations associated with high-field EPR by implementing the first high-power, pulsed EPR spectrometer operating above 3.5 Tesla. This is undertaken by incorporat-

ing a Free Electron Laser (FEL) as a source for pulsed EPR, allowing a increase in power of ~ 5 orders of magnitude over standard sources. The initial progress on this reports on the capability to carry out experiments $\sim 100x$ faster than is possible using other sources at these fields, and the associated benefits of these high powers before discussing the addition of complete phase control to this spectrometer.

Taken together the developments in this work run the gamut from being widely applicable (such as the use of Gd^{3+} -labeling of biomolecules), to offering a unique instrument which is unlikely to be duplicated (in the FELEPR). However, in all cases, the development of theory, instrumentation and technique provide new concepts and background for novel applications and the development of other spectrometers operating at higher frequencies that may be made available widely. Additionally, as new high-field spectrometers are developed, the FELEPR can be expanded to operate at still higher frequencies as the FELs output high powers up to THz frequencies. The extension of technology and methodology to high fields, which can be leveraged in biology and presents important steps towards EPR's continued emergence, of which this dissertation is only part.

1.1 Fundamentals of Electron Paramagnetic Resonance

EPR and NMR emerge fundamentally from the existence of spin in nature. This rather “funny” property, an intrinsic angular momentum carried by some particles, has no true classical analogue, but its existence, which was only understood within the last century, is critical to our understanding of the physical world. EPR and NMR can then be understood fully only within the confines of quantum mechanics, though classical descriptions are possible for a phenomenological explanation these experiments emerge from a quantum mechanical world. In fact, more than simply an example of a system where the mathematics and formalism of quantum mechanics is necessary, magnetic resonance (generically describing EPR and NMR) often provides elegant and simple demonstration of the most basic quantum mechanical behavior.

The mathematical description of EPR and NMR are largely identical (though sufficient differences exist to render them different fields) and many large tomes have been written covering the fields of magnetic resonance. The goal of this introduction is only to provide a sufficient background for the reader in addressing the work of the dissertation. For the more interested reader, books about NMR by Abragam¹⁵, Schlichter¹⁶, and Callaghan¹⁷ are broadly informative, while the EPR book by Weil¹⁸ provides a good background, with Poole¹⁹ providing a good

technical overview and Schweiger²⁰ supplying a modern perspective focused on pulsed EPR.

We start with the fact that electrons, like protons carry inherent angular momentum, called spin: a single electron, acts like its own magnetic dipole. While in principle the total angular momentum for an electron then depends both on its spin and its orbital angular momentum, the orbital angular momentum tends to be quite small for the systems studied here, and so the systems tend to be well described as (nearly) free electrons. Systems with higher spins than $S=\frac{1}{2}$ can be interrogated by EPR (and are important in this dissertation), an understanding of the $S=\frac{1}{2}$ system provides a sufficient background to address higher spin systems.

The spin of an $S=\frac{1}{2}$ system (for instance, a lone electron), can be completely described by a linear combination of two basis states. While principle a wide variety of states span the vector space for a single spin, for EPR we choose the energy eigenstates of the system in an applied, static magnetic field (i.e. under the Zeeman interaction).²¹ That is, we choose the states such that

$$\mathcal{H}|a\rangle = \frac{g_e\mu_\beta}{\hbar}B_0S_Z|a\rangle = \gamma_e B_0 S_Z|a\rangle = E_\alpha|a\rangle \quad (1.1)$$

Here B_0 is the applied field which is, without loss of generality taken along the \hat{z} direction, \hbar is the reduced Planck's constant, S_Z is the spin operator along \hat{z} , $g_e \approx 2.002$ is the electron factor, μ_β is the Bohr magneton, γ_e is the electron gyromagnetic ratio, and $|a\rangle$ is a generic state. Our eigenstates are then simply

$|S_Z; \frac{1}{2}\rangle = |\frac{1}{2}\rangle$ and $|S_Z; -\frac{1}{2}\rangle = |-\frac{1}{2}\rangle$, which is the notation used here to describe the eigenstates of S_Z , which correspond to the spin aligned with, and aligned against the magnetic field (spin-up and spin-down respectively). Note S_Z acts so that

$$S_Z|\frac{1}{2}\rangle = \frac{\hbar}{2}|\frac{1}{2}\rangle \quad \text{and} \quad S_Z|-\frac{1}{2}\rangle = -\frac{\hbar}{2}|-\frac{1}{2}\rangle \quad (1.2)$$

The Zeeman interaction is of critical importance as it is almost always the dominant energy and EPR experiment due to the strong applied field. Other effects can then be represented as perturbations on the eigenstates of the Zeeman interaction. The energy difference that is observed between the spin states in the presence of a magnetic field (the Zeeman Splitting) is $\Delta E = E_{\frac{1}{2}} - E_{-\frac{1}{2}} = g_e\mu_\beta B_0$. This means that for electrons anti-alignment (i.e. $|-\frac{1}{2}\rangle$) is the energetically preferred state; this energy difference forms the basis of EPR.

1.1.1 Continuous Wave Magnetic Resonance

The simplest magnetic resonance experiment is based on the absorption of electromagnetic radiation by a spin system. The photons of frequency ν carry energy $E_{\text{photon}} = \hbar 2\pi\nu = \hbar\omega$. If the energy of the photons matches the energy separation of the $|\frac{1}{2}\rangle$ and $|-\frac{1}{2}\rangle$ states, then the photon can be absorbed and the spin state will “flip”. That is, when on resonance

$$\hbar\omega = g_e\mu_\beta B_0 \quad (1.3)$$

Band Name	Magnetic Field (T)	Spectrometer Frequency for $g = 2$ (GHz)
S	0.11	3
X	0.34	9.5
Q	1.25	35
W	3.4	95
D	5.0	140

Table 1.1: Common Spectrometer Fields and Frequencies. List of common EPR spectrometer frequencies and the associated name of the Band.

we induce transitions between $|\frac{1}{2}\rangle$ and $|\frac{-1}{2}\rangle$ states. The resonance frequency scales linearly with the applied field (with small shifts due to small changes in g_e), and Table 1.1 shows common spectrometer frequencies. The strength of the irradiating magnetic field (B_1) is small compared to the strong applied field (B_0), and so this problem can be addressed using time-dependent perturbation theory. The interested reader can consult a text book on quantum mechanics (for instance Sakurai²¹) for the precise working of the time-dependent, oscillating classical field. The full quantum mechanical approach is in agreement with the physical picture above; transitions are induced between the states when the irradiation is on resonance. Of importance is that both $|\frac{1}{2}\rangle \rightarrow |\frac{-1}{2}\rangle$ and $|\frac{-1}{2}\rangle \rightarrow |\frac{1}{2}\rangle$ transitions are

induced (emission and absorption). However, the rates of these are determined by the populations of the two states. That is

$$\frac{P_{\text{Absorption}}}{P_{\text{Emission}}} = \frac{N_{|\frac{1}{2}\rangle}}{N_{|-\frac{1}{2}\rangle}} \quad (1.4)$$

where $P_{\text{Absorption}}$ is the probability of absorption ($|-\frac{1}{2}\rangle \rightarrow |\frac{1}{2}\rangle$), P_{Emission} is the probability of emission ($|\frac{1}{2}\rangle \rightarrow |-\frac{1}{2}\rangle$), $N_{|\frac{1}{2}\rangle}$ is the number of spin-up spins and $N_{|-\frac{1}{2}\rangle}$ is the number of spin-down spins. Thus, in principle, if the populations of the spin-up and spin-down state are equal, no net absorption (or emission) occurs. In an applied field, the Zeeman interaction forces the energetic preference of the lower energy, state $|-\frac{1}{2}\rangle$, and so we have a net absorption of the radiation. This absorption can be measured experimentally by monitoring the transmission through a paramagnetic sample. Far off resonance, no absorption from spins will occur, but when the resonance condition is achieved, the sample will absorb. In practice, it is far easier experimentally to fix the irradiation frequency and change the magnetic field so that the energy splitting matches the irradiation frequency, while slightly modulating the magnetic field to acquire a derivative spectrum with lock-in detection.¹⁹ This is a typical continuous wave (cw) EPR experiment. Cw EPR remains a common spectroscopic tool though pulsed EPR has emerged as a more powerful technique.

The spin states will obey Boltzmann statistics, so that

$$\frac{N_{|-\frac{1}{2}\rangle}}{N_{|\frac{1}{2}\rangle}} = \exp\left(\frac{\Delta E}{kT}\right) = \exp\left(\frac{g_e\mu_\beta B_0}{kT}\right) \quad (1.5)$$

where k is Boltzmann's constant, and T is the temperature. By decreasing temperature, we can increase the number of $|-\frac{1}{2}\rangle$ spins and therefore, increase net absorption. As we measure the amount of absorption, EPR signal strength increases as the temperature is lowered for an $S = \frac{1}{2}$ sample. Generally, the populations of the two energy levels are not substantially different in EPR. For instance, at $B_0 = 0.35$ T (X-Band) and at room temperature ($T = 300$ K), $\frac{N_{|-\frac{1}{2}\rangle}}{N_{|\frac{1}{2}\rangle}} = .998$, and even at $T = 100$ K $\frac{N_{|-\frac{1}{2}\rangle}}{N_{|\frac{1}{2}\rangle}} = .892$. However, the combination of high magnetic fields and low temperatures can generate nearly completely polarization, where $>99\%$ of the spins are in the $|-\frac{1}{2}\rangle$ state.

An important question therefore becomes, what does the cw EPR signal tell us? At first glance, it appears to be a rather unexciting experiment, which provides the location of the resonance $\hbar\omega = g_e\mu_\beta B_0$, but does not seem to provide substantial information: \hbar , and μ_β are physical constants that are known to extreme precision, B_0 can be measured to high accuracy in other ways, and g_e for a free electron is also known to high precision. However, for a real system electrons exist in an orbital, so the electron g -value is no longer fixed to the free electron value g_e due to the (usually small) components of orbital angular momentum that are not completely quenched.²² In fact, in general the g -value depends on the

degree of spin-orbit coupling, and the orientation of the orbitals with respect to the magnetic field (i.e. $g(\theta, \phi)$).

Additionally, our current description of the spin Hamiltonian does not include any other interactions between the spins and their environment, besides the applied magnetic field. In reality, a multitude of interactions are present. For instance, many nuclear species also have spin (i.e. ^1H , ^{13}C , and ^{15}N are $S = \frac{1}{2}$, while ^2H and ^{14}N are $S = 1$), and the dipole moments of the nuclear spins can interact with the electrons through hyperfine interaction ($\mathcal{H}_{\mathcal{HF}}$). Alternatively, when the paramagnetic species are in proximity to one another (or to another paramagnetic species), they interact leading to spin-spin interaction (\mathcal{H}_{SS}). When multiple spins are strongly coupled, effects can be seen from the Zero Field Splitting (\mathcal{H}_{ZFS}), which makes the energy states no longer degenerate at $B_0 = 0$

Therefore, with the Zeeman term of the Hamiltonian (\mathcal{H}_Z), we can write

$$\mathcal{H} = \mathcal{H}_Z + \mathcal{H}_{\mathcal{HF}} + \mathcal{H}_{SS} + \mathcal{H}_{ZFS} \quad (1.6)$$

where the \mathcal{H}_{ZFS} only contributes if the system has spin $S > \frac{1}{2}$ (a high-spin system). Because the Zeeman term still dominates, the eigenstates of S_Z (namely $|\frac{1}{2}\rangle$ and $|\frac{-1}{2}\rangle$) are still “good” basis kets to describe the system and we can look at the perturbations caused by the other terms (as well as the effect of the orientation-dependent g -values) as simply shifting the energy of the spins. Because each spin experiences a slightly different environment (contributing, potentially, a different g -value, a different coupling to nuclei and a different coupling to other

spins), the EPR transition becomes “smeared” by these other terms. As a result, the shape and location of the resonances are embedded in the EPR spectrum, and the spectrum therefore encodes critical information about the *local* environment surrounding the paramagnetic centers. The term “local” depends on the species and interactions in questions, but can extend from Å-scale to 10 nm.

In order to understand the EPR spectrum, we will consider the major contributors to the EPR Hamiltonian below. Here the focus will be on the relevant parameters for studies of biological systems. However, we first introduce the technique of pulsed EPR and discuss its advantages over cw EPR.

1.1.2 Pulsed EPR

Thus far we have considered the EPR spectrum in the frequency/field domain, as measured by continuous wave EPR. An alternative approach in magnetic resonance is to carry out measurements in the time domain. This is done by applying pulses to excite the spin system, and observing the resulting oscillating emission from the magnetic dipoles. A major advance in NMR spectroscopy came with the development of pulsed NMR, as it allows the entire spectrum to be measured at once by measuring in the time domain, rather than measuring each frequency component separately by sweeping through the resonance. Pulsed NMR offers improved sensitivity and rapidly reduces measurement time, but also allows combinations of pulses to isolate specific parts of the spin Hamiltonian or directly

measure the relaxation of the spin systems. Pulsed NMR has almost entirely replaced cw NMR as a result of the dramatically improved performance and capabilities. Pulsed EPR offers many of the same advantages over cw EPR, but both techniques remain in use as a result of the difficulty of fully exciting the entire EPR spectrum (due to its broadness).

Simple time dependent perturbation theory for a two level system (such as the $S = \frac{1}{2}$ spins) shows that a harmonic potential, tuned to the energy difference between the two states, induces a time-dependent change in the spin state. Assuming that we begin in the $|\frac{1}{2}\rangle$ state, this emerges as a rotation of the spin state of the system by the pulse given by

$$|a_{final}\rangle = \cos(\beta)|\frac{1}{2}\rangle + \exp(i\phi)(1 - \cos(\beta))|\frac{1}{2}\rangle \quad (1.7)$$

where β is the tip angle and ϕ is the phase of the applied pulse. The tip angle is determined by the strength of the B_1 and the length (t_p) of the pulse (which in EPR is usually rectangular) by $\beta = \gamma_e B_1 t_p$.²³ We can represent this on a Bloch sphere by considering the north and south poles of the sphere as representing $|\frac{1}{2}\rangle$ and $|\frac{3}{2}\rangle$ states respectively, the other parts of the surface of the sphere represent the full ket space of the system, composed of the arbitrary (complex) linear combinations of $|\frac{1}{2}\rangle$ and $|\frac{3}{2}\rangle$. Then pulses act to rotate the spins about the Bloch sphere: β determines how far from the z-axis the spins are tipped, and ϕ determines the orientation in the transverse plane. While this description is for

a single spin, the system is a large ensemble of spins, all in different spin states (with only a net preference for the $|-\frac{1}{2}\rangle$ state in thermal equilibrium). However, it is possible to describe the entire ensemble of spins by the net magnetization of the system, and simply examine rotations of this magnetization vector.

In equilibrium, the ensemble of spins is “silent”; though individual spins are constantly reorienting, flipping, and precessing, the sum of these is extremely small. When the net magnetization is no longer anti-parallel to the field axis, a torque is placed on the spins by the large applied field and they begin to precess. This Larmor precession occurs at a frequency that is identical to the resonance frequency (and therefore is determined by the applied magnetic field). The precession of magnetic dipoles in the field generates emission of radiation at the precession frequency, which is then detected. Because the emitted radiation can be measured phase-sensitively, this allows the characterization of M_X and M_Y , corresponding to the magnetization in the x- and y- directions, respectively. The strength of the emission is controlled by the transverse component of the magnetization, so that when the magnetization is fully in the x/y-plane we get a signal maximum, and an absence of signal when the magnetization is parallel or anti-parallel to the magnetic field. The signal measured as a function of time is called the “Free Induction Decay” (FID), and is damped as a result of the distribution of resonance frequencies in the sample—this corresponds physically to all the spins decohering from one-another as they precess. This distribution corresponds to the

lineshape of the spectrum and Fourier Transform (FT) of the time domain signal will yield the same spectrum as observed with cw EPR.

We immediately see the potential power of pulsed EPR, as it allows us to apply a pulse, and measure a decaying signal, and through FT recover the entire spectrum! As these experiments can be carried out with a repetition rate of kHz (and even higher depending on relaxation times), this allows a immense improvement in data collection rate. However, if the distribution of resonance frequencies exceeds the bandwidth of the pulse (due to the pulse being too long), then only a portion of the spectrum is excited. In this case, the pulse does not cover the entire spectrum and the FID only contains spins within the excitation bandwidth and the rest are filtered. This occurs commonly in EPR (where broad lines dominate), and can diminish the advantage of pulsed EPR.

Beyond the potential improvements to data collection, pulsed magnetic resonance is powerful because of its ability explicitly measure the relaxation times of the spins in the system. For EPR in particular, the inhomogeneously broadened lines obscure any information about the relaxation times of the individual spins. However, in practice each spin has two relevant relaxation times: T_1 and T_2 , which control relaxation of the spins back to equilibrium.

The spin-lattice relaxation time, T_1 , controls the spin's return to thermal equilibrium, where spin populations are given by a Boltzmann distribution, which involves a net change in energy of the system. It can be measured with a two

pulse experiment called “inversion recovery” (though there are several other varieties).^{17,20} The first pulse has a tip angle of π , which inverts the magnetization, and generates no signal. A second $\frac{\pi}{2}$ pulse follows which tips the magnetization back into the plane in the -x direction, which can be measured. However, if the two pulses are separated in time, T_1 relaxation drives the magnetization back towards equilibrium, resulting in final magnetization changing from -x to +x. Thus the measured change in the x-magnetization from negative to positive as a function of the inter-pulse spacing characterizes the T_1 time. An alternative, but similar method called “saturation recovery” replaces the inversion pulse with a saturation pulse, so that initial signal starts from 0.^{17,20}

The spin-spin relaxation time, T_2 , characterizes the time for which spins precessing in the plane may stay coherent assuming they have the same central resonance frequency. That is, this relaxation process neglects effects from inhomogeneous broadening, which acts as a constant shift in spins’ resonance frequency. This can also be measured in a two pulse experiment called a “spin echo”, where a $\frac{\pi}{2}$ pulse is applied to excite the spins into the x/y-plane.²⁴ The spins are then allowed to decohere (and the resulting FID damps to zero), at which point a π pulse inverts the spins in the plane, and results in the spins re-cohering, which recovers the FID (now called an echo) at a time after the second pulse equal to the pulse separation. The echo works by eliminating the different static precession frequencies exhibited by spins in the inhomogeneously broadened spectrum.

However, it does not eliminate the random perturbations that cause a spin's frequency to shift dynamically during the experiment. Therefore, not all the spins are refocused into the echo, as those which are disrupted during the echo do not properly refocus. Therefore, as the pulse spacing is extended the echo signal is reduced toward zero at a rate determined by the spin-spin relaxation time T_2 . In EPR we typically do not discuss T_2 , but rather T_M , the "phase memory time"; as we are incapable of exciting the entire EPR spectrum, we are only able to measure a portion of the spectrum at time, and so can not determine a "true" T_2 . It is worth noting that the spin echo is an incredibly robust experiment, and that even in the absence of perfectly set pulse lengths an echo is formed (though it is not optimal).

In addition to offering the capability to quantify the relaxation times directly, pulsed magnetic resonance offers exceptional versatility. For instance, pulses at different frequencies are possible to excite different populations and spin states. This allows probing of interactions between different spin populations. When the frequency and phase can be precisely controlled the nature of interactions can be interrogated to isolate only particular kinds of interactions. NMR makes extensive use of complex pulse sequences with many different frequencies (2, 3, and 4 frequencies in NMR) to untangle the complex web of nuclear couplings. Doing so allows them to assign resonances to specific residues and to determine 3D structures of proteins and biomacromolecules. Currently the same degree of

sophistication is not present in pulsed EPR spectroscopy, but multi-frequency work has now become common, and phase cycling is standard to help suppress artifacts.

1.1.3 Major Components of the Spin Hamiltonian

Zeeman Term and g-Anisotropy

In calculating the Zeeman term we note that, because the electron exists in a non-symmetric orbital, the g -value depends on the relative orientation of the molecule with respect to the external field. Therefore $\mathcal{H}_Z = \frac{\mu_B}{\hbar} \vec{B}_0 \bar{\mathbf{g}} \vec{S} = \frac{\mu_B}{\hbar} g(\theta, \phi) S_Z B_0$ where \vec{S} is the spin operator vector, θ angle between the molecular z-axis and the laboratory z-axis, while ϕ defines the orientation of the projection of the laboratory z-axis on the x/y plane of the molecular coordinates. Here we utilize the principle axes of the g -tensor ($\bar{\mathbf{g}}$) to simplify the expression. Straight-forward applications of Euler rotations show that²⁰

$$g(\theta, \phi) = \sqrt{g_{xx}^2 \sin(\theta)^2 \cos(\phi)^2 + g_{yy}^2 \sin(\theta)^2 \sin(\phi)^2 + g_{zz}^2 \cos(\theta)^2} \quad (1.8)$$

where g_{xx} , g_{yy} , and g_{zz} are the principle values of the g tensor (typically called the g -values). These g -values can contain important information about the structure and shapes of the orbitals the electron resides in. However, typically the g -values are largely determined by the structure of the probe molecule (when one

is used), and so only subtle (though detectable) changes emerge due to the local chemical environment when studying spin-labeled biological systems.

Hyperfine Coupling

The Hyperfine interaction results from the interaction of the nuclei with the electron, and can be written

$$\mathcal{H}_{\mathcal{H}\mathcal{F}} = \sum_k \vec{S} \cdot \bar{\mathbf{A}}_k \cdot \vec{I}_k \quad (1.9)$$

where \vec{I}_k is the spin operator vector for k^{th} nucleus, and $\bar{\mathbf{A}}_k$ is the hyperfine coupling tensor for the k^{th} nucleus. The hyperfine interaction can be broken into two components to describe the interaction between an electron and a nucleus. $\mathcal{H}_{\mathcal{H}\mathcal{F}} = \mathcal{H}_{\mathcal{H}\mathcal{F}}^{\mathcal{D}\mathcal{D}} + \mathcal{H}_{\mathcal{H}\mathcal{F}}^{\mathcal{I}}$, where $\mathcal{H}_{\mathcal{H}\mathcal{F}}^{\mathcal{D}\mathcal{D}}$ is the through-space dipole-dipole interaction and $\mathcal{H}_{\mathcal{H}\mathcal{F}}^{\mathcal{I}}$ is the isotropic, contact interaction. The through-space interaction emerges because the nuclear spin is itself a dipole which interacts with the paramagnetic species by generating a weak magnetic field.

The through-space interaction between two, generic magnetic dipoles (not limited to a nuclear-electron interaction) is given by¹⁵

$$\mathcal{H}_{\mathcal{D}} \sqrt{\lambda \dagger + \nabla} = \frac{\mu_0}{4\pi} \frac{1}{r^3} \mu_1 \mu_2 [\vec{S}_1 \vec{S}_2 - \frac{3}{r^3} (\vec{S}_1 \cdot \vec{r})(\vec{S}_2 \cdot \vec{r})] \quad (1.10)$$

where \vec{r} is the interspin vector, $\mu_1 = \hbar\gamma_1$ and $\mu_2 = \hbar\gamma_2$ are the magnetic moments of the two spins, and \vec{S}_1 and \vec{S}_2 are the spin operator vectors for the two spins.

The angular dependence of the dot products $\vec{S}_1 \cdot \vec{r}$ and $\vec{S}_2 \cdot \vec{r}$ can be eliminated by integrating over the spatial electron distribution (assuming a fixed nuclear center) and then the hyperfine interaction can be written as²⁰

$$\mathcal{H}_{\mathcal{H}\mathcal{F}}^{\mathcal{D}\mathcal{D}} = \vec{S} \cdot \vec{\mathbf{T}} \cdot \vec{I} \quad (1.11)$$

with

$$T_{ij} = \frac{\mu_0}{4\pi} \frac{1}{r^3} \mu_1 \mu_2 \langle \langle \psi_0 | \frac{3r_i r_j - \delta_{ij} r^2}{r^2} | \psi_0 \rangle \rangle \quad (1.12)$$

where r_1, r_2, r_3 are the directions x, y, and z, and $|\psi_0\rangle$ is the ground state wavefunction of the electron.

As opposed to the dipolar interaction, the contact interaction emerges from orbital overlap between the nuclear spin and the electron spin. For instance, an s-orbital, which is spherical, does not vanish at the nucleus, and thus the wavefunctions affect one another. The isotropic component of the Hamiltonian can be written

$$\mathcal{H}_{\mathcal{H}\mathcal{Z}}^{\mathcal{I}} = a_k^{iso} \vec{S} \cdot \vec{I}_k \quad (1.13)$$

where $a_{iso} = \frac{2}{3} \frac{\mu_0}{\hbar} (g_e \mu_\beta) (\hbar \gamma_n) |\psi_0(o)|^2$, where $\psi_0(0)$ is the spin density at the nucleus. Electrons in orbitals other than s (which is the only orbital with a non-vanishing contribution at the origin) can result in isotropic hyperfine interactions through polarization of the s-orbital or through hybridization with s-orbitals²⁵

Hyperfine interactions can be probed with both pulsed and cw EPR (and other double resonance techniques), and allow identification of the local environment of the probe to be investigated; for instance, identifying the degree pH of the solvent nearby,²⁶ or observing coupling to particular nuclear spins.

Spin-Spin Interactions

We consider situations where two spin are close enough to one another to interact. The interaction Hamiltonian can be divided into two components.

$$\mathcal{H}_{SS} = \mathcal{H}_{ex} + \mathcal{H}_{dd} \tag{1.14}$$

where \mathcal{H}_{ex} is the exchange interaction, and \mathcal{H}_{dd} is the dipole-dipole coupling between the spins.

Exchange interactions emerge because of orbital overlap between the two electron spins. When this occurs, the indistinguishable electron spins are able to exchange. As a result of the requirements of symmetry under exchange, an energy difference emerges between the spin triplet states and the singlet states. This emerges only as a result of symmetry considerations, and not as the result of a

spin dependent component of the Hamiltonian.²⁷ Exchange interactions can generally be neglected for situations where the electron spins are localized far apart from one another in solid samples. What constitutes sufficiently far apart depends on the paramagnetic species and its orbital configuration, but for a typical $S=\frac{1}{2}$ system. Alternatively, for liquids the exchange interactions emerge largely from situations where electrons collide and are in close proximity for a short length of time, and so depend on concentration and the rate of collisions.²⁸

Generally more relevant to the work discussed in this dissertation are the dipole-dipole interactions between electron spins. Indeed, the distance dependence of this interactions forms the basis for a wide variety of applications of EPR to biology, as it allows determination of interspin distance, which can be used to determine structure. The dipole-dipole interactions for electron spins is essentially identical to the dipole-dipole coupling component of the hyperfine interaction in Eq. 1.10. Only, instead of describing the coupling between electrons and nuclei, we investigate the coupling between two electrons. We can expand the equation in Eq. 1.10 by writing out the dipolar interaction as a sum of a series of contributions¹⁵

$$\begin{aligned}
\mathcal{H}_{dd} &= \frac{\mu_0}{4\pi} \frac{1}{r^3} \mu^2 (A + B + C + D + E + F) \\
A &= (1 - 3 \cos(\theta)^2) S_Z^1 S_Z^2 \\
B &= -\frac{1}{4} (1 - 3 \cos(\theta)^2) (S_+^1 S_-^2 + S_+^1 S_-^2) \\
C &= -\frac{3}{2} \sin(\theta) \cos(\theta) \exp(-i\phi) (S_Z^1 S_+^2 + S_+^1 S_Z^2) \\
D &= -\frac{3}{2} \sin(\theta) \cos(\theta) \exp(i\phi) (S_Z^1 S_-^2 + S_-^1 S_Z^2) \\
E &= -\frac{3}{4} \sin(\theta)^2 \exp(-2i\phi) S_+^1 S_+^2 \\
F &= -\frac{3}{4} \sin(\theta)^2 \exp(2i\phi) S_-^1 S_-^2
\end{aligned} \tag{1.15}$$

where θ is the angle between the static field B_0 and the interspin vector. Additionally, S_+ and S_- are raising and lowering operators, which raise and lower the angular momentum of a spin state by 1. They are defined by $S_+ = S_X + iS_Y$ and $S_- = S_X - iS_Y$.²¹ We have also assumed that $\mu_1 = \mu_2 = \mu$ as we are generally considering two interacting electrons (which will have identical, or nearly identical, magnetic moments). Looking at this expression for the dipolar interaction, we recognize that, terms C, D, E, and F include flipping spins (through the raising and lowering operators S_+^1 etc) and therefore are not energy conserving interactions. Therefore, these terms will be small compared to the energy conserving terms in the Hamiltonian. A is always energy conserving (it does not change the spin states of the electrons), whereas B *can* be energy conserving, if the flip-flop interaction occurs between two spins with identical transition energies (in this

case, the energetic cost of flipping a $|-\frac{1}{2}\rangle$ to $|\frac{1}{2}\rangle$ is paid by flopping another spin $|\frac{1}{2}\rangle$ to $|-\frac{1}{2}\rangle$. However, typically in EPR the inhomogeneous broadening (due to g -value and hyperfine anisotropies) spread the resonances so that B is not energy conserving. Thus, we typically take the *secular* approximation, which only preserves the energetically neutral term (A), so that

$$\mathcal{H}_{dd}^{secular} = \frac{\mu_0}{4\pi} \frac{1}{r^3} \mu^2 (1 - 3 \cos(\theta)^2) S_Z^1 S_Z^2 \quad (1.16)$$

while term B is referred to as the “pseudo-secular” part of the dipolar interaction. Typically it will be neglected, but becomes relevant in some situations discussed below.

Zero Field Splitting

In the case that multiple electrons are strongly coupled together, they can be represented as a high-spin system, where $S > \frac{1}{2}$.²¹ This generally occurs in situations where multiple unpaired electrons exist in proximal orbitals. In high-spin systems the strong interaction of the electrons eliminates the degeneracy of the energy level at zero field. This emerges as a so-called “zero field splitting” that can be expressed as

$$\mathcal{H}_{ZFS} = \vec{S} \cdot \vec{D} \cdot \vec{S} \quad (1.17)$$

where $\bar{\mathbf{D}}$ is the traceless zero-field interaction tensor.^{20,29} The zero field splitting as most paramagnetic probes used to probe biological systems are $S = \frac{1}{2}$, and so the ZFS does not contribute. However, the work in this thesis includes extensive use of high-spin Gd^{3+} , whose zero field splitting, while small relative to the applied field, plays an important role in determining the spectrum. More details about the specific properties of Gd^{3+} can be found in Sections 2.4 and 3.2.

Neglected Terms

Above we have neglected to discuss explicitly terms associated with the nuclear energy states (excepting the hyperfine interaction, where the nuclear spin directly effects the electron spin). Specifically, there is no mention of the nuclear Zeeman interaction (which gives rise to NMR), nor the Nuclear Quadrupole interaction (where the nuclear spins states interact with gradients of the electrostatic field^{15,20}). The reason for the omission is their small effect compared to the electron spin terms. Although using techniques where nuclear frequencies are probed by EPR, these effects can be seen²⁹ they are generally negligible in EPR, and do not play a major role in the studies here. Notice this is **not** to say that nuclear spins are not relevant in EPR; indeed, they play a critical role in relaxation of electron spins. It is rather to say that the nuclear Zeeman and quadrupolar energies are sufficiently small not to shift the spectral features.

1.2 EPR Distance Measurements in Biological Systems

Electron Paramagnetic Resonance offers a powerful capability to probe structure and dynamics in biological systems that resist other techniques.³⁰ Although some biological systems contain inherent paramagnetic ions in, for instance, metal binding sites, we are not limited to this class of protein thanks to the availability of commercial, stable free radicals which have been functionalized to site-specifically bind to a biological system. The prototypical class of these labels belong to the nitroxide family. As an example consider the most common free radical used by to label proteins for EPR studies, the MTSL ((S-(2,2,5,5-tetramethyl-2,5-dihydro-1H-pyrrol-3-yl)methyl methanesulfonothioate)) radical,³¹ shown in Fig. 1.1. It is a stable nitroxide molecule with a single, unpaired electron localized between the nitrogen and oxygen atoms. It is regularly used to label cysteine residues by forming a disulfide bond between the thiol-groups of the cysteine and the MTSL. When combined with site-directed mutagenesis³² to modify the amino acid sequence of a protein, and place a cysteine at specific location in the protein, the technique is commonly called Site-Directed Spin Labeling.^{33,34} Because using standard biochemistry tools one can usually introduce a paramagnetic probe into a biomolecule in rather arbitrary locations (while labeling can be disruptive, it is not uncommon that many protein residues can be labeled without substantially modifying

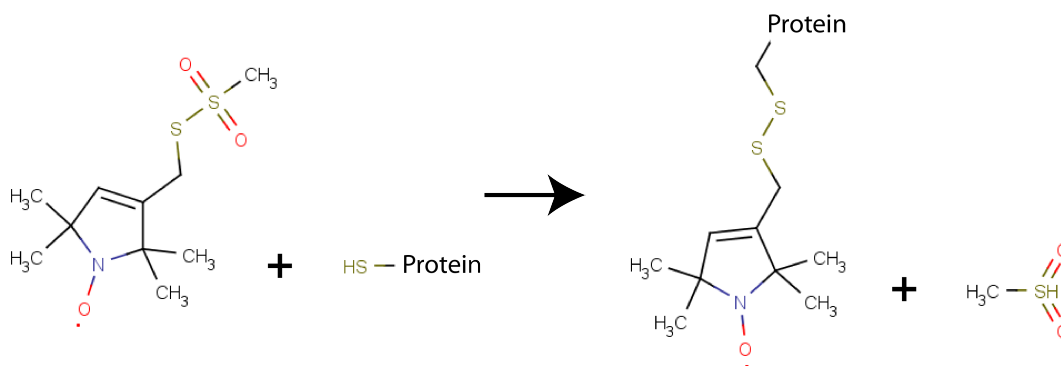


Figure 1.1: MTSL Spin Label. MTSL³¹ is a standard, stable radical molecule that has been functionalized so allow easy labeling of the cysteine residue of a protein. As is shown here, the MTSL forms a disulfide bond with the thiol group of the cysteine residue. Combined with (careful) application of site-directed mutagenesis this allows this stable paramagnetic molecule to be specifically placed at a chosen location within a protein. Similar labeling schemes exist for other kinds of biomacromolecules, which is a fundamental basis for the power of EPR as a site specific probe of local environment and structure in biological samples.

the biomacromolecule's structure or function), this allows targeted investigation of the local environment of parts of proteins, biopolymers, peptides, DNA, and other important biological systems.^{31,35-37} While a wide variety of structural and dynamics information are therefore accessible in a site-specific fashion, one of the most important applications of EPR is for distance measurement between spins labels, which is what will be a focus of this dissertation.

The combined ability to both introduce spin labels with residue-specific control, and to measure the distance between the spin labels opens the door to determine sparse, targeted structural information. In particular, two kinds of distance measurements are usually undertaken in biology. The first probes intramolecular distances, meaning that the two spin labels are introduced onto a single biomacro-

molecule (for instance a protein), and then the distance measured corresponds to the distance between these two parts of the protein. These techniques have proven useful in allowing targeted investigations of structure for cases where more global structural techniques (such as x-ray crystallography or NMR structural determination) fail to resolve the structure.^{30,38,39} This is in particular helpful for proteins that resist crystallization and proteins which are too large to be studied with NMR. Further, EPR has emerged as an important technique to study membrane proteins, which are only functional when embedded in a lipid membrane, or detergent micelles.⁴⁰ In these cases, the increased complexity of the environment complicates other measurements. However, due to its targeted nature EPR studies are often able to address specific questions of structure. Further, these measurements can address functional conformational changes by monitoring changes in specific distances during following activation.^{39,41}

Alternatively, EPR can be used to probe intermolecular distances, where the organization of many biological molecules can be monitored by, for instance, labeling two proteins that are believed to interact with one another. It is in this realm, which includes studies of oligomerization (where multiple proteins interact to form a larger structure) that EPR can sometimes be most powerful as these large structures are substantially difficult to crystallize, and are generally too large for NMR structural determination.⁴² Other work in this field has examined oligomerization of membrane proteins.⁴¹

While the details of the spin-labeling process may differ between the desired system and whether intermolecular, or intramolecular distances are probed, the EPR techniques remain the same. We will discuss the two most commonly used techniques for distance measurement: cw-lineshape analysis and Double Electron Electron Resonance (DEER). As discussed in Section 1.1, the interaction of electron spins can be described by the combination of a dipolar (through-space) effect, and an exchange interaction. While both reveal information about the spins system, we will here largely neglect the exchange interaction. It is generally the case that for $S=\frac{1}{2}$ spin label systems in frozen environments, the exchange interaction can be neglected for distances below ~ 0.8 nm.⁴³ As the strength of EPR is typically seen to be its ability to investigate long distances (>1 nm), it often (though by no means always) has a small or negligible effect for EPR distance measurements. It is worth adding the caveat that these distance limits, while generally valid, hold strictly for a through-space, or through-solvent exchange interaction (that is, when the spins exist on different molecules and are approaching each other). Through-bond exchange interactions, where the electron-electron exchange effect can be relevant even if though the spins are >1 nm apart, emerge in ruler like molecules, with varying degrees of exchange depending on the details of the molecular structure.⁴⁴ Thus, regardless of the details of the sample, the spin label or the technique, at its heart the majority of EPR distance measure-

ment (and all those discussed here) rely on probing interspin distances through the dipolar interaction.

1.2.1 cw-lineshape Analysis

The dipole interaction of neighboring spins can be observed in several different ways. The simplest experimentally is through the lineshape effect that occurs as a result of the dipolar interaction between spins. We can consider a single spin (spin 1), which yields a single resonance line (infinitely narrow in this approximation) at ω_0 . If we introduce a second spin (spin 2) some distance away, we can then see that this spin will generate a local magnetic field at spin 1, which will depend on the spin state of spin 2. If spin 2 is $|\frac{1}{2}\rangle$, then its magnetic field will add to that of the applied field, thus increasing ω_0 . Alternatively, if spin 2 is $|-\frac{1}{2}\rangle$, then ω_0 will be decreased. These changes in lineshape allow us to investigate structure as the strength of the field from spin 2 will depend on the separation of the two spins, as well as the relative orientation of the interspin vector.

An explicit calculation of the lineshape resulting from dipolar broadening of pairwise interacting spins was first carried out by Pake⁴⁵ in examining coupling between nuclear spins, which we follow here. From Eq. 1.15, we immediately dismiss contributions from terms C-F as they are not energy conserving. In following Pake's work, we will keep the pseudo-secular term (B), and arrive at the result that

$$B_{dipolar} = B_{original} \pm \frac{3}{4} \frac{\mu_0 \mu (3 \cos(\theta)^2 - 1)}{4\pi r^3} \quad (1.18)$$

where $B_{dipolar}$ is the location of the resonance with the dipolar interaction, while $B_{original}$ is the original resonance location. Thus, for a particular distance and orientation of the spins, we expect to observe two lines “split” from the original resonance. However, for a spin-labeled protein, the orientation of the interspin vector is randomly distributed in space, which gives rise to a variety of splittings, with a particular distribution called a Pake pattern. Its functional form is⁴⁵

$$P(r, B) \propto \begin{cases} (\frac{B}{\alpha} + 1)^{-\frac{1}{2}} & -\alpha \leq B \leq 2\alpha \\ (-\frac{B}{\alpha} + 1)^{-\frac{1}{2}} & -2\alpha \leq B \leq \alpha \end{cases} \quad (1.19)$$

where $\alpha = \frac{3}{4} \frac{\mu_0}{4\pi} \frac{1}{r^3} \mu_2$. In this expression, we have assumed that the $|\frac{1}{2}\rangle$ and $|\frac{1}{2}\rangle$ states are equally populated. For an $S = \frac{1}{2}$ spin at X-Band, this is a good approximation down to low temperatures, but begins to break down at higher magnetic field. For a single unpaired electron, $\alpha = \frac{1.39}{r^3}$ mT nm³, and Fig. 1.2 shows a typical Pake pattern, with its distinctive shape, which includes large peaks at $\pm\alpha$. It is worth emphasizing that, as $\alpha \propto \frac{1}{r^3}$, the width of the entire Pake pattern increases rapidly as the interspin distance is reduced.

The approach of Pake⁴⁵ is carried out generally for two spins, but is particularly applied to protons. For protons, the inclusion of the pseudo-secular term is generally justified, as the resonance frequency in protons is degenerate when in the same chemical environment. However, for the case of electron spins, the

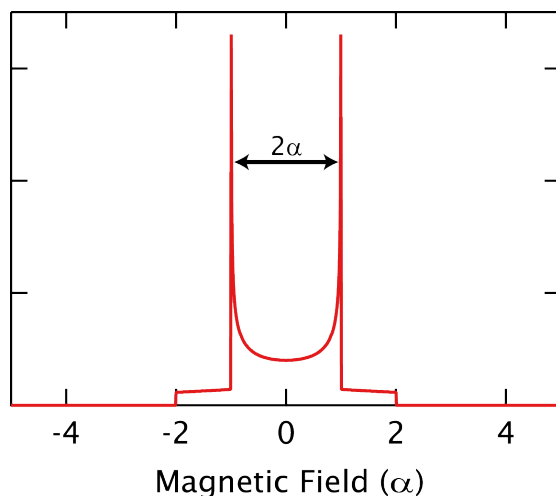


Figure 1.2: $S = \frac{1}{2}$ Pake Pattern. The Pake pattern describes the dipolar broadening of an infinitely narrow resonance due to the presence of neighboring spins of a fixed interspin distance. The shape emerges due to the weightings imposed by having an isotropic distribution of orientations of the interspin vector. When combined with a known distance distribution, the Pake pattern allows determination of the full broadening pattern in a system.

inclusion of the pseudo-secular term in the calculation is not always appropriate. For nitroxide based labels, the inhomogeneous broadening that emerges from orientation dependence of the g - and A -values, means that two neighboring spins are (often) not degenerate. In particular, previous work has distinguished between strong and weak dipolar coupling regimes,^{44,46} determined by the extent of the EPR spectrum relative to the dipolar interaction. In cases where the unbroadened linewidth is much smaller than the dipolar interaction, the EPR transitions are nearly degenerate, and the strongly broadened Pake pattern (above) should be used. Alternatively, when the nitroxide spectrum is substantially broader than the dipolar interaction, the Pake broadening maintains the same *form*, but nar-

rows slightly. Thus, for these weakly coupled cases we can still utilize Eq. 1.19, with the exception that we replace α with $\alpha_{weak} = \frac{1}{2} \frac{\mu_0}{4\pi} \frac{1}{r^3} \mu = \frac{0.93}{r^3} \text{ mT nm}^3$. That is, the splitting is reduced by a factor of $\frac{2}{3}$ as a result of neglecting the pseudo-secular terms.⁴⁴ In nitroxides measured at X-Band, strong coupling is dominant for interspin distances below $\sim 0.7 \text{ nm}$, while fully weak-coupling emerges above $\sim 1.5 \text{ nm}$, with a region of intermediate coupling in between.⁴⁶ In this intermediate region, where neither strong or weak coupling is complete, there is some error in these calculations.⁴⁴

The Pake patterns above describe the interactions between a single pair of spins, and hence characterizes the dipolar broadening at a single interspin distance, for an infinitely narrow line. In practice, of course, EPR lineshapes are substantially inhomogeneously broadened, and a single, fixed distance is rarely observed in real biological systems (if for no other reason than the linker for the paramagnetic probe can often form different conformations). Thus a Pake pattern, where one could simply read-off a distance from the splitting, is not observed and more involved technique is necessary to measure distances from the EPR spectrum. In particular, Steinhoff et al.,⁴³ and Rabenstein and Shin⁴⁷ have developed a technique based on the idea that the spectrum in the presence of dipolar broadening can be represented by the a convolution of the unbroadened lineshape with the broadening function. The unbroadened (often called “intrinsic”) spectrum

then encodes all the information of the inhomogeneous line broadening that is already part of the system. Thus, we can write

$$S_{broad} = \int S_{intr}(B)D(B - B^*)dB^* \quad (1.20)$$

where $D(B)$ is the dipolar broadening pattern, S_{broad} is the broadened spectrum, and S_{intr} is the intrinsic spectrum. In the case of a single, fixed interspin distance the broadening function would simply be the Pake pattern, however, a more general broadening pattern can be generated if the distance distribution is known:

$$D(B) = \int_0^\infty W(r)P(r, B)dr \quad (1.21)$$

where $W(r)$ is the distribution of distances.

Thus, experimentally, it is possible to determine the distance between two spins using two measurements: a measurement of the EPR spectrum where the spins are coupled, and a measurement where they are not. A typical approach for studying a particular protein structure (for instance, asking how far apart two protein residues are in a particular conformation) would be to generate 3 samples. In the first, both residues are labeled with a paramagnetic species (through SDSL), and this spectrum represents S_{broad} . A second pair of measurements are made on the pair of singly-labeled protein (that is, the protein with only one of the residues labeled); these two measurements are then averaged to determine S_{intr} .

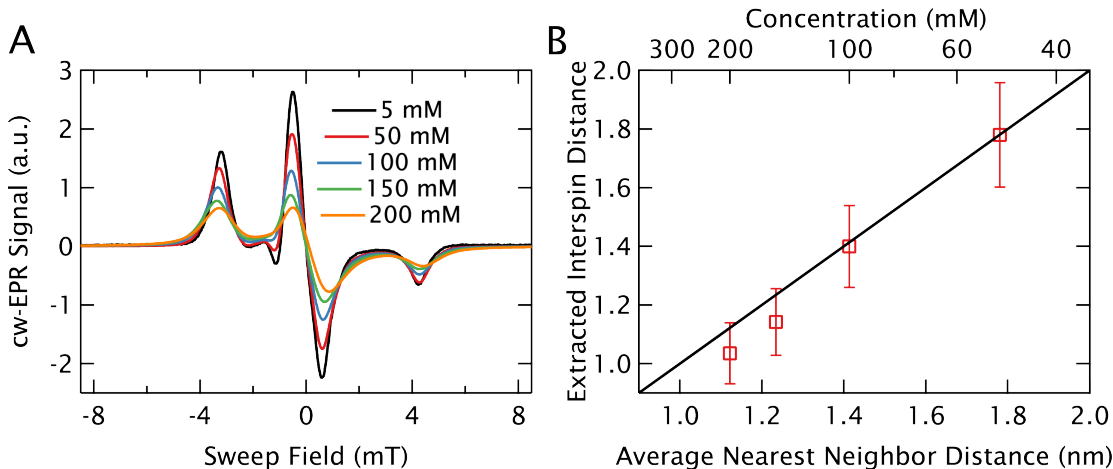


Figure 1.3: cw Distance Measurement using Nitroxides. A: A concentration series shows increasing dipolar broadening of the 10 GHz, cw EPR spectra of nitroxide radicals. **B:** By fitting to the parameters of a Gaussian distance distribution, we are able to extract the average interspin distance (and width) from the spectra. Here they are plotted against the “known” distances from the concentration and show reasonable agreement.

The process of then using this information to extract a distance distribution can follow several possible paths, but the most generally successful is then to use Eq. 1.20 to fit S_{broad} using a parametrized model of the distance distribution (the most common is of a Gaussian, or multi-Gaussian distance distribution). While the assumption of a particular model is a practical limitation of the approach (we will see below that Double-Electron-Electron Resonance can allow a model free measurement of the distance distribution), it is often sufficient for applications (as it gives both an average distance, and some understanding of how broadly distributed the range of distances is).

Consider, as an example, the case of a concentration series of nitroxides, where increasing concentration is used to tune the average interspin distance. The sam-

ples used were 4-Amino TEMPO, which are nearly identical to the nitroxide spin label MTSL, but are soluble to high concentrations. Fig. 1.3A shows the 10 GHz, cw EPR (derivative mode) spectrum of the samples measured in a frozen (water/glycerol) solution. These spectra are typical of the “powder pattern” of a nitroxide, where the odd shape emerges from the interplay of the g- and A-anisotropies. As concentration increases (corresponding to reducing the average distances), the features of the spectra begin to change and broaden out. A fitting program can be used to determine the best fit distance and distribution (assuming a Gaussian shape), for each broadened spectrum. The resulting fit values are compared to the “known” average interspin distance based on concentration in Fig. 1.3B. The results are encouraging, and show generally good agreement. The broadening becomes subtle below ~ 2.0 nm but for shorter distances cw EPR certainly is capable of distinguishing interspin distances in this distance range.

1.2.2 Double Electron-Electron Resonance

While cw EPR offers a powerful methodology to study interspin distances, it requires the ability to resolve weak dipolar interactions on the otherwise broadened lineshape, which limits applications to short distances. If we could utilize a line of extreme narrowness, the distance range would be necessarily longer, but the features on the nitroxide spectrum can not be narrowed. Pulsed EPR measurements offer the potential to isolate only the dipolar interactions, by uti-

lizing frequency resolved pulses. The most common approach for this is utilizing two frequency excitation, which is known most commonly as Double Electron-Electron Resonance (DEER, but also called Pulsed ELectron DOuble Resonance: PELDOR). As discussed in a retrospective on the development of the DEER technique⁴⁸, the original implementation of this technique evolved in the Soviet Union by Milov et al.^{49,50} and utilized 3 pulses to directly measure the dipolar coupling between spins. This enabled studies of distances⁵¹ and there was awareness that this raised the potential of combining SDSL with DEER to measure biological distances. However, the technique’s capabilities exploded with the “minor” technical improvement of adding another refocusing pulse.⁴⁸ This four pulse DEER⁵² is now the standard applied in biology and finds applications in a wide variety of systems including polymers⁴⁴ biomacromolecules^{38,39}, DNA^{53,54}, and a wide variety of reviews of the technique are available^{20,55–59} Despite the widespread utility (and the focus on it in this dissertation) of 4 pulse DEER, the technique is still being developed. For instance, a 5 pulse DEER sequence has been introduced which has been shown to yield dramatic improvements in sensitivity.⁶⁰

DEER utilizes a pulse sequence as shown in Fig. 1.4A to modulate the dipolar interaction between spins, which can be observed by measuring a refocused echo on the observer frequency (ν_1). The first two pulses are simply a $\frac{\pi}{2}$ and π spin echo pair, which creates an echo (shown partially transparent, surrounded by dashed lines) after $2\tau_1$. This echo is not observed, but rather it is refocused again by

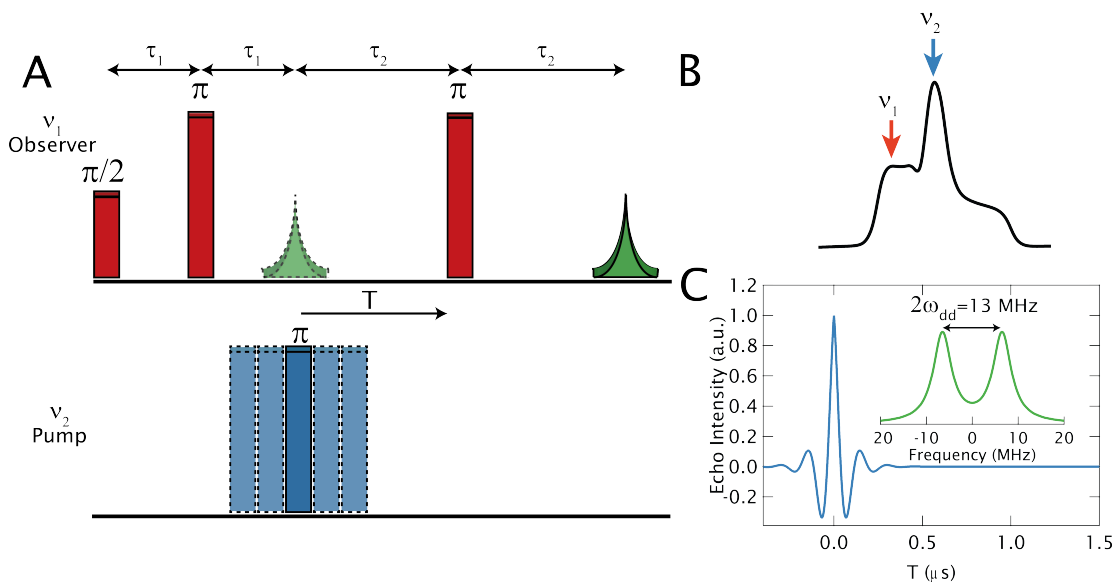


Figure 1.4: Four Pulse DEER Sequence. **A.** The 4 pulse DEER sequence⁵² generates a refocused echo using 3 pulses ($\frac{\pi}{2}$, π , π) at the observer frequency (ν_1), which is set far enough off the center of the spectrum so as not to overlap with the pump pulse. The pump pulse is a π pulse that inverts a population of spins at ν_2 which is set on the maximum of the nitroxide spectrum. The pump pulse flips the spins, which modifies the precession of the observed spins. As the pulse is moved in time this modulates the intensity of the observed echo with a frequency given by the dipolar coupling. **B** Typical locations of the observer and pump frequencies (ν_1 and ν_2 respectively) on the nitroxide spectrum; the frequency spectrum typically used is ~ 65 MHz. **C** A simplified (illustrative) example of a DEER oscillation assuming Eq. 1.22 shows that for single distance the frequency can be read directly off the oscillations, or from the frequency domain (inset). In more complex (and realistic) applications, more advanced processing (based on Tikhonov regularization) can be used to extract a distance distribution from the time domain data.

the third observer pulse to generate the refocused echo after $2(\tau_2 + \tau_1)$ (this echo is shown solid), and this echo is the DEER signal. Once the sequence is assembled, appropriate delay times are chosen, and then this observer sequence is not changed (except for cycling of the pulse phases to eliminate artifacts and spurious echos). Thus employed, this sequence would give us no direct information about the dipolar coupling between spins. Instead, another π pulse is applied, this time at the pump frequency (ν_2). The timing of this pump pulse is varied throughout the time between the two refocusing pulses. This pump pulse inverts the spins in the system suddenly, during or after the formation of the first (unmeasured) echo. As shown in Fig. 1.4B, the pump pulse affects spins in a different part of the nitroxide spectrum than the observer, and the excitation bandwidth is chosen to avoid spectral overlap. This inversion still affects the measured echo through the dipolar coupling between spins at ν_2 and those at ν_1 . This coupling has a frequency $2\pi\nu_{dd} = \omega_{dd}(r) = \frac{\mu_0 \mu^2}{4\pi r^3} (3 \cos^2(\theta) - 1)$ so inverting the spins at ν_2 changes the resonance frequency of the observer spins by $\omega_{dd}(r)$. If this pulse is applied such that it overlaps with the center of the echo (at time $2\tau_1$, which we call T=0), then this does not affect the second echo amplitude (from $2\tau_1$ to $2\tau_1 + 2\tau_2$), as the only result is that the spins precess at a slightly different frequency. However, when the inversion pulse is moved away from the first echo, the location of the pulse and $\omega_{dd}(r)$ result in modulations of the resulting echo intensity.

If we neglect the pump pulse, then between $2\tau_1$ and $2\tau_1 + 2\tau_2$, we expect each spin (of resonance frequency ω_i) to precess by (i.e. gain phase) $(\omega_i + \frac{1}{2}\omega_{dd}(r))\tau_1$. However, following the observer refocusing pulse, each spin will precess $-(\omega_i + \frac{1}{2}\omega_{dd}(r))\tau_1$. Thus, the total phase is 0, and all the spins to recohore at once, yielding maximum echo intensity. However, if we now introduce the inversion pulse at T, we will have precession of: $(\omega_i + \frac{1}{2}\omega_{dd}(r))T$, $(\omega_i - \frac{1}{2}\omega_{dd}(r))(\tau_2 - T)$, and $-(\omega_i - \frac{1}{2}\omega_{dd}(r))\tau_2$ in the three regions. Thus, the total acquired phase in this setup is $\omega_{dd}T$. When the total phase $\neq 0$ the dipolar shifted spins do not fully recohore into the echo, reducing the echo intensity and modulating it by $\cos(\omega_{dd}T)$.

Additionally, there are effects from other spins that are randomly distributed coupled spins (for instance, in a doubly spin-labeled protein, these would be spin-spin interactions between different proteins, as distinct from pair-wise interactions between nitroxides on a single protein). These do not contribute to an oscillation, but rather a decay of the signal. Thus in the earliest papers, the DEER effect can be described quite simply as a functional form⁵²

$$I_{DEER}(T) \propto \cos(\omega_{dd}T) \exp(-k|T|) \quad (1.22)$$

where k is numerical parameter that takes into account the coupling between non-pairwise spins, the concentration of unpaired electrons spins, and the fraction of electron spins excited by the microwave pulses.⁵² A calculated time domain

trace for a 2 nm interspin distance is shown in Fig. 1.4C, and the corresponding Fourier Transform in the inset shows the splitting of $2\omega_{dd}$.

While for simple cases, with a narrow distance distribution, and relatively short distances, it is possible to directly read interspin distances from the DEER trace (or through Fourier Transform), typically DEER signal is necessarily more complicated. For instance, we must include effect of the random orientations of the interspin-vectors. Further not all coupled spins are within the bandwidth of one of the two pulses, so the degree of echo modulation is < 1 . Thus, even for a single interspin distance, we more generally find the DEER decay is given by³⁹

$$V(T) = 1 - \lambda \left[1 - \int_0^1 \cos(\omega_{dd}(1 - 3 \cos^2(\theta)Td \cos(\theta))] \exp(-k|T|^{\frac{D}{3}}) \right] \quad (1.23)$$

where λ is the modulation depth, and is determined by the fraction of coupled spins that are inverted by the pump pulse, θ_i is the orientation of the interspin vector, and $\exp(-k|T|^{\frac{D}{3}})$ is the exponential decay function, which depends on D , the dimensionality of the randomly distributed spins. For soluble protein monomers $D = 3$, but D may approach 2 when working in a quasi-2 dimensional environment like vesicles. In the case where we then have a distribution of distances, we deal with a combination of signal from all the possible spin pairs in Eq. 1.23.

If a single (or dominant) distance is being probed, dipolar oscillations can often be observed directly in the time or frequency domain. However, extensive work has pushed the capabilities of DEER spectroscopy by investigating how to

robustly determine the full distance distribution. That is, Eq. 1.23 describes the DEER trace in the presence of a single distance, and can be used to build up the DEER signal in the case of a distance distribution. This answers the problem of predicting the DEER signal given a distribution of distances, but the far more relevant question is taking a DEER signal and predicting the full distance distribution. This is an ill-posed problem, and it is easy for noise or artifacts in the DEER data to result in significant errors in the predicted distance distribution. To alleviate these problems, Tikhonov Regularization is commonly utilized^{61,62} as a method for producing robust solutions by fitting the data, and extensive work has investigated ways to make extraction of distance distributions more robust⁶³. The majority of this work is now codified into the program DEERAnalysis which has become the standard processing software for studying DEER traces.⁶¹ Therefore, it is now entirely standard to be able to acquire high quality DEER spectra and by Tikhonov regularization (or if one wishes, a user model), to determine the full distance distribution. Though the process is not entirely automated, and it requires some experience to identify the optimal parameters, it is an accessible technique with some training.

1.2.3 Comparing the Capabilities of cw and pulsed EPR for Distance Measurement

The generally accepted distance range for cw EPR measurements can depend on the precise system. It is typically considered acceptable to apply this method to distances longer than ~ 0.8 nm⁴³, which is limited by the onset of significant exchange interactions between nitroxides. It is worth noting that broadening effects are present for shorter distances (and indeed become more severe), but the process of extracting distances through a convolution approach could fail as a result of not accounting for strong exchange interactions. Also, distances < 1.5 nm falls into an intermediate coupling regime, which introduces some error into the interspin characterization. It is generally estimated to be ≤ 15 %⁴⁴, making it an important consideration, but not a fundamental limitation of these measurements. The long distance ~ 2.5 nm, while subsequent publications⁴⁴ generally find a limit of ~ 2.0 nm. Further work examining several distance measurement techniques⁴⁶ suggests an even more limited distance range of ~ 1.8 nm, but the message is simple: cw-distance measurement techniques are suitable for studying comparatively *short* distances in biological systems.

The range of distances accessible by DEER also depends on the specifics of the system under study, but is typically substantially longer than is possible with cw distance measurements. Perhaps surprisingly, the short distance limits of DEER are more restrictive than those of cw EPR in many cases. Fundamentally, for dis-

tances shorter than ~ 2.0 nm,⁴⁴ the limited excitation bandwidth of the applied pulses is smaller than the dipolar coupling, which artificially reduces distances below 2.0 nm. This can be artificially corrected by including the estimated excitation bandwidth in the calculations, but even this fails for distances below ~ 1.6 nm.^{38,46} The long distance limits of DEER are determined by the length of the maximum usable dipolar evolution time (meaning the longest possible range over which T can be swept in Fig. 1.4A. If the phase memory time limits the length of τ_2 , then the range over which we can move T is similarly reduced. As ω_{dd} becomes smaller for longer distances, the period of the oscillations increases and larger values of T are necessary to trace out an oscillation for longer distances. It is estimated⁶⁴ that for a maximum evolution time T_{max} the full distance distribution can be trusted for distances out to 3 nm $(\cdot \frac{T_{max}}{2\mu s})^{\frac{1}{3}}$, while the mean distance and the width can be trusted out to 4 nm $(\cdot \frac{T_{max}}{2\mu s})^{\frac{1}{3}}$, and just the mean distance can be trusted out to 5 nm $(\cdot \frac{T_{max}}{2\mu s})^{\frac{1}{3}}$. Typically, site-directed spin labeling with nitroxides, allows distances out to ~ 6 nm to be measured, and in some cases out to ~ 8.0 nm.³⁹ Deuteration of the solvent is commonly employed as a way of lengthening relaxation times to achieve longer distance measurements.⁵⁵ Once the solvent is deuterated, the limiting factor in for phase memory time has been shown to be the protons on the protein itself; when these are removed through deuteration, the distance limit is raised to ~ 10.0 nm (in a soluble protein).⁵⁴ Another factor that affects the ability to observe long distances is the overall spin

concentrations. If the exponential decay in Eq. 1.23 is too rapid, a long oscillation can not be observed before the signal decays. Using commercially available, 10 GHz instruments, sample concentrations down to 100 μM can be measured reliably, which is typically sufficiently low. However, there are situations where high local concentrations emerge (resulting in substantial decay) even though the overall concentration remains low—for instance, when proteins are packed into lipid vesicles⁶⁵.

In comparing the capabilities of DEER and cw-EPR we immediately recognize that DEER is the intuitively more useful technique, as it allows substantially larger distances to be evaluated. However, cw EPR tends to be more easily applicable, and can be applied to a wider range of situations, in particular at higher temperatures. Despite this, pulsed EPR has become far more common due to the breadth of distances that can be evaluated, as well as the power of direct access to the entire distance distribution (without the necessity of assuming a model). Thus, DEER is the workhorse of biological EPR distance measurements, with cw EPR being relegated to more specific tasks (for instance, when distances are known to be close, or when only short distances are of interest). Nonetheless, the advantages of cw EPR mean that, should methods exist to extend the distance range, it could become an important alternative to DEER, particularly for applications where samples are kept > 200 K.

1.3 Opportunities and Challenges of High-Field EPR

The potency of EPR as a tool for studies of structure in biological systems has become one of the major applications of EPR spectroscopy. While EPR is not yet a “standard” technique in biomolecular structural studies, the equipment necessary for advanced EPR experiments at 10 GHz, including DEER, are commercially available. This availability has helped popularize the use of EPR as a technique complimentary to other common bio-physical measurements (including x-ray scattering and NMR). However, most groups utilizing EPR for biological samples are doing so with commercial instruments at fields <1 T (and most commonly at X-Band), despite the fact that EPR (like its cousin NMR) becomes more powerful at high magnetic fields. Thus, unlike high-field NMR, high-field EPR remains a far less common approach, undertaken generally only in labs which specialize in the development of high field EPR. It is incorrect to suggest that important science is not ongoing in this field (that is, the community *is* both developing and applying high-field EPR), but for a biologist, or biochemist interested in addressing a specific question, high-field EPR has not reached the maturity level for it to be easily utilized.

NMR has seen dramatic expansion of its capabilities by increasing magnetic field: since the first commercial NMR spectrometer at 4.6 T (200 MHz) was re-

leased in 1964, NMR spectrometers have steadily increased in magnetic field, and the current state of the art reaches to 23 T (1000 MHz). NMR has so readily moved itself to larger and larger magnets to leverage the dramatic increases in both resolution and sensitivity. Increased resolution separates lines which overlap at lower fields, allowing better identification of peaks. Sensitivity is enhanced with increasing field as the power emitted from a precessing magnetic dipole increases rapidly with frequency,⁶⁶ and increasing the field increases the sample magnetization (which determines signal intensity as in Sec 1.1). It is typically found that $\text{SNR}_{NMR} \propto \omega^{\frac{3}{2}}$, which has proved paramount in expanding the limited sensitivity of NMR.¹⁷ The progression towards higher fields in NMR has been consistent as the technical challenges for increasing the spectrometer field is largely located in the challenge of generating that field (and doing so with sufficient homogeneity). Though the NMR frequency increases with field, these frequencies are still at or below 1 GHz, meaning that high-power amplifiers, and low-noise detection systems can be readily designed.

In the case of EPR, sensitivity is also predicted to increase with magnetic field, though the precise scaling becomes more complicated^{67,68} as a result of the use of resonators which can limit sample volumes at high frequencies (where the resonator dimensions are reduced), and the fact that high-power excitation is not always available at higher magnetic fields. However, it has been demonstrated that high magnetic fields greatly expands the sensitivity of DEER.^{69–73} One impressive

instrument operating at 95 GHz has shown the capability to carry out DEER on samples as dilute as $1\mu\text{M}$,⁷¹ yielding an order of magnitude improvement in concentration sensitivity over commercial X-Band spectrometers. Such sensitivities have important financial and practical applications (by reducing the amount of previous sample required), but more generally greatly expand the kinds of systems which can be studied by DEER as many proteins and biomacromolecules can not be made in large amounts, can not be utilized at such high concentrations, or do not exist physiologically at these concentrations.

The development of high-field EPR has a long history, and comprehensive reviews can be found in literature^{74,75} but the highlights are mentioned here. High-field EPR dates back to work by Lebedev in the 1970's^{74,76}, and in 1977 they introduced what is commonly considered the first “modern” high-field EPR spectrometer operating at 170 GHz.⁷⁷ Further work saw the emergence of spectrometers at 250 GHz⁷⁸ and spectrometers at 95 GHz⁷⁹, with commercial spectrometers now available at both frequencies.⁸⁰ However, only recently have high-power amplifiers become available at these sorts of fields, with Extended Interaction Klystrons amplifiers offering ~ 1 kW at 95 GHz,^{69,71} while smaller amplifiers based on IMPATT diodes offer several Watts at 95 GHz^{70,81} and 100's of mW at 130 GHz.^{82,83} Above 95 GHz, both the technological capabilities and (as a result) the quantity of spectrometers falls off steeply. This emerges from the “Terahertz gap”⁸⁴⁻⁸⁶, which is the portion of the electromagnetic spectrum between 100 GHz and 5 THz, where

neither lasers (which can be used at higher frequencies), nor electronics (which can be used at lower frequencies) offer substantial powers.

The effect of limited source power is to substantially reduce the effectiveness of pulsed EPR (cw EPR does not rely on high powers) as it is optimal in pulsed EPR to excite the spins rapidly relative to the rate at which they relax. In order to excite the spins rapidly, high intensity (during the pulse) is necessary at the sample, which can be achieved either through a high incident power, or from the use of a cavity with a large Q. However, low-power sources can not be entirely compensated for by high-Q cavities, as with too high a Q, the cavity substantially reduces the bandwidth of the spectrometer (only exciting a narrow region of frequency space), and can increase dead-time due to ringing. Additionally, at frequencies >100 GHz, the wavelength of light is only ≤ 2 mm, which makes single mode cavities difficult to build and use and can dramatically limit the usable sample volume (sample volume $(V_S \propto \omega_0^{-3})$).⁷¹ Thus, many high-field EPR spectrometers do not use cavities unless necessary, and tend to make use of a Fabry-Perot style cavities^{78,87} (though some works have utilized cylindrical cavities as well⁷¹). Though a low-Q cavity can be used, high-power sources remain desirable to obtain the maximum sensitivities and time resolutions as non-resonant sample loading at 95 GHz was shown to substantially expand sensitivity in applications where power is not limited.⁷¹

We are most interested in frequencies >100 GHz, where spectrometers and experiments are both comparatively rare. The majority of the work in this thesis was done on a 240 GHz spectrometer, and so this frequency is mentioned explicitly for reference. For the frequencies above 100 GHz, the most common sources are non-linear, frequency multiplication.^{74,87,88} A low-powered source operating at ~ 15 GHz (where microwave electronics are well developed), is then amplified and sent through frequency multipliers based on Schottky diodes.⁸⁹ These multipliers can be connected in multiplier chains to reach frequencies up to 2 THz, but as the multiplication process is nonlinear, the power drops substantially at each step. Nonetheless, recent devices of this kind have demonstrated powers up to ~ 100 mWs at 240 GHz, and these types of sources are generally the best possible available at these frequencies (though developers of gyrotrons and amplifiers hope to change this). At this power level pulse lengths on the order of 100's of ns are necessary to excite an $S = \frac{1}{2}$ spin,⁹⁰ and the low-power, 240 GHz spectrometer used in these studies, a typical $\frac{\pi}{2}$ pulse is ~ 600 ns. At X-Band excitation pulses are typically on the order to 10 ns, and even at 95 GHz high-specialized work has achieved similar (or better) pulse lengths.⁷¹ If we consider the nitroxide spectrum, which extends across ~ 40 mT at 240 GHz, these pulses excite far less than 0.1 mT. Similarly, it becomes impossible to carry out pulsed experiments in situations where the spins relaxation times (T_1 and T_M) are substantially shorter than the pulses (this sets a rough limit for T_M of ~ 600 ns, but even this is likely optimistic

and depends on having strong signal). As a result, existing 240 GHz spectrometers can not offer high sensitivity in pulse mode, and further almost always need to be run at cryogenic temperatures (to achieve relaxation times longer than $1\mu\text{s}$).

It should be emphasized that there are several groups that have been instrumental in developing high-field EPR, notably Freed at Cornell, Griffin at MIT, the team at the National High Magnetic Field Lab, Britt at UC Davis, and a handful of other groups. Indeed, it is as a result of their work that the ground is now so ripe for further development. However, the lack of adequate sources at high fields and the challenges associated with development have limited the number of high-field EPR spectrometers in use. This serves to strongly limit development of high-field EPR techniques and methods as compared to lower field measurements (even those utilizing traditional, low-power sources for the high-field measurements). Much of the development of high-field EPR has largely focused on technology and bringing existing techniques from low fields to high fields. Yet, at the heart of high field EPR, is a much larger Zeeman splitting (24x larger at 240 GHz than at 10 GHz), which can be leveraged in developing *new* methods and techniques that would not be fruitful at low fields. It is not the case the low-field EPR techniques see no improvements at high fields, but the potential exists to uncover new techniques at high fields.

We argue, therefore, that high-field EPR (above 100 GHz) suffers from two major limitations that can be addressed in order to expand its capabilities (in-

spired by the advances at high-fields realized in NMR). First, immense ground remains to uncover new techniques and methods that are suitable only at high magnetic fields, and have not been investigated due to the limited number of investigators focused on high-field EPR. Second, there is the constant problem at high-fields that the unavailability of high-power sources obstructs the achievement a fast, high-powered, pulsed EPR spectrometer. The work in this dissertation was undertaken at 240 GHz and 95 GHz in an effort to address both these problems to expand technique and technology to revolutionize high-field EPR. The rest of the thesis is divided into two parts. Part 1 describes work utilizing existing high-field spectrometers to enable new developments for distance measurement between spins with both a new technique, and new spin labels. Together, these methods highlight specific examples of the potential of high field EPR that are not feasible at lower fields, and invite further development to maturing high field EPR. Part 2 describes our work to utilize a Free Electron Laser as a source for high-powered EPR at 240 GHz, exceeding the power capabilities of existing spectrometers by 3-4 orders of magnitude. Currently, the Free Electron Laser (FEL) at University of California Santa Barbara (UCSB) is the only source capable of generating ~ 100 's of Watts of power at 240 GHz, in a way that is suitable for EPR. Beyond fundamentally expanding the ceilings of high-power EPR, the spectrometer discussed here is the first of its kind with which to test and expand the capabilities of high field EPR with high-power sources. It is far from our expect-

tation that the future of high-field pulsed EPR lies with Free Electron Lasers for other groups (due to cost and size), but as alternative sources are developed, the FELEPR offers the only spectrometer capable of doing ultra-fast EPR excitation and detection at these fields, provides a testbed for techniques and methods, and (because the FEL can be run easily at frequencies up to 1 THz) can be scaled to continue pushing the boundaries of high-field EPR.

More specifically, Part 1 contains Chapters 2, 3, and 4, while Part 2 contains Chapters 5 and 6. Chapter 2 details efforts made with a low-powered, 240 GHz spectrometer to make use of the behavior of spin decoherence at low temperatures to determine interspin distances, eventually discussing Gd^{3+} as a new probe that is ideally suited for pulsed EPR at high fields. Chapter 3 uses the same spectrometer to carry out cw EPR measurements of Gd^{3+} to measure long interspin distances at temperatures and conditions that can't be achieved with DEER. Concluding Part 1, Chapter 4 discusses the use of DEER at 95 GHz and 10 GHz for measurements of a spin labeled protein oligomer, in order to both test the capabilities of the new label, as well as address an open question in regards to the protein's oligomeric structure. Chapter 5 addresses the question of utilizing a Free Electron Laser as a source for EPR, specifically introducing the efforts necessary to match the FEL to an EPR application and some interesting physics that can only be observed at high fields using short pulses. Finally, Chapter 6 provides an in-depth discussion of a new method to control the phase of FELEPR pulses through post processing,

despite the phase instability of the FEL itself. The concluding section provides a short discussion of the scope of the cumulative efforts in the thesis and the potential future of high-field EPR.

Part I

New Distance Measurement

Techniques at High Fields

As discussed expansively in Chapter 1, EPR has emerged as an important distance measurement tool for elucidating structure in complex biological systems.^{30,38,58,65,91} While most distance measurements (whether cw or pulsed) are applied at low magnetic fields, high-field EPR has become important in a wide variety of fields, and high fields have been used to realize important gains in sensitivity.^{71,72} Despite the advantages of moving to higher fields, the current pedigree of EPR experiments for studying biological systems evolved in an environment where only low-field EPR was generally mature. This work, and the expanding technological capabilities at high field beg the question of what other measurements become possible at high magnetic fields. This part of this dissertation addresses the question of what new experiments are possible utilizing existing spectrometer technology. It is worth noting that these applications were not in mind when the spectrometer was first developed. Instead they emerged from other projects and investigations, and their capabilities to studying a biological system was realized as a result of the exciting applicability to SDSL for EPR measurements on biomacromolecules.

Chapter 2 investigates how the silencing of a decoherence pathway *only* at high fields using low temperatures allows probing of interspin distances and potential applications for clustering. At the tail of Chapter 2 we introduce Gd^{3+} as a new potential spin label, whose properties appear to dramatically expand the distance range that can be probed through spin bath quenching. The properties of Gd^{3+}

make it only suitable for measurements at high magnetic fields (and in many way it is superior to traditional nitroxide spins labels at these fields). Chapter 3 investigates the potential application for Gd^{3+} as a probe for long distances using cw EPR, which offers an important alternative to DEER for cases where measurements above cryogenic temperatures are desired. Finally, Chapter 4 brings the use of Gd^{3+} as a probe to fruition by investigating the oligomerization of a membrane protein using high-field DEER with Gd^{3+} spin labels. Together these techniques sample both new experimental methods (in spin bath quenching) and new approaches to existing methods (the use of Gd^{3+} for both cw and DEER distance measurements)

Chapter 2

Probing Interspin Distances through Spin Bath Quenching

Portions of this chapter (covering Sections 2.1, 2.2, and 2.3), including figures, and some detailed experimental information for this work in Appendix A are originally published in Ref 92 (available online), and are reproduced by permission.

2.1 Exploiting High Polarizations at High Fields

While the extension of existing EPR techniques to higher fields has enabled important improvements, at these high magnetic fields new techniques can be developed that utilize phenomena that are negligible at low fields. For instance, at 8.5 T, one can tune the polarization of the electron spins from 6% to 99% simply by varying the temperature between 100 and 2 K—temperatures easily achieved with standard liquid Helium cryostats. Polarization this high at 0.35 T would require temperatures below 100 mK, requiring more exotic cryostats. As a result of these high polarizations, we find that from the viewpoint of electron spins,

the system is quieted substantially as a result of eliminating fluctuations that drive decoherence. Beyond being phenomenologically interesting, the strength of fluctuations depends on the average interspin distances, which allows a new window to address distances in spin-labeled systems.

In this chapter we will discuss the spin bath quenching effect and the capabilities of leveraging it to obtain distance information. The topic will be introduced by reporting on the quantification of distances across randomly-distributed nitroxide radicals from the temperature-dependence of their phase memory times at high magnetic fields. The ability to fully control the polarization of the nitroxide spin bath allows us to explicitly observe spin bath quenching, determine the electron spin phase memory time in the absence of electron spin bath fluctuations, and then map the strength of the electron spin dipolar interaction to average inter-electron probe distances. This was realized experimentally by studying a concentration series of frozen nitroxide solutions. The use of deuterated solvent reduces electron spin decoherence originating from protons, allowing the observation of ensemble-average, inter-electron distances out to roughly 6.6 nm in frozen aqueous nitroxide solutions. We additionally investigate the limits of this in ‘non-ideal’ environments that would become relevant in a biological system and address the role of the nuclear spin bath, as well as the potential for application on a ‘model’ biological system consisting of spin labeled vesicles.

The potential power of the characterization of spin bath quenching arises on two fronts. First, while for nitroxide-based probes the distances limits are found to be seriously restricted in non-deuterated systems, by utilizing the high-spin system Gd^{3+} we find promise of longer range sensitivities. Second, the ability to monitor average interspin distances of an ensemble, rather than probing simply nearest-neighbor interactions can be important in biological systems. While nearest-neighbor distances are most commonly seen as the goal for structural determination (see Sec. 1.2), many systems aggregate, cluster or clump. The capability to address these systems, and quantify not necessarily simply the nearest-neighbor, but rather generally how the spin-network is inter-connected, presents opportunities in studying these sorts of system. These two outlooks will be addressed in the final section of this chapter.

2.2 Spin Bath Quenching(SBQ) and Distances

In any system of spins, the dynamics of the local magnetic fields plays a critical role in determining the EPR signal. Paramagnetic species, whether nuclei, electrons, or high-spin ions, all contribute to the local magnetic fields and we typically rely on observing the magnetic coupling between these to learn about structure. In this regard, decoherence is usually viewed as an enemy of information, as it destroys the coherent interactions between spins from which we can extract information about distance, orientation, motion, and dynamics. However, decoherence

itself can encode important information about the system under study, as the fluctuations in the paramagnetic system also act as a source of decoherence. Thus, the structure of the spin system is intimately linked to the decoherence that emerges, making studies of decoherence an additional tool to address information about the spin system. For instance, when undertaking distance measurements on a spin-labeled protein with DEER, concentrations must be kept low in order to be able to maintain sufficiently long T_M to measure long distances.⁵⁶ That is, if the spin-labeled protein concentration is too high, the interactions of the spins with each other results in fast relaxation and the phase memory time directly encodes some information about the interspin distances. Of course, the direct measurement of the phase memory time can not be use to determine distances directly, as the relaxation effect is complex and includes contributions from both intra- and inter-biomolecule interactions as well as effects from the nuclear spins. DEER's immense utility results from isolating only the interactions that occur between spin-pairs. We discuss in this chapter another approach to isolate the interactions of the electron spins, in this case through the phase memory time.

A number of potential relaxation effects emerge from spins close enough to one another that their magnetic fields are coupled. The distance range for which contributions are relevant depends strongly on context, but is substantially larger for electrons than nuclei, as their gyromagnetic ratio is substantially smaller ($\frac{\gamma_e}{\gamma_P} \approx$ 660 with γ_e and γ_P the gyromagnetic ratios of electrons and protons respectively).

One particularly strong relaxation mechanism occurs as unexcited spins (that is, those not directly probed with radiation) with similar resonance frequencies but of opposite spin states can flip-flop with one another (i.e. $|\frac{1}{2}, -\frac{1}{2}\rangle \leftrightarrow |-\frac{1}{2}, \frac{1}{2}\rangle$). As this transition is energy conserving, it can happen readily; however, while total energy is conserved the local magnetic field around these spins is modified. Thus, when these unexcited spins (or B-spins) undergo these energy conserving flip-flops ($|\frac{1}{2}, -\frac{1}{2}\rangle \leftrightarrow |-\frac{1}{2}, \frac{1}{2}\rangle$), nearby excited spins (A-spins) see a shift in their local fields, and as a result lose phase coherence with other A-spins in the sample. As these fluctuations are time-dependent, they drive the precession of spins out of resonance with others, destroying the coherence in the spin system irreversibly.

These kinds of fluctuations are common in a variety of systems, for instance the fluctuations of protons in a solvent is known to severely reduce the phase memory times in pulsed EPR measurements.⁵⁵ The strong effect of protons (as opposed to other nuclei) emerges from the ease with which they can couple to each other. Protons have substantially higher gyromagnetic ratios than most nuclei ($\frac{\gamma_P}{\gamma_D} = 6.5, \frac{\gamma_P}{\gamma_C} = 4$, with γ_D and γ_C the gyromagnetic ratios of 2H and ^{13}C respectively), which increases their flip-flop probability. Protons also tend to be present in high concentrations (110 M in pure water). It is worth noting that other nuclei also contribute to relaxation (but the process is most commonly dominated by solvent protons), and efforts to deuterated entire proteins (in addition to solvent) have been shown to substantially increase phase memory times.⁹³

If we specifically consider flip-flopping between paramagnetic neighbors such as electrons, we see that a combination of high magnetic fields and low temperatures begins to change the phenomena. Nuclei are typically only weakly polarized even at very large fields and cryogenic temperatures (protons are $\approx 0.5\%$ polarized at 8.6 T and 2 K), which is in stark contrast to the already-discussed high polarizations possible at these fields for paramagnetic species. In this case, as the temperature is lowered, fewer and fewer $|\frac{1}{2}, -\frac{1}{2}\rangle$ pairs remain, as Boltzmann statistics require that more and more spins are in the $|-\frac{1}{2}\rangle$ state. One can imagine that at low enough temperatures, where nearly all the spins are in their ground state, this effectively eliminates the flip-flop transitions from occurring between spins, and this relaxation process is eliminated. At intermediate temperatures, where $|+\frac{1}{2}\rangle$ spins are becoming rare, the effective distance in any $|\frac{1}{2}, -\frac{1}{2}\rangle$ pair is increasing and the probability of the pair flip-flopping is reduced. This process is termed “spin bath quenching” as it results from using high magnetic fields and low temperatures to quench the fluctuations of the spin bath. This was first observed looking in diamond samples, where the polarization of nitrogen impurities quenches their mutual flip-flop processes and dramatically increases the phase memory times of nearby nitrogen-vacancy centers.⁹⁴ The effect of spin bath quenching on phase memory times can provide quantitative information on the local environment of the electron spin, and is of critical interest in situations like

quantum information processing, where achieving long relaxation times requires isolating and eliminating all unnecessary sources of decoherence.^{95,96}

Spin bath quenching can be modeled in a physical description by assuming that the spins undergo flip-flops at a rate of W (which is depends on the dipolar coupling spins and is therefore temperature independent). We then weight this rate by the probability of having a spin-up and spin-down pair; these probabilities carry the temperature dependence of the model and account for the variation in the relaxation rates due to the spin bath polarization. Thus, we can write^{94,97}

$$\frac{1}{T_M}(T) = P_{\uparrow}(T)P_{\downarrow}(T)W + \Lambda = \frac{W}{(1 + \exp(\frac{T_Z}{T}))(1 + \exp(\frac{-T_Z}{T}))} + \Lambda \quad (2.1)$$

where T is the temperature, $P_{\uparrow}(T)$ and $P_{\downarrow}(T)$ are the probabilities of a spin-up and spin-down electron, $T_Z = \frac{\hbar\omega}{k_b T} \approx 11.5$ K is the Zeeman temperature of the electrons at 8.5 T, k_b is Boltzmann's constant, \hbar is Planck's constant, $\omega = 2\pi\nu$ is the angular frequency of the EPR radiation ($2\pi \cdot 240$ GHz), W is the flip-flop rate for B-spins, and Λ represents the residual decoherence rate of the A-spins at complete polarization of the B spins. As the temperature is lowered below the Zeeman Temperature, the B-spin bath becomes partially polarized and the flip-flop rate is diminished until it is essentially eliminated below 2 K, where all B-spins are in their lowest energy state. This causes the measured phase memory time (T_M) of the A-spins to increase dramatically as temperature is lowered and

plateau below 2 K. This allows the rate of these fluctuations to be isolated through W .

Of particular interest is the dependence of the SBQ on average interspin distance. The flip-flop transitions occurring between spins are modulated by a dipolar interaction. The strength of this interaction depends on distance as distant spins are far less likely to flip-flop than nearby spins. Thus, W depends on the average interspin distance, and closer distances result in a stronger effect on T_M . In the case of Takahashi et al.,⁹⁴ the B-spins which are flip-flopping are a network of substitutional nitrogen impurities ($S=\frac{1}{2}$) in diamond, which is then probed through the relaxation of the NV centers. In their work, the measurements allow the determination of the coupling W of the nitrogen spins, which can then be used to estimate the concentration of nitrogen impurities. A rigorous exploration of the distance dependence of the spin bath quenching effect, as well as the potential for application in biology is addressed in this chapter.

2.3 Spin Bath Quenching in Nitroxide Radicals and Spin-labeled Vesicles

2.3.1 Solution Study of Nitroxides

Preliminary experiments to observe spin bath quenching in solutions of nitroxides were performed using 4-Amino-TEMPO

TEMPO Concentration (mM)	Average inter-electron distance (nm)	Residual relaxation Λ (kHz)
50	1.8	33.2 ± 8.2
30	2.1	19.3 ± 1.1
10	3.1	19.1 ± 2.6
5	3.8	20.0 ± 1.7
2.5	4.8	19.6 ± 1.1
1	6.6	26.34 ± 0.3

Table 2.1: Nitroxide Concentrations, Interspin Distances, and Residual Relaxation Rates. List of the studied sample concentrations of 4-Amino-TEMPO in deuterated solvent with corresponding average nearest-neighbor inter-electron distances from Eq. 2.2. The extracted values of the residual decoherence rates (Λ) for different samples show consistent relaxation times at low temperatures for all samples except $\bar{r} = 1.8$ nm (50 mM)

(4-Amino-2,2,6,6-tetramethylpiperidine-1-oxyl) dissolved in D_2O and deuterated glycerol. 4-Amino-TEMPO is a convenient test system as its structure is similar to that for common, nitroxide based spin labels (i.e. MTSL) but is readily soluble in water up to high concentrations. For these randomly distributed systems, the nearest-neighbor, inter-electron distance (\bar{r}) can easily be tuned with nitroxide concentration following⁹⁸

$$\bar{r} = 0.554n^{-\frac{1}{3}} \quad (2.2)$$

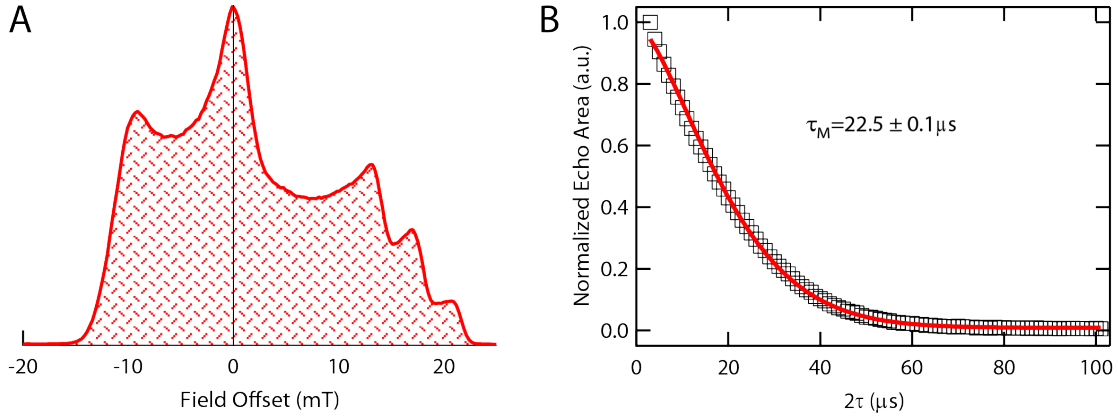


Figure 2.1: 240 GHz Nitroxide Spectrum and Echo Decays. **A:** Typical nitroxide spectrum of 4-Amino-TEMPO in deuterated glass with $\bar{r} = 2.1$ nm (30 mM). The overlaid black bar shows an example of a narrow excitation bandwidth of ~ 0.1 mT, which approximates that achieved with ~ 650 ns pulses. **B:** Echo area decay profile fit to a stretched exponential of the form $\propto \exp(-(\frac{2\tau}{\tau_M})^{3/2})$ as described in the text

where n is the nitroxide concentration. The average nearest-neighbor distances ranged from 1.8 nm to 6.6 nm, and are listed with the corresponding concentration in Table 2.1.

A typical nitroxide spectrum at 240 GHz spans nearly 40 mT, while our long pulses - which exceed 500 nanoseconds - excite less than 1/10 of a mT. This narrow bandwidth is illustrated by the black line overlaying a representative frozen nitroxide spectrum in Fig. 2.1A. Unlike for diamond samples, we are not dealing with two distinct spin systems (i.e. nitrogen impurities and NV centers). Instead, the B-spins are simply those portions of the nitroxide spectrum unexcited by the pulses.

The phase memory time (T_M) was measured at 240 GHz using a spin-echo sequence of 650 ns - τ - 750 ns - τ , in which the optimum lengths of the first

and second pulses were found to give the best echo intensity and shape. A non-exponential decay of the integrated echo area was observed, which is commonly reported in echo decay experiments.^{99–103} We employed the stretched exponential function of the form $\propto \exp(-(\frac{2\tau}{\tau_M})^\xi)$ to extract τ_M using $\xi = \frac{3}{2}$ after it was empirically found to give the best fits as shown in Fig. 2.1B. The average decay time was then calculated by $T_M = \Gamma(1 + \frac{1}{\xi})\tau_M$ where the Γ function provides a prefactor correction.¹⁰⁴ As comparison, previous work¹⁰² found $\xi > 2$ in a system where slow nuclear spin bath flip-flops dominated decoherence. For systems where electron-spins drive decoherence, ξ values between 1 and 2 are predicted for several models in literature,^{99–101} making $\xi = \frac{3}{2}$ a reasonable value—though it was chosen empirically and not based on a model.

The data for the samples in Fig. 2.2 show a clear temperature dependence of the phase memory times from 2 to 20 K. The region of rapid change in T_M from 3 to 10 K and the plateau below 2 K qualitatively match the temperature dependence of the electron spin polarization, as shown in the top panel of Fig. 2.2. Saturation recovery experiments²⁰ measured the spin-lattice relaxation time (T_{1e}) to always exceed 1 ms at 20 K and exceed 100 ms at 2 K. These long T_{1e} values imply that the spin-lattice relaxation is not limiting T_M , which never exceeds 60 μs .

The temperature dependence of T_M can be well described by fitting to the model of Eq. 2.1 up to 20 K with free parameters W and Λ . This is shown in Fig.

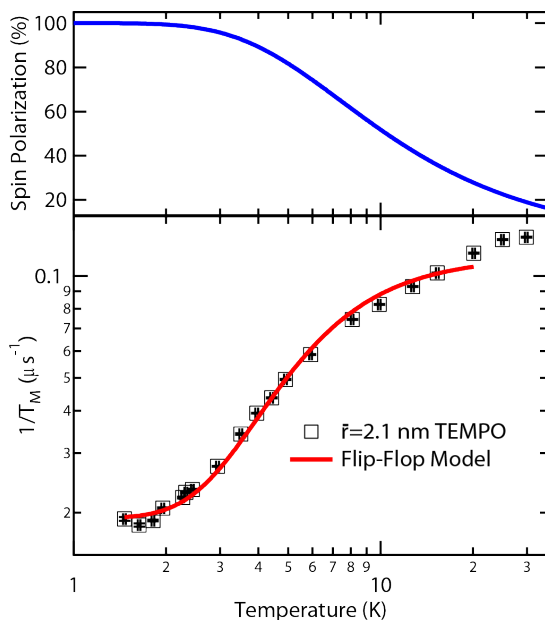


Figure 2.2: Spin Bath Quenching Affects T_M . Inverse phase memory times for $\bar{r} = 2.1$ nm (30 mM) Amino-TEMPO in deuterated solvent with the fit to Eq. 2.1. The top panel shows electron spin polarization for comparison.

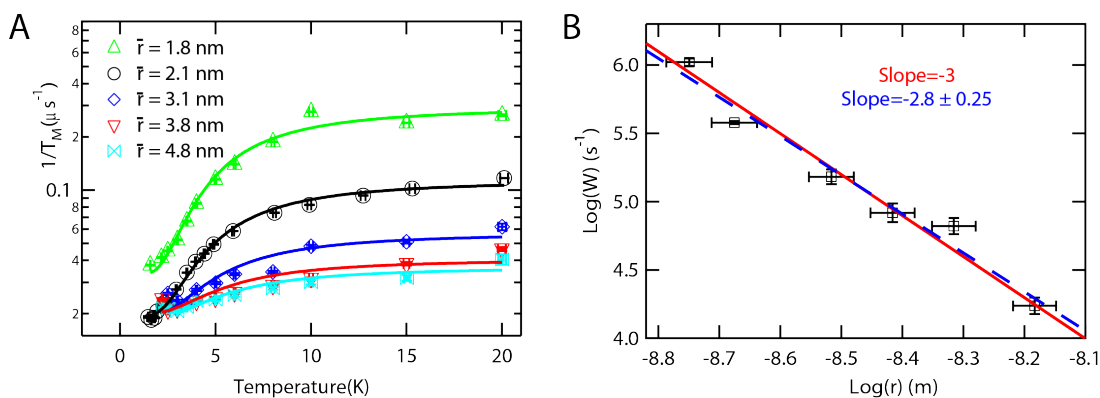


Figure 2.3: Dipolar Coupling Rates in Nitroxide Solutions. A: Temperature dependent $\frac{1}{T_M}$ values for several different samples of 4-Amino-TEMPO in a deuterated solvent. Solid lines are fits to Eq. 2.1. **B:** The extracted parameter W from Eq. 2.1 as a function of inter-electron distance shows a $\frac{1}{r^3}$ dependence. The solid red line shows a line with fixed slope of -3 as expected for $W \propto \frac{1}{r^3}$, while the dashed blue line is a linear fit to the data which agrees with a slope of -3 to within fitting error. The resultant correlation coefficient of -0.985 confirms that the linear regression is justified.

2.3A for several different nitroxide radical concentrations, corresponding to inter-electron spin distances from 1.8 to 4.8 nm. Fig. 2.3A clearly demonstrates that the relaxation at high temperature (i.e. ~ 20 K) strongly depends on the average inter-electron spin distances. As is sensible, samples with shorter inter-electron spin distances have substantially shorter phase memory times. At 2 K, the T_M 's for all samples except $\bar{r} = 1.8$ nm coalesce to roughly $50 \mu\text{s}$ ($\frac{1}{T_M} \approx 20$ kHz). This is consistent with the proposed flip-flop model of Eq. 2.1, where the effects of the B-spin bath are quenched at low temperatures, and only the processes contributing to Λ remain (which should be constant across samples). Thus, the T_M values in the plateau correspond to the temperature-independent residual decoherence term Λ . The extracted values of Λ for nitroxides in deuterated solvents are given in Table 1. The Λ values are consistent for all the samples, except for $\bar{r} = 1.8$ nm, which is reproducibly larger than the rest. This may be due to additional decoherence mechanisms arising from closely interacting nitroxide radicals.

The flip-flop rate (W) in Eq. 2.1 represents a characterization of the average rate at which B-spins will interact and swap quantization directions. As we expect these transitions to be mediated by dipolar coupling, we expect¹⁵ $W \propto \frac{1}{\bar{r}^3}$ to be valid in a simplified model. Although \bar{r} specifically represents the average distance between B-spins, the narrowness of the excitation bandwidth ($< 5\%$ of total spins are excited) makes inter-B-spin distances indistinguishable from the nearest neighbor inter-electron spin distance in the sample. The values of W

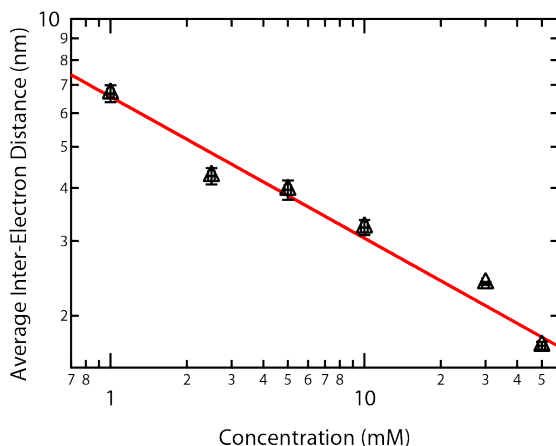


Figure 2.4: Determining Nearest-Neighbor Distances. The average nearest-neighbor inter-electron distance is determined from the extracted value of W for nitroxides in a deuterated solvent. The proportionality constant determined by calibration in the text was used to map the extracted W values to average inter-electron distances. The solid line shows that average nearest-neighbor distance as a function of concentration from Eq. 2.2. The calibration generated a single proportionality constant that provides consistent distance extraction from 1.8-6.6 nm.

determined from fits of the data with Eq. 2.1 present trends that are consistent with the $\frac{1}{\bar{r}^3}$ dependence, as shown in Fig. 2.3B. The data (in Log/Log form) is well described by a linear regression with a high correlation coefficient, the slopes of linear fit agrees with the model to within the uncertainty of the fit, and the scatter does not appear systematic. Therefore, the simple flip-flop model does describe the experimental data well. In the case of free-in-solution nitroxides from Fig. 2.3B the scatter is consistent with 1σ error bars.

Experimentally verifying $W \propto \frac{1}{\bar{r}^3}$ is equivalent to showing that W is linear in concentration (n) as $\bar{r} \propto \frac{1}{n^{1/3}}$ in a 3D system. With the $\frac{1}{\bar{r}^3}$ dependence observed for W , we can map W to the known average distance in these samples, determined

from concentration following Eq. 2.2. This amounts to an empirical determination of the proportionality constant in $W \propto \frac{1}{r^3}$. Fig. 2.4 confirms using this average proportionality constant with our values for W yield consistent distances from 1.8-6.6 nm.

The clear distance dependence observed in the spin bath quenching effect allows this techniques to be employed to gauge and compare inter-electron distances even in in the case of the broad distance distribution of a random solution. Further, when a reference measurement can be used for calibration, as done here, this approach could be used for determination of an unknown distance. Direct determination of a distance without a calibration requires a full model of the electron flip-flop process. However, we can compare our result to literature work investigating proton-pair flip-flop rates for which $W_P \approx \frac{1}{10} \frac{\mu_0}{4\pi} \frac{\gamma_p \hbar}{r^3}$.¹⁰⁵ Alternatively, our calibration yielded $W_P \approx \frac{1}{10.2} \frac{\mu_0}{r\pi} \frac{\gamma_p \hbar}{r^3}$. This comparison is informative, but the proton model does not fully account for some of the intricacies of examining electron spin flip-flops in nitroxides. Firstly, our estimate of W relies on electrons performing energy conserving flip-flops, which is only possible for electron pairs with similar resonance frequencies. As the nitroxide spectrum extends over ~ 40 mT, some spin pairs will not contribute making the distance between partners larger and causing an overestimate of W . Alternatively, we consider only nearest neighbor spin-pairs in our calculation, which neglects the effect of multiple B-spin pairs driving decoherence, and likely causes us to underestimate W . A complete

description of spin bath quenching to include these effects would require a complex computation of W , taking into account the EPR spectrum, the orientation, and distance distributions of the spins, but could make the spin bath quenching effect a quantitative method for distance measurement with a single measurement. Nonetheless, the agreement with the model for the proton flip-flops suggests that these effects seem to cancel out and therefore shows that the simple dipolar flip-flop model is empirically valid.

2.3.2 Residual Relaxation and Distance Limits

In order to resolve distance information through the temperature dependence of T_M , the first term in Eq. 2.1 must dominate the decoherence process. Therefore, reducing the second term, the residual decoherence rate Λ , is the key to the observation of spin bath quenching at longer inter-electron distances, where the electron-electron interaction becomes weaker. Conversely, a dramatic increase in the Λ value would be a substantial threat to the observation of spin bath quenching. The previous investigation of spin bath quenching of nitrogen impurities in diamond proposed that the residual decoherence is due to the neighboring nuclear spins, in their case largely from ^{13}C .⁹⁴ Similarly, the most likely candidate for residual decoherence in our system is the proton/deuterium spin bath, which can be broken down into the deuterons of the solvent, the residual protons of the solvent, and the protons of the TEMPO molecule itself.

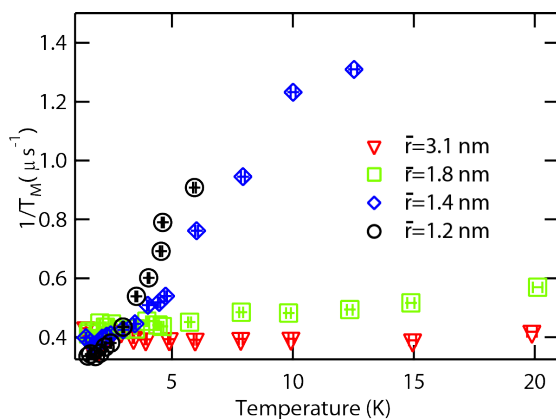


Figure 2.5: Effect of Solvent Deuteration of Residual Relaxation. $\frac{1}{T_M}$ values for solutions of 4-Amino-TEMPO in H₂O/glycerol solution. Temperature dependence is only observed for $\bar{r} < 1.5$ nm due to the extremely high residual relaxation from protons in the solvent.

Measurements of nitroxide solutions show that T_M values are shortened by more than an order of magnitude in an H₂O/glycerol solvent compared to the original perdeuterated solvent. For inter-electron distances longer than ~ 1.5 nm, the fast decoherence from the solvent protons overwhelms the effects from the electron spin bath, and T_M is independent of temperature. However, in samples with inter-electron distances shorter than 1.5 nm, decoherence driven by the electron spin bath is sufficiently fast to compete with the nuclear spins. Thus, the T_M values in Fig. 2.5 again display the characteristic temperature dependence expressed in Eq. 2.1.

Given the immense, though not unexpected, effects of a non-deuterated solvent on Λ , the role of the methyl protons of the TEMPO molecule itself was investigated with deuterated 4-Amino-TEMPO dissolved in the original D₂O/d-glycerol

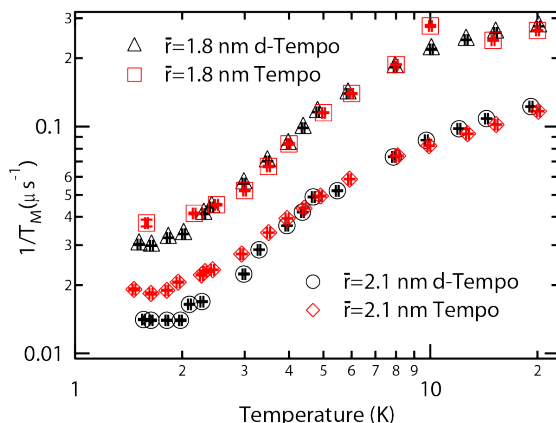


Figure 2.6: Effect of Deuterated TEMPO on Residual Relaxation. Temperature dependent $\frac{1}{T_M}$ for two different samples of deuterated 4-Amino-TEMPO compared to standard 4-Amino-TEMPO. Differences are only apparent at low temperatures which is consistent with TEMPO protons increasing the relaxation of the nuclear spin bath. The discrepancy in the residual relaxation Λ is apparent for the $\bar{r} = 1.8$ nm samples.

solvent. We found that T_M as a function of temperature is similar for deuterated and non-deuterated TEMPO molecules, except at temperatures below 3 K, as can be seen in Fig. 2.6. Decoherence times approaching $77 \mu\text{s}$, 1.5x longer than the $50 \mu\text{s}$ measured with non-deuterated TEMPO, are achieved in deuterated TEMPO at 2 K. Thus contribution of TEMPO methyl protons to residual decoherence Λ is discernible, but only below 3K, and only in an already completely deuterated environment.

The residual relaxation, Λ , provides a means of identifying the electron spin decoherence processes that are unrelated to the dipolar interactions between electron spins. At the lowest temperatures of our measurements, the phase memory time was considerably longer in deuterated than non-deuterated solvents, impli-

cating fluctuations in the nuclear spin bath as the dominant contributor to Λ . The immense increase in Λ in H_2O compared to D_2O demonstrates that protons of water are a substantially stronger relaxation agent than the molecular protons on the nitroxide radical. The lack of influence that molecular protons have on decoherence is expected from their reduced involvement in spin diffusion resulting from the large shift in resonance frequency given their proximity to the unpaired electron.^{38,55,93,102} This has been observed experimentally for nitroxides at X-Band, where the methyl protons—located within the estimated 6 Å diffusion barrier of the electron spin—are found to not contribute significantly to the proton-mediated electron spin decoherence process.¹⁰² This diffusion barrier explains the minimal effect of eliminating the nitroxide’s protons, though the data below 3 K shows that these molecular protons are not entirely irrelevant as a source of decoherence.

As shown in Table 1, the $\bar{r} = 1.8$ nm nitroxide sample shows a consistently larger Λ than other samples, though the relaxation rates still plateau below 2 K. While this did not affect the observed distance dependence, it is interesting that it also appears in samples prepared with deuterated TEMPO, as can be seen in Fig. 2.6. This suggests that for shorter inter-electron distances, an additional contribution to residual relaxation may emerge. Deuteration of the TEMPO molecule still reduces the residual relaxation for the $\bar{r} = 1.8$ nm sample, which indicates that the nuclear spin bath remains an important contributor to residual electron

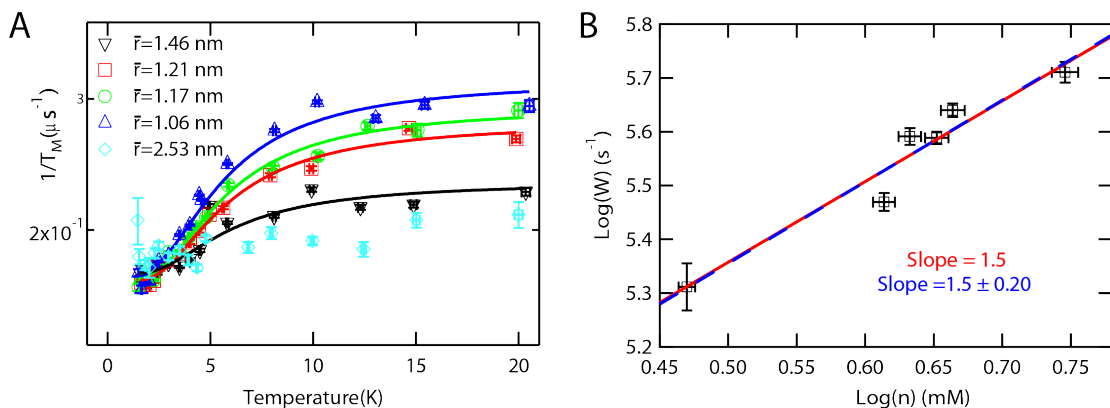


Figure 2.7: Spin Bath Quenching in Spin-Labeled Vesicles. **A:** $\frac{1}{T_M}$ as a function of temperature for various PC-TEMPO distances in DOTAP vesicles. Clear distance dependence is observed, and is well described by Eq. 2.1 except for $\bar{r} = 2.53$ nm, where the spins are far enough apart that $\frac{1}{T_M}$ is roughly constant. **B:** Values of W , extracted from fits to Eq. 2.1 plotted against the PC-TEMPO concentration show the $W \propto n^{\frac{3}{2}}$ dependence expected in a quasi-2D system. The solid red line shows a line with fixed slope of 1.5 as expected for $W \propto n^{\frac{3}{2}}$, while the dashed blue line is a linear fit to the data which agrees with a slope of 1.5 to within the fitting error. The resultant correlation coefficient of -0.969 confirms that the linear regression is justified.

spin relaxation, and any additional relaxation source is not dominant. For nitroxides in a protonated solvent (in Fig. 2.5), where short inter-electron spin distances were probed, no substantial increases in Λ are observed with increasing concentration—likely because they are masked by fast decoherence from protons in the solvent. While the cause of the increase in residual relaxation cannot be identified from these measurements, it is possible that additional spin-spin interactions are present at short distances, or that the high radical concentration caused modification of the glassing and partitioning of spins upon freezing.

2.3.3 Application to A Model Membrane

We have thus far determined that the use of spin bath quenching with protonated spin labels freely dissolved in deuterated solvents is sensitive to inter-electron distances from 1.8 to 6.6 nm. We now address how the spin labeling of biomolecules will affect measurements of spin bath quenching. Here, non-deuterated spin labeled lipid vesicles are used as model systems to investigate whether distance-dependent spin bath quenching can be observed in biological systems. Unilamellar vesicles of 200 nm diameter were prepared from DOTAP(1,2-dioleoyl-3-trimethylammonium-propane (chloride salt)) lipids mixed with varying fraction of PC-TEMPO(1,2-dioleoyl-sn-glycero-3-phospho(TEMPO)choline), a lipid functionalized with a nitroxide spin probe off the headgroup. The preparation of vesicles followed published techniques¹⁰⁶ and details of the vesicle composition can be found in Table 2.2. Measurements were carried out on protonated lipid vesicles in a deuterated solvent to prevent the dramatic reduction of T_M seen previously. In Fig. 2.7A, a clear temperature dependence is observable for average inter-electron distances less than ~ 1.5 nm (corresponding to a $\sim 8-15$ % PC-TEMPO/DOTAP fraction). What is most striking is that small differences of 0.1 nm in average inter-electron spin distances can be easily observed in the spin bath quenching in this disordered biological system, even though the overall distance range is limited. At 2 K the values of T_M coalesce and plateau to ~ 6.25 μs —a rate ~ 8 x faster than for non-deuterated nitroxide probes freely dissolved in

a fully deuterated solvent. The temperature dependence is again well described by Eq. 2.1, as depicted with the solid fit lines in Fig. 2.7A. Phase memory times of these samples with an average inter-electron distance of $\bar{r} = 1.5$ nm and longer are independent of temperature, and consistent with the low temperature plateau found in more concentrated samples. This is depicted by the vesicle system with $\bar{r} = 2.5$ nm trace in Fig. 2.7A, which no longer shows significant temperature dependence.

We did not attempt distance extraction for the vesicle samples, but the characteristic flip-flop rate (W) determined by the fits to Eq. 2.1 show a clear dependence on the PC-TEMPO concentration in Fig. 2.7A. On the surface of lipid vesicles, we expect the characteristic flip-flop rate is still simply related to average inter-electron distance by $W \propto \frac{1}{\bar{r}^3}$. However, as the spin labels are bound to the quasi-2D vesicle surface we have $\bar{r} \propto \frac{1}{n^2}$, rather than $\bar{r} \propto \frac{1}{n^3}$ as in a 3D system. This implies $W \propto n^{3/2}$ for 2 dimensional systems, which agrees well with the data shown in Fig. 2.7B. The data (in Log/Log form) is well described by a linear regression with a high correlation coefficient, the slopes of linear fits agree with the model to within the uncertainty of the fit, and the scatter does not appear systematic. Therefore, the simple flip-flop model does describes the experimental data of this model system well. The data from the spin-labeled vesicles presented in Fig. 2.7B has slightly larger than expected scatter. This may result from greater sample-to-sample variation in these more complex samples, such as variation in

per-vesicle spin-label concentration. However, the data is still most consistent with the expected dipolar interaction in 2-dimensional system.

Notice the dependence in Fig. 2.7B is clearly distinct from a 3D system where W was shown to increase linearly in concentration and confirms we are accessing inter-electron distances on the 2D surface of a vesicle. This finding demonstrates that a calibration curve could also be employed to map B-Spin flip-flop rates to inter-electron distance in this important and common biological surface.

In order to investigate the residual relaxation process in a different lipid vesicle system, the $\bar{r} = 2.5$ nm sample was compared to an identical concentration (with similar inter-electron distance) of PC-TEMPO distributed in DOPC (1,2-dioleoyl-sn-glycero-3-phosphocholine) lipid vesicles. T_M for the DOPC/PC-TEMPO vesicles was also temperature independent, but only 70% of the T_M value of the DOTAP/PC-TEMPO sample (4 μ s vs 5.5 μ s). In the case of vesicle systems, it is reasonable to observe faster residual decoherence rates than for free nitroxide solutions, as the spin-label is tethered to a macromolecular surface with high proton concentrations, and thus is subject to additional decoherence mechanisms. The comparison of T_M of vesicles with different lipid compositions confirms that decoherence effects arising from the vesicles themselves limit the low temperature phase memory times. The faster relaxation in DOPC vesicles may be attributed to the longer hydrophilic headgroup region of the DOPC compared to the DOTAP lipid, which means the TEMPO label is located closer to the molecular protons of

the vesicle surface than in DOTAP vesicles. Interestingly, much as for nitroxides in a protonated solvent, spin-labeled vesicles (in Fig. 2.7) with short interspin distance do not display substantial increases in Λ at increased concentration (as emerged for free-in-solution nitroxides). This supports the supposition that the effect for nitroxides in protonated solvent was masked by the fast proton relaxation (and is now masked by the relaxation effects from the lipids, rather than the solvent).

2.3.4 Potential Distance Limits and Application for Studying Geometry and Clustering

A concentration series of nitroxides in fully deuterated solvent mimics an 'ideal' system, making it a good gauge of distance ranges which may be resolved through spin bath quenching with nitroxide labels. Inter-electron distances out to roughly 7.2 nm should be resolvable based on the longest distance where temperature dependence can be observed. This is crudely estimated by the inter-electron distance at which the first term of Eq. 2.1 is 5x smaller than the second term at 20 K with $\Lambda = 20$ kHz. The prediction is sensible as we correctly measure $\bar{r} = 6.6$ nm, but the temperature dependence is relatively weak. The use of deuterated TEMPO radicals resulted in a roughly 40% decrease in the residual relaxation rate. In this case, the estimate for a long distance limit rises to ~ 8.1 nm, which approaches the limits of pulsed EPR distance measurements. In real biological systems, the

protons of the solvent, buffer, or the biomolecule itself will be large contributors to Λ . Thus, it is likely that the deuteration of nitroxides would only be useful for extending the range of distance measurements via spin bath quenching in samples which are otherwise already fully deuterated.

Conversely, measurements down to roughly 1.1 nm are possible based on our ability to measure the full temperature dependence of the phase memory time. This was determined from the inter-electron distance that, at 20 K and $\Lambda = 20$ kHz, gives a phase memory time of 1 μ s—a rate that can be reliably measured using the 650 ns pulses typical for our system. Although no distances this short were measured for our samples in deuterated solvent, Fig. 2.5 shows that TM below 1 μ s were measured for concentrated samples in non-deuterated solvents. For short distances, our work with lipid vesicles demonstrates that average inter-electron distances can be differentiated with ~ 0.1 nm resolution. While this resolution may decrease at longer inter-electron distances, where the dependence of W is no longer as responsive to changes in distances, for short distances this gives excellent sensitivity for changes in inter-electron distance.

Measurements of free-in-solution nitroxides show that distances above 6 nm are accessible in systems with broad distance distributions, so long as the residual decoherence rate, from the nuclear spins for instance, can be kept slow. In addition to solvent deuteration, common EPR techniques for lengthening phase memory times can be employed, such as: strategic spin labeling of molecular sites

known to present longer phase memory times, or utilization of deuteration of the biomolecule itself, as is routinely done in NMR spectroscopy, and also has been employed in DEER measurements to lengthen the accessible distance ranges.⁹³ Further, this approach is not limited to nitroxide probes, and previous work has investigated carrying out distance measurements with different paramagnetic species. For instance, the effects of fast relaxing, high-spin Fe(III) on nitroxide T_{1e} have been investigated and used for distance measurements,^{107,108} and both Gd³⁺-nitroxide^{109,110} and Gd³⁺-Gd³⁺^{111,112} distances have been measured using DEER. Thus, many possibilities exist to expand on this work, pushing towards EPR distance measurements in non-pairwise systems with wide distance distributions out to, or beyond, lengths currently achievable with DEER.⁴⁶ The potential of this with a high-spin ion is discussed in Section 2.4

Beyond distance measurements, the dependence of the extracted spin flip-flop rate (W) on concentration (n) provides information about the geometry, arrangement or assembly of biological constituents. In isotropically dispersed systems, like that of freely dissolved nitroxide molecules in 3D solution, we expect a dependence of $W \propto n$. Alternatively, in a 2D environment, such as for nitroxides bound to the surface of a 200 nm diameter lipid vesicle, a $W \propto n^{\frac{3}{2}}$ dependence is expected. Interestingly, there are also important 1D systems in biology, such as elongated amyloid fibers found in neuro-degenerative brain tissues.¹¹³ There are many examples of biomolecular systems where the geometry of growth and

assembly processes are not known, for instance in the early and transient stages of the aggregation of proteins to oligomers and soluble fibrils, or the assembly of proteins on lipid membrane surfaces. Previous work has used cw-EPR lineshape analysis at 10 GHz to examine dimensionality in dendrimer systems.¹¹⁴ We suggest that, in addition to providing nanometer scale distance information, quantification of spin bath quenching can discern the geometry of growth and arrangement of complex biomolecular systems presenting considerable disorder, where the direct extraction of the dipolar frequency through DEER is not possible. Further investigation of the capabilities of spin bath quenching to study dimensionality as well as clustering in biological systems is presented in Section 2.5.

2.4 Observing Long Distances by Decoherence in Gd³⁺

After identifying the mechanism of spin bath quenching and exploring its ability to reflect interspin distances, the question of applicability rises. A key limitation in applying spin bath quenching in nitroxides is the effect of residual relaxation (Λ) overwhelming the temperature dependence, as is observed in spin-labeled vesicles. This inspires the investigation of alternative spin systems to study spin bath quenching. Certain spin labels may better isolate the paramagnetic species from the nuclear environment and reduce the effects of residual

relaxation. Alternatively, the increased strength of dipolar interactions between high-spin species should increase the effect of spin bath fluctuations over residual relaxation. Therefore, spin bath quenching with other labels may prove easier to observe in a complex biological system or at longer distances than with nitroxides. It is found that Gd^{3+} in particular offers an exciting combination of advantageous traits. As Gd^{3+} plays a large role in Part 1 of this dissertation, we take a moment to outline its status as a nearly ideal spin system for high-field EPR due to its well understood chemistry, high spin, and symmetric orbital configuration. As we propose using Gd^{3+} in biological systems, Section 2.4.1 begins by discussing the existing capabilities of utilizing Gd^{3+} as a spin-label, before addressing the advantages of Gd^{3+} as a high-field, pulsed EPR probe (Section 3.2 addresses the Gd^{3+} spectrum in more detail).

2.4.1 The Gd^{3+} Ion as Suitable Probe for Pulsed, High Field EPR on Biological Systems

Gd^{3+} in MRI and NMR

Gd^{3+} is a spin $7/2$ ion resulting from the stable arrangement of 7 unpaired electrons in a half-filled 4f-orbital. It has emerged as the contrast agent of choice for use with MRI due to its ability to shorten relaxation times (T_1 and T_2) of nearby protons, allowing enhancement of MRI signals in water around the ion. The figure of merit for a relaxation agent is its relaxivity¹¹⁵ which is defined as

the change in the T_1 or T_2 of protons per concentration of contrast agent. Gd^{3+} 's high spin, resulting from the largest number of unpaired electrons (7) in a known ion, is part of its suitability as a contrast agent.¹¹⁶ However, other ions have larger magnetic moments due to orbital angular momentum, but the symmetry of Gd^{3+} half-filled f orbital results in a comparatively long relaxation times (100's of ps to several ns in water), which allow it to better relax water protons than these spins with larger magnetic moments.¹¹⁶ Despite these features, Gd^{3+} itself seems to be a poor choice for any medical or biological application due to its acute toxicity.^{117,118} As a result, Gd^{3+} is always embedded into a coordination complex, which binds tightly to the ion through a series of coordination bonds (ideally 8). A wide variety of these coordinating complexes exist offering different properties, binding affinities, and relaxivities^{116,119} and development is ongoing to improve their capabilities (with continued interest in systems besides Gd^{3+}).¹²⁰ Clearly, gadolinium contrast agents represent an entire field of research, existing at the intersection of chemistry, biology and medicine. But the extensive knowledge of Gd^{3+} coordinating-complex chemistry from MRI makes it an attractive probe for spin-labeling as it provides a information reserve for the chemistry of coordinating Gd^{3+} .

Indeed, lanthanides in general, and gadolinium specifically have already found use for magnetic resonance studies of structural biology in NMR. Due to the same strong relaxation effects leveraged in MRI, the binding of Gd^{3+} to a biomacro-

molecule substantially affects the NMR signal of nuclei near the binding site. Early work focused on applications to proteins which inherently bind a metal ion to study the local environment near the binding sites,¹²¹ and the technique has seen substantial quantitative development with multidimensional NMR to identify the specific residues where binding occurs and the binding pKa's.¹²² Increasing capabilities of protein chemistry have seen the development of a variety of techniques to label biomolecules with Gd^{3+} , allowing it to be used as a part of structural determination.¹²³⁻¹²⁵ As a result a variety of Gd^{3+} labeling schemes have been developed.¹²⁶⁻¹²⁹ While not all of these structures are ideal for EPR spin-labeling, the existence of this work for labeling proteins is fortuitous as a variety of Gd^{3+} -labels do exist, and we are assured that optimal design of both coordinating complexes and labeling schemes are possible with existing chemical synthesis knowledge.

Gd^{3+} in EPR

Gd^{3+} 's half-filled 4f orbital results in an ion with no orbital angular momentum and a symmetric wavefunction. The ground state of the system is ${}^8Gd_{7/2}$ as a result of having no orbital angular moment. This $S=\frac{7}{2}$ ion then has 8 possible spin states: $|\pm \frac{1}{2}\rangle, |\pm \frac{3}{2}\rangle, |\pm \frac{5}{2}\rangle, |\pm \frac{7}{2}\rangle$. These levels are not fully degenerate at zero magnetic field due to zero-field splittings (ZFS), which emerge from interactions of the unpaired spin with one-another as well as the electrostatic field of the

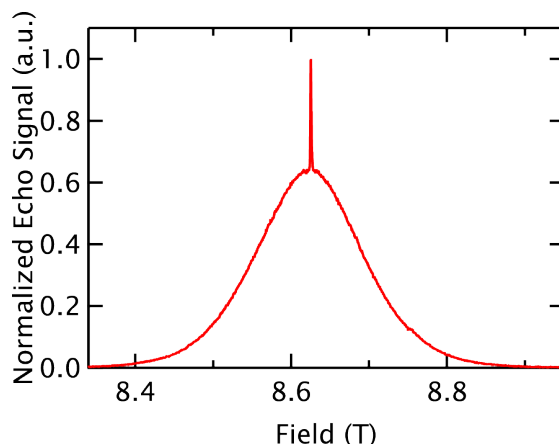


Figure 2.8: The Gd^{3+} Spectrum at 240 GHz. The 5 K echo-detected spectrum of GdCl_3 at $\bar{r}=3.8$ nm (5 mM) shows the narrow $| -1/2 \rangle \leftrightarrow | 1/2 \rangle$ transition centered on the broad peak associated with the transitions of the other states.

surrounding environment.^{22,130} However, as a result of the symmetry of the orbital and lack of angular momentum, the ZFS is small and at high magnetic fields, the Zeeman term dominates by many orders of magnitude (typical values for ZFS are 10's of mT). Thus, to a very good approximation, the given Zeeman kets $|m_Z\rangle$ are “good” eigenstates for discussing the system.

The observed EPR signals emerge from the allowed transitions (i.e. $\Delta S_Z = \pm 1$), meaning there are 7 allowed transitions of the form $| -\frac{7}{2} \rangle \leftrightarrow | -\frac{5}{2} \rangle$, $| -\frac{5}{2} \rangle \leftrightarrow | -\frac{3}{2} \rangle$, \dots . If only the Zeeman transition were considered, each transition would occur at an identical frequency, but the ZFS lifts this degeneracy, and spreads the total resonance over 100's of mT (still a fraction of the applied field).

Given the spherical symmetry of the orbital, the g -value for Gd^{3+} is unaffected by rotation, meaning that the Zeeman term of the Hamiltonian is not dependent on the relative orientation of the Gd^{3+} ion in the magnetic field. As a result of the

isotropic g -value, the zero-field interactions are the major factor that determines the spectral lineshape of Gd^{3+} and this becomes critical when evaluating the cw EPR spectra, as will be done in Chapter 3. However, for the sake of discussion of measurements of the relaxation times of Gd^{3+} , it is sufficient to note that the spectrum is quite broad at 8.5 T, covering ~ 0.2 T due to broad distributions of ZFS parameters and the orientational dependence. As will be covered in more detail in Chapter 3, the central transition ($|-\frac{1}{2}\rangle \leftrightarrow |\frac{1}{2}\rangle$) is unaffected by ZFS to first order,¹¹² and thus is quite narrow (and becomes narrower as B_0 is increased). This yields a very narrow central transition on the back of a broad, rather featureless distribution of the other transitions. A representative, field swept echo measurement is shown in Fig. 2.8

In looking at the properties of Gd^{3+} for pulsed EPR, there are several key advantages when compared to nitroxide based radicals. The isotropic g -value is an advantage for DEER at high fields as orientation selection of the spectrum complicates measurements of nitroxides at these fields.¹¹² Further, the T_{1e} relaxation time of Gd^{3+} complexes remain rather short even at low temperatures ($< 300 \mu\text{s}$ at 95 GHz and 25 K^{112,131} and shorter when measured at 240 GHz). By comparison, the T_{1e} for nitroxides is much longer (at 240 GHz ~ 1 ms at 50 K and ~ 5 ms at 25 K),³⁸ which affects the rate at which spectra can be averaged. As low temperatures are typically necessary for pulsed EPR at high magnetic fields (as a way

of lengthening T_M), decreases in T_{1e} and the associated increases in experimental repetition time can dramatically improve the quality of data collected.

Finally, a high-spin ion couples more strongly with the applied pulses, resulting in a $\frac{\pi}{2}$ pulse which is 4x shorter than for an $S = \frac{1}{2}$ system as can be realized by examining the \hat{S}_X operator for an $S = \frac{7}{2}$ system (see Appendix B). The importance of this is easily understood at high magnetic fields, where source power is highly limited. A factor of 4 decrease in pulse length is equivalent to a factor 16 increase in available power. This significantly shortens pulse sequence, opening the door to measurements of more rapidly relaxing systems, including the option of moving to higher temperatures.¹¹²

2.4.2 Measurements of the Temperature Dependence of T_M in Gd^{3+}

The suitability of Gd^{3+} as a spin probe for pulsed EPR at high fields, combined with its suitability as a spin-label for studying biology raises exciting questions about whether it can be utilized to improve the distance ranges accessible with spin bath quenching. This hope is raised as a result of Gd^{3+} being a high-spin ion. Therefore, the dipolar interactions between the spins can be substantially larger; for instance, the $|\frac{7}{2}\rangle$ state generates a dipolar field 7x larger than for a $|\frac{1}{2}\rangle$. As a result, one expects that the dipolar coupling is relevant over a wider range of distances, which may increase the range over which spin bath quenching is visible.

In order to address this, identical studies as in Section 2.3 were carried out using a Gd^{3+} paramagnetic species. In this case, GdCl_3 was used as it is widely available, easily soluble in water, and small. As with the study in Section 2.3, we utilized random solutions in D_2O and d-glycerol. The phase memory time (T_M) was measured at 240 GHz using a spin-echo sequence of 175 ns - τ - 275 ns - τ , in which the optimum lengths of the first and second pulses were found to give the best echo intensity and shape. Notice that these lengths are consistent with the expectation that for high-spin Gd^{3+} , the pulse lengths should be reduced by a factor of 4 (for $S = \frac{1}{2}$ in nitroxides we used 650 ns and 750 ns respectively). The echo decay was measured at the point of maximum signal, corresponding to the center of the $|\frac{1}{2}\rangle \leftrightarrow |-\frac{1}{2}\rangle$ transition. The echo decay shapes (shown in Fig 2.9A) were found to be largely exponential (in contrast to the decays in nitroxides), and therefore fits for the echo area $\propto \exp(-(\frac{2\tau}{T_M})^\alpha)$, with $\alpha = 1$. Notice that $\tau_M = T_M$ in this limit as $\Gamma(2) = 1$.¹⁰⁴

As with the phase memory times of nitroxide at 8.5 Tesla, we observe a strong temperature dependence of T_M for GdCl_3 at temperatures below 20 K as is shown for an $\bar{r} = 4.8$ nm (2.5 mM) sample in Fig. 2.9B. However, the temperature dependence is not the same as observed with nitroxides: though T_M flattens some for temperatures above ~ 20 K, there is no corresponding plateau below 2 K, and the shape of the temperature dependence does not follow that in Eq. 2.1. However, this is not unexpected; the model proposed in Eq. 2.1 is derived specifically

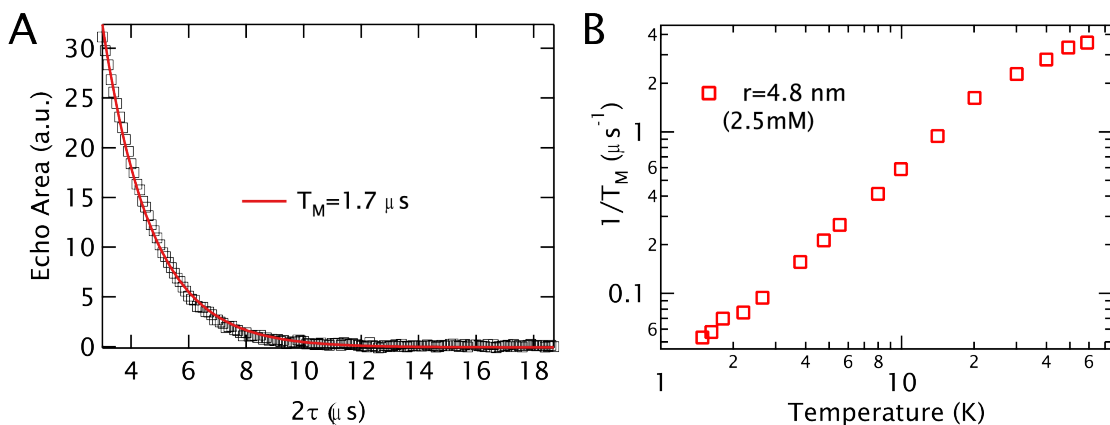


Figure 2.9: The Gd^{3+} Echo Decay in GdCl_3 . **A.** The decay of the echo area of an $\bar{r}=4.8$ nm (2.5 mM) sample of GdCl_3 in $\text{D}_2\text{O}/\text{d-glycerol}$ measured at 240 GHz and 10 K. The decay was fit to a simple exponential of the form $\propto \exp(-(\frac{2\tau}{T_M}))$. **B.** The phase memory times ($\frac{1}{T_M}$) for the $\bar{r}=4.8$ nm (2.5 mM) sample of GdCl_3 as a function of temperature show a strong temperature dependence, though it is not characteristic of spin bath quenching in Eq. 2.1.

for an $S = \frac{1}{2}$ system, whereas now we have an $S = \frac{7}{2}$, with 8 energy levels, whose populations depend strongly on temperature (and in a more complex way). Phenomenologically similar flip-flop models exist in literature for high-spin systems,⁹⁶ but they do not appear to describe the data well, suggesting that the mechanism is not fully encapsulated. Further, this model assumed that the relaxation is based on a flip-flop process involving energy conserving transition between spins. Now, however, we find that the spin-lattice relaxation time is comparable to T_M . For instance for the sample in Fig. 2.9, T_{1e} ranges from $\sim 2 \mu\text{s}$ to $60 \mu\text{s}$ between 50 and 2 K. In this case, it is possible that individual spin flips may begin to contribute to the relaxation process, which would render the flip-flop model inapplicable (though it is, of course possible that *both* processes contribute).

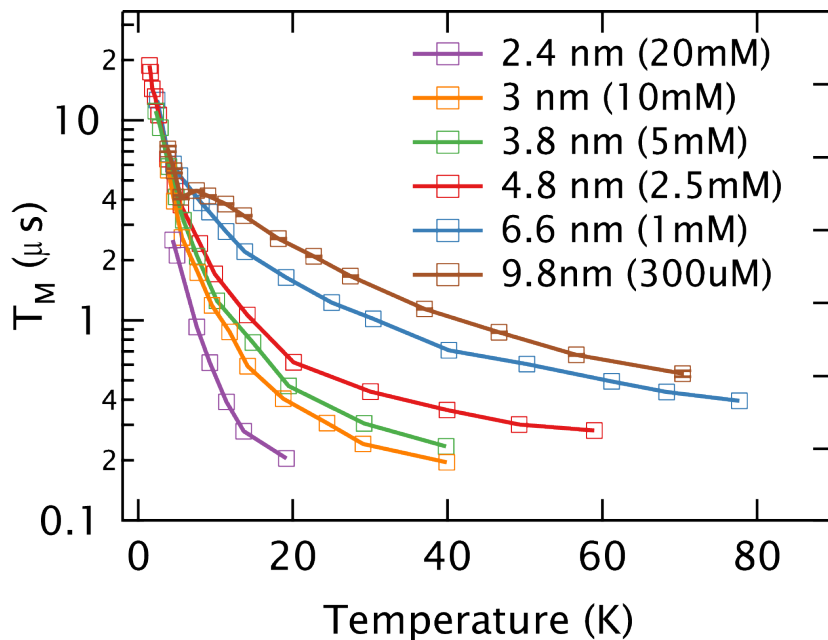


Figure 2.10: Temperature Dependence of the Phase Memory Time of $GdCl_3$. Temperature dependent $\frac{1}{T_M}$ values for several different samples of $GdCl_3$ in a deuterated solvent. While the shape does not follow that of nitroxides in Fig. 2.2B or given in Eq. 2.1, we see that T_M still coalesces as low temperatures, and is strongly dependent on average nearest neighbor distance at high temperatures. We see dependence on distance out to ~ 10 nm, far longer distances than in nitroxides.

Despite incomplete understanding of the shape for the temperature dependence, measurements were carried out on a concentration series of GdCl_3 with the results shown in Fig. 2.10. The shape of the temperature dependence is similar in all samples, but we see clear trends reminiscent of the nitroxide concentration series. At high temperatures, though the traces do not flatten out (as would be expected in spin bath quenching), there is a clear dependence of the T_M values based on the interspin distances, with the shortest interspin distances yielding substantially shorter relaxation times. Alternatively, at low temperatures, while the traces do not plateau, they do all coalesce. This behavior indicates sensitivity in the temperature dependence to the average interspin distances, which results directly from spin-spin coupling (as it is evidently quenched at low temperatures). While the precise mechanism needs to be investigated, there are clear effects out to very dilute concentrations (corresponding to long interspin distances). As compared to nitroxides, where effects vanished around $\bar{r} = 6.6$ nm (1 mM), we see effects out to $\bar{r} = 10$ nm (300 μM), and are in the process of investigating even longer distances.

It appears that the high-spin state of Gd^{3+} expands the range over which the temperature dependence of T_M depends on average interspin distance. However, the description of this as spin bath quenching is currently not complete. Though the behavior is indicative of a resolvable difference in behavior, it can not be connected to a simple mechanism as was possible in the nitroxide case.

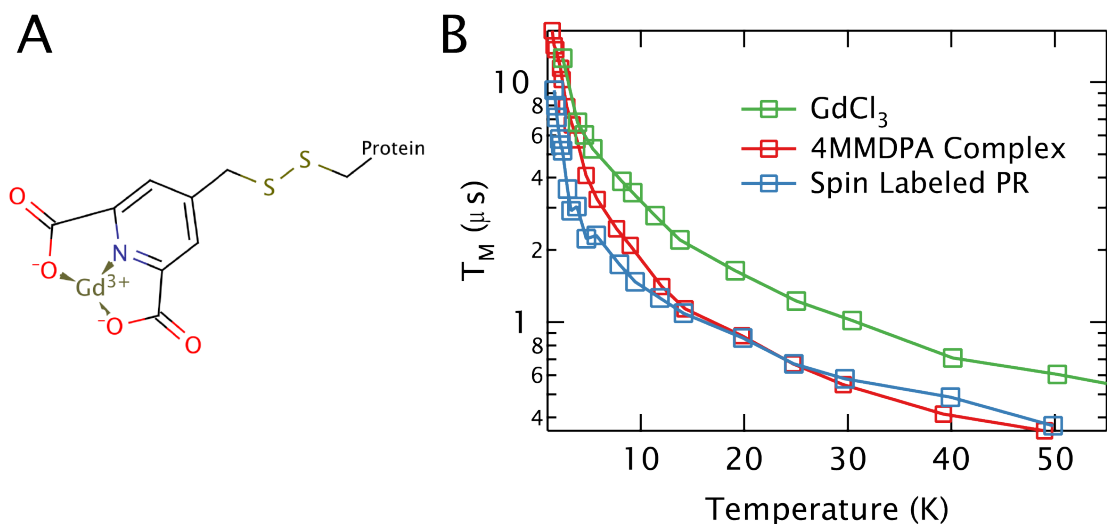


Figure 2.11: Phase Memory Times During Spin Labeling. **A.** Shows the structure of 4MMDPA (bound to the cysteine residue of a protein),¹²⁹ which is commercial available, binds Gd^{3+} and labels protein similarly to MTSL. **B.** The temperature dependence of T_M is shown for a 1 mM concentrations of several different forms of Gd^{3+} . Upon binding (in a 1:1 ratio) of $GdCl_3$ with the 4MMDPA complex, the phase memory time shortens, but maintains the same shape (shown in red and green respectively). When 4MMDPA is bound the protein, the phase memory time does not drop substantially, suggesting that Gd^{3+} is less prone to fast relaxation as a result of labeling a biomacromolecule.

However, the extended distance range is exciting enough to warrant further investigation. A critical concern is whether or not such work could ever be utilized in a biological situation. As was observed for nitroxides, upon spin-labeling of a biomacromolecule, we see that the potential exists for the interaction between the spins to be obscured by relaxation from other sources.

In order to address this, we carried out measurements using a Gd^{3+} coordinating complex that can easily be functionalized to the cysteine residues of a protein (through SDSL).¹²⁹ The structure of 4MMDPA, a dipicolinic acid that chelates

Gd^{3+} is shown in Fig. 2.11A. We investigate the effect of coordinating Gd^{3+} to the tag, and the effect of then attaching the tag to a water-exposed site on a protein (in this case, Proteorhodopsin, a membrane protein that acts as a light-driven proton pump).^{41,132} We see that, when complexed with the 4MMDPA agent, there is a drop in the phase memory time of Gd^{3+} . However, when the 4MMDPA is functionalized to the protein, it appears that the phase memory times do not change substantially across the majority of the temperature range (though at low temperatures there is some discrepancy). Thus, the majority of difference is observed upon binding of the Gd^{3+} to the complex, which is not unexpected as in the coordinating complex 3 fewer sites are filled in D_2O , which may increase relaxation. Additionally, when using 4MMDPA complex, a lower d-glycerol concentration was used (in preparation for eventually binding to Proteorhodopsin) than when utilizing GdCl_3 , which may also contribute to the observed change in relaxation. However, the change in relaxation upon coordination is less than a factor of two, which is small compared to the order of magnitude change observed when the nitroxide radical was bound to the spin-labeled vesicle (for instance, in Fig. 2.7). Thus, this suggests that even in spin-labeled biomacromolecules (like the Proteorhodopsin presented here), the phase memory time remains long enough to support the potential for observing long distances, though this would need to be subjected to further studies to confirm.

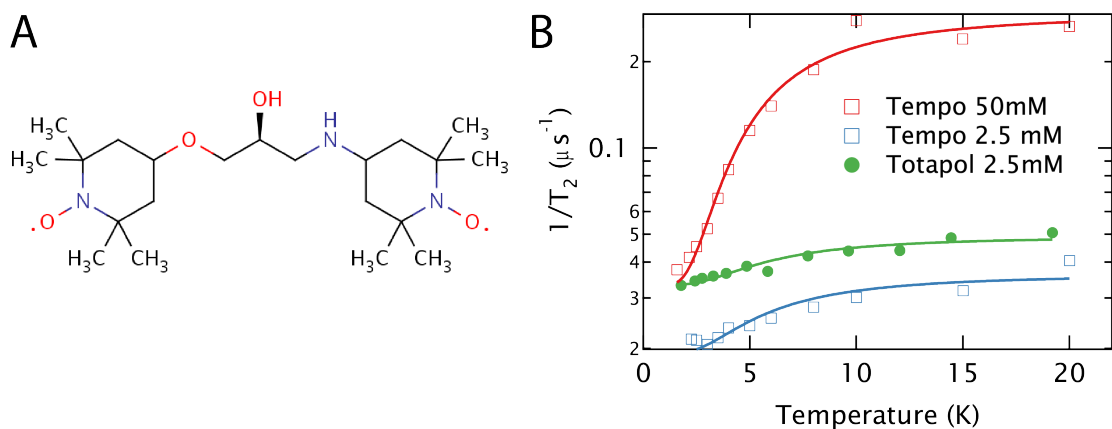


Figure 2.12: Spin Bath Quenching in TOTAPOL. **A.** TOTAPOL is a rigid bis-nitroxide structure with a ~ 1.3 nm interspin distance.¹³³ **B.** The temperature dependence of $\frac{1}{T_M}$ for TOTAPOL is well described by Eq. 2.1. The curve appears different than our measurements of a short interspin distances (Tempo 50 mM) and the comparable concentration of Tempo (2.5 mM). However, fits to Eq. 2.1 shown in Table 2.3 suggest that the Λ and W are controlled by two different relevant distances.

2.5 Studying Pairwise Systems and Clustering with Spin Bath Quenching

The work presented in this chapter has, up to this point, solely targeted random distributions of spins in either 3D or 2D systems. However, it is interesting to consider the case of probing more rigid distances (or even to approach attempting pairwise distance evaluation). In order to investigate the potential for this, we conducted studies to examine the effect of spin bath quenching in flexible bridge molecules, where a pair of spins is tethered together with a linker. We begin by considering the original, $S = \frac{1}{2}$ example of studying nitroxide based probes. A commercially available radical pair called TOTAPOL was utilized (a sketch is

shown in Fig. 2.12A), where the rigid linker separates two nitroxide moieties (in this case, the molecule acts like a ruler due to the rigid interspin distance).¹³³ The distance between the spins is ~ 1.3 nm,¹³³ which is short by the standards of the study in Section 2.3. However, when working at a molecular concentration of 2.5 mM (corresponding to 5 mM spin concentration), the phase memory times are substantially longer than, for instance, the $\bar{r} = 1.78$ nm (50 mM) samples (taken from Fig. 2.3), as shown in Fig 2.12B.

At first, this discrepancy may seem unexpected, as the spin bath quenching model predicts that shorter inter-B-spin distances should lead to strong spin bath quenching effect. However, in the case of the TOTAPOL molecule, while each spin has a nearest neighbor that is close, the corresponding *next* nearest neighbor (with which we expect the nearest neighbor to flip-flop), is quite far away ($\bar{r} = 4.8$ nm if we neglect size exclusion effects). For comparison, we also plot $\frac{1}{T_M}$ for the $\bar{r} = 4.8$ nm (2.5 mM) concentrations (taken from Fig. 2.3). We can see that the temperature dependence of T_M for the TOTAPOL molecule is different from both of the nitroxide curves, which might suggest that neither relevant distance (the “short” distance of ~ 1.3 nm, nor the intra-TOTAPOL distance $\sim \bar{r} = 4.8$ nm) is solely controlling T_M .

To investigate this further, we carried out fits to Eq. 2.1 and found that, like the curves for nitroxides, the temperature dependence of T_M can be well described by the model. By examining the result in Table 2.3, we can see that the two pa-

rameters of Eq. 2.1 seem to reflect the two relevant distances in the system. For reasons which remain unclear, when working with concentrated systems like the $\bar{r} = 1.78$ nm (50 mM) sample, the residual relaxation Λ was found to increase substantially (see Table 2.1). A similar residual relaxation is found in the TOTAPOL molecule. However, W , the term that is linked to the dipolar flip-flop rate (and hence average distance between next nearest neighbors), is found to agree almost exactly between the TOTAPOL molecule and TEMPO molecule, when both are at similar concentration. This suggests that Λ is strongly affected only by nearest-neighbor distances (and evidently only for close distance), whereas W (as was explained above for the spin bath quenching model) rather reflects the average distance between next nearest neighbors.

Further investigation of this was done utilizing Gd^{3+} molecules bound in coordinating complexes tethered together. In this case, we utilized a Gd^{3+} coordinating complex based on DOTA contrast agents from MRI (Gd595 shown for reference in Fig. 2.13A),¹³¹ which binds the Gd^{3+} in a highly symmetric environment. Two tethered molecules were investigated, one where a pair of Gd595 are tethered together, and one where three Gd595 moieties are tethered (Fig. 2.13C and Fig. 2.13B respectively). The linker structure is flexible, yielding a broad distribution of distances, but the maximum of the distribution is ~ 1.6 nm¹³⁷ in the dimer and is expected to be similar in the case of the trimer. Measurements of the phase memory times in Fig. 2.14 show that a strong temperature depen-

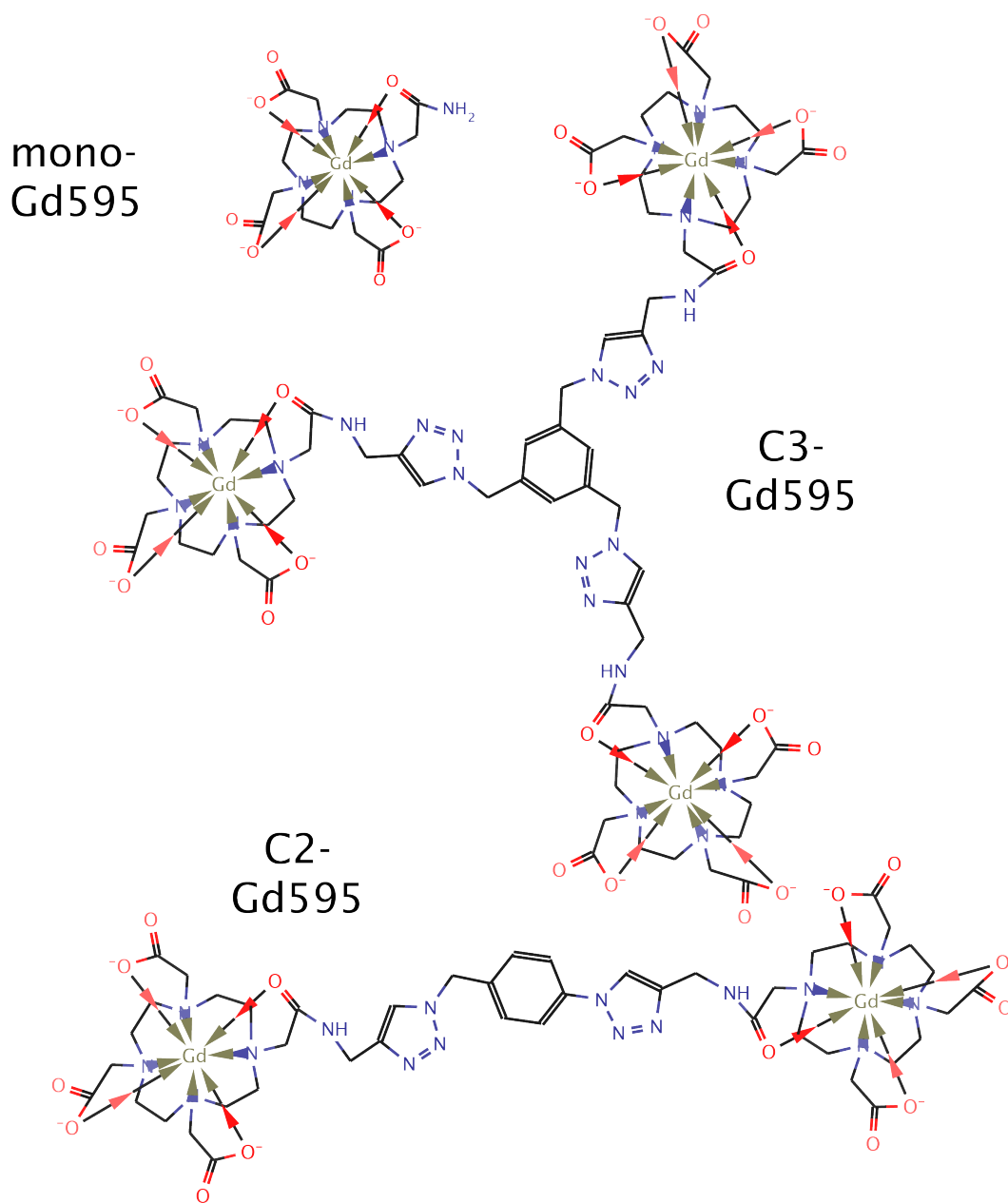


Figure 2.13: Structure of Gd^{3+} Coordinating Complexes. Show the three Gd^{3+} coordinating complexes used in the study. In all cases Gd^{3+} is complexed in a similar environment, but then tethered with flexible bridge structures.^{131,134–136}

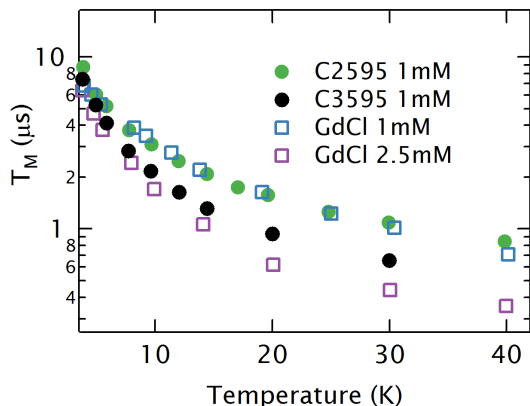


Figure 2.14: Temperature Dependence of the Phase Memory Time of Complexed Gd^{3+} . The phase memory times (T_M) of various samples containing Gd^{3+} are shown, all of which demonstrate a strong temperature dependence. We see that the bis- Gd^{3+} molecules C2-Gd595 has a nearly identical behavior to a free solution of GdCl_3 at the same concentration, despite the existence of very short (~ 1.6 nm) nearest neighbor. When the tris- Gd^{3+} complex C3-Gd595 is used, the temperature dependence of the phase memory time changes, but is not equivalent to a 2.5 mM GdCl_3 solution (which is approximately the same total spin concentration).

dence is still observed in these bridge structures, and at low temperatures the relaxation times coalesce with measurements of the free-in-solution GdCl_3 . The dimer molecule has nearly identical temperature dependence as free-in-solution GdCl_3 , which agrees with the measurement in TOTAPOL suggesting that the depth of the temperature dependence emerges largely from the distance between the molecules (as this is the next nearest neighbor distance). Alternatively, we see that when the trimer is measured, T_M drops (giving a larger depth) indicative of spin bath quenching. Thus, these measurements distinguish between the number of spins complexed, rather than being controlled solely by concentration.

This, together with the nitroxide data suggests that spin bath quenching is sensitive to the clustering of spins, rather than simply pairwise distances (which do not change substantially between the dimer and trimer). This is sensible, as the spin bath quenching model requires two B-spins to interact, and in a dimer molecule the distance between B-spins is controlled by the intermolecular distance (not the distance of the ruler). When spin begin to cluster, there are more nearby B-spins, which should increase the strength of the spin bath quenching. More work is necessary to confirm and quantify these clustering effects, however, the ability to address clustering, rather than pairwise distances is important. Many biological systems oligomerize, or cluster (in different dimensions), and the ability to unravel the structure, or number of interacting spins could be critical to identifying these structures.

2.6 Impact of Spin Bath Quenching

This chapter provides a comprehensive overview of the distance dependence of spin bath quenching at high fields and low temperatures for nitroxide based spin probes. While spin bath quenching does act as a probe of interspin distance, it is strongly limited for nitroxides when other relaxation terms dominate. This was found to strongly limit its application. However, the promising outlook is that alternative, Gd^{3+} probes appear to be more sensitive to spin bath quenching (that is, out to long distances), and less affected by the surrounding nuclear spin

bath. This is demonstrated for a random solution of GdCl_3 , and with a spin-labeled protein. Further, the application of this to study clustering as well as distances is evident, as different relaxation effects appear to be controlled by different relevant distances. Unfortunately, even for nitroxides the model used was incomplete, and though it described random solutions well, it likely must be refined to treat more complex distance distributions. The case in Gd^{3+} is in fact worse, as spin bath quenching is not explicitly observed (though the temperature dependence is phenomenologically similar). Thus, it seems that an improved model (either for nitroxides, or for Gd^{3+}) should be developed to help quantify the newest experimental results.

PC- TEMPO Concentra- tion (mM)	DOTAP Concentra- tion (mM)	DOPC Concentra- tion (mM)	Percent Spin Label(%)	Average Interspin Distance (nm)
0.98	35.84	0	2.76	2.53
2.95	35.84	0	8.23	1.46
4.11	35.84	0	11.47	1.24
4.49	35.84	0	12.56	1.18
4.61	35.84	0	12.86	1.17
5.57	35.84	0	15.54	1.06
0.94	0	45.98	2.04	2.93

Table 2.2: Vesicle Compositions, Interspin Distances. Vesicle compositions. The concentration of various vesicle samples prepared for this work with corresponding average inter-electron distances calculated as described in Appendix A

Compound	Molecular Concentration (mM)	Average Inter-molecular Distance (nm)	Pairwise Distance (nm)	Dipolar Coupling W (kHz)	Residual relaxation Λ (kHz)
TEMPO	50	1.8	—	1,050	33.2
TEMPO	2.5	4.8	—	68.8	19.6
TOTAPOL	2.5	4.8	1.3	64.0	33.2

Table 2.3: TOTAPOL and TEMPO Comparison. Compares the rigid distance and average intermolecule distances for the samples of 4-Amino-TEMPO and TOTAPOL in Fig. 2.12. The resulting values of the flip-flop rate W and residual relaxation rates Λ are included from fits to Eq. 2.2. The results suggest the intermolecular distance controls W while there is an effect from strong coupled spins (from a close nearest neighbor) in Γ .

Chapter 3

Distance Measurements using Gd Lineshapes

Material in this chapter, as well as Appendix D, including figures and some detailed experimental information for this work in Appendix A, are originally published in Ref. 138 (available online), and are reproduced by permission of the PCCP Owner Societies.

3.1 Introduction

As discussed in Sec. 1.2, when nitroxide spins are less than ~ 2.0 nm apart, their dipolar coupling broadens the EPR lineshape beyond the intrinsic linewidth an interspin distances between 0.8 to 2.0 nm can be quantified through extraction of the broadening function from the continuous-wave (cw) EPR spectrum.^{43,46,47} When distances become longer than 2.0 nm, the intrinsic linewidth of the nitroxide probe prevents observation of the dipolar broadening.⁴⁶ and powerful pulsed distance measurement techniques (for instance DEER)^{50,52,139} are necessary, which

can access distances and distributions as long as 6-8 nm.^{56,140} However, pulsed EPR distance measurements have limitations. Despite recent advances demonstrating measurements of short distances on an immobilized protein in solution at room temperature,¹⁴¹ pulsed EPR measurements most often require temperatures below 100 K. Finally, in studies of lipid membrane systems, the effect of high local spin concentration can dramatically reduce the phase memory time of spins, rendering PDS difficult, particularly for long distances.¹⁴² Thus, if the distance range of cw EPR-based measurements could be extended beyond 2.0 nm, it would offer an important alternative to pulsed EPR for rapid measurements of long length scales relevant to structural biology. These measurements offer the advantages being applicable in orientationally disordered samples, and under milder experimental conditions. Most dramatically, at temperatures above the protein-glass transition temperature proteins begin to explore their natural conformational space.¹⁴³⁻¹⁴⁵ Thus, the capacity to measure distances beyond 2.0 nm above 200 K offers the opportunity to study the structure and dynamics of proteins in an environment more representative of ambient biological conditions, while also allowing for the possibility to track motion. Here we discuss the opportunities of utilizing cw-EPR for measuring long distances using the Gd^{3+} spins introduced in Sec. 2.4.

In this chapter we use a concentration series of GdCl_3 , which acts as a good model of potential Gd^{3+} spin labels in a system with a broad distance distribution,

as a case study to explore the potential limits for cw EPR distance measurements. We show that the cw EPR spectra of frozen, random solutions of GdCl_3 in deuterated water/glycerol glass at 240 GHz and 10 K are sensitive to dipolar broadening at average interspin distances up to 5 nm. Calculations of the expected lineshape broadening for Gd^{3+} agree with the experiments in random solutions, confirming that broadening is visible at longer distances than with nitroxides. As these measurements occurred in a random solution (and therefore a necessarily large distance distribution), the actual pairwise distance sensitivity is estimated to be ~ 3.8 nm. Measurements of bis- Gd^{3+} complexes with a flexible bridge with ~ 1.6 nm inter- Gd^{3+} distances shows dramatic broadening, consistent with that found for a GdCl_3 sample with comparable average interspin distances, suggesting cw EPR measurements will be useful for measuring distances in pairwise systems. The trends in both experimental and calculated broadening effects are found not to change at 260 K, introducing the exciting prospect of extending cw EPR distance measurements out to ~ 3.8 nm at much higher temperatures than are typically possible with DEER using nitroxides. In addition to dipolar broadening, a second contributor to the EPR lineshape was also encountered at high concentrations, which results from the large change in the refractive properties of these samples on resonance, an effect we call refractive broadening. This effect did not interfere with observation of dipolar broadening at long distances, and is irrelevant for the low spin probe concentrations typically used in biological distance measure-

ments. However, it is discussed and analyzed in detail to provide a comprehensive understanding of EPR lineshape effects caused by Gd^{3+} dipolar broadening.

3.2 Spectroscopic Properties of Gd^{3+}

In the Section 2.4, Gd^{3+} was introduced as a potential probe of distances through measurements of the phase memory times (T_M). As discussed there, many advantages of gadolinium are realized in pulsed experiments; however, here we address the lineshape of gadolinium, and so this section will focus on the properties of Gd^{3+} in a cw EPR experiment. The suitability of Gd^{3+} as a probe in biological systems emerges from the extensive knowledge of coordination chemistry for the ion. As gadolinium is commonly used in MRI and NMR as a relaxation agent, a great deal is known about ideal ways to bind the ion, and then label proteins and biomolecules. More details can be found in section 2.4.1.

The Hamiltonian of a single Gd^{3+} ion is generally given (in frequency units) by²²

$$H = g_e \mu_\beta B_0 S_Z + D[S_{Z_c}^2 - \frac{1}{3}(S(S+1))] + E[S_{X_c}^2 - S_{Y_c}^2] \quad (3.1)$$

where μ_β is the Bohr magneton, B_0 is the applied magnetic field, $g_e \sim 1.992$ is the isotropic g-value of Gd^{3+} , the S_i 's and S_{i_C} 's are the spin operators in the laboratory and zero-field frames respectively, while D and E are the axial and non-axial zero-field splitting (ZFS) parameters. Both ^{155}Gd and ^{157}Gd have nuclear

magnetic moments and are present in appreciable amounts at natural abundance (~ 30 combined); although these isotopes will contribute to the Gd^{3+} lineshape through hyperfine coupling, it is generally neglected as a small effect. The first term of Eq. 3.1 dominates at high fields and simply gives the eight Zeeman levels, yielding seven allowed EPR transitions. The second two terms are the zero-field splitting, which further shift the energy levels, spacing the allowed transitions by tens of mT from each other. Generally, the coordinating environment controls the strength of the ZFS, and more symmetric coordinating environments lead to smaller values of D . However, the central $|-\frac{1}{2}\rangle$ and $|\frac{1}{2}\rangle$ levels are not affected by the zero-field splitting to first order in perturbation theory. This result is worked through in Appendix C.

The zero-field shifts of the non-central transitions depend on the strength and symmetry of the zero-field interaction (expressed by the D and E values) and the orientation of the ZFS principal-axis frame with respect to the applied magnetic field. In a randomly distributed, frozen glass, both the orientation and magnitude of the Gd^{3+} ZFS are broadly distributed. This causes all the resonances—with the exception of the $|-\frac{1}{2}\rangle \leftrightarrow |\frac{1}{2}\rangle$ transition—to broaden substantially, leading to the nearly featureless, broad component of the Gd^{3+} echo-detected spectrum of Fig. 3.1.¹⁴⁶ Because the central line is affected starting at second order, its linewidth scales with $\frac{D^2}{(g_e\mu_0)^2 B_0}$ leading to a narrowing of this central line with increasing magnetic field (this is covered explicitly in Appendix C).²² Previous

work has helped characterize the ZFS parameters and distributions in commonly used MRI contrast agents at fields up to 8.6 T.^{146,147} Values of $\frac{D}{g_e\mu_0}$ on the order of 10-60 mT are common in the literature for Gd³⁺ chelates. At 8.6 Tesla fields (240 GHz Larmor frequency), the central line reaches peak-to-peak widths as narrow as ~ 0.5 mT, which is shown to be sufficiently narrow to be sensitive to dipolar broadening of distant electron spins at several nanometers.

3.3 Dipolar Broadening in for Gd³⁺

As discussed in Section 1.2, line broadening emerges from dipolar interactions of the spins. This has been worked out and applied as a distance probe using S = $\frac{1}{2}$ systems such as nitroxides.^{43,47} The Pake pattern⁴⁵ describes the broadening pattern of a single, fixed distance in the case where the interspin vectors are isotropically distributed for a S = $\frac{1}{2}$ system. We can expand the definition of this Pake pattern more generally to include higher spin systems. The basic pattern is expressed in Eq. 1.19.

The form of the distribution is the result of the potential dipolar shifts based on the different orientation present in an isotropic distribution. In the limit that we can neglect effects to the Zeeman states based on the ZFS (i.e. so long as $D \ll B_0$), we can simply expand this by “adding” the higher spins states. The new terms differ from these terms only in the breadth which they cover, which is to say, the splittings are increased proportionally to the spin state. Additionally,

we must now pay closer attention to the populations of each of the spin states. For the $S = \frac{1}{2}$ system, at low magnetic fields (where cw distance measurements are commonly applied), the populations of the two spin states are roughly equal (even at 2 K the polarization reaches only $\sim 11\%$). Obviously, at high magnetic fields and with many spin states, the population of the various energy levels begins to vary substantially with temperature. In general, we must require that the broadening pattern of each spin state is normalized based on its population, that is

$$\int_{-\infty}^{\infty} w_n(B, T, r) dB = P_n(T) = \frac{1}{Z} \exp\left(\frac{n\hbar\omega}{k_b T}\right) \quad (3.2)$$

where $n = \pm\frac{1}{2}, \pm\frac{3}{2}, \pm\frac{5}{2}, \pm\frac{7}{2}$, and $Z = \sum_{n=-\frac{7}{2}}^{\frac{7}{2}} \exp\left(\frac{n\hbar\omega}{k_b T}\right)$ is the partition function. However, the total width of each spectrum is determined only by $\alpha_n(r) = 2n\alpha(r)$ and so we can simply normalize each spin state's broadening by a factor of $\frac{P_n(T)}{\alpha_n(r)}$. Notice that we either use $\alpha_{strong} = \frac{3}{4} \frac{\mu_0}{4\pi} \frac{1}{r^3} \mu_2 = \frac{1.39}{r^3} \text{ mT nm}^3$ or $\alpha_{weak} = \frac{1}{2} \frac{\mu_0}{4\pi} \frac{1}{r^3} \mu = \frac{0.93}{r^3} \text{ mT nm}^3$, depending on whether we are in the strong or weak coupling regime discussed in Sec. 1.2. We could write a generally applicable model for this approximation of a high spin Pake pattern, but for the sake of being terse, we write it out only for $S = \frac{7}{2}$.

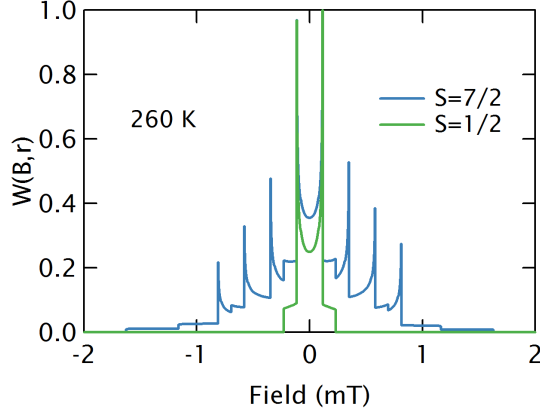


Figure 3.1: High Spin Pake Patterns. Pake patterns demonstrating the broadening profile of spins at a distance of $r = 2.0$ nm for both an $S = \frac{1}{2}$ and $S = \frac{7}{2}$ spin system based on Eq. 1.19 and Eq. 3.4 respectively.

$$\begin{aligned}
 W_{\frac{7}{2}}(B, T, r) &= \sum_n \frac{f_n(B, T, r)}{\alpha_n(r)} \\
 w_n(B, T, r) &= \begin{cases} P_n(T) \left(\frac{B}{\alpha_n(r)} + 1 \right)^{-\frac{1}{2}} & : -\alpha_n(r) < B < 2\alpha_n(r) \\ P_{-n}(T) \left(-\frac{B}{\alpha_n(r)} + 1 \right)^{-\frac{1}{2}} & : -2\alpha_n(r) < B < \alpha_n(r) \end{cases} \quad (3.3) \\
 \text{for } n &= \pm \frac{1}{2}, \pm \frac{3}{2}, \pm \frac{5}{2}, \pm \frac{7}{2} \\
 f_n(B, T, r) &= \sum_n \frac{f_n(B, T, r)}{\alpha_n} \quad (3.4)
 \end{aligned}$$

The result of modeling these dipolar interactions is to show that the existence of the higher spin states is directly responsible for a broader broadening profile. For instance, simply calculating the broadening profile for an interspin distance of 2.0 nm for the $S = \frac{1}{2}$ and $S = \frac{7}{2}$ results in a clearly broader patterns as is shown in Fig. 3.1.

As was discussed in Sec. 1.2, the goal of cw distance measurement is to determine a pairwise distance (and perhaps distribution) based on measurements of a spectrum where dipolar broadening is present, and where it is negligible. Thus, all of the existing machinery utilized for cw distance measurements (See Sec. 1.2.1) applies here using a modified broadening pattern.^{43,46,47} By following Eqs. 1.20 and 3.4 we can then generate dipolar-convolved spectra, representing an expected broadening (based either on a known or guessed/fit distance distribution). An advantage of this approach is that only the unbroadened spectra and a distance distribution are necessary to calculate the dipolar-convolved spectrum, so there is no need for complete spectral simulation, which would necessitate careful determination of many spin-parameters (most notably for Gd^{3+} the zero-field interaction parameters). In these calculations, exchange interactions were neglected as the 4f electrons are found to be well shielded by the 5s and 5p outer electrons, and at both 260 K and 10 K the samples are highly viscous (or completely frozen).¹⁴⁸

In our work, the Pake pattern is calculated in the “weak-coupling” approximation where the pseudo-secular parts of the dipolar interaction are neglected.⁴⁴ This is justified by the broad extent of the Gd^{3+} spectrum ($>.2$ Tesla) compared to the dipolar interaction strengths. However, for the $|-\frac{1}{2}\rangle \leftrightarrow |\frac{1}{2}\rangle$ transition, the width becomes comparable to the dipolar interaction for shorter distances, and so the quality of this approximation should be discussed. In Sec. 1.2 it is shown that for nitroxides measured at X-Band, strong coupling is dominant for interspin

distances below ~ 0.7 nm, while fully weak-coupling emerges above ~ 1.5 nm, with a region of intermediate coupling in between.⁴⁶ Our calculations suggest that the broadening in Gd^{3+} is increased by a factor of ~ 3.5 (See Fig. 3.9), and thus by a scaling argument we expect the distances range to be increased by $\sqrt[3]{7} = 1.9$, yielding intermediate coupling between 1.3 nm and 2.9 nm. Thus, while for the majority of spin states, the coupling is likely well described in the weak interaction regime, there is a large distance range where the broadening from neighboring $|\frac{1}{2}\rangle$ and $|\frac{1}{2}\rangle$ are of intermediate broadening. In nitroxides, measuring in a range of intermediate broadening introduces an uncertainty in estimating distances that is $\sim 10\%$.⁴⁴ However, given that we only expect this to occur for a fraction of the broadening pattern, this is likely an upper limit for the Gd^{3+} spectrum; in fact, for low temperatures the $|\frac{7}{2}\rangle$ and $|\frac{5}{2}\rangle$ states contain $\sim 90\%$ of the spins, and only $\sim 3\%$ are in the $|\pm \frac{1}{2}\rangle$ states, suggesting that at these temperatures the effect will be truly small (though becoming relevant at higher temperatures).

3.4 Dipolar Broadening in Test and Model Systems

3.4.1 Solutions of Gd^{3+}

A concentration series of Gd^{3+} ions allows us to evaluate its capabilities as a cw-distance probe by observing the lineshape as the average interspin distance is

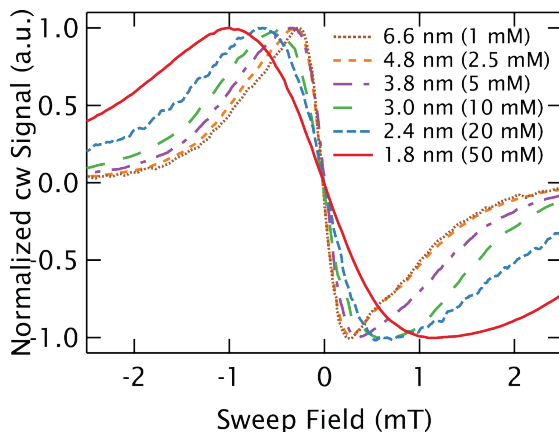


Figure 3.2: Broadening of the Central Transition of Gd^{3+} . cw EPR spectra of GdCl_3 at 10 K show evidence of dipolar broadening out to $\bar{r} = 5$ nm (2.5 mM). For longer interspin distances, the linewidths remain constant as the effects of dipolar broadening are too small to resolve on the intrinsic lineshape.

varied. Due to the $\frac{1}{r^3}$ falloff of the dipolar interaction, we approximate the distance distribution with the nearest-neighbor distance distribution. For the remaining discussion, we will refer to the average nearest-neighbor interspin distance, rather than concentration, as in a random 3D solution these are related by Eq. 2.2. To probe the effects of dipolar broadening in Gd^{3+} , the 240 GHz cw-spectra of different concentrations of GdCl_3 , dissolved in a D_2O and deuterated glycerol solution, were measured at 10 K. The concentration was varied between 100 μM and 50 mM, to tune the average nearest-neighbor interspin distance from 1.8 to 14.1 nm. Deuterated solvents were used to minimize broadening due to hyperfine interactions with the water ligands. As these ions are freely dissolved in solution, the actual interspin distances are distributed about the average values. The measurements show that as the average interspin distance increases, the central

transition narrows for average, nearest-neighbor distances up to $\bar{r} \sim 4.8$ nm (2.5 mM). It is important that in a random solution the distance distribution is broad and at longer average distances the shorter distances (in the wings) are primarily responsible for the broadening. Thus, for a more biologically relevant, narrow distribution a somewhat shorter distance limit likely exists and will be addressed in calculations. At longer distances, the central linewidth ceases to change, as expected when the broadening due to the local dipolar field is substantially smaller than the intrinsic linewidth. Fig. 3.2 demonstrates the narrowing of the central transition as a function of interspin distance in the cw spectra at 10 K using derivative detection. Though not shown in Fig. 3.2 for the sake of clarity, the most dilute sample measured was 100 μ M, which still showed a strong signal with a $\text{SNR} = \frac{V_{P-P}^{\text{signal}}}{2V_{\text{RMS}}^{\text{Noise}}} \approx 80$.⁸⁷

The broadening can be clearly visualized through the peak-to-peak linewidths of the spectra as plotted in blue boxes in Fig. 3.3A. As the quality of measurements improved with modification of the sample holder and loading procedures, multiple measurements were taken at each concentration. These are subjected to an average in Fig. 3.3A where the results are weighted by an estimate of the resolution with which the peak-to-peak width could be determined (which depended largely on the sweep rates and noise). The unbiased, weighted variance was used to incorporate the sample-to-sample variations observed for repeated measurements into the uncertainty. For samples with interspin distances at or below $\bar{r} = 3.0$

nm (10 mM), the sample shape and volume are found to measurably affect the lineshape, leading to a substantial scatter at shorter interspin distances seen in the large error bars in Fig. 3A. For example, the peak-to-peak linewidths of the $\bar{r}=1.78$ nm (50 mM) samples ranged between 2.2 and 3.6 mT with widely varying lineshapes, several of which are shown in Fig. 3.4. This variation is caused by refractive broadening, emerging when the change in a sample's susceptibility on resonance is large enough to change its refractive properties. This effect becomes so dramatic at the highest concentrations ($\bar{r} = 1.8$ nm (50 mM)) that the spectrum of some samples no longer display a single peak, as can be seen in Fig. 3.4. However, lineshapes at longer interspin distances ($\bar{r} > 3.0$ nm or below ~ 10 mM) are found to be reproducible with different sample volumes and holders.

The average nearest-neighbor distance distribution for a given spin concentration can be easily calculated from literature.⁹⁸ Utilizing these distributions with an intrinsic spectrum, Sec. 3.3 allows us to generate the expected dipolar-convolved spectra for any concentration. The lineshape was experimentally found not to change with average interspin distance above $\bar{r} = 5$ nm (2.5 mM), ensuring that the $\bar{r} = 14.1$ nm (100 μ M) samples are a good approximation of the intrinsic spectrum. Dipolar-convolved spectra are compared to experimental results in Fig. 3.3B and Fig. 3.3C for the cases of $\bar{r}=3.8$ nm (5 mM) and $\bar{r}=3.0$ nm (10 mM), respectively. As refractive broadening will further broaden the line, we have minimized its impact by comparing with the narrowest line observed. By gener-

ating a series of dipolar-convolved spectra for various spin concentration (where the distance distribution is well known), we obtain the expected lineshape, and from this the expected linewidth as a function of the corresponding average interspin distance in a random solution. The expected linewidths are overlaid in Fig. 3.3A and agree well with the narrowest lineshapes observed for samples with average interspin distances longer than $\bar{r}=2.4$ nm (20 mM). For shorter distances we consistently measure substantially broader lineshapes. At $\bar{r}=1.8$ nm (50 mM), the difference between the experimental data and the dipolar-convolved linewidth is dramatic. However, as will be discussed below, the experimental and dipolar-convolved linewidths agree when calculations are used to remove the refractive broadening from the experimental lineshapes, leaving only the dipolar effects. The overall agreement observed utilizing the dipolar-convolved spectra clearly demonstrates the potential to use fitting of broadened spectra to determine the broadening function and extract interspin distances in Gd^{3+} lineshapes.

Similar measurements were carried out at high temperatures (~ 260 K) with identically prepared GdCl_3 solutions. Given the large concentration of glycerol used in the systems (d-glycerol: D_2O 60:40 by volume, 65:35 by mass) the freezing temperature is ~ 230 K,¹⁴⁹ for a non-deuterated sample. Though deuteration of water raises the freezing temperature slightly, we assume the effect of deuteration will remain small enough that the sample is a highly viscous fluid. Following calculations in literature¹⁵⁰ we find that at 260 K the viscosity of this mixture

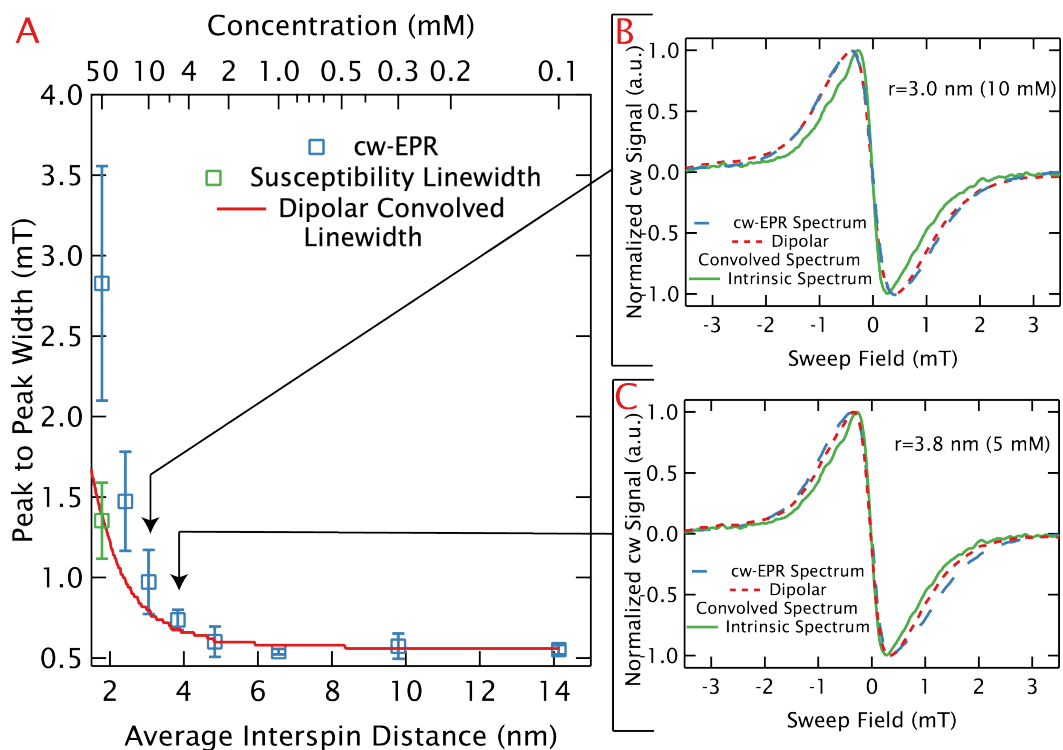


Figure 3.3: Distance Limits of Dipolar Broadening in Random Solutions of GdCl_3 . **A:** The measured peak-to-peak linewidths are plotted in blue squares as a function of average interspin distance for random, frozen solutions of GdCl_3 at 10 K. The wide scatter of linewidths at higher concentrations resulting from refractive broadening is apparent. The best-fit values for the peak to peak linewidth in the presence of refractive broadening are shown in a green square for $\bar{r}=1.8$ nm (50 mM). The linewidths from the dipolar-convolved spectra are shown with the red line and agree well with the narrowest linewidths measured up to $\sim \bar{r}=3.0$ nm (10 mM). **B** and **C** confirm this by demonstrating the experimental lineshape (blue, dashed line) and dipolar-convolved lineshape (red, dotted line) agree well at $\bar{r}=3.0$ nm (10 mM) and $\bar{r}=3.8$ nm (5 mM). Each plot includes the intrinsic linewidth (the experimental $\bar{r}=14.3$ nm (0.3 mM)) as a solid green line.

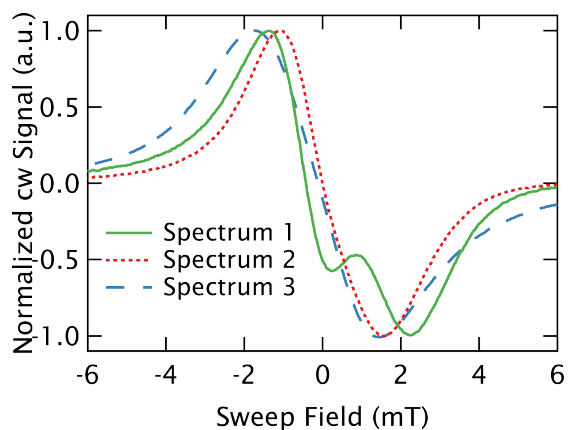


Figure 3.4: Refractive Broadening at High Concentrations. Three different cw spectra of $\bar{r} = 1.8$ nm (50 mM) GdCl_3 using different sample holders and sample volumes are plotted. The lineshape inconsistency is evidence of the effects refractive broadening, which can even result in the extreme lineshapes of Spectrum 1 (blue, dashed line).

is roughly 140 x larger than that of water at 298 K. The peak to peak linewidth again decreases with increasing interspin distances until reaching the intrinsic linewidth between $\bar{r}=3.8$ nm and $\bar{r}=6.6$ nm as shown in Fig. 3.5 (utilizing the same analysis approach used for the 10 K data). The central, peak-to-peak linewidth was typically narrower than the linewidths at 10 K, but the overall trend was found to be comparable.

For GdCl_3 at higher temperatures, the dipolar-broadening function is different than at 10 K due to the temperature dependence of the Zeeman-level populations for a high-spin system at high magnetic fields. Using the lowest concentration lineshape (1 mM ($\bar{r} = 6.6$ nm)) measured at 260 K as the new unbroadened spectrum, we again compute the expected dipolar-convolved linewidths as a function of average nearest-neighbor distance, this time at 260 K. The resulting linewidths

(overlaid in Fig. 3.5) show agreement in the onset of broadening and are comparable to the experimental linewidths for interspin distances down to $\bar{r} = 3.0$ nm (10 mM).

However, these calculated, dipolar-convolved lineshapes significantly underestimate the width of the experimental spectrum for shorter distances. Some effect from refractive broadening can be expected at the highest concentrations, but does not account for the ~ 0.1 mT discrepancy at $\bar{r} = 3.0$ nm (10 mM), where refractive broadening should be absent at these temperatures. This work assumes that the sole broadening mechanism emerges from static, dipolar interactions, which is clearly valid in frozen situations. However, other effects can cause broadening at these temperatures, in particular modulation of the dipolar interaction by motion¹⁵¹ or by the longitudinal relaxation (T_{1e}).^{152,153} However, neither of these interactions should play an extensive role due to the extremely high viscosity of the solvent under these conditions. Based on models for T_{1e} of DOTA contrast agents in liquid,¹⁵⁴ which can not be directly measured, we estimate that the T_{1e} exceeds 100 ns due to the increased viscosity of the sample. This corresponds to a ~ 0.1 mT FWHM linewidth, which is $< \frac{1}{10}$ of the intrinsic linewidth. Alternatively, the effect of dipolar enhanced relaxation can only emerge from translational motion (as rotational motion does not significantly modulate the dipole interaction between neighboring monomers). However, we can estimate the translational correlation times from literature where $\tau = \frac{a^2}{D_f}$ where a is the distance of clos-

est approach for two gadolinium and D_f is the diffusion constant of one complex relative to the other. Based on values in literature,¹⁵⁵ $\tau \sim 300 - 700$ ps at 298 K in water, which can be scaled by the approximate viscosity difference (140) to $\tau \sim 42 - 100$ ns. Previous work has shown that dipolar interactions in $S = \frac{1}{2}$ systems are sufficiently averaged when $\tau \geq \left(\frac{\mu_0}{4\pi} \frac{3\pi g_e^2 \mu_b^2}{r^3 2\pi\hbar}\right)^{-1}$. This corresponds to when motion is slow enough that the strongest dipolar anisotropies are not averaged.^{151,156} As in estimating the distance limits, we approximate the broadening of the $S = \frac{7}{2}$ to be ~ 3.5 times larger than for $S = \frac{1}{2}$, thus scaling the cutoff distance time by $\sqrt[3]{3.5}$, and suggesting that the dipolar interaction is static for distances shorter than at least 4.1 nm (and up to 5.2 nm if the longer correlation time of ~ 100 ns is assumed). As this falls at the limit of our resolution of dipolar interactions, the effect of dipolar relaxation enhancement is assumed to be negligible for these systems (though would naturally emerge for less viscous liquids, i.e. in water at room temperature).

3.4.2 Linewidths of Coordinating Complexes

A brief investigation of Gd^{3+} coordinating structures was undertaken to identify ligands compatible with spin labeling that also have a narrow line. These studies examined the peak-to-peak linewidth of the central transition at 240 GHz and 10 K. To ensure these measurements represented the intrinsic linewidth, a concentration of 1 mM ($\bar{r} \sim 6.6$ nm) was used. Dipolar broadening was shown to

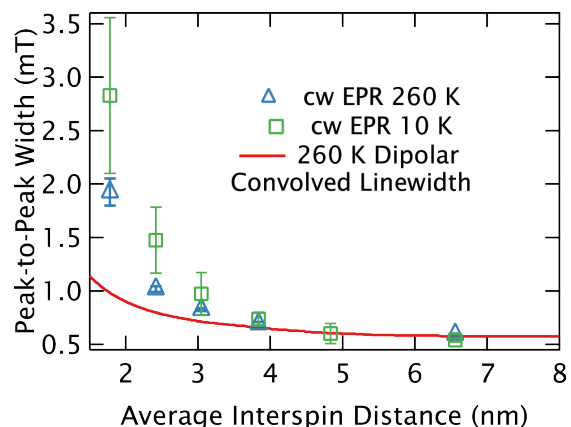


Figure 3.5: Dipolar Broadening at High Temperatures. The 260 Kelvin, experimental linewidths are plotted in blue squares, with average values of the 10 K measurements (from Fig. 3.3) in green squares for comparison. The 260 K measurements have routinely narrower linewidths, as is expected from the reduced dipolar broadening at high temperatures. This is demonstrated by comparison with the 260 K dipolar-convolved linewidths plotted as a solid, red line.

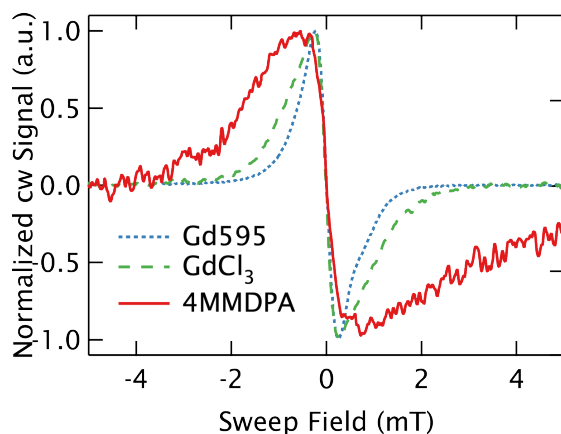


Figure 3.6: Intrinsic Linewidth of Gd^{3+} Chelates. The cw EPR spectra compare the central transition of Gd^{3+} at 1 mM ($\bar{r} = 6.6$ nm) in three different coordinating environments. Gd595 is plotted as a blue, dashed line, and shows a linewidth slightly narrower than freely dissolved $GdCl_3$ (green, dashed line), where the Gd^{3+} is coordinated by the solvent. 4MMDPA, plotted as a red, solid line, shows a linewidth nearly twice as broad.

be negligible at 1 mM in the GdCl_3 measurements. As reported above, GdCl_3 dissolved in solution, where the hydrated Gd^{3+} ion is coordinated by 9 water molecules, presents a narrow intrinsic linewidth of ~ 0.55 mT resulting from the relatively small ZFS compared to other Gd^{3+} chelates.¹⁴⁶ 4MMDPA, a dipicolinic acid (shown in Fig. 2.11A) that chelates Gd^{3+} and can be functionalized to cysteine residues of proteins (introduced in Fig. 2.11) shows a much broader intrinsic linewidth of ~ 1.3 mT at a 1:1 Gd^{3+} :ligand ratio.^{111,129,157} Because 4MMDPA has several stable ligation states, there is some contribution from Gd^{3+} bound to two 4MMDPA ligands (i.e. $\text{Gd}^{3+}-(4\text{MMDPA})_2$) as well as free Gd^{3+} . The former contributes to the broadness of the experimental line, as it has a larger ZFS than the single coordinated species, but is not expected to occur in spin-labeled proteins.¹⁵⁷ Alternatively, Gd595 (shown in Fig. 3.7A) is a Gd^{3+} chelating structure that embeds the high-spin ion in a highly symmetric environment and is similar to the coordinating complexes developed for spin-labeling of bio-molecular structures.⁴⁶ This symmetric environment yields a small ZFS ($D \sim 20$ mT),¹³¹ resulting in a peak-to-peak linewidth of 0.45 mT, making it the narrowest chelate studied. In Fig. 3.6, the cw EPR lineshapes at 10 K and 240 GHz are shown for the 1 mM samples of each species. As Gd595 offers a linewidth narrower than GdCl_3 and therefore compatible with long-range distance measurements, we utilize bis- Gd^{3+} complexes based on Gd595 as a case study to observe the dipolar broadening in a system of spin-pairs (Sec. 3.4.3).

When using cw lineshapes for distance measurements, a narrow intrinsic linewidth is important to resolve long interspin distances. Therefore, details of the Gd^{3+} chelating structure, which affects the zero-field parameters and in turn the intrinsic EPR linewidths, is critical in evaluating the suitability of Gd^{3+} labels for distance measurements using cw EPR. The highly symmetric environment of Gd^{3+} in water—surrounded by 9 water molecules—gives the narrow line observed. Three equivalent Cl^- ions serve as counter ions to Gd^{3+} in GdCl_3 solution, but are not directly coordinating the central ion. Meanwhile, in Gd595 Gd^{3+} is coordinated by 4 oxygen and 4 nitrogen atoms that are symmetrically distributed, and one water molecule, yielding a similar, though measurably narrower lineshape. In contrast, 4MMDPA, which is easily employed as a commercially available, cysteine-compatible spin label, is coordinated by two oxygen atoms, one nitrogen atom, and six water molecules, and has a substantially broader line resulting from the less symmetric environment. This makes 4MMDPA non-ideal for lineshape-based distance measurements. Fortunately, the availability of alternative Gd^{3+} chelates and significant ongoing research efforts in this area makes the task of developing Gd^{3+} -based spin labels with narrower linewidths beneficial for cw-distance measurements a surmountable problem. Recent work by Yagi et al.^{134,158} provide a glimpse at a very promising outlook: they employed the symmetric DOTA ligands¹²⁹ with exceptionally narrow EPR linewidth (expected to

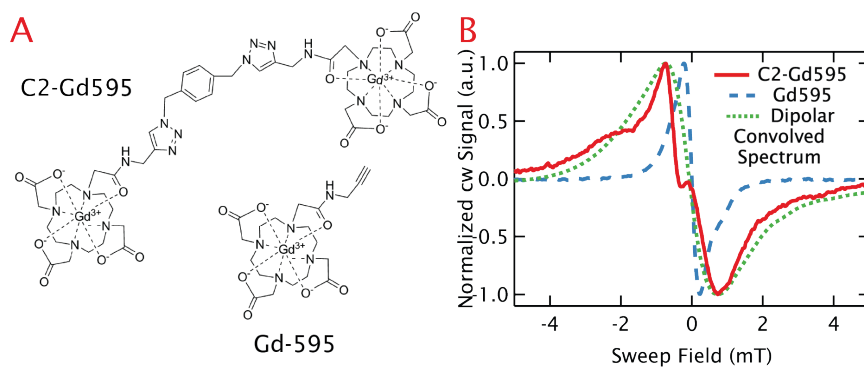


Figure 3.7: Dipolar Broadening in Spin-Pair System. **A:** Shows the chemical structure of Gd595, a single Gd^{3+} chelating structure, and C2-Gd595 where two of these molecules are separated by ~ 1.6 nm. These are included here for clarity, but are also presented in Fig. 2.13 **B:** The central cw-EPR lineshape at a 1 mM concentration for bis-C2-Gd595 is plotted as a red, solid line and the mono-Gd595 line is plotted as a blue, dashed line. The dramatic lineshape broadening can be attributed to strong dipolar coupling between the Gd^{3+} pair. This is confirmed from the agreement of the C2-Gd595 with the dipolar-convolved lineshape shown as a green, dotted line, where the Gd595 line was numerically broadened based on the interspin distance distribution from literature.¹³⁷

be ~ 0.45 mT at 240 GHz) as cysteine-binding spin labels, upon custom chemical modifications to ensure high rigidity for the Gd^{3+} compound.

3.4.3 EPR on a Bis- Gd^{3+} Complex

Two Gd595 moieties can be tethered with a flexible chemical linker as a bis- Gd^{3+} (C2-Gd595) complex with a flexible bridge, which was used as a model for a flexible, doubly-labeled biomolecular structure.¹³¹ Recent Ka-band (32 GHz) DEER measurements with examined the distance distribution of C2-Gd595, which is peaked at ~ 1.6 nm. The study utilized a specialized dielectric resonator and short, well separated microwave pulses to reliably measure even short interspin

distances. The study claims reliable distribution information down to ~ 0.8 - 0.9 nm, but we have sampled from the full published distribution, which extends down to 0.5 nm.¹³⁷ Both the mono-Gd³⁺ and bis-Gd³⁺ structures are shown in Fig. 3.7A. As discussed above, the central transition of a frozen solution of 1 mM Gd595 has a peak-to-peak linewidth of only 0.45 mT at 240 GHz and 10 K (Fig. 3.7B). In contrast, the spectrum of a frozen solution of 1 mM C2-Gd595 taken under identical conditions (overlaid in Fig 7B) shows a central linewidth of ~ 1.5 mT, which is more than three times broader than that of Gd595. This demonstrates that strong broadening is visible for a close interspin distance even with flexibly tethered spin-pairs. Further analysis shows that the observed broadening is consistent with the dipolar broadening observed in random solutions of GdCl₃ with comparable average interspin distances.

For the bis-Gd³⁺ complexes studied here, the distance distribution is known from recently reported DEER results.¹³⁷ We use the Gd595 spectrum as a reasonable estimate for the unbroadened spectrum of C2-Gd595, as the moieties around the Gd³⁺ ion are largely identical. The resulting, computed, dipolar-convolved spectrum is overlaid on to the experimental bis-Gd³⁺ spectrum in Fig. 3.7B. This demonstrates reasonable agreement with the experimentally measured peak-to-peak linewidth, though the more complex features are absent from the dipolar convolved spectrum.

In applying the dipolar broadening for random solutions at 10 K, we see good agreement to the measured lineshapes for sufficiently dilute systems where refractive broadening is negligible. However, in the case of the C2-Gd595 flexible bridge, the dipolar convolution fails to capture the details of the experimental spectrum, though it did predict the spectral width. The precise source of these discrepancies could not be identified unequivocally. However, given the broad distance distribution centered at a short distance (~ 1.6 nm), a sizable population of very short (< 1 nm) distances is expected. These distances present potential problems for the distance analysis here. For instance, exchange interactions are neglected in our analysis, and through bond exchange could reasonably exist in the bis-Gd³⁺ complex. Alternatively, while through-solvent exchange interactions are predicted to be weak in Gd³⁺, given the extremely short distances samples, they may become important and could cause some of the spectral features. As discussed above, at 10 K the effect of strong dipolar coupling of the $|-\frac{1}{2}\rangle$ and $|\frac{1}{2}\rangle$ spin states is negligible due to the high spin polarization, but it is possible that at very short distances some sizable populations of other spin states enter the strong coupling regime. Finally, the distance distribution below ~ 0.9 or 0.8 nm may be incomplete as this fell outside the range accessible with the DEER measurements.¹³⁷ More work remains with the particulars of these short distances to accurately produce the experimental shapes, but does not detract from the strong broadening, which

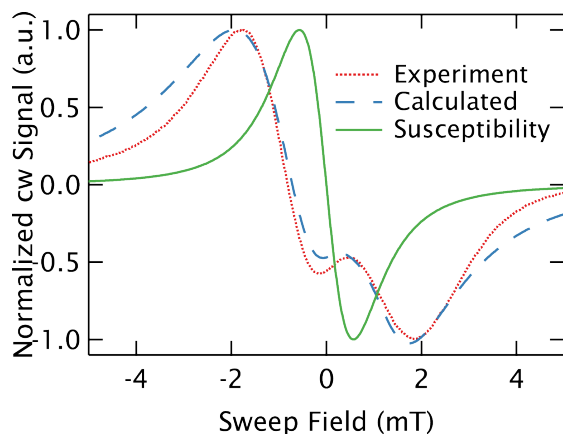


Figure 3.8: Eliminating the Effects of Refractive Broadening. The complex lineshape of an $\bar{r} = 1.8$ nm (50 mM) GdCl_3 sample (Spectrum 3 of Fig. 3.4) is plotted as a dotted, red line and can be well described by accounting for the effects of refractive broadening in a simple calculation of the resonance (dashed, blue line). This allows the determination of the true width of the resonance from the susceptibility response, which is shown with the solid, green line and demonstrates how dramatically the refractive broadening artificially broadens the measured lineshape at high concentration.

can act as a rough ruler of interspin distance at short distances, and does not impinge on the region of greatest relevance, which are longer distances.

3.5 Refractive Broadening

As mentioned in section 3.4.1, in addition to the effects of dipolar broadening, large susceptibilities were found to contribute to line broadening in high concentration samples. This effect is clearly observed at high Gd^{3+} concentrations where the linewidths and lineshapes proved to be strongly dependent on sample size and geometry. The origin of this lineshape effect, which we call refractive broadening, is not generally observed in EPR, and only emerges in our work because of the

high spin of the Gd^{3+} probes, the high magnetic field, the narrowness of the central transition, and the high concentrations used to access short (i.e. $\bar{r} < 3.0$ nm or above ~ 10 mM) average interspin distances in this study. This effect has been discussed previously as a “propagation effect”, and was treated similarly to the discussion here.¹⁵⁹

Generally in EPR, the magnitude of the complex susceptibility ($\chi = \chi' + i\chi''$) is small compared to one, and so the change in reflection from a sample is linear in χ . As our spectrometer measures the reflection from the sample, the cw-EPR signal for most systems is given by the real and imaginary parts of the susceptibility, independent of the sample geometry. However, in the case that χ' or χ'' approach one, due to a strong and narrow resonance, the refractive properties of the material change appreciably around resonance, so that in these cases the reflection is a more complex function of χ , and must be computed from a model. The method of calculating the reflection is discussed below and in Appendix D, where the explicit equations are presented. We estimate that for Gd^{3+} , χ' and χ'' approach ~ 0.1 (and therefore no longer $\ll 1$) at $\bar{r} = 3.0$ nm (10 mM). This agrees well with the Gd^{3+} concentration above which our experiments become difficult to reproduce and confirms that refractive broadening is expected to be irrelevant in biological samples as even short interspin distances are pursued in strategically doubly spin labeled biomolecules at overall concentrations of order 100's of μM or less. For comparison, at 10 GHz and 10 K, a nitroxide concentration in excess

of 5 M is necessary to reach a strong enough susceptibility response to expect refractive broadening.

The effects of refractive broadening were investigated by using the Fresnel equations to explicitly calculate the reflection from the sample and mirror to obtain theoretical lineshapes that could be compared to the experimental spectra. In order to model the reflections from the sample, a flat sample directly backed by a mirror was used as an approximation of the sample geometry. Further, we approximate the complex susceptibility response (i.e. the real and imaginary parts of the susceptibility as a function of magnetic field around resonance) as a simple Lorentzian. Thus, the model of the sample reflections depends only on the thickness of the sample, and the width and amplitude of the Lorentzian response. The amplitude of the response is set by known parameters such as temperature, static field and concentration, so that only the width of the susceptibility response remains a variable. The width of the susceptibility response is the critical parameter as it corresponds to the true EPR linewidth, which will include dipolar broadening effects, but is obscured at high concentrations by refractive broadening in the reflection from the sample.

As expected, the calculated sample reflection is identical to the susceptibility response when the susceptibility response amplitude is taken to be small (corresponding to low concentrations). However, at larger susceptibility response amplitudes (corresponding to high concentrations), the calculated reflection is substan-

tially different than the assumed susceptibility response. We demonstrate this in Fig. 3.8 for the case of an $\bar{r} = 1.78$ nm (50 mM) sample, where we are able to reasonably reproduce the experimental spectrum with the theoretical model, but only with a susceptibility response much narrower than the measured lineshape. We can identify the true EPR linewidth for each of the $\bar{r} = 1.78$ nm (50mM) samples whose lineshapes show substantial variations from batch to batch by repeating this process and determining the width of the susceptibility response that best reproduces the experimental lineshapes. The determination of the best fit widths is described in full detail with accompanying error landscapes in the Appendix D.

In Fig. 3.3, we present the best estimate of the corrected linewidth for the $\bar{r} = 1.8$ nm (50 mM) samples. This is based on an average of the extracted linewidths weighted by the confidence of the linewidth determined from the error landscapes. The error bars are based on the unbiased, weighted variance to faithfully incorporate the sample-to-sample variation. The average of these corrected linewidths agrees well with the computed, dipolar-convolved, linewidth for $\bar{r} = 1.8$ nm (50 mM) (1.35 mT vs 1.40 mT). Further, the extension of this technique to spin-pair systems is supported by the agreement between these corrected GdCl_3 linewidths and the measured linewidth of C2-Gd595 (1.35 mT vs 1.46 mT), which represent similar average interspin distances (though the bis- Gd^{3+} is slightly shorter and therefore slightly broader). From these calculations and the uncertainty in the experimental linewidths, we expect that refractive broadening

also affects the $\bar{r} = 2.4$ nm (20 mM) and the $\bar{r} = 3.0$ nm (10 mM) samples. However, the distortion of the lineshape was too subtle to unambiguously determine corrected susceptibility widths with our fitting model at these concentrations.

3.6 The Limits for Gd^{3+} -based cw Distance

Measurements

3.6.1 Temperature Effects

In order to further investigate the limits of broadening we undertook calculations using dipolar convolution (Sec. 3.3). In addition to the calculations carried out for random solutions at different temperatures, we carried out identical calculations assuming $S = \frac{1}{2}$ spins, to compare to the dipolar line broadening caused by the high-spins of Gd^{3+} . As seen in Fig. 3.9, the calculations show that as observed in experiments, broadening for Gd^{3+} is somewhat weakened at higher temperatures, but is still substantially stronger than would be expected with conventional $S = \frac{1}{2}$ probes (at high or low temperatures). The reduction in broadening at high temperatures is a result of the relatively symmetric Pake pattern at high temperatures being narrower than the Pake patterns at lower temperatures. Still, although the dipolar broadening is reduced at higher temperatures, Fig. 3.9 demonstrates that substantially longer distances are accessible by cw EPR lineshape analysis at 260 K with Gd^{3+} compared to nitroxide probes.

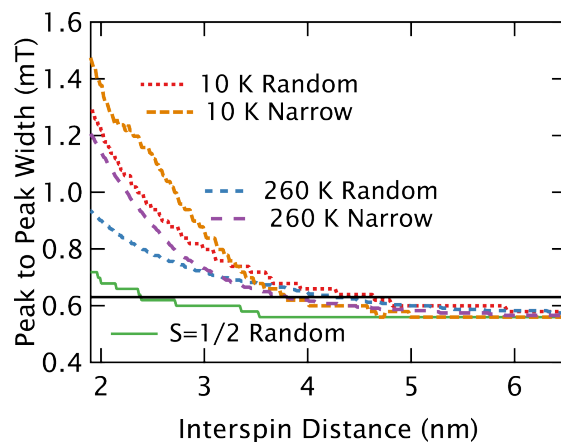


Figure 3.9: Calculated Broadening from Dipolar Interactions. The peak-to-peak linewidths of the calculated dipolar-convolved spectra are shown as a function of average interspin distance for several different scenarios. When the large distribution of nearest-neighbors found in a random solution is used, the broadening at both 10 K (dotted, red line) and 260 K (dashed, blue line) from the $S = \frac{7}{2}$ species is substantially stronger than the $S = \frac{1}{2}$ species (which is largely independent of temperature between 10 K and 260 K) plotted with a solid, green line. When the random solutions are compared to a model of pairwise interactions, where the distribution width is fixed, at both 10 K (dotted, orange line) and 260 K (dashed, purple line) we find that the limit of observing long distance interactions is reduced, but still substantially longer than for an $S = \frac{1}{2}$ spin. For illustration, the black, horizontal line indicates a width of ~ 0.62 mT, corresponding to a roughly 10% broadening of the intrinsic line.

3.6.2 Distance Limits

The calculations applied earlier address the experimental conditions where the distances distribution is random. In these cases, calculations in Fig. 3.9 suggest distance limits of ~ 4.2 nm at 260 K and ~ 4.8 nm at 10 K. However, the case which is more relevant for biological studies is that of a narrow distribution about a mean. With a broad distribution, the $\frac{1}{r^3}$ dependence of the dipolar interactions makes the shorter distances in the wings of the distribution the dominant contributor to broadening. To address this and establish an idea of the relevant distance limits for narrow distance distributions, calculations were carried out using narrow Gaussian distance distributions, where the full-width-at-half-max of the distribution was fixed at 0.4 nm . The results of these calculations are plotted in Fig. 3.9 for both 10 K and 260 K. As expected, the region between 4 nm and 5 nm becomes more difficult to resolve in the case of narrow distances. Nonetheless, in both the 260 K and 10 K cases we can observe meaningful broadening (here defined as a line broader than 0.62 mT, corresponding to $\sim 110\%$ of the intrinsic width) at ~ 3.8 nm. Opportunities to extend this distance range would exist if the intrinsic linewidth could be further narrowed.

Although we have identified Gd^{3+} species with linewidths sufficiently narrow to dramatically extend the distance ceiling, we have not undertaken a systematic study to determine the chemical makeup that provides the narrowest possible central linewidth. Thus, the current long distance limit may be further extended

by alternative Gd^{3+} -based spin labels optimized for a narrow central transition. Moving to higher magnetic fields can further narrow the central line for samples where the ZFS is the dominant source of the central transition's intrinsic linewidth. For Gd595, the contribution of the ZFS ($D \sim 20$ mT) to the linewidth is estimated¹³¹ to be only ~ 0.3 mT, while the measured width is > 0.4 mT. We expect the intrinsic line to be ~ 0.25 mT if we approximate the line as a Voigt combination of the ZFS width (Gaussian) and an intrinsic width (Lorentzian). Therefore even for Gd595, the narrowest chelate investigated, moving to higher fields may help reduce the linewidth. However, even doubling the field to reduce that ZFS width by a factor of 2, would only reduce the line to ~ 0.34 mT, offering a very modest increase in the distance range ($\sim 10\%$). Due to the rough approximation of the ZFS width, measurements at higher fields would be necessary to confirm this. Alternatively, for chelates with larger zero-field splitting parameters, such as 4MMDPA spin-labels, the line is likely narrowed at higher fields, making them more attractive distance probes.

3.7 Impact and Outlook

With an extended distance range, cw EPR becomes a potential alternative to DEER in situations where measurements above 200 K are desirable. Because DEER relies on phase memory times long enough to observe the dipolar oscillation, it is not easily applied at non-cryogenic temperatures. In addition, such

measurements are highly susceptible to short T_{1e} values that cause random flips that will destroy the DEER effect. Alternatively, we report line broadening at ~ 3.8 nm up to 260 K in a viscous solution, and work with nitroxides suggests that cw EPR distance measurements are possible at room temperature (if rotational tumbling is sufficiently slow).¹⁵⁶ Further, cw EPR can be run in an hour, allowing multiple samples to be measured in a single day and even without a resonator a good SNR is demonstrated at 100 μM with ~ 10 μL of sample. This is comparable to typical concentration sensitivities of X-band DEER on commercial spectrometers, but X-Band DEER generally requires ~ 50 μl of sample. These sensitivity levels suggest that Gd^{3+} can find broad use in systems currently suitable for many kinds of application, with the (at times critical) advantage of operating at higher temperatures. The state-of-the-art in DEER has pushed the sensitivity limits beyond the levels commonly encountered at standard commercial X-band spectrometers, often by leveraging higher magnetic fields with sufficiently high power.⁷⁰⁻⁷³ While currently cw-measurements of Gd^{3+} at 240 GHz do not offer this level of concentration or absolute sensitivity and appear best applied at or above 100 μM concentrations, further optimization of the spectrometer may offer improved sensitivity, particularly in achieving a uniform, flat sample as the current “bucket-style” holder can give rise to variable sample shapes.

This work promises exciting prospects, as simple cw-EPR lineshape analysis can exploit the potential of Gd^{3+} -based spin labels at high fields and frequen-

cies for the determination of long interspin distances. As this technique can be applied at higher temperatures than DEER it offers important advantages. For instance, proteins studied at temperatures well above the protein glass transition will better represent the sampling of conformational states found under biological conditions.^{143–145} In addition, any conformation changes that modulate the dipolar coupling on the time scale of sub- μ s to μ s at these temperatures should be visible as changes to the broadening of the linewidth, offering the potential of using EPR to track aspects of conformational changes out to ~ 4 nm. More work is necessary to account for discrepancies between the dipolar-convolved spectra and experimental lineshapes of the bis-Gd³⁺ model sample, and to develop suitable fitting methods. However, it should already be possible to use Gd³⁺ to gauge long-range distances and distance changes in biological samples, even without the full capability of distance extraction.

Chapter 4

Double Electron-Electron Resonance (DEER) Studies of a Membrane Protein

The material in this chapter is being prepared in a different format for publication as: Edwards, D.T.; Stone, K.; Hussain, S.; Kinnebrew; Ilia Kaminker; Erez Matalon; Sherwin, M.S.; Goldfarb, D.; Han, S. “Measurement of multiple distances in a Proteorhodopsin hexamer utilizing Gd^{3+} spin probes.”

4.1 Gd^{3+} as a Spin Probe for DEER of Oligomers

The opportunity to perform DEER at higher magnetic fields is attractive as it offers increased sensitivity, which alleviates the problems of limited sample amounts available for most biological samples. Several W-Band (3.5 Tesla, 95 GHz) spectrometers have been demonstrated offering sufficient pulse power to perform Double Electron-Electron Resonance (DEER) with increased sensitivity.^{70,71} However, at high fields the lineshape of a nitroxide broadens substantially

and is susceptible to orientational selectivity.^{160,161} In cases where orientation-specific information reflects the ordering of the labels (and not the biomolecule), the orientational effects provide no additional information, but can require several measurements and advanced data analysis to account for.¹⁶² Recent work has shown that new spin labels based on Gd^{3+} coordinating complexes offer advantages over nitroxides when utilized for high-field EPR as orientational selectivity is abolished.^{111,112} Thus, beyond utilizing the Gd^{3+} as a cw distance probe (discussed in Chapter 3), we investigated the capabilities of Gd^{3+} for DEER studies of membrane proteins. In addition to the advantages of Gd^{3+} for high-field, pulsed EPR discussed in Section 2.4.1, the central transition of the $S = \frac{7}{2}$ Gd^{3+} ion (i.e., $|\frac{1}{2}\rangle \leftrightarrow |-\frac{1}{2}\rangle$) is narrower than the nitroxide spectrum (Chapter 3) and can be treated analogously to an $S = \frac{1}{2}$ system in data processing.¹¹² The potential of Gd^{3+} as a high-field distance probe, used in conjunction with DEER has been demonstrated in model bis- Gd^{3+} complexes,^{112,131} proteins,^{111,158} peptides,¹⁵⁷ and DNA,¹⁶³ and between mixed nitroxide- Gd^{3+} labels.¹¹⁰

The immense reduction in sample volume possible at high fields (3 μL at W-Band vs 50 μL at standard X-Band, using comparable concentrations) without the difficulties presented by the orientational selectivity of nitroxides, substantially reduces the sample burden of performing DEER.^{70,112} However, beyond advances in sensitivity there remain limitations to nitroxide-based DEER when applied to complex biological systems. As a result of the large modulation of the nitroxide

echo generated by the pump pulse, significant multi-spin effects can emerge in systems where multiple spins are coupled together. These effects obscure the distance distributions^{164,165} and can lead to ghost peaks during studies of oligomeric systems where many proteins interact.¹⁶⁶ Oligomeric proteins are functionally important, and difficult to study with other techniques due to their size and complexity, making a reliable DEER distributions an important goal. An additional problem with nitroxides is that variations in the local environment can result in an inability to utilize DEER at specific sites where the phase memory time of nitroxides is short. Gd^{3+} shows the potential to resolve these problems. First, the spin physics of Gd^{3+} yields small DEER modulation depths,¹¹² which should eliminate or dramatically reduce artifacts emerging from multi-spin effects.^{164,165} Further, as a result of use of Gd^{3+} in a coordination complex, it is expected that the Gd^{3+} ion will interact less strongly with the local environment of the spin, yielding more uniform relaxation times for different labeling sites around a biomacromolecule. However, neither of these ideas have been demonstrated experimentally. Therefore, we undertook a study to investigate the capability of Gd^{3+} DEER to study protein oligomerization to both address the suitability of Gd^{3+} to study these complex systems, and answer a biologically relevant question about the structure of the oligomers in a bacterial membrane protein.

The organization of membrane proteins into oligomers is observed in a wide variety of membrane proteins, and is critical to the protein function. However,

the precise functions of oligomerization remains debated, and oligomerization may serve different roles in different systems, for instance amplifying or regulating a response.^{167,168} Due to the large size of the complexed system, and the varying rigidity of the oligomers, they remain difficult to study by traditional methods in structural, molecular biology (i.e. x-ray crystallography and NMR structural measurements).³⁰ For this reason, EPR has emerged as an important tool to address large oligomers due to its ability to provide targeted structural information in the nm range.

In particular, the membrane protein Proteorhodopsin (PR) has attracted great interest as a light-driven proton pump found in many marine bacteria.^{132,169} Proteorhodopsin has been shown to oligomerize into different states^{170,171} depending on, for instance the medium and method of reconstitution and may affect the function of PR as a proton pump.¹⁷² The hexamer is found to be a common oligomeric structure, and the structure has been investigated through AFM and cw EPR.^{41,171} AFM provides important structural information of the oligomers, but does not provide sufficient resolution to identify the orientation of the individual PR, and cw EPR fails to offer long range distance constraints (that is, it primarily addresses the closest parts of the proteins). Current work has show clear evidence that the functional dynamics of different oligomers can be very different, making a full understanding of the oligomeric structures important for functional understanding of PR.

This work targets the hexameric PR that has been previously studied,⁴¹ by using DEER to investigate the longer-range features. This is done utilizing both traditional, nitroxide-based DEER at 10 GHz, in combination with Gd³⁺-labeled measurements at 95 GHz. Two types of PR samples are prepared, each singly labeled at one site in order to measure the distance between distinct proteins in the oligomer. The first is labeled near to the center of the oligomer, and second is labeled near the outside edge. DEER measurements are able to show consistent measurements of the nearest and next-nearest neighbor distances which agree with hexamer^{41,171} and demonstrate the potential advantages of Gd³⁺ over nitroxides as DEER probe molecule to study complex, oligomeric systems.

4.2 Pulsed EPR Measurements of Protein

Oligomers

Measurements of spin-labeled PR were done for mutants labeled at both site 58 and site 177. Previous work has shown that the PR organizes in the hexamer such that site 58 should be close to the center of the hexamer (i.e. facing the other proteins), while 177 is on the outside of the hexamer. This was determined through cw-EPR to observe the close interspin distances between PR mutants labeled at residue 55, which are found to be within ~ 1.6 nm of each other.⁴¹ A

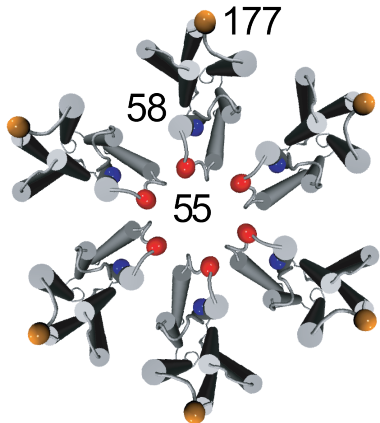


Figure 4.1: Proteorhodopsin Hexamer. A sketch of the structure of the Proteorhodopsin hexamer based on AFM¹⁷¹ and cw EPR.⁴¹ The positions of the spin-labeled mutants used in this study are shown at sites 177 and 58. Additionally, site 55 is shown for reference displayed dipolar broadening in Stone et al.⁴¹.

sketch of the proposed organization of the PR oligomer is shown in Fig. 4.1 and includes the labeling site 55 used in the previous study.

Gadolinium labeling was done using the 4MMDPA¹²⁹ spin label introduced in Sec. 2.4, and MTSL was used as a nitroxide spin label for X-Band DEER. For each label, the same procedure is used to mutate the targeted site to a cysteine, which is then reacted with the label to form a disulfide bond. In the case of the Gd³⁺ labeled samples, GdCl₃ was then added at the appropriate ratio, while for nitroxide labels the system was diluted with unlabeled protein. To distinguish the two sites and two labels we will refer them as 177Gd, 58Gd, 177MTSL, and 58MTSL, respectively.

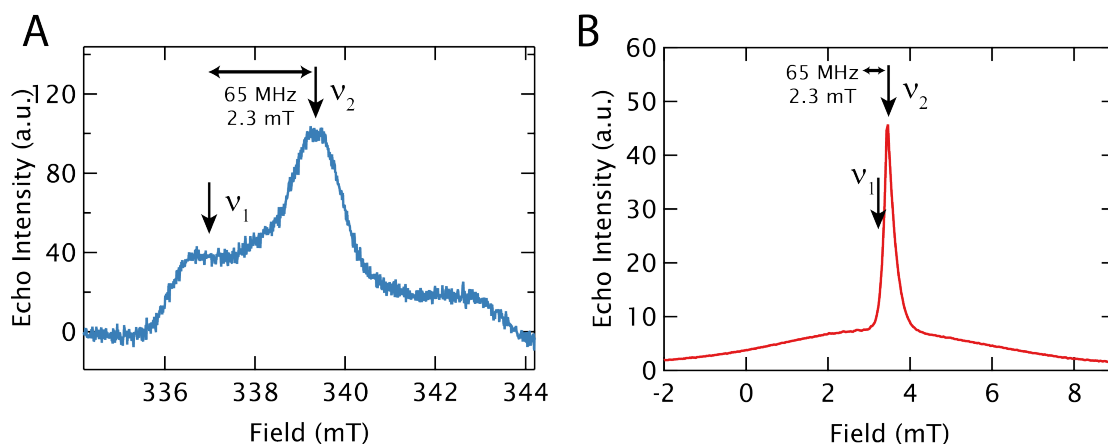


Figure 4.2: Field Swept Echo Spectra of MTSL- and Gd^{3+} -labeled Proteorhodopsin. **A.** The X-Band spectrum of 177MTSL at 50 K. The diagram shows the 65 MHz spacing used between the pump and observer pulses in the DEER measurements. The spectrum and separations did not change appreciably between the different mutants. **B.** The W-Band spectrum of 177Gd at 20 K. The diagram shows the 65 MHz spacing used between the pump and observer pulses in the DEER measurements. The spectrum and separations did not change appreciably between the different mutants.

The spin label concentration for Gd^{3+} was $\sim 200 \mu M$ for all samples. Similar concentrations of label were used for MTSL ($\sim 200 \mu M$) as with the Gd^{3+} labeled measurements, but a larger sample volume was required ($\sim 50 \mu L$ compared to $\sim 3 \mu L$). As mentioned, different spin dilutions were used to control for multi-spin interactions. The nitroxide DEER demonstrated substantially larger modulation depths ($\sim 50 \%$) than the Gd^{3+} measurements (1-2 %) and the oscillations appear more clearly than in the case of the Gd^{3+} measurements. !

4.2.1 Field Swept Echo Measurements

The field-swept-echo spectrum for spin-labeled PR hexamers labeled at 177MTSL (at X-Band) and 177Gd (at W-Band) are shown in Fig. 4.2. For both species, the spectrum did not change substantially as a result of labeling at different locations, or with different spin dilutions. Fig. 4.2 also shows the locations of the pump and observer pulses on top of the spectrum, and measurements of the phase memory time were made at the signal maximum (which corresponds to the location of the pump pulse, ν_2).

4.2.2 Comparison of Phase Memory Times

For the DEER measurements at both X-Band and W-Band a critical parameter is the length of the phase memory time of the spin, as this affects the maximum possible evolution times which limits the distance ranges accessible (as well as affecting the signal-to-noise ratio (SNR) of the spectra that can be achieved for a given evolution time). Reasons for the difference in phase memory time can often be attributed to the local nuclear environment;^{55,56} if the MTSL labeled is buried in a protein it tends to show a substantially shorter phase memory time compared to a site exposed to the deuterated solvent. This can be investigated further by examining the phase memory time as a function of spin-label type and location. Fig 4.3 shows the resulting echo decay curves for both Gd³⁺- and nitroxide-labeled proteins, demonstrating the extreme sensitivity of nitroxides to label position. Due

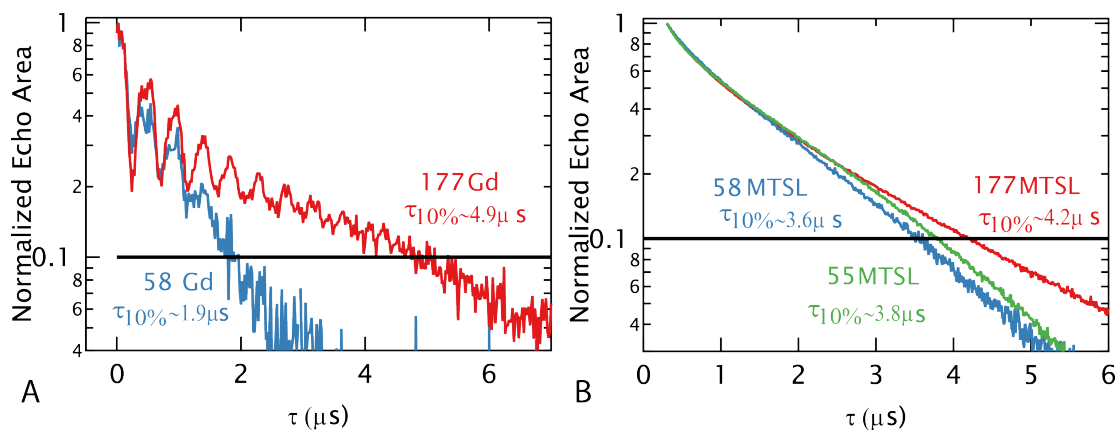


Figure 4.3: Phase Memory Times of Different Site in Proteorhodopsin.

A. Shows the W-Band decay of the echo signal in a spin echo experiment for 4MMDPA- Gd^{3+} labeled mutants as a function of labeling position at 20 K. The decay rate is largely similar for all sites; there is $\sim 20\%$ variation in the interpulse spacing ($\tau_{10\%}$) needed to reach 10% of the initial values (shown in black). **B.** Shows the X-Band decay of the echo signal in a spin echo experiment for MTSL labeled mutants as a function of labeling position at 50 K. The decay rate is highly heterogeneous; there is substantial variation in the interpulse spacing needed to reach 10% of the initial values (shown in black). The oscillations in spectrum are indicative of coupling to deuterium in the solvent, which disappears at high magnetic fields.

to the strong nuclear modulations of the X-Band decays, we use the interpulse spacing resulting in an echo intensity 10 % of its maximum value ($\tau_{10\%}$), as a rough gauge of the decay rate. For nitroxides, $\tau_{10\%}$ is approximately 2.5x shorter for the 58MTSL mutant, which is expected to be at least partially buried in the hexamer, compared to the 177MTSL mutant, which is solvent exposed.¹⁷² By comparison, in Gd³⁺-labeled mutants there is only a roughly 20 % in $\tau_{10\%}$.

These results have an important impact on the DEER studies moving forward. In particular, when working with 58MTSL, the short phase memory times lead to poor signal to noise and short evolution times. Further, these simple measurements demonstrate that, indeed, the Gd³⁺ spin-labels appear to be less sensitive to the location of the labeling when compared to nitroxides. This raises the possibility of using Gd³⁺ as labels in situations where MTSL labels appear to be strongly interacting with the protein, causing short phase memory times. This can perhaps be considered the opposite approach of deuterating the protein;⁹³ instead of reducing coupling to the protein by eliminating protons in the protein, we simply utilize a spin label which is intrinsically more isolated. Notice that this is not to say that the two approaches result in the same extent of advantages (it appears protein deuteration dramatically extends T_M), nor does it suggest that the Gd³⁺-labels could not be utilized in a deuterated protein.

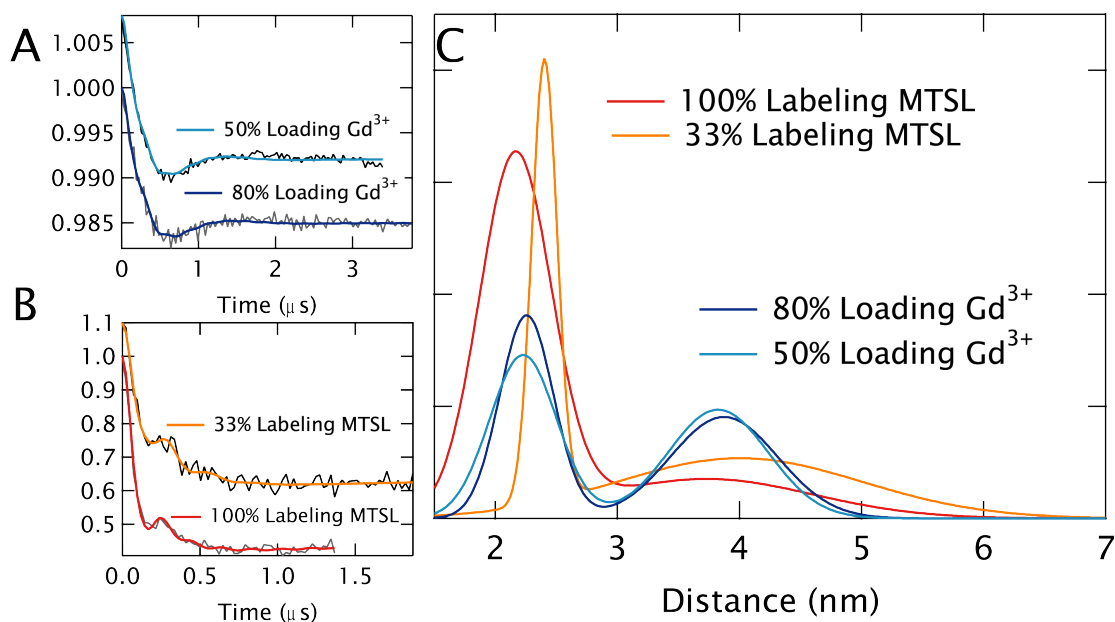


Figure 4.4: DEER Results for Site 58 of Proteorhodopsin. **A.** The DEER time curves, after background subtraction 58Gd for two different loading levels shows a small modulation depth, and only one obvious oscillation. **B.** The DEER time curves, after background subtraction for 58MTSL at two different labeling levels shows a larger modulation with clear features indicative of two distances. **C.** The resulting distance distributions using a 2-Gaussian model of the distances (based on the results from Tikhonov Regularization). The two mean distances observed are consistent across all measurements, though the shapes of the distributions vary. Additionally, the MTSL labeled samples required non-equal populations of the two distances, likely as a result of multi-spin effects.

4.2.3 DEER on the 58C Mutant

DEER measurements of the samples labeled at residue 58 are shown in Fig. 4.4. We begin by discussing the Gd^{3+} -labeled measurements, whose background-subtracted time domain data are shown in Fig. 4.4A. Measurements on 58Gd were carried out at Gd^{3+} -loading levels of 50% and 80%. The data show a clear DEER oscillation and the low modulation depth is in agreement with earlier data using the 4MMDPA tag.¹¹² Data analysis of the time-domain data using a Tikhonov analysis, showed the emergence of two distances. We associate the short distance with the nearest neighbor spin in the hexamer, whereas the longer distance is associated with the next-nearest neighbor. However, as a result of the broadness of the distributions, better results were obtained using a model utilizing two distances, each with a Gaussian distribution. This was confirmed to be a good model as the peak centers were not substantially different (from the Tikhonov results). As the neighbor and nearest-neighbor distance should be equally populated (regardless of the loading level), we fixed the populations of the distances in the model to be 50/50. As shown in Fig. 4.4C, the derived distance distributions were similar using the two-Gaussian model for the distance distribution (Fig. 4.4C). and the the locations of the average distances is found to be 2.22 nm and 3.82 nm for the 50%, and 2.22 nm and 3.86 nm for the 80% sample. These distances are consistent with the the understood organization of the PR hexamer based on EPR and AFM.^{41,171} Further, within a hexamer the nearest neighbor and next-nearest-

neighbor distance should be related by $\kappa = \frac{r_{\text{next-nearest}}}{r_{\text{next-nearest}}} = \sqrt{3} = 1.73$, which agrees well with the measured ratio of $\kappa = 1.63$.

The DEER data on 58MTSL demonstrated substantially larger modulation depths ($\sim 50\%$) than the Gd^{3+} measurements, as can be seen in the time domain data in Fig. 4.4B. Further, the oscillations appear more clearly than in the case of the Gd^{3+} measurements, and the two oscillation frequencies can be clearly resolved. A short distance is visible from the bump at ~ 200 ns, while the longer distance is visible in the slower oscillations. For nitroxides, labeling ratios of 100% and 33% were used and the increased labeling led to an increased modulation depth, as expected. Application of the Tikhonov regularization again showed 2 distances, but we again utilize a 2-Gaussian distance distribution to describe the DEER data. However, the resulting best-fit distributions are not as consistent as for the Gd^{3+} -labeled protein. We were forced to allow the relative populations of the two distance to vary in the Gaussian fit, to achieve reasonable agreement with the Tikhonov fit. Distances of 2.4 nm and 4 nm for the 33 %, and 2.1 nm and 3.7 nm for the 100% sample were found as shown in Fig. 4.4C. These yield $\kappa = 1.66$ and $\kappa = 1.76$ respectively, in good agreement with a hexamer shape. It is worth noting that the population of the short distance is 43% for the 33%-labeled sample (near to the expected 50%), while it is 75% in the 100%-labeled sample.

Fig. 4.4C highlights the most important aspects of the experiment. We are able to identify two interspin distances in both the nitroxide and Gd^{3+} DEER mea-

surements. While the distributions are different using different labeling schemes, the peak distances are entirely consistent, and the small differences in distances fall well within the uncertainty resulting from using different labeling molecules. The inability to describe the distance populations as 50/50 when using nitroxides is consistent with expectations that the multi-spin effects strongly (and artificially) enhance short distances.^{164,165} This is confirmed by the fact that reduction in the spin label concentration (from 100% to 33%) moved the best fit substantially closer to a 50/50 population. The apparent insensitivity of Gd^{3+} to these effects (as demonstrated by the good fit obtained using the 50/50 model) is consistent with the $> 10x$ smaller modulation depth (λ), as the three-spin effect should fall off with λ^2 .^{164,165} Finally, the extremely short evolution times used for nitroxides (Fig. 4.4B) are the direct result of the short relaxation times reported in Fig. 4.3. The direct impact of this is to restrict the confidence with which we can assign the longest distance (according to estimates presented in Section 1.2, we should only trust the location, and not the width of the distribution for nitroxides, while with Gd^{3+} we should trust both the mean and width of the longer distance).

4.2.4 DEER on the 177C Mutant

Similar measurements using Gd^{3+} were made on PR hexamers labeled at residue 177, which is expected to show a much longer interspin distance as a result of its position on the outside of the hexamer (Fig. 4.1). The DEER traces

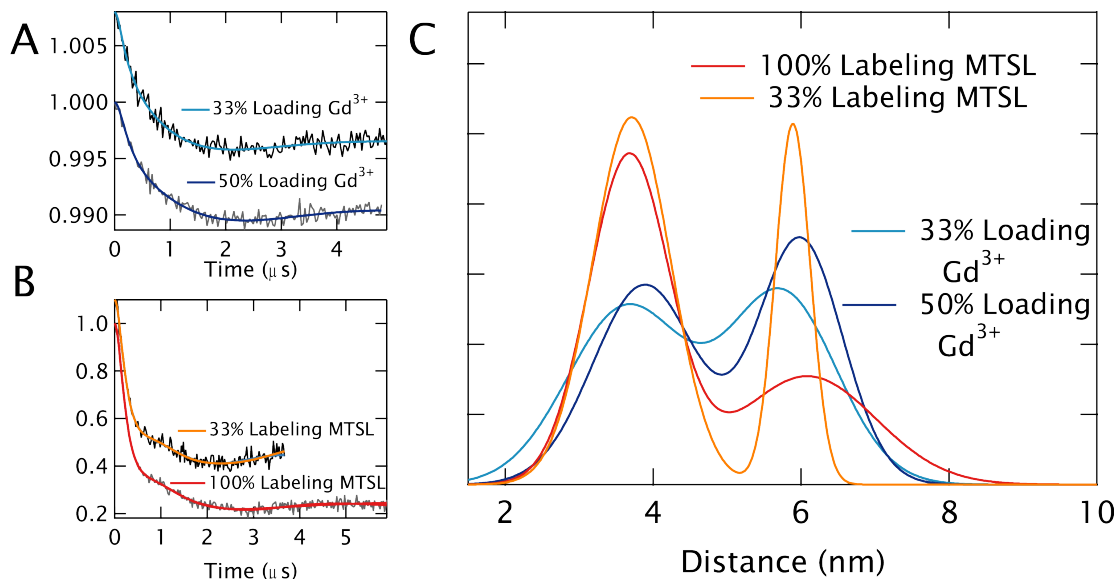


Figure 4.5: DEER Results for Site 177 of Proteorhodopsin. **A.** The DEER time curves, after background subtraction 177Gd for two different loading levels shows a small modulation depth, and only one obvious oscillation. **B.** The DEER time curves, after background subtraction for 177MTSL at two different labeling levels shows a larger modulation with clear features indicative of two distances. **C.** The resulting distance distributions using a 2-Gaussian model of the distances (based on the results from Tikhonov Regularization). The two mean distances observed are consistent across all measurements, though the shapes of the distributions vary. Additionally, the MTSL labeled samples required non-equal populations of the two distances, likely as a result of multi-spin effects.

are shown in Fig. 4.5A for a 177Gd sample loaded at 33% and 50%. Though a clear DEER-decay is observed for these longer distances, the oscillation is not as clear as for the case of 58Gd as can be seen in Fig. 4.4A. The distance extraction using a two Gaussian fit of 50/50 gave average distances of 3.7 nm and 5.68 nm for the 30%, and 3.9 nm and 5.98 nm for the 50% sample. The locations of these distances were consistent with the results from Tikhonov regularization, but better isolated the two distances. As with the 58Gd mutants, the observation of two distance were consistent with the expectation from the known organization of the PR oligomer, and yielded a distance ratio ($\kappa = 1.5$), that is consistent with the expected hexagonal organization. Considering the width of the distributions (~ 1.5 nm), the difference between the position of the peaks between the 33% and 50% Gd³⁺ loading samples (0.2-03 nm) is within experimental error.

The X-Band DEER measurements of 177MTSL also shows multiple distances in the time domain data. In this case, the distances are significantly longer than the 58MTSL mutant, which is consistent with the Gd³⁺ results, as can be seen in Fig. 4.5B. As in the other measurements, the modulation depth is larger for the higher labeling concentration, and the modulation depth is substantially deeper than for the Gd³⁺ measurements. Under Tikhonov regularization, the mean distances observed are similar to those found in the Gd³⁺ measurements. In this case the Gaussian fit gave good results as well, but as was the case with the 58MTSL mutants, we were forced to allow the populations of the short and long

distances to vary from the expected 50/50. Instead, as shown in Fig. 4.5C, we find distances consistent with the Tikhonov fits: 3.72 nm and 5.89 for 33%-labeled and 3.675 nm and 6.083 nm for 100% labeling. Unlike in the case of the 58C mutant, we see no major change in the percent population of the shorter distance between the 33%-loaded and 100%-loaded samples.

As with the 58MTSL sites, Fig. 4.5C shows consistent mean distances across multiple samples, and the differences in distances fall within the uncertainty resulting from using different labeling molecules. Interestingly, the differences in distributions, while present, are not as severe as is the case in the 58C samples. This suggests that the multi-spin effect is less prevalent, which is sensible as a result of the longer interspin distances present. However, note that 50/50 distributions were still not fully suitable using MTSL labels, suggesting that some effect remains. Alternatively, the longer distance for this site is at the limit of what can be resolved with the evolution times and so the unequal populations may result from this experimental limitation. The evolutions times used were more consistent across the spin labels for this site, likely due to the fact that 177 is known to be a solvent exposed site.¹⁷²

4.3 Impact of Gd^{3+} and Nitroxide Studies in Oligomers

Gd^{3+} appears to offer some potential advantages over nitroxide labels. The first is largely practical: as has been reported clearly in the past,⁶⁹⁻⁷³ working at high magnetic fields can dramatically improve the sensitivity DEER. Gd^{3+} does not have problem of orientational selectivity present in nitroxide spectra at high fields, rendering data processing straight-forward. In this way these spectra were measured using $\sim 10\times$ less sample volume (at similar concentrations) to what would be used for DEER with a commercial instrument at X-Band. This dramatically reduces the cost of the experiments. Also, for samples which are not soluble at high concentrations other spectrometers exist (in specialized labs) that are capable of measuring at substantially lower concentrations (though somewhat larger volumes).⁷¹

The Gd^{3+} ion appears to be well shielded from its environment. This may emerge from the shielding of the unpaired electrons (in f-orbitals) by outer filled orbitals, or as a result of the use of Gd^{3+} in coordinating complexes. This is demonstrated experimentally through the phase memory times reported in Fig. 4.3. This is advantageous as is shown for the 58C residue in Fig. 4.4, where the Gd^{3+} samples can be measured with substantially longer evolution times, yielding better estimates of long distances. However, it should be noted that the size of

the Gd^{3+} complexes can be as big as, or substantially bigger than nitroxide labels. Thus, this raises concerns about the labels disrupting the function or structure of the protein, and may make the labeling process more difficult, or less efficient.

Finally, and most relevant to studying complexation, Gd^{3+} is insensitive to the effects of multiple coupled spins. This emerges directly from the relatively small modulation depth observed in Gd^{3+} DEER traces,¹¹² which results in the higher-order couplings being negligible. This advantage is particularly critical when studying complexation, where many proteins may come into close contact with one another. The results in Sec 4.2 show that, particularly in the presence of short interspin distances, longer distances are artificially masked by multi-spin effects. Indeed, if one considered studying only the 100% labeled 58MTSL samples, the existence of the longer (~ 4 nm) distance may be questioned, due to the broadness and weakness of the feature. Other experimental techniques, such as spin-dilution (which helped confirm the multi-spin effect in this study), or the use of longer (more selective) pulses¹⁶⁴ can be utilized to minimize these effects, but these all make some sacrifices in signal quality, which is not necessary utilizing Gd^{3+} .

The nature of protein-protein interactions and the higher-level structure of multiple proteins in oligomers or during aggregation are important questions in biology which can be difficult to quantify, particularly for membrane proteins (which are themselves difficult to study). These structures may be difficult to crystallize in large amounts intact, are generally too large for NMR methods, and

other techniques may offer insufficient resolution. For instance, consider the specific example provided in this work. The oligomeric structure was observed in lipid bilayers through AFM,¹⁷¹ but did not yield sufficient resolution to identify the orientation of the protein within the oligomer. Meanwhile, the crystal structure of monomeric Proteorhodopsin is available in literature, but does not include protein-protein interactions.¹⁷³ Thus, EPR became an important complimentary technique to address the arrangement of the protein within the oligomer through cw EPR⁴¹ and with the work in this chapter. While clever use of cw EPR allowed the orientation of the protein to be identified in the oligomer, DEER was necessary to determine several distances in the oligomer. The consistency of the mean distances across different labels and labeling ratios help confirm that neighbors and next-nearest neighbors are being observed. We are able to both confirm the structural model generated in literature and confirm that the oligomerization appears to generate semi-rigid distances and structure, and this is not a mere ‘clustering’ of proteins. It is important to emphasize that these results could be determined from the Gd³⁺ measurements alone, utilizing significantly less sample volume, without the need to account for multi-spin effects or significant heterogeneity in the phase memory times and the ability to varying loading levels by simple stoichiometric addition of GdCl₃.

Part II

Free Electron Laser-powered EPR (FELEPR) Spectroscopy

The first part of this dissertation directly addressed new techniques and methods utilizing the unique advantages of high-field EPR. As spin bath quenching requires the ability to tune electron spin polarization from $\sim 0\%$ to $\sim 100\%$ it can not be observed at low magnetic fields. Similarly, at low fields the Gd^{3+} spectrum does not display the narrow central transition which is utilized in both pulse and cw measurements. These new approaches offer new ways to probe interspin clustering and demonstrate that the “toolbox” of spin probes should be expanded to include Gd^{3+} (particularly for studies requiring moderate temperatures or for studies of oligomerization). Further, these examples suggest that a wealth of unrealized methods are possible at high magnetic fields.

However, as covered in detail in Section 1.3, the limits for high-field, pulsed EPR are currently throttled by the unavailability of high-power sources. University of California, Santa Barbara offers the opportunity to overcome this limitation as a result of the Free Electron Laser(FEL) facility, which generates high-power radiation in the 100’s of GHz to THz range. Immense opportunity exists to expand the capabilities of high-field, pulsed EPR as a result of the extremely short pulses that can be employed when the FEL is used as a source for EPR (FELEPR). Chapter 5 covers the basic principle of operation of the FELEPR (including how it is frequency locked, and used to generate $2 < 10$ ns pulses), goes on to discuss basic one and two pulse measurements, and ends by investigating the observation of a transient shift in the Larmor frequency. In Chapter 6 the addition of

phase-sensitive detection and phase cycling are introduced as a way of dramatically improving signal acquisition and the versatility of the pulse sequences (phase cycling is a standard component of NMR and low-field, pulsed EPR). With these developments, the Free Electron Laser-powered EPR spectrometer is positioned to carry out experiments that were previously impossible at high fields; for instance, on rapidly-relaxing systems or biological systems above 200 K.

Chapter 5

Development of a Free Electron Laser-powered EPR (FELEPR) Spectrometer

5.1 The Need for a High Power, 240 GHz Spec- trometer

As was discussed full in Sec. 1.3, a critical limitation in development of pulsed EPR at high magnetic fields is the drastic reduction in the available microwave power as frequency increases due to the “Terahertz gap.” Recent work has demonstrated that extended-interaction Klystron amplifiers can be used to generate radiation at frequencies ~ 100 GHz^{69,71}. However, the capabilities of these amplifiers continues to be limited at higher fields. Figure 5.1 shows the field and power for a sample of existing spectrometers with commercial spectrometers in green triangles and home-built spectrometers in blue squares. One sees that above ~ 100 GHz (~ 3.5 T) the available power falls off rapidly for both commercial and home-built

spectrometers. Additionally, high-Q cavities are not ideal to compensate for these low powers at high fields due to their small dimensions, limited sample volumes, and ringdown (though some low-Q resonators may be useful).⁸⁷ Work at 95 GHz has made clear that high incident powers are the ideal way to achieve optimal spectrometer performance at high-fields (which then do not require cavities).^{69,71}

Thus, while a low-Q cavity may offer some modest reductions in pulse lengths, we see that at 240 GHz, any substantial improvements in pulsed EPR performance must start from dramatic increases in the available source power. The UCSB Free Electron Lasers (FELs) were built in the early 1980's and over the past 30 years have been important tools for Terahertz spectroscopy as they are one of the few sources capable of providing high-power, quasi-cw radiation across the entirety of the "Terahertz gap." The FEL can provide ~ 100 's W of power at 240 GHz in a pulse that is \sim several μ s long, which can be used to do EPR.

This chapter begins by outlining the operation of the FELEPR spectrometer. We first describe the FEL source, how it is injection-locked, and made to generate pulses. Second is a discussion of the measurements that can be realized with two fast pulses. These include measurements of Rabi oscillations on a concentrated sample, as well as spin echo measurements at temperatures approaching 200 K. This section demonstrates the capabilities of the spectrometer, and how it can be leveraged for studies of systems that could not be studied in the past. The final part of the chapter investigates the particular problem of

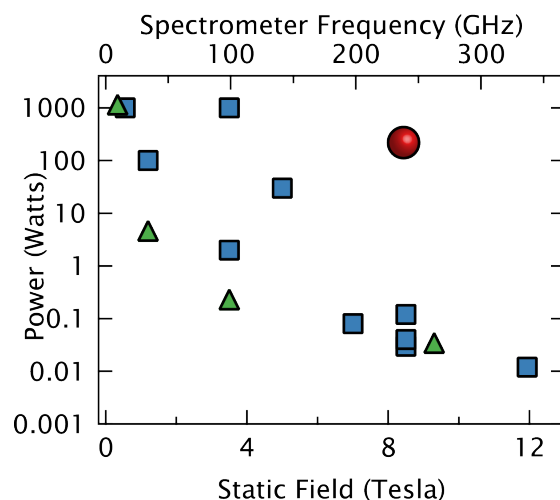


Figure 5.1: Power Limitations of EPR at High Fields. The powers and frequencies of some currently available pulsed EPR spectrometers as pulled from literature, with commercial instruments shown in green (all from Bruker Biospin). The list is not exhaustive, but rather illustrative of the dramatic difference in power available in spectrometers at fields above 100 GHz. UCSB's FELEPR is shown as the red sphere, and is the only current technology capable of carrying out ultra-fast EPR at these fields. The commercial spectrometers are those available from Bruker, the other spectrometers are: at 17 GHz in Ref. 174, at 30 GHz in Ref. 73, at 95 GHz in Refs. 71 and 70, at 140 GHz in Ref. 175, at 200 GHz under development from the DNP spectrometer in Ref. 176, at 240 GHz in Refs. 88, 177 and Private Communications with Professor Susumu Takahashi (for 100 mW), and at 336 GHz in Ref. 177

studying high-concentration systems, and demonstrates that some aspects of previously measured spectra can be understood by considering the effect of sample magnetization on the spin system.

5.2 Spectrometer Design

While the heart of the FELEPR spectrometer is the FEL itself, a wide variety of technique development is necessary to render the FEL a suitable source with

which to do pulsed EPR. The instrument itself is built 'on top of' a traditional, low-powered pulsed EPR spectrometer. This system was used in the preceding chapters of the thesis, and is described in detail in Appendix A. The detector system is based on Schottky-diode mixers that mix the 240 GHz signal first to 10 GHz. This is then mixed with a 9.5 GHz oscillator (that is unlocked to the source) down again to 500 MHz. The only major difference in the detection employed for FELEPR is the use of 9.5 GHz local oscillator. When a low power, solid-state source is used, the detector can be locked to this source, providing a consistent phase reference for the detector. In the case of FELEPR, the FEL can not be locked to the detection directly (in hardware), and so we are forced to utilize an unlocked detection phase. The correction of this limitation is the topic of the Chapter 6. Fig. 5.2 shows a sketch of the detection system for both low-powered EPR and FELEPR.

While the FEL as built provides high-power, quasi-cw pulses by itself, the frequency profile of the pulse is too broad for EPR, and the pulses ($>1\mu\text{s}$) are far longer than the desired <10 ns. Thus, the FEL must be made to lase consistently at a single frequency, and then we must be able to generate short pulses from this long pulse, which is challenging due to the lack of switches that operate at 240 GHz. As a result of the complexity involved in the project, we divide the spectrometer into several parts: the FEL, the injection locking, the cavity dumping system, and the pulse slicer. Each will be addressed in order below, but further details

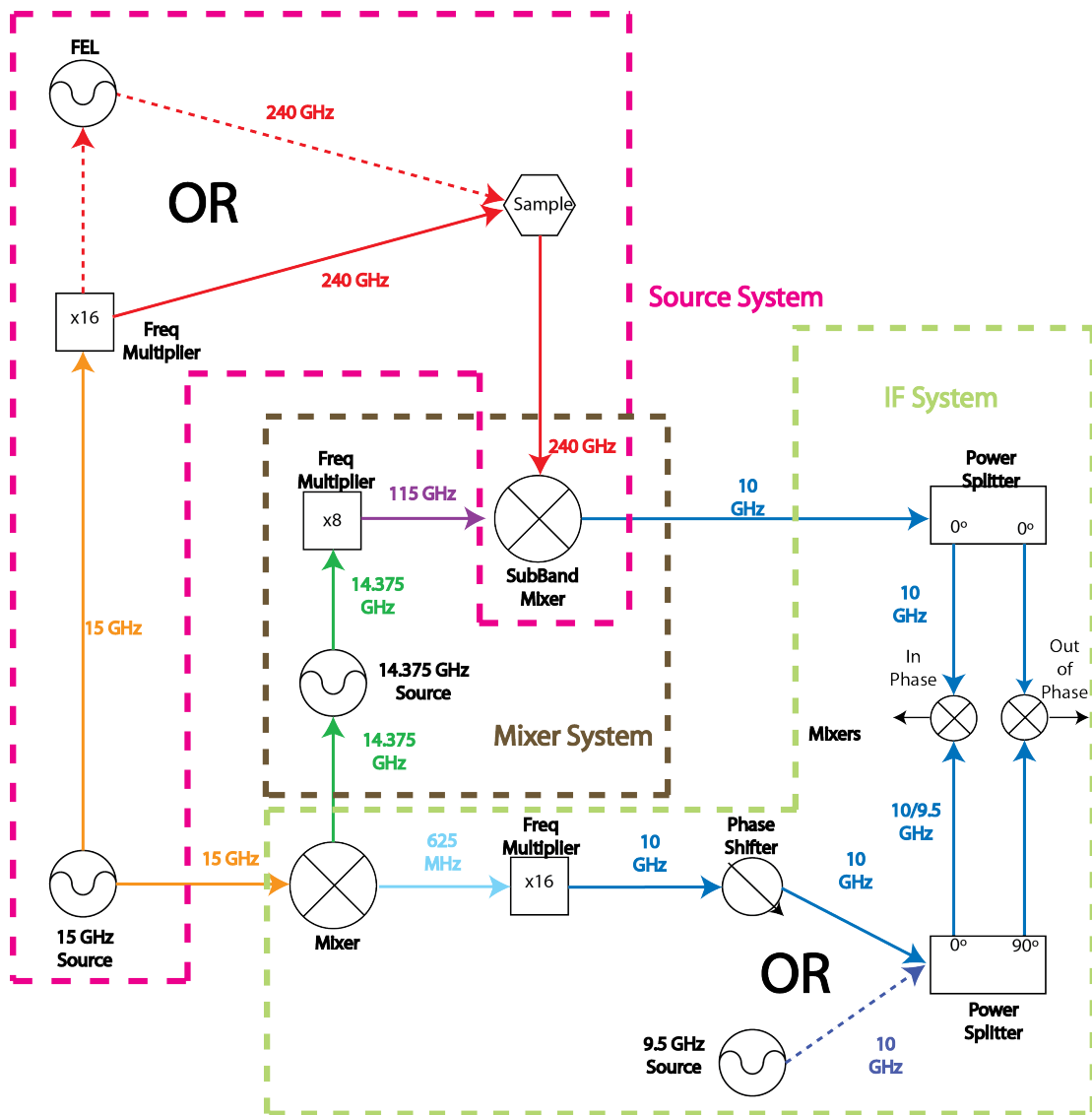


Figure 5.2: 240 GHz Detection. A graphical overview of the super-heterodyne detection system used with the 240 GHz spectrometer and described in the text. Low-powered EPR is done using a local oscillator signal derived from the source and detector signals to mix the the EPR signal to 0 frequency. FELEPR uses the low-powered source to injection lock the FEL (see Sec. 5.2.2) and an unlocked local oscillator at 9.5 GHz as shown with the dotted arrows.

are in literature for FELs^{178,179}, injection locking,¹⁸⁰ cavity dumping,¹⁸¹ and the FELEPR spectrometer.^{88,182}

5.2.1 Free Electron Laser

A Free Electron Laser is a source of strong radiation that utilizes the radiative properties of a beam of electrons. A variety of FELs exist throughout the world, and they generally are parts of facilities as they require dedicated space and maintenance staff. The UCSB FEL is one of the less common, electrostatic accelerator-based FELs. A high voltage (2-6 MeV) accelerator is used to generate a several μs -long electron beam moving at relativistic velocities ($>95\%$ the speed of light). The electron beam is steered using a magnetic beam line consisting of steering and focusing coils (to counteract diffraction of the beam). The electron beam is then passed through the undulator, an array of fixed magnets positioned periodically, where radiation is generated. After passing through the undulator, the electron beam (with some energy extracted in generating radiation), is returned to the accelerator. Typically $>90\%$ of the total current (ideally $\sim 99\%$) is recirculated to keep the terminal of the accelerator at a high voltage, as the beam current far exceeds the constant charging current.

The force of the periodic magnetic fields on the electron beam causes the beam to “wobble” and the associated accelerating charge generates electromagnetic radiation.⁶⁶ The frequency of the oscillation is determined by the period of the

magnets (which is fixed), the strength of the period magnetic field, and the energy of the electron beam. By changing the terminal voltage of the accelerator, the electron beam energy can be continuously tuned, allowing continuous tuning of the frequency (within a window defined by the limits of the accelerator and the geometry of the undulator). For the millimeter wave FEL used here, frequencies between ~ 150 GHz and ~ 700 GHz can be achieved. The undulator structure is contained within a quasi-optical resonator, with a fixed mirror at either end. The length of the resonator leads to modes spaced by ~ 25 MHz (due to the roughly 40 ns round trip time in the cavity). Light is coupled out of the resonator using a piece of high-resistivity silicon. Because the bandgap of silicon is far larger than the energy of 240 GHz photons, it is largely transparent at these frequencies. However, a small portion (several percent) of the radiation is reflected by the silicon wafer, and is therefore coupled out for use. The use of the silicon wafer allows employment of “cavity dumping” which will be discussed in detail below.

The output of the FEL is therefore a several μs long pulse of radiation with a peak power of ~ 500 Watts at 240 GHz. This beam is transported from the FEL vault to the user labs using an evacuated quasi-optical transport system, where curved mirrors and lenses are arranged to prevent beam diffraction.¹⁸³ Losses in the transport system lead to ~ 300 Watts reaching the FELEPR laboratory. However, the “raw” FEL beam is not sufficient for carrying out EPR for two

principal reasons: it is far too long (with slow rising and falling edges), and it is not of a single, fixed frequency.

5.2.2 Injection Locking

Those utilizing the FEL for high-power Terahertz spectroscopy usually find its frequency spectrum to be comparatively narrow, as the bandwidth covers < 1 GHz. Other sources of Terahertz radiation (for instance FEL's designed using different accelerators), tend to generate short pulses, which lead to a broad Fourier Transform limited bandwidth.¹⁸⁴ However, for EPR, where linewidths are on the order of MHz, such a broad spread of frequencies would make EPR impossible.

The spread of frequencies in the UCSB FEL results from the amplification of the FEL pulse in the resonator from noise. As mentioned above, the resonator has a mode spacing of ~ 25 MHz, and the radiation emitted from the electrons can couple into. Due to the ~ 1 GHz range of energy of frequencies emitted from the electron beam, this leads to the potential amplification of many modes across a roughly GHz range (the center of which will be defined by the electron beam energy). The precise mode structure is effectively random, as the amplification occurs from noise, meaning that the pulse-to-pulse spectrum changes dramatically. To combat this, the spectrometer utilizes injection locking, which induces lasing on a single mode of the resonator and is described in full detail for this project in Takahashi et al.¹⁸⁰ Briefly, a 240 GHz solid state source is coupled into the

FEL resonator using quasi-optics (and a pair of isolators, to prevent the FEL pulse from from damaging the source). If the source frequency overlaps one of the resonator modes, then instead of amplifying from noise, the FEL will lase *only* on the injected frequency (so long as the power in that mode is substantially larger than the noise). Only relatively small power levels are necessary to fulfill this condition, however, and since publication of Ref. 180, the injection source has been moved into the main EPR lab, and the radiation coupled through the FEL transport line to the resonator. The matching of the injection source to the resonator mode is done by modifying the frequency of the injection source by small amounts (< 10 MHz), which is accomplished by varying its 100 MHz phase reference.

5.2.3 Silicon Switches and Cavity Dump Coupling (CDC)

Unlike many other sources, where a low frequency signal is up-converted in frequency, the radiation from the FEL is generated at 240 GHz. In multiplier-based sources, the output can be modified by modulating the low-frequency components (for instance, switching a 15 GHz signal before it is multiplied to 240 GHz to generate pulses at 240 GHz). This is clearly impossible using the FEL, and so it is necessary to employ specialized switching technology which can be both fast, and handle the high FEL powers. As no such device currently exist, homemade, photo-activated silicon switches were developed and utilized.

The principle of silicon switching is covered in detail in literature from Hegmann et al.¹⁸⁵ and Doty et al.¹⁸⁶ and it is outlined here as it applies to the FEL. As described in discussing the out-coupler of the FEL, a high-resistivity silicon wafer is largely transparent to 240 GHz radiation. However, when silicon is irradiated at a frequency above the bandgap, electrons are promoted out of the valence band and generate electron-hole pairs. The existence of electrons in the conduction band at the surface of the wafer causes it to become reflecting and act as a mirror. The activation of the reflection is determined by the length of the laser pulse, and thus rise times can be as short as the laser pulses. Alternatively, recombination controls the relaxation of the switch, and so for high-resistivity silicon the reflectivity decays over relatively long (~ 100 ns to $1 \mu\text{s}$) times.

Thus, silicon finds its use in the FEL itself as a cavity dump coupler (CDC). Radiation is coupled out of the FEL using a silicon wafer that reflects only a few percent of the radiation. However, by irradiating the wafer with a high-powered 532 nm laser, the cavity resonance is broken. This couples the energy out of the FEL resonator all at once, and prevents the FEL from continuing to lase. The FEL output power suddenly increases for 40 ns (corresponding to the energy stored in the resonator being suddenly coupled out), followed by the cessation of lasing. Thus, the CDC offers two potential benefits: it generates $\sim 2\text{-}4\times$ increase in the power of the FEL pulse for a short period, and it stops the FEL from lasing to act as an off switch.

5.2.4 Pulse Slicer

The μs long pulse generated from the FEL is not suitable for the ultra-fast EPR which we wish to do using the high-power pulses. Therefore, we must implement a way to “slice” much shorter pulses from the long FEL pulse. In order to generate high-contrast pulses from the FEL, multiple switches are necessary to overcome the long decay times of the silicon switches. Further, a complex system is necessary to generate the two pulses that are desired for the most basic EPR experiments (including echo based measurements). This pulse slicer system allows the μs -long FEL pulse to be used to generate two separate pulses, each of tunable length and separation. The basic design of each pulse is rather simple, and a single “switch” is made up of 2 wafers, the first turns the pulse on (by directing radiation toward the sample), and the second turns the pulse off (by directing the radiation into an absorber). A diagram of the current setup is shown in Fig. 5.3, and a previous implementation is discussed in Takahashi et al.⁸⁸

The FEL pulse is coupled out of the optical transport system and into free space within an isolation box, which is a box of thin aluminium, with the insides covered in absorbing foam (ECCOSORB from Emerson Cumming). This box prevents scattered light from being reflected out of the beam path and into the room. Scattered light at these frequencies becomes a pervasive source of background signal. Inside the isolation box, the FEL pulse is coupled into a pair of back-to-back feedhorns. The horns are matched to freespace to couple $\sim 98\%$ of

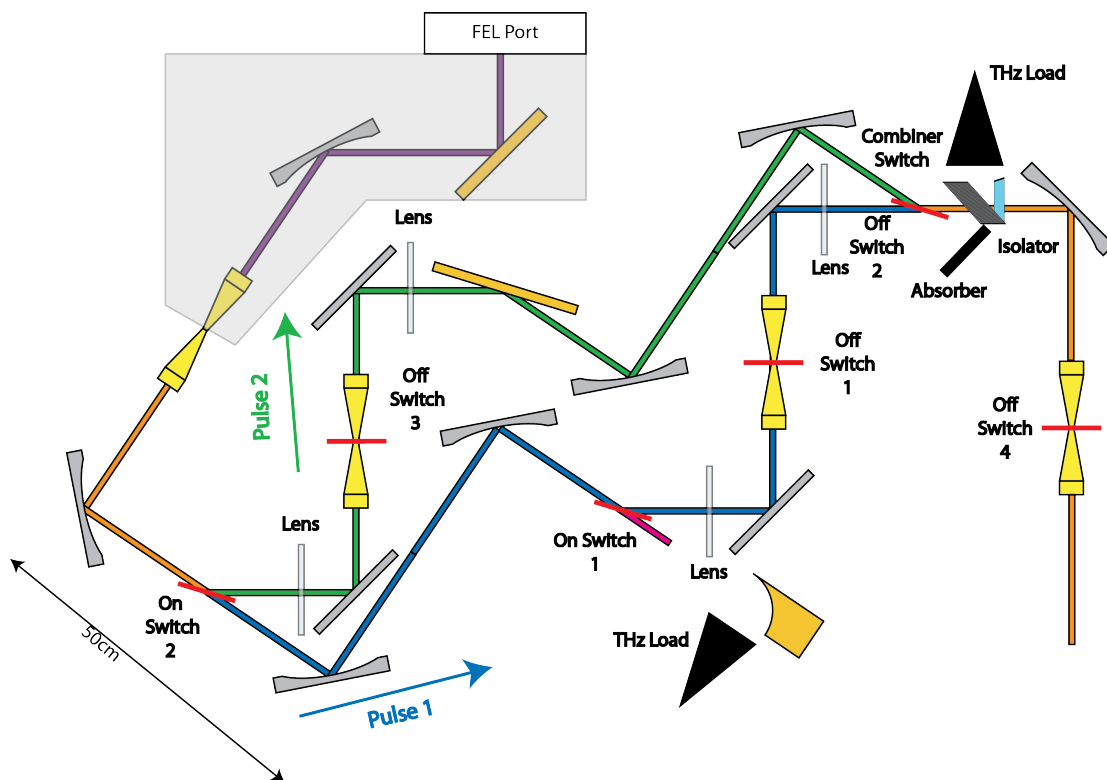


Figure 5.3: FELEPR Pulse Slicer. The pulse slicer uses silicon on and off switches to generate up to two short (down to 1 ns) pulses from the long ($\sim 1 \mu\text{s}$) FEL pulse. The two generated pulses are split from the incident FEL beam in orange (after it is filtered from the FEL output in purple). Initially, the pulse passes through on switch 2, and the activation of on switch 1 begins the first pulse (in blue), which is then halted by off switches 1 and 2. The second pulse is started by activation of on switch 2 (in green), and is turned off by off switches 3 and 4. The two paths are recombined and directed to the sample (in orange) at the combiner switch (which doubles as off switch 2).

the radiation into them.¹⁸⁷ These horns then taper to a single mode waveguide (WR 4.3) at their center. Because the single mode section only supports the lowest order mode, and is polarization selective, this pair of back-to-back horns acts as a high quality filter, turning the FEL pulse into in a high-quality, nearly-Gaussian freespace beam. The filtering process is, however, lossy, and ~ 3 dB of insertion loss is encountered, dropping typical powers at the start of the pulse slicer to 150 W.

Once filtered, the FEL is directed into the two-pulse pulse slicer. Large (4 inch) wafers (shown in red in Fig. 5.3) are used as on switches. These switches are placed with a high angle of incidence ($> 70^\circ$) for reasons which are explained in the next paragraph. However, these high angles of incidence make the projection of the FEL beam on the wafer larger in the x-direction (~ 4 inches) than in the y-direction (~ 2 cm). To activate these switches optimally, the whole region of the wafer would be uniformly excited with a high energy laser. In practice, obtaining full cover of the wafer is technically challenging, and we typically achieve reflections of only $\sim 80\%$. These limitations will be addressed with more careful optical design, but 80% switching is acceptable at this stage.

A consistent problem with typical silicon switches is that, though they are largely transmissive at 240 GHz, some reflections do emerge. Even if the reflections are only a few %, when utilizing 100's W of power, these small reflections from the on switches would prevent EPR (by saturating the EPR line). Two meth-

ods are used to correct for this problem. The first is operating the switches at Brewster’s Angle, where no reflections off the surface are expected. From solving the Fresnel equations, Brewster’s angle is $\theta_{Brewster} = \arctan(\frac{n_{mat}}{n_{air}})$, where n_{mat} is the index of refraction for the material, and $n_{air} \approx 1$, meaning $\theta_{Brewster} \approx 72^\circ$ for silicon.⁶⁶ However, we find that this approach still generates sufficient reflections that we pursue a more involved methodology found in literature.¹⁸⁶ Here we tune the thickness of the wafer so that the reflections from the back surface are 180° degrees out of phase with the reflections from the front surface. This causes the reflections to cancel out, and reduces the reflection from the wafer surface. The required thickness for this can be calculated from geometric considerations (see Doty et al.¹⁸⁶), and the optimal thickness (T) is given by

$$T = \frac{m\lambda}{2(\frac{n_{Si}}{\cos(\theta_t)} - n_{air} \tan(\theta_t) \sin(\theta_i))} \quad (5.1)$$

Here $n_{Si} = 3.42$ is the dielectric constant of silicon, $\lambda = 1.25\text{mm}$ is the wavelength of the light, θ_i is the angle of incidence, and θ_t is the angle at which the beam propagates through the material (and is given by Snell’s law from θ_i by $\theta_r = \arcsin(\frac{n_{air}}{n_{Si}} \sin(\theta_i))$). For a wafer at Brewster’s angle using 240 GHz, the result is a thickness of $\sim 190 \mu\text{m}$. Wafers of these thicknesses can typically be purchased, and the final thickness could be tuned by mechanical polishing (for coarse changes) and finally etched to achieve the desired thickness. In practice, we found that for thickness between $\sim 185\text{-}195 \mu\text{m}$, we achieve reflections that are

less than -60 dB of the input, which are sufficiently small. The best cases that were observed in the experiments were better than -80 dB.

There are 2 wafer on switches (one for each pulse) utilized in this setup. As labeled in Fig. 5.3 “On Switch 1”, activates the first pulse; before it is activated, the FEL pulse is dumped (thought a mirror) into the low-reflection load. “On Switch 2” activates the second pulse by directing light into the other beam path. However, another wafer switch is necessary to act as a beam recombiner; because the two pulses follow different paths (green and blue respectively in Fig. 5.3) the two paths must be combined, which occurs at the “Combiner Switch.” Thus, to activate the second pulse we must activate two switches (“On Pulse 2” and “Combiner Pulse”).

While identical, wafer-based switches can be used as off-switches (and initially, this is indeed how pulses were turned off), but they offer a distinct problems. The $\sim 80\%$ reflection that is reproducibly obtainable is far too low to achieve clean excitation pulses, and light that is not reflected continues to reach the sample, resulting in a persistent “on” effect. While hard work on the optics is able to generate better quality off-switches (with contrast close to), they still remain too inefficient. To combat this, the FELEPR utilizes horn-based off switches. Free-space horns, which taper to a 5 mm cylindrical waveguide are placed back-to-back, with a piece of silicon in between them. As a result of the horn’s constriction, the fully active region of the wafer is only 5 mm. Unlike the filtering horns, these

do not taper to a single mode structure, and therefore don't filter and have a low insertion loss. 5 mm is a substantially smaller area to irradiate than for the wafer switches, allowing full coverage and much higher energy densities. These switches are found to give, under optimal conditions ~ 40 dB of isolation per switch. The optical alignment of these switches is slightly more challenging, as the laser beam must be passed through the quasi-optical mirrors (shown in grey in Fig. 5.3), but the improved performance far outbalances the increased difficulty. An additional advantage is that only 1-3 mJ of energy is necessary to full activate the horn switches, whereas closer to 30 mJ is necessary to optimally drive the wafer switches.

While the horn switches work far better than the previous, wafer off switches, we utilize a pair of off switches for each pulse to ensure a high contrast ratio for the pulses. For the 1st pulse, "Off Switch 1" and "Off Switch 2" are used. Notice that due to the constraints of physics space, an additional back-to-back horn could not be installed, and so "Off Switch 2" is also the "Combiner Switch". This wafer off switch typically provides ~ 20 dB of isolation, when driven at very high energies. For pulse 2, horn switches "Off Switch 3" and "Off Switch 4" are used.

A final wafer switch is used in the FELEPR setup which is not depicted in Fig. 5.3. The detector is protected from the extremely strong FEL pulse with a silicon switch, which only couples the induction signal to the detector following activation by a laser. Before this "detector switch" is triggered, when the detector

is in its quiescent state, only \sim -60 dB of the induction signal is coupled to the detector, so that the FEL pulse is observed, but does not damage the detector. Upon activation of the switch we expect to achieve \sim 80% coupling to the detector.

Two final components of the pulse slicer are the absorbers and loads, and the quasi-optical isolator. The loads and absorbers are designed to minimize reflections and act as dumps at places where radiation is likely to leak out. The quasi-optical isolators are devices which allow linear polarized radiation to pass, but prevent the reflections from propagating. This prevents the formation of standing waves.¹⁸⁸

5.2.5 Laser System

Whether employed as full wafers, or as small pieces inside of back-to-back horns, all the silicon switches are driven by 532 nm (green) lasers. In order to generate the 10-100's of mJ of energy necessary to trigger the switches, we employ Nd:YAG (neodymium-doped yttrium aluminium garnet) lasers at 1064 nm which are Q-switched to generate \sim ns long pulses. Frequency doubling crystals are then used to convert these pulses to 532 nm. The cavity dump coupler is control by one such Nd:YAG laser (Big Sky Laser, CFR200) that generates > 100 mJ, whereas the detector switch is controlled by a smaller Nd:YAG laser (Litron Nano-T-250-10) outputting \sim 40 mJ. Both of these lasers are traditional Q-switched YAG lasers which generate \sim 5 ns pulses, and are synched at to the FEL firing at \sim 1 Hz.

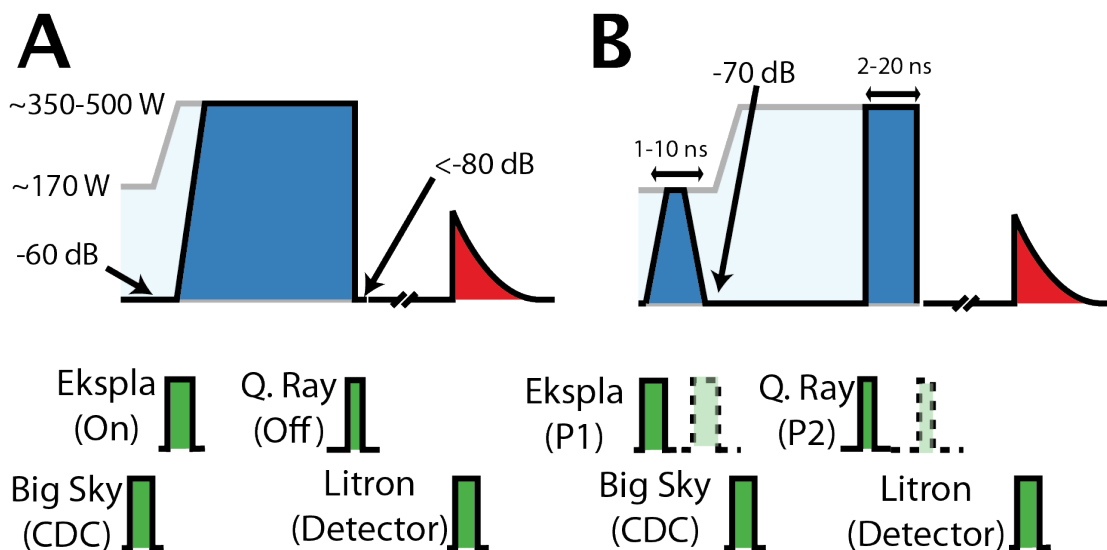


Figure 5.4: FELEPR Timing Diagram. The timing diagrams indicating the way pulses are sliced from the long FEL pulse using the laser system. Here the full FEL pulse is sketched in faded blue, and the activated pulses are in dark blue. The pre-pulse contrast is better than -60 dB, while the contrast following pulses is -70 to -80 dB (and better following the end of the CDC). The detected signal from the spins (here and FID) is in red. Finally, the YAG laser pulses are shown in green, with dashed and faded green indicating a portion of the same pulse being delayed. In each case the cavity dump coupler (CDC) is show in use (from the Big Sky Laser), but either pulse sequence can be utilized without it. Typical powers from the FEL that couple into the pulse slicer are ~ 170 W without the CDC, and 350 - 500 W with the CDC. Additionally, the activation of the detector switch is always controlled by the Litron Laser, whose position can be tuned (but must be fired after the end of the pulses to protect the detector). **A.** For one pulse experiments, a single laser is used for the on and off switches respectively. In order to get as ‘clean’ an off switch as possible, the faster Ekspla laser is used. **B.** When two pulses are used, each laser is used as both the on and off switches for a single pulse.

The silicon switches of the quasi-optical pulse slice are driven with a pair of high-power, frequency-doubled Nd:YAG lasers. The first offers a 150 ps long pulse (due to use of Backward Brillouin Scattering to shorten the pulses) with up to 120 mJ of energy at 532 nm (Ekspla, SL312). The second is a slower, 5 ns Nd:YAG laser with up to 230 mJ of pulse power (Spectra Physics, Quanta Ray GCR-150). Both these Nd:YAG lasers are synchronized to the firing of the FEL through an advanced trigger which runs the Nd:YAG flashlamps at 10 Hz, while firing the laser (by triggering the Q-switch) only coincident with the FEL firing at ~ 1 Hz.

There are two primary modes of operation for the FELEPR: one pulse, and two pulse.

One Pulse Laser Setup

For this setup, only one pulse is used, and it is implemented with “On Switch 2” in Fig 5.3, and utilizes “Off Switch 3” and “Off Switch 4.” The on switch is controlled by the slow, Nd:YAG laser (Spectra Physics, Quanta Ray GCR-150), and the two off switches are controlled by the fast Nd:YAG laser (Ekspla, SL312). This allows the pulse length to be adjusted over the entire length of the FEL pulse (up to several μs) by electronically changing the delay between the laser pulses. This mode is depicted in the timing sketch in Fig. 5.4A

Two Pulse Laser Setup

For a two pulse setup, the switches are used as described in Subsection 5.2.4. The pulses are generated by splitting each Nd:YAG laser into two beams to drive both the on and off switches for a single pulse. The pulse lengths are tuned between ~ 1 -15 ns by an optical delay line (precision ~ 10 ps), which delays the arrival of the laser pulse that triggers the off switch from the corresponding on switch. The first pulse is controlled by the slower, Nd:YAG laser (Spectra Physics, Quanta Ray GCR-150) and the second pulse is controlled by the fast YAG laser (Ekspla, SL312). The spacing between the two pulses can be arbitrarily controlled by changing the firing times of the two lasers (out to the length of the FEL pulse). This mode is depicted in the timing sketch in Fig. 5.4B

5.3 EPR Results

The technical work carried out in Sec. 5.2 allows the generation of one or two FEL pulses. The contrast ratios of the pulses is sufficiently high (>60 dB on both sides) for these to be described as distinct pulses, but the shape of the pulses is not necessarily square, due to the slow YAG laser pulses (~ 5 ns). Nonetheless, the instrument has been demonstrated to be suitable for a variety of EPR experiments. The manuscript from Takahashi et al.⁸⁸ describes some of these same experiments in this section though the overlap is not complete.

5.3.1 One Pulse Measurements: Simple Rabi Oscillations

The simplest form of experiments that can be carried out in pulsed EPR utilize a single pulse, followed by a measurement of the free induction decay (FID). The Rabi oscillation measures the FID (corresponding to the transverse magnetization) as the length of the excitation pulse is varied resulting in a rotation of the magnetization as in Eq. 1.7. Due to our use of a two-phase, mixer detection system, we measure both M_X and M_Y , though due to the instability of the phase, we typically record the magnitude of the transverse magnetization ($M_{tr} = \sqrt{M_X^2 + M_Y^2}$). Changing the length of the excitation pulse changes the tip angle $\beta = \gamma_e t_p B_1$ with t_p the pulse length and B_1 the magnetic field strength in the applied pulse. This is valid for a rectangular pulse, but naturally if the pulse has a more complex shape, then the pulse profile also matters.

Short pulses then yield small tip angles and the resulting signal is small. As the pulse length, and therefore tip angle, increases, a larger transverse magnetization is generated, and so the signal increases. Maximum signal is achieved for $\beta = \frac{\pi}{2}$, at which point increasing the pulse length begins to 'over-rotate' the spins, reducing the measured signal until it reaches a minimum at $\beta = \pi$ where the magnetization has been inverted and no precession should occur. As the spins are tipped further, transverse magnetization emerges again and therefore another signal maximum appears at $\beta = \frac{3\pi}{2}$, but it is again nulled at $\beta = 2\pi$.

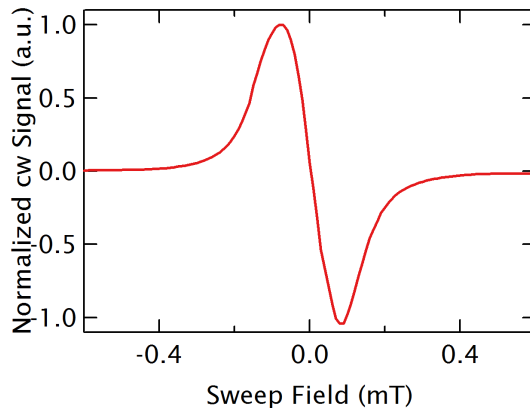


Figure 5.5: Typical cw EPR Spectrum of a BDPA grain. A typical cw EPR spectrum of a BDPA grain is shown at 240 GHz. The narrow line results from the high spin concentration in this undiluted grain. Linewidths vary from sample to sample, and are not always a single clean line. The resonance field is ~ 8.58 T, corresponding to a roughly free electron g value.

We utilize a single grain of BDPA as a test sample due to its narrow line (from exchange narrowing) and strong signal. An example cw EPR spectrum is shown in Fig. 5.5 for a single grain of BDPA, which were then used for a Rabi oscillation. The results of a typical Rabi Oscillation experiment carried out with the FEL on a BDPA sample is shown in Fig. 5.6A, and displays the expected periodic dependence on the pulse length. The distance between the two maxima (between $\beta = \frac{\pi}{2}$ pulse and $\beta = \frac{3\pi}{2}$) is found to be ~ 11 ns. Therefore, the length of a $\frac{\pi}{2}$ pulse is given by ~ 5.5 ns. This is roughly 50-100x faster than can be achieved utilizing the low-powered sources that have been necessary for pulsed EPR at 240 GHz in the past.

The shape of the Rabi oscillations differs slightly from the optimal experiment:

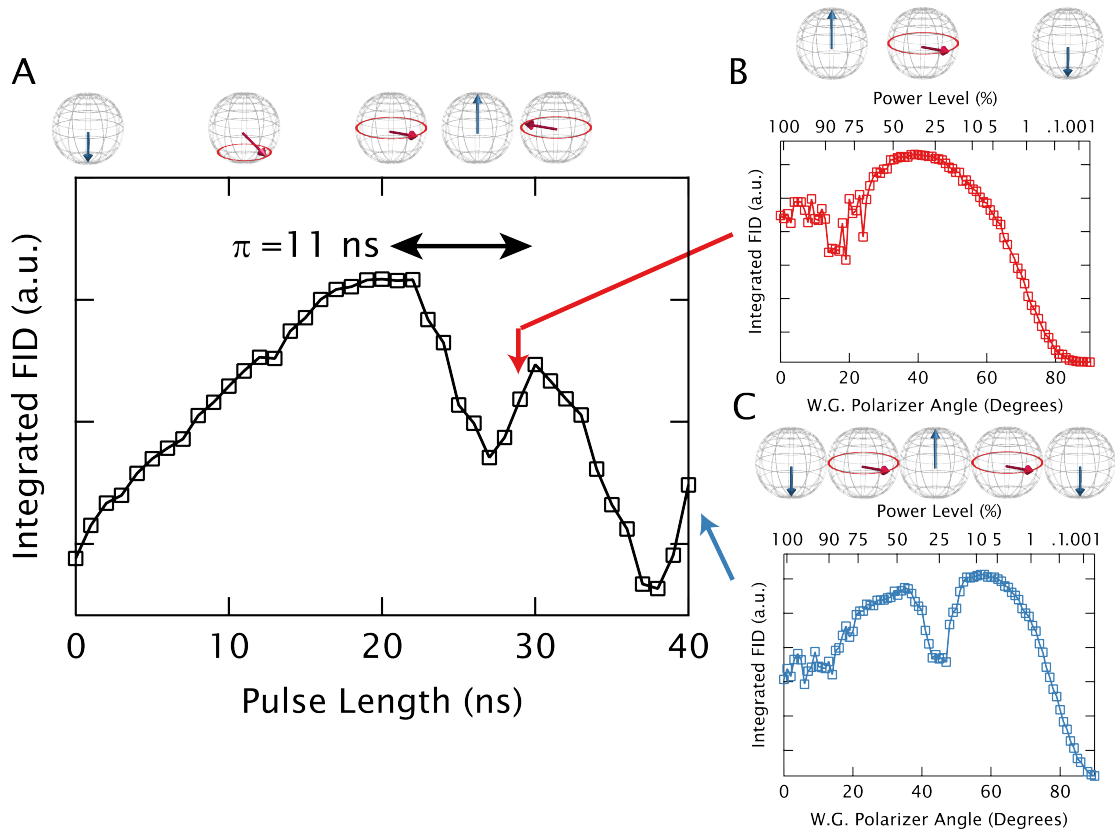


Figure 5.6: Rabi Oscillations with an FEL. **A.** The magnitude signal of the FID of a BDPA grain is shown as a function of pulse length in a single-pulse measurement. Characteristic Rabi oscillations are observed that are indicative of rotating the spin magnetization as described in the Bloch spheres above the figure, with the length of a $\beta = \pi$ pulse being ~ 11 ns. **B.** and **C.** demonstrate the effect of attenuating the FEL pulse with a wiregrid polarizer with various pulse lengths. Similar oscillations are observed as the tip angle is now modulated by the pulse intensity (rather than pulse length). The estimated corresponding attenuations (as a function of grid angle) are shown in the top axes. **B.** shows a single maximum, as is expected from reducing the power under a π pulse, while **C.** shows two peaks, as is expected when starting from a 2π pulse.

1. The slow activation of the oscillations (from 0 to 20 ns) is the result of the pulse structure, where small leakages occurring after the firing of the pulses results in small signal. This can be reduced by tuning the timing of the firing of the CDC to cut this off.
2. One would expect that the signal magnitude would return to zero during an inversion pulse (at ~ 27 ns). One explanation for this result is a distribution of the pulse power within the sample. If different spins see different strength pulses, not all spins will display the same Rabi oscillation frequency. While a minimum exists where the majority of spins are being inverted some of the spins experience a different B_1 and therefore not inverted, resulting in remaining signal. The distribution of effective B_1 is not unexpected given that B_1 in the waveguide should be radially dependent. Further, the wavelength of the radiation is only ~ 1.25 mm, meaning that the sample thickness (~ 100 's of μm) is a significant fraction of the wavelength, and so the B_1 is not constant over the sample.
3. The non symmetry of the two minima is unexpected. If simple B_1 in homogeneity were the only cause of the incomplete inversion at ~ 27 ns, then one would expect that under a full 2π rotation (at ~ 38 ns), a similar nonzero level would be reached. Instead, the signal is far closer to zero at this point. This is not consistent with the inhomogeneity discussed above, but we find

a partial explanation in Sec. 5.4, as this is the result of a large demagnetization effect.

A careful measurement of the dependence of the oscillation on power was done to confirm that the oscillations are Rabi oscillations. To do this a wiregrid polarizer (which passes radiation of a particular linear polarization, and reflects the orthogonal polarization) was used to attenuate the pulse powers. When two grids are used, and the first one is free to rotate, this acts as a power attenuator, with the final polarization of the light being defined by the orientation of the last grid. The power dependence of such an arrangement should be approximately $\propto \cos^4(\chi)$, where χ is the angle between the incident polarization and the rotation of the polarizer (i.e. $\chi = 0^\circ$ is full power, and $\chi = 90^\circ$ is the highest attenuation).

Figs. 5.6B and 5.6C show measurements done with a fixed pulse length, but modifying the intensity of the FEL pulse by utilizing a wiregrid polarizer. In Fig. 5.6B when the pulse length is fixed so that the full-power tip angle is $\beta \approx \pi$ and the pulse power attenuated we see a small drop in signal intensity (corresponding to reaching the π pulse), and then we see the signal intensity increase as the diminishing power is reducing the tip angle of the pulse, to be $\frac{\pi}{2} < \beta < \pi$. The peak at a wiregrid position of $\chi \sim 40^\circ$ corresponds to a $\beta = \frac{\pi}{2}$ tip angle, and for greater attenuations the signal decreases to zero. Given that we started with a $\beta \sim \pi$ tip angle, we would expect an attenuation in power of $\frac{1}{4}$ (corresponding to a factor $\frac{1}{2}$ in B_1) would be necessary, which is consistent with $\chi = 40^\circ$ ($\chi = 45^\circ$

would give precisely $\frac{1}{4}$) In Fig. 5.6C when the pulse length is fixed so that the full-power tip angle is $\beta \approx 2\pi$ we see the same behavior, except with another oscillation as would be expected for passing through signal maxima at tip angles of both $\beta \sim \frac{\pi}{2}$ and $\beta \sim \frac{3\pi}{2}$. In this case we would expect $\chi = 30^\circ$ and $\chi = 60^\circ$ would result in maxima, while $\chi = 45^\circ$ would be a minimum, which is consistent with the measurements here. Taken together, these traces confirm that the oscillations observed are Rabi oscillations (but do not give a clear source for the discrepancies addressed above). However, a more careful study of the one pulse experiments will be discussed in Sec. 5.4 and will clarify some of the effects observed in a one pulse experiment.

5.3.2 Two Pulse

A wide variety of two pulse experiments are possible in magnetic resonance, and the most common is the simple spin echo, where a second pulse is used to refocus the signal into an echo. A simple echo decay measurement allows quantification of T_M (see Sec. 1.1.2). It is generally the case that when relaxation times become rapid compared to pulse lengths, it is difficult or impossible to observe an echo signal. Thus, if the spins largely decay in 100 ns, an echo sequence utilizing 600 ns long pulses (as is typical using solid-state based sources) would not show a signal. As a result rapidly relaxing spins can not be measured with pulsed EPR at high magnetic fields. However, utilizing the short pulses demonstrated

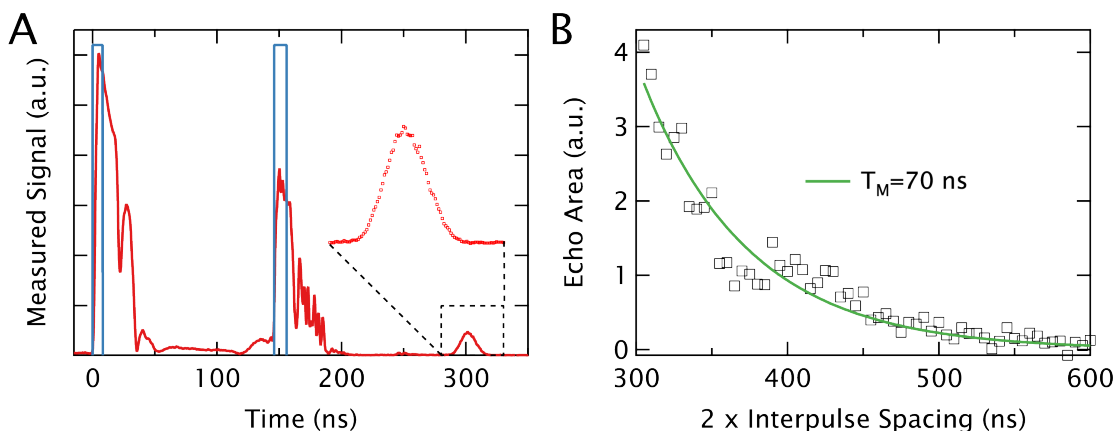


Figure 5.7: FELEPR Nitroxide Echo. **A.** The trace in red shows a two pulse echo measurement using the FELEPR on a 50 mM nitroxide radical solution at 190 K in D_2O and d-glycerol. The two pulses are ~ 10 ns each (and do not correspond to a $\frac{\pi}{2}$ and π pulse), but scattered light and the sensitivity of the detector makes the pulses look longer. The trace in blue shows the approximate “true” pulse shape, and the echo is expanded in the inset. **B.** The measured echo area is plotted as a function of twice the interpulse spacing, to demonstrate a measurement of the phase memory time (determined from a fit to an exponential decay) that is $\sim 10x$ shorter than can be measured without the FELEPR.

in Sec. 5.3.1, we should be able to measure rapidly decaying spins utilizing a two-pulse, spin echo experiment.

A test sample of 50 mM, 4-Amino-TEMPO was prepared in D_2O and deuterated glycerol and the two-pulse echo measured at 190 K. Fig. 5.7A shows in red the time trace of the 2-pulse experiment which shows both pulses and the echo signal. It is worth noting that the pulse lengths are only ~ 10 ns, which is far shorter than they appear in the plots. The discrepancy emerges from the substantial amounts of scattered radiation generated when the off switches are activated. The estimated true pulse lengths are overlayed in Fig. 5.7A in blue. Notice that the shapes of the pulses at their peak (that they appear to decay after

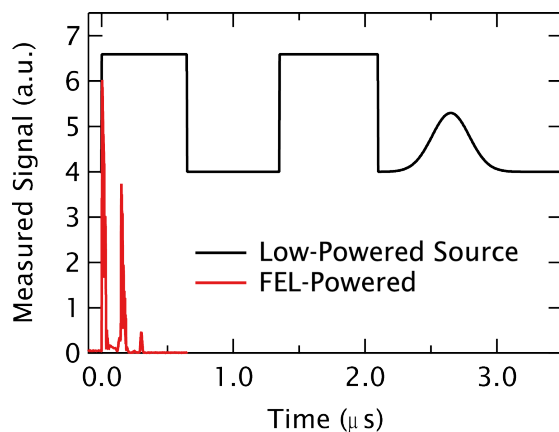


Figure 5.8: Fast Echo Sequence with FELEPR. The FELEPR echo sequence from a nitroxide radical is shown in red (same data as Fig. 5.7A). This is compared to the sketch of a typical low-powered EPR echo measurement, demonstrating the ability to measure rapidly decaying signal.

initial activation), is consistent with the pulses saturating the detector, and not the actual pulse profiles. The echo signal is shown expanded in the inset.

Varying the interpulse spacing results in a change in the intensity of the echo signal. The echo areas are plotted versus twice the interpulse spacing in Fig. 5.7B. A fit to an exponential of the form $\text{Area} \propto \exp(-\frac{2\tau}{T_M})$ gives a best fit estimate of the phase memory time $T_M = 70$ ns. These measurements take place at a temperature that is $\sim 2\text{-}3\text{x}$ higher than temperatures at which a signal could be observed using the long pulses of a low-powered source, and $T_M = 70$ ns is a roughly 10x shorter T_M than could be probed without the FEL. Because the TEMPO molecule is a good model of a biological spin-label, this confirms that the FEL can measure biological samples at much higher temperatures than previously possible. In order to emphasize the immense difference in measurements of fast

relaxation Fig. 5.8 shows a typical echo measurement of a nitroxide spin label with FELEPR and using a standard low-powered source (which is sketched). The entirety of the FELEPR echo sequence takes place within the first pulse of the low-powered measurement, allowing measurements of dramatically faster T_M .

In order to expand on the measurements of the nitroxide radical, we also made measurements on GdCl_3 at lower concentrations (2.5 mM and 1 mM), which was aided by the narrow central transition of Gd^{3+} . The previous work in this thesis has demonstrated some of the possibilities of utilizing Gd^{3+} as a spin label, and so this acts as a test of the possibilities of using measurements of T_M as probe of protein structure and dynamics at higher temperatures. A typical time domain trace is shown in Fig. 5.9A using a 2.5 mM sample in D_2O and deuterated glycerol at 175 K. The signal-to-noise ratio (SNR) is substantially better than was measured with above in TEMPO as a result of the narrow central line of Gd^{3+} . Measurement of this signal at temperatures above ~ 70 K is impossible using a low-powered source, as is demonstrated in Fig. 5.9B, which shows the phase memory time (extracted from $\text{Area} \propto \exp(-\frac{2\tau}{T_M})$) as a function of temperature from <10 K up to 200 K. This range of temperatures could not be accessed previously. The improved signal to noise of utilizing Gd^{3+} is emphasized in Fig. 5.9C and Fig. 5.9D where the echo decay curves are showed for 100 K and 200 K respectively.

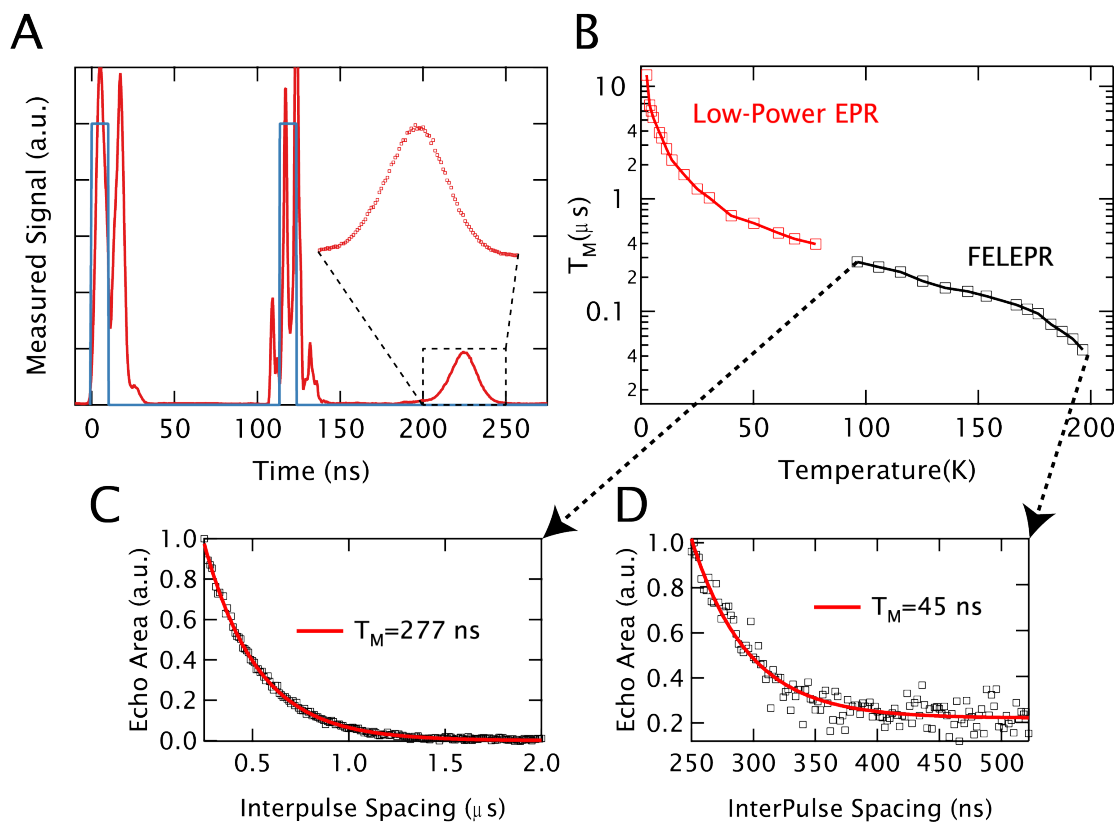


Figure 5.9: FELEPR Echo on Gd^{3+} . **A.** The time domain trace in red shows an echo carried out on a 2.5 mM $GdCl_3$ solution in D_2O and d-glycerol at 175 K, with more accurate estimates of the pulses drawn in blue. **B.** A temperature series of T_M for 1 mM $GdCl_3$ solution in D_2O and d-glycerol showing the substantially higher temperatures (and shorter relaxation times) that can be probed with the FELEPR. **C** and **D** show the FELEPR echo decays at 100K and 200K respective as evidence of the high signal to noise observed in Gd^{3+} samples (due to the narrow resonance).

5.4 Transient Larmor Shifts due to Paramagnetic Demagnetization

As discussed in Section 5.3, some of the discrepancies observed for the Rabi oscillations in Fig. 5.6 can be explained by a spatially inhomogeneous B_1 field at the sample, causing different parts of the sample to experience different rotations. However, another effect has been observed which better explains some features of the data. The investigation began when tuning the B_0 field in small increments about the resonance resulted in unexpected changes to the shape of the Rabi oscillations. Fig. 5.10 shows measurements of the Rabi oscillations at different fields around the central resonance. The original trace from Fig. 5.6 is shown in red (labeled: “On Res.”). Moving to slightly higher fields destroys the minimum located at ~ 27 ns (corresponding to an inversion pulse) as shown in blue. Alternatively, shifting to lower fields (as shown in green, purple and orange respectively) increases the depth of this first oscillation, yielding a better looking oscillation.

The source of the discrepancy is not immediately obvious. It is well known that, when working off resonance in a Rabi experiment, the frequency of the oscillation can be reduced as described by¹⁸⁹

$$\Omega_{off} = \sqrt{\Omega_{on}^2 + \Delta\omega^2} \quad (5.2)$$

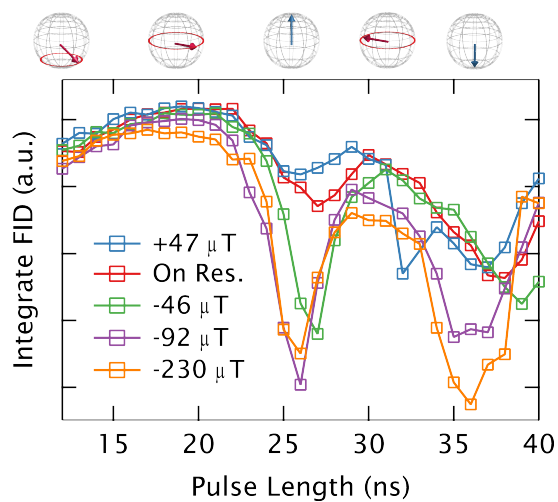


Figure 5.10: Off-Resonance Rabi Oscillations. The signal magnitudes of FIDs of a BDPA grain are shown as a function of pulse length in a single pulse measurement. Characteristic Rabi oscillations are observed that are indicative of rotating the spin magnetization as described in the Bloch spheres above the figure. As the measurement is tuned nominally off resonance, the quality of the oscillations appears to improve, most notably, the inversion pulse generates near zero transverse magnetization for $\Delta B_0 = -230 \mu\text{T}$.

where Ω_{off} and Ω_{on} are the on- and off-resonance Rabi frequencies, and $\Delta\omega$ is the difference between the transition frequency and the irradiation frequency. For our experiments, where 6 ns is a $\frac{\pi}{2}$ pulse, we have $\frac{\Omega_{on}}{2\pi} \approx 41.7$ MHz. Then even with the largest shift (0.23 mT \sim 6.4 MHz), $\frac{\Omega_{off}}{2\pi} \approx 42.2$ MHz, which is consistent with the small change in the Rabi frequency. Additionally, given that the pulses here are ~ 10 's of ns, the excitation bandwidth of the pulse is substantially broader than the < 10 MHz shift, and so no substantial effect should be related to the excitation bandwidth of the pulse. Further evidence that neither of these effects contribute results from the lack of symmetry in the effect of moving field: both the excitation bandwidth and the Ω_{off} should effect the curve identically in either direction.

Evidence for an unexpected effect came from more careful measurements of the Rabi oscillations, and from looking explicitly at the resulting signal. New Rabi oscillation experiments were made, which largely agree with the original measurements as shown in Fig. 5.11 (the Rabi oscillations are slightly longer in the new scan, ~ 13 ns vs. 11 ns). However, when examining the signal from FIDs under a magnitude Fourier transform, we observe that the location of the peak (i.e. the Larmor precession frequency) depends on the pulse length (Fig. 5.12A). Note that the IF frequency of 500 MHz corresponds to 240 GHz (due to mixing the signal down). These shifts are unexpected in the experiment as the Larmor precession frequency should only depend on the applied magnetic field

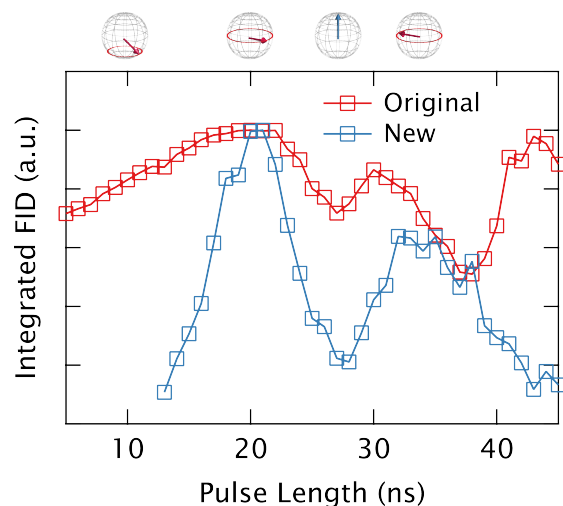


Figure 5.11: Reproduced Rabi Oscillations. The signal magnitude of FIDs is shown as a function of pulse length in a single pulse measurement comparing original data (from Fig. 5.6) to a new trace. Characteristic Rabi oscillations are observed (as described with the Bloch spheres above the figure), and are consistent between the two traces (with a slight change in the Rabi frequency, due to different FEL powers).

(B_0). However, the frequency shift observed is substantial (shown in Fig. 5.12B) and covers around 10 MHz, which would correspond to a field shift of ~ 0.2 mT (the linewidth of the absorption spectrum is only ~ 0.5 mT, corresponding to the ~ 0.2 mT peak-to-peak width in Fig. 5.5). The cause of the shift can be determined by the period of the oscillation, which is found to be twice the frequency of the Rabi oscillation as shown in Fig. 5.12B. Therefore, the largest shift in frequencies is observed at the same pulse length as the inversion pulse, which corresponds to the largest change in sample magnetization. This implicating the paramagnetic magnetization of the sample as driving the shifts in Larmor precession frequencies.

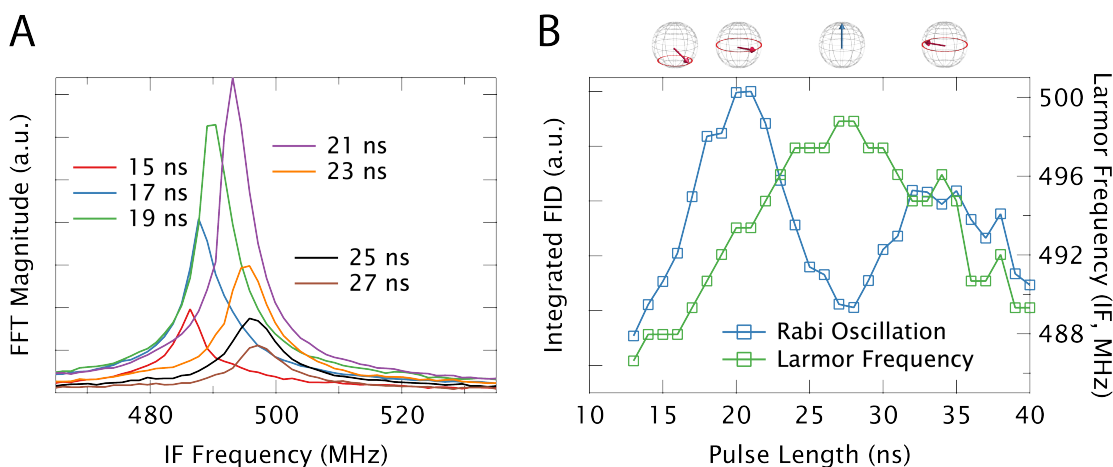


Figure 5.12: Dependence of Larmor Frequency on Pulse Length. **A.** The magnitude FFT of the FIDs from a series of one pulse measurements using the FELEPR. The shifting Larmor frequency is not typically expected, as the oscillation should only be determined by the static field. **B.** The Larmor frequency is plotted in green and compared to the signal strength (same as the “New” trace in Fig. 5.11) as a function of pulse length. The period of the oscillation in the Larmor frequency is found to be twice that of the Rabi oscillation.

The total sample magnetization results only from the population difference in the spin states. That is, only excess $|\frac{1}{2}\rangle$ spins matter: for every $|\frac{1}{2}\rangle$ with a corresponding $|\frac{1}{2}\rangle$, the net dipole field is zero across the sample. Thus as there is typically only a small excess of spins in the $|\frac{1}{2}\rangle$ state (as given by Eq. 1.5) paramagnetic species tend to have small net magnetization. However, by moving to high fields we substantially increase the polarization of the energy levels (even at room temperature) and can begin to see that effects of the resulting increased magnetization (for instance, at low temperatures the polarization reaches 99% and we can observe spin bath quenching as discuss in Chapter 2). As each paramagnetic spin creates a small magnetic field, there is a (net) paramagnetic field

generated by the spins. Of course, the effect of the the dipole moment of the spins is precisely what is detected for distance measurement (See Chapters 2, 3, and 4). These are the effects of *local* dipolar interactions of the closest neighbors, which leads to broadening effects. The net paramagnetic field here is a sample wide magnetic field induced by the overall aligning of the spins (which follows a Boltzmann weighting for a paramagnetic system). This field can generally be neglected due to the low polarizations and low concentrations of spins; that is, the magnetization and concentrations are generally small enough that the sample magnetization does not contribute to the magnetic field felt by the sample.

However, the undiluted grains of BDPA used in these studies have extremely high concentrations, so that even with the small polarizations ($\sim 2\%$ at 240 GHz and 300 K) encountered at room temperatures, we can expect a sizable contribution from the spins to the magnetic field (here, sizable is related to our resolution of the line, which covers only ~ 0.3 mT, not sizable compared to the static field of 8.5 Tesla). For instance, we can estimate the sample magnetization (which is along the magnetic field)²⁷

$$\begin{aligned} \vec{M}_0 &= -\frac{N}{V} g_e \mu_\beta J B_J \left(\frac{g_J \mu_\beta J B}{kT} \right) \hat{z} \\ B_J(x) &= \frac{2J+1}{2J} \coth\left(\frac{2J+1}{2J}x\right) - \frac{1}{2J} \coth\left(\frac{1}{2J}x\right) \end{aligned} \quad (5.3)$$

where B_J is the Brillouin function, and J is the spin of the system ($J = \frac{1}{2}$), N is the number of spins and V is the volume (i.e. $\frac{N}{V}$ is a number density).

Here we denote \vec{M}_0 as the magnetization in thermal equilibrium. Then, for our BDPA sample the only remaining component is the number density $\frac{N}{V}$, which can be estimated. The molecular weight of BDPA is $MW = 495.63$ g/mol, and assuming that the density is the same as water ($\rho = 10^6 \frac{g}{m^3}$), yields a density of $\frac{N}{V} = 1.21 \cdot 10^{27} \frac{1}{m^3}$, which results in a magnetization of $M_{Z0} = -217 \frac{A}{m}$.

Note that this component of the magnetization is the thermal equilibrium magnetization that emerges from the paramagnetic species. This is distinct from the TOTAL sample magnetization, which would include contributions from the nuclear spins (which like the electron spins are dipole moments and have some magnetic ordering due to Boltzmann statistics), and the magnetization of the diamagnetic electrons (i.e. those in paired orbital or bonds) which responds to the applied field.¹⁹⁰ We have not discussed these components as they are not modulated during the experiment, and thus simply contribute to a static magnetization. The paramagnetic contribution is important precisely because the pulsed EPR experiment rotates the spins, and thus modifies the magnetization during the experiment. For instance, under an inversion pulse the paramagnetic magnetization is flipped ($M_Z = +217 \frac{A}{m}$), and generally, for another pulse both M_X and M_Y components of the magnetization are generated. As the magnetization generates a magnetic field at the sample, modifying the magnetization modifies the applied field (slightly), thus resulting in the differing Larmor frequencies observed in Fig. 5.12.

The calculation of the magnetic field resulting from the sample magnetization is complex and requires precise knowledge of the sample geometry, distribution of spins, and results in a field that depends on position within the sample. However, we make the approximations (following Levitt et al.¹⁹⁰) that the sample is homogeneous and ellipsoidal in geometry, so that the resulting field is given by¹⁹¹

$$\vec{B} = \vec{B}_0 + \vec{B}_{Demag} = \vec{B}_0 + \mu_0 \sum_i \left(\frac{1}{3} - N_i\right) M_i \hat{q}_i \quad (5.4)$$

where B_0 is the applied field, \hat{q}_i are the unit vectors \hat{x} , \hat{y} , and \hat{z} , and the summation is over the indices $i = x, y, z$. The N_i values are called the demagnetization factors, and are controlled by the geometry. The power of the approximation of the ellipsoidal sample is that the resulting expression for B does not depend on location within the sample. The values of N_i can be found in literature,¹⁹¹ by knowing the semi-principal axis lengths a , b , and c . For a sphere, $a=b=c$, $N_X = N_Y = N_Z = \frac{1}{3}$, and thus no effect is observed. For the sample studied here we approximate a roughly circular bottom ($\frac{a}{b} = 1$) and a sample that is $\sim 3x$ thinner than the radius of its based ($\frac{a}{c} = \frac{1}{3}$). For this geometry, $N_X = N_Y = 0.1855$ and $N_Z = 0.62889$. The particulars of these numbers will not be critical, we use them only to demonstrate conceptually reasonable numbers (the number of approximations taken make exact agreement impossible).

If we consider how this will effect the EPR experiment we turn to the Bloch equations, which are differential equations which classically describe the evolution

of magnetization in an applied field. With the Bloch equations we have (neglecting relaxation for the moment)

$$\frac{d\vec{M}}{dt} = \gamma_e \vec{M} \times \vec{B} \quad (5.5)$$

where \vec{B} will be given by Eq. 5.4, but will include the B_1 during the pulses. However, simply by considering Eq. 5.4, we see that we can actually *neglect* the transverse components of the magnetization as they don't affect the evolution of the spins (in this approximation) as

$$\begin{aligned} \vec{M} \times \vec{B}_{Demag} &= \vec{M} \times (\mu_0 \sum_i (\frac{1}{3} - N_i) M_i) \\ &= \mu_0 \vec{M} \times ((\frac{1}{3} - N_X) \vec{M} + (\frac{1}{3} - N_Z - N_X) M_z \hat{z}) \\ &= \mu_0 \vec{M} \times \eta M_z \hat{z} \end{aligned} \quad (5.6)$$

with $\eta = \frac{1}{3} - N_Z - N_X$. Above we have use the fact that $N_X = N_Y$ for factoring, and that $\vec{M} \times \vec{M} = 0$. However, this result means we can rewrite Eq. 5.5 as

$$\vec{B} = (B_0 + \eta M_z) \hat{Z} + \vec{B}_1. \quad (5.7)$$

Which is to say, that under these assumptions the ONLY effect that the magnetization has is to shift the applied field slightly (without an effect from the

transverse fields).¹ This immediately explains the results in Fig. 5.12B, as when no pulse is applied, $M_Z = M_{Z0} = 217 \frac{A}{m}$, and so $\vec{B}_{Demag} = \eta\mu_0 M_z \hat{z} \approx -.13 mT$, which corresponds to the Larmor frequency observed for short pulse lengths (i.e. $\omega_0 = 486$ MHz). As longer pulses are used, we can write $M_Z = M_{Z0} \cos(\beta)$. Thus, for $\beta = \frac{\pi}{2}$ $\vec{B}_{Demag} = 0$, which corresponds to the frequency at full excitation (i.e. $\omega_0 = 491$ MHz) and when $\beta = \pi$ a maximum frequency ($\omega_0 \sim 498$ MHz) is reached as $\vec{B}_{Demag} \approx .13 mT$. The total change in Larmor frequency should then be $2\vec{B}_{Demag} \approx 0.26 mT$, while the data shows a total shift of ~ 12 MHz $\sim 0.42 mT$. Given the roughness of the approximation of the density of the sample and the sample geometry, the agreement is then quite good. This helps confirm that the source of the Larmor shifts observed during the Rabi oscillation experiment is from a demagnetization effect.

The connection of this to the *shape* of the Rabi oscillation experiment is not as easily derived. The process of tipping the spins, which in turns modifies the Larmor frequency, can lead to complex dynamics. In NMR these effects have even been studied as they give rise to “spin turbulence” and chaotic dynamics.¹⁹² These effects emerge fundamentally from the nonlinear nature of the Bloch equations when we include a magnetization-dependent field in Eq. 5.5. To address the effect of this on the Rabi oscillation experiment, we therefore carried out simulations of the experiments by carrying out numeric integration of the Bloch equations using

¹We notice that if $N_X \neq N_Y$ then this statement is no longer true. Further work is necessary to establish the effect of this on the spin evolution.

a differential equation solver in Matlab. Generalizing from the well known Bloch Equations in the rotating wave approximation¹⁵ we can include the effect of the magnetization and solve the coupled differential equations

$$\begin{aligned}
 \frac{M_x}{dt} &= (\omega_0 - \omega - \eta M_z)M_y - \gamma_e M_z B_y - \frac{M_x}{T_2} \\
 \frac{M_y}{dt} &= (\omega_0 - \omega + \eta M_z)M_x + \gamma_e M_z B_x - \frac{M_y}{T_2} \\
 \frac{M_z}{dt} &= \gamma_e (M_x B_y - M_y B_x) - \frac{-(M_z - M_0)}{T_2}
 \end{aligned} \tag{5.8}$$

In order to *best* describe the data we used the experimental data to determine any unknown parameters in the model. The resulting Rabi oscillations are shown in Fig. 5.13. As shown in green, when the effect of the magnetization is neglected (for instance, with $\eta = 0$ in Eq. 5.8) the FID magnitude shows a “proper” Rabi oscillation, which approaches zero using an inversion pulse. When we introduce the magnetization term, and fix the intensity to be $2|B_{mag}| = 0.42 \text{ mT} = 12 \text{ MHz}$ (based on the data in Fig. 5.12) we find that the Rabi oscillation becomes distorted, as shown in red. In particular, we notice that the π pulse does not result in proper inversion, but the 2π pulse does return us to a near minimum. By moving slightly “off resonance” (shown in blue) to partially compensate for the act of driving the spins off resonance with the pulse, we return to a Rabi oscillation nearly identical to the case where the magnetization is neglected. The shift of 0.2 mT ensures that our excitation frequency (which remains fixed even as the Larmor frequency shifts), is positioned in the middle of the range of Larmor frequencies

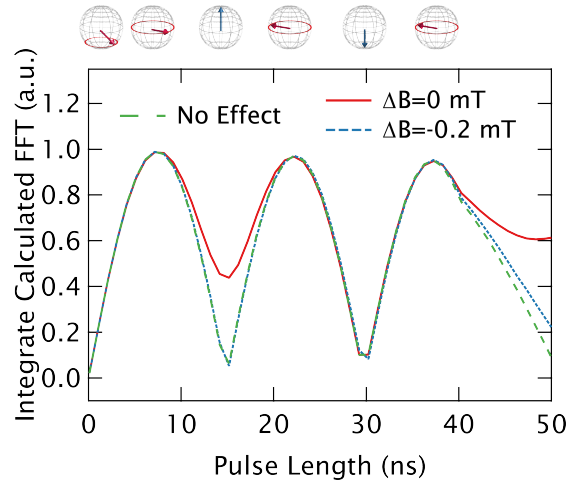


Figure 5.13: Calculated Rabi Oscillations. The total transverse magnetization in a Rabi oscillation experiment, based on numeric integration of the Bloch Equations. Normal oscillations are observed when the effect of sample magnetization is neglected (dashed green). Alternatively, when the effect is included (from experimental data), the oscillations change, and the π inversion does not return towards zero (in solid red). However, moving slightly off resonance, to compensate for the dynamically changing magnetization under the pulses, the Rabi oscillation recaptures most of its original form.

that are accessed (rather than on an edge). In comparing the experimental results for the Rabi oscillation (Fig. 5.10) we see that the calculations in Fig. 5.13 describe the asymmetry observed during inversion pulses (π and 2π), as well as the return of symmetry (that of the normal Rabi oscillation) that results from working off resonance.

Thus, we can understand some of the discrepancies in the data based on the effect of the demagnetization shift occurring in the sample *during* the pulses. Some discrepancies remain in the experimental Rabi oscillation data of Fig. 5.10. For instance, even when working off resonance, and observing the proper inversion

pulses, the intensity of the second peak (at ~ 30 ns, associated with the $\frac{3\pi}{2}$ pulse) is weaker than the first (at ~ 20 ns, associated with the $\frac{\pi}{2}$ pulse). This suggests that there is still a component of B_1 inhomogeneity, which is acting to damp the Rabi oscillation. Further, in general, only several oscillations are visible in the data taken here, where in principle the oscillation should continue until it is damped out either by B_1 inhomogeneity or T_2^* effects. This is still not fully understood, and there may be additional effects associated with the magnetization shift discussed above which are absent in calculations due to the approximations used (for instance, the ellipsoidal sample), and so further work remains.

5.5 Future of FELEPR

Once adapted to perform properly as a pulsed EPR source, the Free Electron Powered-EPR (FELEPR) spectrometer represents a major step forward in ultra-fast, high-field EPR. This opens the door to studies of faster relaxing systems, and at higher temperature that had been possible in the past. Further, as FELEPR is the first high-powered EPR spectrometer at this field, it offers a critical tool for testing and developing methodology of high-field EPR. For instance, while the study of the demagnetization shift appears a minor note, it proved critical in understanding the simplest of experiments: the Rabi Oscillations. Because no one had done these sorts of experiments with such high powers at these fields, it took dedicated investigation to identify and unravel the source of these effects.

This highlights the wide ranging “new ground” that is being investigated, and the need for practical explorations of the techniques. While currently the FELEPR is a unique instrument in the framework of EPR spectrometers, we expect that improving source technology and ongoing innovation will eventually allow high-powered EPR spectrometers based on other sources; it is hoped that the work of the FELEPR generates both motivation, as well as technique-based knowledge for the expansion of high-powered, high-field EPR.

Chapter 6

Phase Cycling the FELEPR

Material in this chapter, including figures and some detailed experimental information for this work in Appendix A, are originally published in Ref. 193 (available online), and are reproduced by permission of the PCCP Owner Societies.

6.1 Introducing Phase to the FELEPR Experiment

The previous chapter (Chapter 5) addresses how the millimeter (mm)-wave Free Electron Laser (FEL) at the University of California at Santa Barbara (UCSB) can be used as a transformative solution to the dearth of power that is typical in a high-field, pulsed EPR spectrometer. A spectrometer offering broadband, fast excitation pulses at these frequencies opens up new opportunities, such as the capability to study biological systems at temperatures above 200 K, where the rapid spin relaxation times are the roadblocks for studies with low-power EPR

spectrometers. Further, this instrument offers an important first platform to learn, test, and improve key technologies and methodologies of high-power, pulsed EPR above 100 GHz.

Thus, while the spectrometer is operational and capable of one- and two-pulse measurements, development is ongoing to expand its capabilities. While the FEL offers extremely high powers at these frequencies, it does not offer all the advantages that a high-power amplifier might. In particular the FEL does not allow for the direct locking of the detector reference phase to the source. Although the FEL is injection-locked to a frequency- and phase-stable, solid-state source, this only ensures that the FEL lases exclusively on a single longitudinal mode of the cavity, but does not lock the phase to that of the injection source. Thus, the phase of the FEL pulse, and therefore also the phase of the EPR signal, varies from pulse to pulse. In the absence of a stable phase reference it is therefore necessary to measure the signal magnitude, effectively discarding the advantage of phase-sensitive measurements. This explains why the work in Chapter 5 is done with magnitude detection: the detector phase was not properly (or consistently) defined. Further, without a stable pulse phase, it is impossible to implement phase cycling that would be crucial to increase signal quality and remove artifacts (further improving the overall sensitivity), as well as dramatically expand the versatility of possible pulse sequences.^{194,195} Fortunately, the new developments described below demonstrate that not only can FEL-powered EPR spectra be

collected phase coherently, but the phases of both pulses can be effectively tuned and independently modulated.

In this chapter, we present a two-fold approach to achieve effective phase cycling for pulsed EPR using an FEL source by first utilizing post-processing to define a reference phase, and then modifying the relative phase of two pulses with dielectric materials. The direct measurement of the applied pulse allows for the phase of the spectra to be retrospectively corrected and accumulated phase-coherently. By collecting the full information of the pulse digitally, this improves on a previously published approach where the pulse was mixed down in hardware and used to generate a trigger signal to lock the reference phase to the pulse phase.¹⁷⁵ We demonstrate that as the reference oscillator is not locked to the injection source, we achieve a stochastic phase cycling when many scans are accumulated, as the relative phase of the FEL pulse and detector is random and samples all possibilities. This approach is shown to eliminate several artifacts as the random phase cycling—in the limit of many pulses—is comparable to the CYCLOPS (CYClical Ordered Phase Sequence) phase cycle that is included in virtually all phase sensitive magnetic resonance experiments.¹⁹⁶ For a weak signal, we show that coherent signal averaging allows us to extract a signal that was entirely obscured by noise in a single scan. When adding a second FEL pulse to the EPR experiments, we demonstrate the ability to determine the relative phase of the two pulses by measuring the oscillation in signal intensity as a function of

the field offset from resonance. Furthermore, we demonstrate that a $\sim 200 \mu\text{m}$ piece of silicon, when inserted into the path of one pulse, shifts the relative phase of the two pulses by roughly 180° , indicating that the relative phase of the pulses can be stepped by a fixed amount determined by the properties of the dielectric material. Finally, either by using a dielectric material or by making small changes to the quasi-optical path length, we show that the relative phase of the two pulses can be tuned to a precise value. These approaches, undertaken together, present a generally applicable methodology to carry out full phase cycling of microwave pulses to suppress undesired signal and optimize pulse sequence performance using any high-power source with stable frequency.

6.2 Locking Detector Phase to FEL Pulse

For these experiments a BDPA grain was used as a sample, the magnetic field was centered at the BDPA resonance ($\sim 8.58 \text{ T}$), and a single pulse measurement was carried out as shown in Fig. 5.4A and described in Sec. 5.2.5. The phase correction procedure (described below) was carried out on the traces through post-processing analysis using the software Igor Pro (Wavemetrics), though it has now been directly implemented in the measurement software (Labview 8.0, National Instruments Corporation) to carry out the correction during measurements. In order to demonstrate the stochastic phase cycling approach, a large series of traces were measured with identical pulse settings on a sample with strong signal from

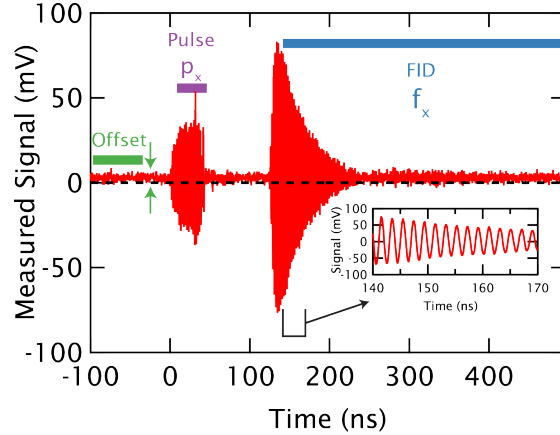


Figure 6.1: Typical Time Domain Trace for Single Pulse FELEPR. The time domain trace of the real component of a single pulse experiment is shown with the background offset, pulse region (p_x) and FID (f_x) region highlighted. The inset shows the signal oscillating at the IF frequency of ~ 500 MHz.

BDPA. For these measurements the ~ 35 ns long pulse from the FEL was followed by a ~ 80 ns delay before the detector switch was fired, and 360 ns of the FID was recorded. A 30 dB attenuation in the 10 GHz stage detection was used to avoid saturation of the electronics. Some further experimental details can be found in Appendix A.

The original data set, recorded directly from the digitizer, consists of $N_{tr} = 993$ complex traces $s_k = s_{kx} + \imath s_{ky}$ (with $1 < k < N_{tr}$) of 4096 points with real and imaginary parts s_{kx} and s_{ky} . Each trace contains a pulse region ($p_k = p_{kx} + \imath p_{ky}$) and an FID region ($f_k = f_{kx} + \imath f_{ky}$). Before the beginning of the pulse, the trace should ideally be zero (plus noise), however due to receiver offsets of the two channels, both the real and imaginary parts of the traces have a DC offset. The real component of a typical time domain trace is shown in Fig. 6.1, where the pulse

and FID regions are highlighted and the DC offset indicated. The spectrometer uses a 500 MHz intermediate frequency, which corresponds to the oscillations seen in the pulse and FID regions of the trace.

6.2.1 Correction Procedure

Our approach to analyzing and correcting for the varying phase of the FEL pulses is broken down into 4 simple steps.

Step 1: Baseline correction. The first step is to remove the baseline offset of the real and imaginary parts of each trace. The baseline offsets were determined from the experimental data by averaging the first 500 points (i.e. the part before the beginning of the pulse) separately for the real and imaginary parts of each trace. This estimate for the baseline offset for each trace is subtracted before continuing.

Step 2: Determination of relative pulse phases. The (complex) data points $p_k = p_{kx} + ip_{ky}$ representing the pulse are extracted from each (complex) trace s_k . The number of data points selected is chosen to cover the entirety of the pulse while avoiding the rising and falling edges. For this demonstration, the pulse region covered 30 ns (150 points, from 1650 to 1800). The phase of the pulses is not stable from pulse to pulse, as demonstrated in Fig. 6.2A, where the real parts of the FFT of five pulses ($P_k = \text{FFT}[p_k]$) taken within ~ 30 seconds of each other

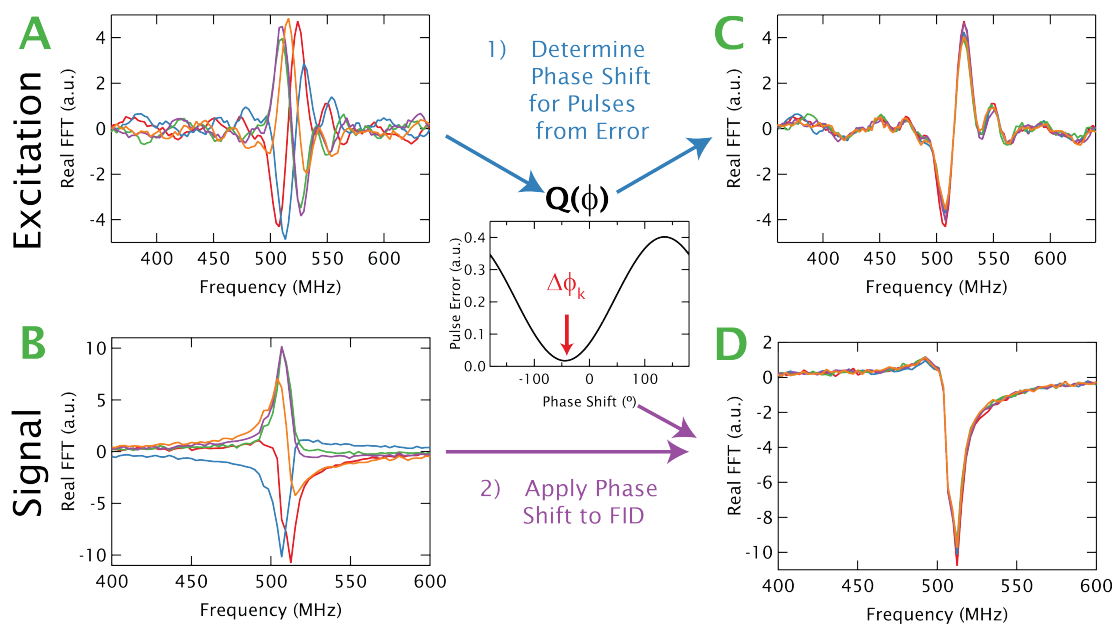


Figure 6.2: Retrospective Correction of Phase. **A:** The real part of the FFT of the FEL Pulse for several different pulses (taken within ~ 30 seconds of one another) shows fluctuating phases, as expected from using an unlocked detector. **B:** By calculating the phase shift $\Delta\phi_k$ (shown in the center of the panel) for each pulse relative to the first pulse, the pulses can be corrected to show consistent phase. **C:** The real parts of the FIDs, corresponding to the pulses in A, are shown to also have varying phases. **D:** The application of the same phase shifts $\Delta\phi_k$ to the FIDs yields a consistent phase for each spectrum. A subsequent, common phase shift could be applied to all the traces to achieve a normal, absorptive spectrum.

are shown. The first pulse is taken as a reference to determine the relative phase of each subsequent pulse, using the following procedure.

We calculate the function

$$Q(\phi) = \sum_{l=1}^{N_p} |e^{-i\phi} p_k(l) - p_1(l)|^2 \quad (6.1)$$

for $-180 \leq \phi \leq 180$, where N_p is the total number of points in p_k . The minimum of $Q(\phi)$ provides an estimate of the phase shift $\Delta\phi_k$ of the k^{th} pulse relative to the phase of the first pulse. The center of Fig. 6.2 shows a typical error function, $Q(\phi)$, and the minimum value is indicated as $\Delta\phi_k$. This approach yields a phase shift that, when applied to the pulses ($p'_k = e^{-i\Delta\phi_k} p_k$), ensures the phase for each pulse agrees. Fig. 6.2B shows that the corrected pulses have identical real components of their FFT ($P'_k = \text{FFT}[p'_k]$).

Step 3: Each FID is phase corrected and Fourier transformed. The (complex) FID $f_k = f_{kx} + i f_{ky}$ is extracted from each (complex) trace s_k . As with defining the region of the pulse, the FID region depends on the experiment, and is selected to avoid the distortion present during the activation of the detector. Here the FID region covered 353.2 ns (1766 points, from 2330 to 4096). As the phase of the FID is determined by the phase of the pulse, it is not stable from scan to scan as shown in Fig. 6.2B with the real parts of five spectra (i.e. the FFTs of the FID: $F_k = \text{FFT}[f_k]$) corresponding to FIDs measured from the five pulses shown in Fig. 6.2. Each (complex) FID is multiplied by the phase factor $e^{-i\Delta\phi_k}$

($f'_k = e^{-\Delta\phi_k} f_k$) to correct for the phase shift $\Delta\phi_k$ of the k^{th} pulse relative to the first pulse. This makes all FIDs f'_k phase coherent. After Fourier transformation, each phase corrected FID f'_k results in a spectrum ($F'_k = \text{FFT}[f'_k]$) in which the signal has the same phase (up to errors in the determination of $\Delta\phi_k$ in step 2). Following these phase shifts, we find that the five spectra now offer identical, real FFTs as shown in Fig. 6.2D.

Step 4: Calculate average spectrum. The spectra $F'_k(\nu)$ (for $k = 1, \dots, N_{tr}$) can now simply be added to form the average spectrum:

$$F'(\nu) = \frac{1}{N_{tr}} \sum_{k=1}^{N_{tr}} F'_k(\nu). \quad (6.2)$$

The resulting average spectra can then be manipulated as necessary. For instance, the signals shown in Fig. 6.2D are all phased identically, but are not phased so that the real component is the pure absorptive signal. A subsequent 0-order phase shift can be applied to the averaged spectrum to yield the absorptive shape, and higher-order phase corrections are possible as well. For instance, a phase that is linear in frequency can be applied to eliminate the characteristic phase problems associated with a non-zero deadtime. The data presented in Fig. 6.2D are part of a larger data set, and the averaging and advantages of the stochastic phase cycle are addressed in Section 6.2.3.

6.2.2 Screening Pulse Quality from the FEL

A potential problem that arises from the use of the FEL as a source for EPR is the sporadic instability of FEL pulses. Due to slight variations in electron-beam tuning, electronics, and changes in ambient conditions, the FEL occasionally fails to fire, fires weakly, or fires at a slightly different frequency. Clearly such instabilities affect the corresponding FIDs. A convenient extension of the determination of the phase shift is the ability to observe the consistency of the FEL pulses through the properties of the error function $Q(\phi)$. If each of the pulses p_k are truly identical except for a phase difference, then it should be possible to perfectly match them with a phase shift (up to the noise in the traces). Thus, we expect the minimum value of $Q_{min}(= Q(\Delta\phi_k))$ to be close to zero, and a deviation from this indicates that for pulse p_k , the FEL fired differently than it had for other pulses. When the FID is sufficiently strong to be seen in a single scan, we can also quantify the consistency of an individual FID with respect to the first FID (taken as a reference, and assumed to be a representative signal) by calculating the modified error function for the FID

$$W(\phi) = \sum_{l=1}^{N_p} |e^{-i\phi} f_k(l) - f_1(l)|^2. \quad (6.3)$$

Low values of $W_{min}(= W(\Delta\phi_k))$ indicate that the k^{th} FID is identical to the original FID (f_1) up to a phase factor, whereas larger values suggest that the frequency or amplitude of the FID is different from the reference FID. Fig. 6.3

shows a plot of W_{min} against Q_{min} (each normalized by the number of points in the FID and pulse respectively) for all 993 traces in the full data set. As expected, we find that pulses which are dissimilar to the original pulse (with larger Q_{min} values) lead to changes in the FID (with larger W_{min}). We can then retrospectively eliminate scans with pulses displaying large Q_{min} values. The inset of Fig. 6.3 shows three magnitude FFT spectra compared to the original signal (in purple) to demonstrate discrepancies in the FID shapes. For this data set we chose a cut off marked by the hatching on the plot, eliminating 103 traces ($\sim 10\%$) as having unacceptably large error. The choice of $Q_{min} \sim 20 * 10^{-5}$ as a cutoff was based on eliminating dissimilar pulses without discarding extensive amounts of data. More careful analysis may help identify an optimized cutoff, and this is discussed further in Section 6.2.5.

6.2.3 Stochastic Phase Cycling

When the $N_{tr} = 890$ traces that remain after screening for the quality of the excitation pulse are taken in succession, the relative phase, $\Delta\phi_k$, of each pulse is found to be effectively random. The average of all the phase vectors ($= \frac{1}{N_{tr}}(\sum_k \cos(\Delta\phi_k), \sum_k \sin(\Delta\phi_k))$) is found to be (0.011,-0.029). As this is a small remnant, it indicates the pulses at least approximate a random sampling of phases. This variation of the pulse phase, when corrected, can be used to act as a random phase cycling, achieving cancellation of spectral artifacts that emerge.

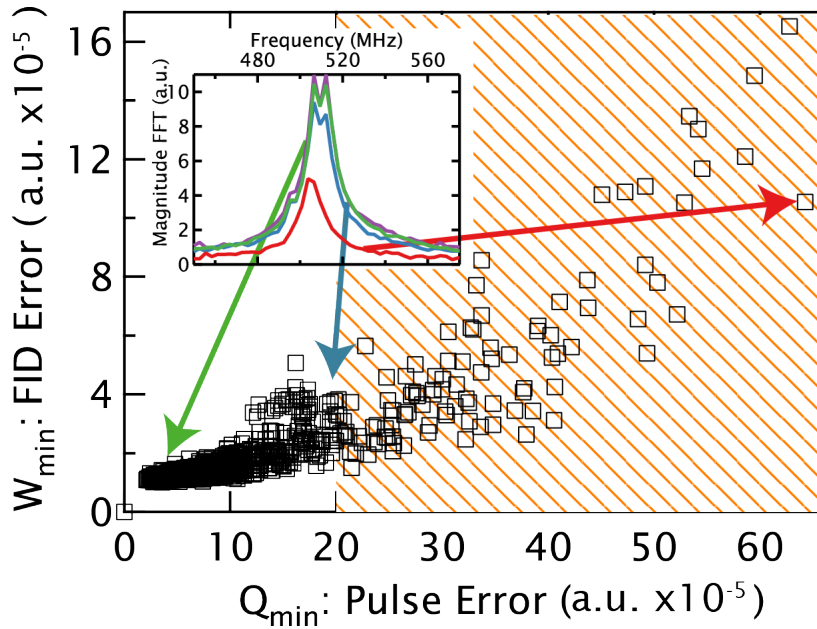


Figure 6.3: Eliminating Inconsistent FEL Pulses. The best-fit error values for the FID (W_{\min}) are plotted against the best-fit error values for the pulse (Q_{\min}). High error values indicate that the pulse (or FID) differs from the first, reference pulse (or FID) by more than a simple phase shift. By excluding traces with large pulse deviations (shown in orange hatching), we improve the quality of the data by not allowing 'misfires' of the FEL to affect the data. Inset: The inset shows representative spectra from low, medium and large pulse errors (green, blue, and red lines respectively) compared with the original FID (purple line).

The magnitude spectrum of a single, raw FID is plotted in Fig. 6.4A and shows three features: the signal at frequency $\nu=500$ MHz, a transmitter spike at frequency $\nu=0$ MHz, which emerges due to the DC offset in the time-domain data, and a mirror peak located at frequency $\nu=-500$ MHz due to imbalances in the detector hardware. In the absence of phase corrections, the only approach for averaging the spectra is by averaging the magnitude of the individual spectra (i.e. $F^{mag} = \frac{1}{N_{tr}} \sum_{k=1}^{N_{tr}} |F(\nu)_k|$). This neglects the phase parameter entirely, but does allow us to improve the signal-to-noise ratio of the spectrum. However, when the uncorrected signal is added up in magnitude mode, both the transmitter spike, the mirror peak, and any consistent spectral artifacts remain as they also add up constructively with the signal (Fig. 6.4B, red). By comparison, these spurious peaks are eliminated entirely when the full process of phase-coherent averaging is applied (Fig. 6.4B, green). Finally, in order to highlight the elimination of spurious signal as a result of the cycling of the pulse phase, we present the results of the same data processing, only without initial elimination of the DC-offset (i.e. step 1) (Fig 6.4B, blue). In this case, the transmitter spike is still averaged to nearly zero, without the aid of elimination of the DC-offset.

We calculated the signal-to-noise ratio (SNR) of the real component of a single trace to be $\text{SNR} \approx 204$. When the $N_{tr} = 890$ spectra are average phase coherently, the SNR of the real spectrum is found to be $\text{SNR} = 5669$. The noise level in the real spectrum (characterized by the standard deviation far from resonance),

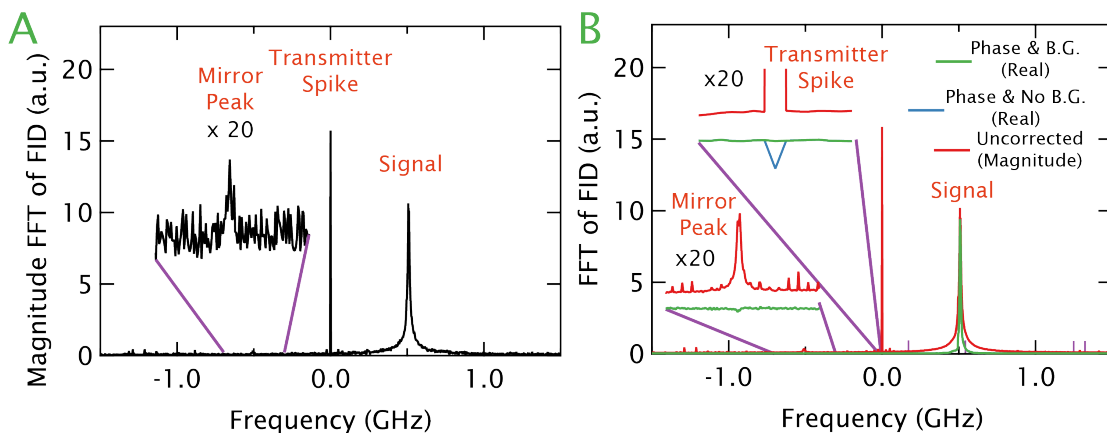


Figure 6.4: Phase Cycling to Eliminate Artifacts. **A:** A single magnitude FFT spectrum, showing three features: the FID signal, a transmitter spike and a mirror peak. **B:** Comparison of 3 approaches to signal averaging. The uncorrected averaging (red) is done by simple averaging the one-shot magnitude spectra, and does not eliminate any artifacts. When the real component is plotted in the case of both phase correction and background subtraction (“Phase & B.G.”, in green), both the transmitter spike and the mirror peak are eliminated. For demonstration, we also carry out phase correction without background subtraction (“Phase & No B.G.”) in blue (again showing just the real component) to demonstrate that even without background subtraction, the phase cycling efficiently averages the transmitter spike towards 0 in the limit of many pulses. Additionally, as expected, the real component of the signal, plotted after phase correction, produces a substantially narrower resonance than the magnitude spectrum.

is found to be reduced by a factor of ~ 29.6 , which is consistent with $N_{tr} = 890$ ($29.6^2 = 876$). For comparison, when the spectra are magnitude averaged small, but consistent detector artifacts, spaced by 25 MHz, are present in the spectra (visible in Fig. 6.4B in the expanded view of the mirror peak). Therefore, when we examine the noise level based on the variance far from resonance (now, necessarily, measured from the magnitude, not real, spectrum) these artifacts contribute to this noise estimate, though they are not random noise. As these artifacts add constructively in the case of magnitude averaging (but are eliminated in phase coherent averaging), they dominate the attempt to estimate the noise level, and averaging appears to reduce the noise level only by a factor of ~ 2 . When these artifacts are removed by hand the estimated noise level drops substantially and better reflects the 'true' noise level due to random noise. Thus, magnitude averaging successfully reduces the random noise in the spectrum, but does not affect consistent detection artifacts, which, even when small, can obscure the signal.

The reduction in spurious signals results directly from correcting for the random phase of the pulses. The phases of the receiver artifacts are independent of the pulse phases, so when the phase of each FID is corrected to add coherently, the artifacts now add destructively. This is conceptually similar to the CYCLOPS pulse sequence, where the pulse and receiver phase are cycled 4-times, shifting by 90° at each step.¹⁹⁶ This causes artifacts from imperfect detection hardware (such as DC-offsets, as well as receiver amplitude and phase mismatches) to perfectly

cancel after all four steps. The stochastic phase cycling achieves the same result in the limit of many measurements, but is not as efficient (in requiring many pulses), as we cannot pick the phases of each pulse to sample the required four, 90° phase shifts. Fig. 6.4B also clearly demonstrates a further advantage of phase sensitive detection, namely the pure absorptive spectrum is substantially narrower than the comparable magnitude spectrum, providing better spectral resolution.

6.2.4 Expanding Spectrometer Sensitivity with Coherent Averaging

For strong signals, it is easy to distinguish the signal from artifacts in the spectrum, allowing for improved quality spectra to be generated by simply averaging the magnitude spectra. In such cases, the advantages of phase-correction emerge from the stochastic phase cycling and the ability to access information that is carried in a particular signal phase. However, it is more typical to measure weak signals, where the signal may not be visible in a single scan. In these cases, coherent averaging leads to substantially clearer spectra.

This is demonstrated by taking a series of $N_{tr} = 223$ traces where the BDPA FID was intentionally weakened, so that a single spectrum showed no signal. This one-pulse measurement utilized a ~ 35 ns long pulse from the FEL, followed by a ~ 180 ns delay between the end of the pulse and the activation of the detector, and the FID was recorded ~ 280 ns after the detector switch was activated. The pulse

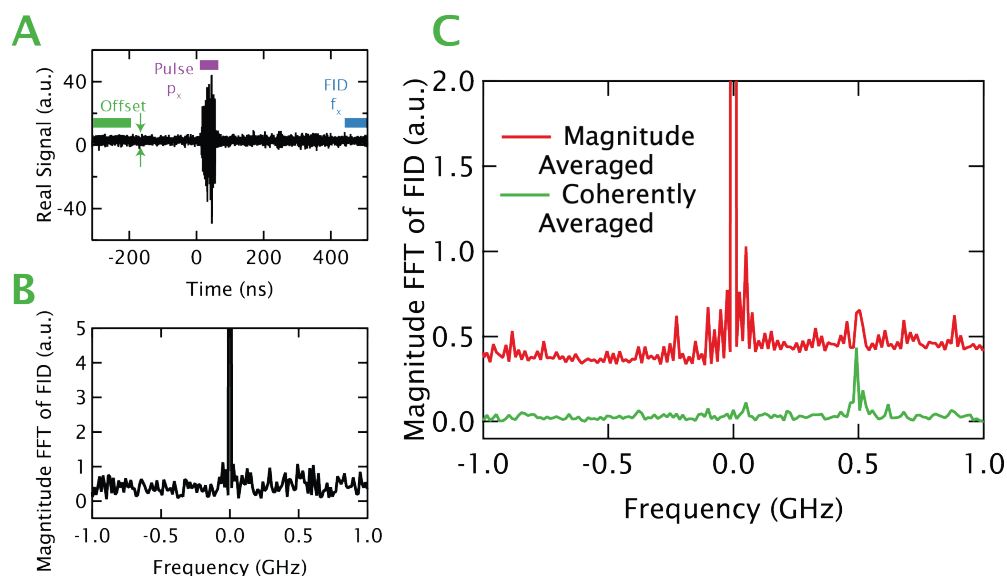


Figure 6.5: Improved Sensitivity with Phase Cycling. **A:** The time domain FID from BDPA with the signal intentionally attenuated and with the FID recorded long after the pulse. **B:** The resulting FT spectra from a single scan shows no clear signal at 500 MHz, though a 0-frequency peak remains from the background offset. **C:** The averaging of magnitude spectrum of each of the 223 scans is compared to the magnitude of the phase coherently averaged spectra of the same 223 scans. While a feature is present at 500 MHz in the magnitude averaged spectra, it is not substantially larger than noise features. The coherent averaging presents a clear 500 MHz peak, demonstrating the capability to pull very small signals from the noise even in cases where no signal is visible in an individual scan.

region (p_k) for these measurements was 30 ns (150 points, from 1650 to 1800), but the FID region covered only the final 79.2 ns of the trace (396 points, from 3700 to 4096). The signal was attenuated by 45 dB at the 10 GHz stage in order to reduce the signal. No screening was applied to eliminate sub-optimal FEL pulses. Fig. 6.5A shows the time domain trace of a single scan; there is no signal visible nor is there any in the FFT spectrum shown in Fig. 6B. Utilizing simple magnitude averaging leads to a spectrum where the signal is difficult to discern from surrounding features, even after >200 scans. Alternatively, in the case where the signal is coherently averaged by applying the phase correction protocol, the spurious signal is reduced and the desired signal distinct from the background. The two cases are compared in Fig. 6.5C.

6.2.5 Impact of and Considerations for a Coherent Detector Phase

The extension of spectrometer sensitivity through coherent-averaging of spectra, and the reduction in receiver artifacts through phase cycling dramatically improve the capabilities of the spectrometer. The high-power, short pulses possible with the FEL-EPR already dramatically expand both the sensitivity and time resolution of pulsed EPR above 100 GHz. The ability to more readily isolate the signals from noise and artifacts will further improve the capacity to measure samples with short relaxation times, and therefore broader lines and weaker signal.

Additionally, although work is underway to minimize the spectrometer dead-time, the improved sensitivity reduces the extent to which the dead-time limits the capabilities of the FEL-EPR. As low temperatures are commonly used to lengthen relaxation times and increase signal intensity, these developments improve the capability of measuring spin-labeled biological systems at temperatures closer to their biologically viable condition ($>200\text{K}$), where many biomolecular systems begin to explore their conformational space.^{143–145} Finally, the absorption spectrum offers a narrower line than the magnitude spectrum, as demonstrated in Fig. 6.5C, which further improves the spectral resolution available at high fields.^{20,197}

In the case of this chapter, the processing was carried out separately from the collection of data, but it is greatly preferable to have access to the properly phased spectra during data acquisition. The ~ 1 Hz repetition rate of the FEL makes the implementation of “real-time” correction during measurements easy, and has now been implemented into the data acquisition software. As one pulse is used as a reference to phase subsequent spectra and screen subsequent pulses, it is important for the reference to be a faithful representation of the other pulses. The current approach simply uses the first experiment as the reference, and this approach is necessary for phase correction carried out during the experiment. However, this is susceptible to problems if the first pulse is not consistent with the majority of the other pulses (i.e. the reference that is chosen is itself a bad pulse). This can, of course, be screened by eye and the second experiment used for the reference in the

case of a problem. An alternative is to use post-processing to choose a reference that is a good match to the greatest number of other pulses, while still using the current approach during collection as a rough phase correction. A further alternative is to directly measure the frequency of a pulse and use the function $\exp(i\omega_{meas}t)$ as the reference in post-processing, which would eliminate problems emerging from noise and artifacts in the reference pulse.

The improvements of the spectrometer capabilities for coherent signal averaging are important, but the capability to measure, correct for, and control the pulse and signal phase offers a fundamental improvement to FEL-powered EPR experiments. This approach allows some of the limitations of the FEL source to be minimized or eliminated entirely. We demonstrate that by screening the consistency of the FEL pulses we can improve the reproducibility of spectra by only collecting (or processing) spectra emerging from proper pulses. Thus, for practical purposes the FEL pulses become identical (except for phase), just as the output of an amplified solid-state source is expected to be repeatable. This also allows the opportunity for more advanced screening, for instance recording the strength and frequency of each FEL pulse for reference.

Determination of the cutoff level for discarding experimental misfires was done empirically in this chapter, but can be further rationalized, though the details of the choices may depend strongly on the specific experiment. Based on the assumption (supported by Fig. 6.3), that the majority of pulses (and therefore FIDs) are

consistent, the effect of varying the cutoff is to slightly vary the consistency of the FIDs. A larger cutoff would admit more pulses not matching the original pulse, causing some reduction in the signal due to cancellation in averaging as a result of slightly differing magnitude and phase of the FID. However, the shape or phase of the averaged signal could be systematically affected if a number of the high-error pulses differed from the original pulse in the same way. In such a case, identifying all the erroneous pulses would become an important part of signal processing. A smaller cutoff has the disadvantage of discarding data and thus slowing the process of data collection.

While hardware based techniques could be used to discard FEL misfires, the post-processing approach is preferable as it allows the criteria for these cutoffs to be further modified and optimized after data acquisition. Further, the preservation of the complete data set allows us to diagnose the cause of systematic problems and identify methods for improvements. Nonetheless, some simple hardware cutoffs could be implemented in cases where, for instance, the FEL fails to fire, which would reduce or eliminate the occurrence of “empty” data sets.

An additional advantage of this retrospective processing is the ability to accurately set the receiver phase to allow specific measurement of the in-phase and out-of-phase components. This allows us to selectively measure the in-phase or out-of-phase signal (or any combination of the two), so that we can properly combine signals for more advanced two-pulse phase cycles. Without this capability,

signals could only be combined in magnitude mode, preventing cancellation of spurious signal when utilizing phase cycling.

These advantages are not limited to FEL-EPR and they can find use in other spectrometers, where the source is not sufficiently phase stable, or cannot be locked to the detector phase. Indeed, for high frequency EPR spectrometers, where the wavelength is of order several millimeters, very small changes in room conditions can modify path lengths and cause slow (i.e. minutes and tens of minutes) drifts in the reference phase. Therefore, the possibility of measuring and correcting for the pulse phase through the direct evaluation of the pulse may be a generally useful approach to improve phase stability in these situations.

6.3 Measuring and Modifying Relative Phase in the Two Pulse Experiment

While we have been able to address the issue of defining a proper reference phase for each pulse in Section 6.2, in a two pulse EPR experiment the relative phase of the two pulses plays a critical role in the resulting signal. The FEL-EPR pulse slicer utilizes two distinct, physical paths when creating two pulses (see Fig. 5.3A). Thus, we expect that, although the FEL pulse itself has a random phase the two pulses are sliced from the same pulse and so their phases should be related by a fixed relative phase (Δ) determined by the difference in path length. Given that

at 240 GHz the wavelength is ~ 1.25 mm, very small adjustments to the quasi-optical setup are likely to shift this relative path length by a substantial fraction of a wavelength. In order to probe this relative phase, we conduct a simple, two pulse measurement of the FID using tip angles $< 45^\circ$, a pulse separation of 30-60 ns and observe oscillations in the FID intensity as the Larmor frequency is swept

6.3.1 Combined Effects of Offset Frequency and Pulse

Phase for 2-Pulse Excitation

If we neglect relaxation and excitation bandwidth effects and work perfectly on resonance, then no precession occurs in the rotating frame (that is a frame rotating at the frequency of the FEL pulse) during the pulse sequence, as the pulse frequency (ω_{pulse}) matches the Larmor frequency (ω_0). Therefore, the resulting signal depends only on the relative phase of the two pulses and their tip angles. When the pulses are identically phased, they rotate the spins in the same direction and act cooperatively, whereas if the pulses are 180° out of phase the spins rotate in opposite directions, and thus at least partially cancel the effects. Thus, for tip angles of 45° the resulting signal magnitude (or equivalently the transverse magnetization) is maximized for pulses of the same phase, and minimized for pulses of opposite phase. For ideal delta function pulses of tip angle β and σ and relative phase Δ , the magnitude of the transverse magnetization is given by

$$M_{tr} = \sqrt{M_X^2 + M_Y^2} = \sqrt{1 - (\cos(\beta) \cos(\sigma) - \cos(\Delta) \sin(\beta) \sin(\sigma))^2} \quad (6.4)$$

where M_x and M_y are the x- and y- components of the magnetization.

Alternatively, if the field is set so that the spins are off-resonance with the FEL pulse, then the magnetization is no longer stationary in the rotating frame (i.e. $\omega_0 \neq \omega_{pulse}$) and we expect precession to occur during the entire pulse sequence, which rotates the magnetization in the time between the pulses. Therefore, pulses with identical phase may not add constructively as the precession of the magnetization has altered the effect of the second pulse. This may be considered in an intuitive, physical picture as a modification of the “effective phase” of the second pulse, defined as $\Delta^{eff} = \Delta - \omega t$, where $\omega = \omega_{pulse} - \omega_0$ is the angular offset frequency and t is the length of the pulse sequence (as precession will occur during the entire sequence, even during pulses). This effective phase measures the relative orientation of the B_1 field of the second pulse (in the plane) with respect to the orientation of the transverse magnetization component created by the first pulse based on the combined effects of the difference in the pulse phases (Δ), and the precession of the magnetization (ωt). The net effect on the transverse magnetization in the absence of relaxation and the limit of ideal, delta-function pulses of tip angle β and σ respectively is

$$M_{tr} = \sqrt{1 - (\cos(\beta) \cos(\sigma) - \cos(\omega t - \Delta) \sin(\beta) \sin(\sigma))^2} \quad (6.5)$$

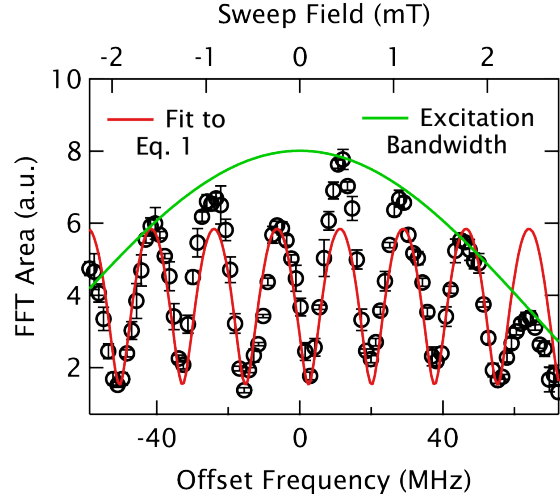


Figure 6.6: Oscillations from Offset Frequency. The integrated absolute value of the FFT is plotted as a function of offset frequency (and field) for the case of a 55 ns spacing between two $< 45^\circ$ pulses. The oscillations can be well described by the model in Eq. 6.5 with a theoretical pulse spacing of 57 ns as shown with the solid, red line. The falloff in intensity likely emerges from the excitation bandwidth, which is estimated in the solid, green line.

This result can be arrived through careful use of generalized rotation matrices by computing

$$\begin{pmatrix} M_X \\ M_Y \\ M_Z \end{pmatrix} = \underbrace{R_Z(-\Delta)R_X(\sigma)R_Z(\Delta)}_{R_\Delta(\sigma)} R_Z(\omega t)R_X(\beta) \begin{pmatrix} 0 \\ 0 \\ 1 \end{pmatrix} \quad (6.6)$$

where R_X , R_Y , R_Z are the rotation matrices about the x-, y-, and z-axes respectively, $R_\Delta(\beta)$ is a rotation of phase Δ and we have, without loss of generality, assumed that the first pulse has a phase of 0 (i.e. is about the x-axis).

6.3.2 Observation of Offset-dependent Modulations of the FID Magnitude

Here we describe a procedure for measuring this relative phase without requiring any post-processing. The two pulses were generated using the lasers as described in Section 5.2.5. The magnetic field was swept through the center of the BDPA resonance (~ 8.58 T) and the free induction decay (FID) at each field value was measured after applying a simple pulse sequence consisting of two $< 45^\circ$, 240 GHz pulses. As the BDPA grain is highly concentrated, the exchange narrowing results in a homogeneous EPR line, and there is no refocused echo. In order to measure the total transverse magnetization, the area under the signal peak in the magnitude Fast Fourier Transform (FFT) of the FID was recorded as a function of the magnetic field. During one of the field sweeps, the Larmor frequency at each magnetic field was also recorded. Some variations from a linear relationship are observed between the Larmor frequency and the magnetic field due to contributions of the large sample magnetization (resulting from the same effect as in Section 5.4), but the variations were small compared to the range of Larmor frequencies accessed. Therefore, the effect was neglected, and a linear fit was used to generate a map from magnetic field to frequency that was used for the other experiments.

Measurement of the two-pulse FID of BDPA shows the modulations in intensity as expected from Eq. 6.5. This is shown in Fig. 6.6 for an experiment with

an interpulse spacing of ~ 55 ns. The best fit to equation Eq. 6.5 is also shown in red. As the tip angle for each pulse is not known, they were freely varied in the fit resulting in $\beta = 16^\circ$ and $\sigma = 9^\circ$. However, in the case where the tip angles are $< 45^\circ$ (as in this case), the tip angles only affect the depth of the oscillation and do not affect the phase or frequency. Therefore, the determination of the tip angles is not critical, though their size relative to each other controls the depth of the oscillation. Neglecting the effects of finite pulse lengths, we find excellent agreement with an interpulse spacing fit value of 57 ns. Given that the nominal pulse spacing of 55 ns was calibrated 'by eye' and Eq. 6.5 neglects the pulse lengths (during which time precession still occurs), this is a realistic result for the pulse spacing. The fit to Eq. 6.5 also fails to account for the effects of relaxation and the effect of finite excitation bandwidth, which likely accounts for the experimental profile. We roughly estimate that our pulses are ~ 10 ns long (neglecting the effect of pulse rise and fall times). If we approximate the excitation bandwidth of a single 10 ns pulse by examining the transverse magnetization calculated through numeric integration of the Bloch Equations, we find that the shape of the excitation bandwidth describes the envelope of the oscillation profile well.

As expected from Eq. 6.5, the period of oscillations is found to clearly depend on the interpulse spacing. This can be seen for a series of experiments in Fig. 6.7, where several traces covering nominal interpulse spacings of 30-55 ns are shown

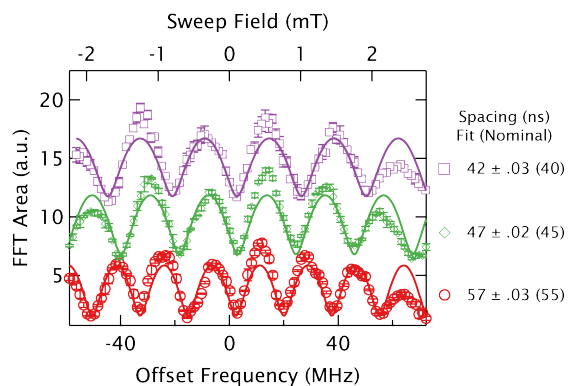


Figure 6.7: Effect of Interpulse Spacing on Oscillation Frequency. The experiment shown in Fig. 6.6 is duplicated by varying the separation of pulses. The integrated absolute value of the FFTs are offset from one another vertically for clarity, but show clear decreases in the period of oscillation with increasing pulse spacing. Each trace is well described by fits to Eq. 6.5 with reasonable theoretical pulse spacings.

vertically offset from each other. As expected, a longer interpulse spacing increases the frequency of the oscillations, as the magnetization can accumulate larger phase offsets more rapidly. We again fit to Eq. 6.5 to investigate the parameters. In this case, as only the pulse separation was varied, the same tip angles found above ($\beta = 16^\circ$ and $\sigma = 9^\circ$) were fixed and only the amplitude, phase and spacing were varied. We find that the oscillations are well described by interpulse spacings that are consistent with the experimental setup. Most critically, the changes in the pulse spacing are consistent between the fits and experimental values. For instance, lengthening the spacing by 5 ns in the experiment leads to a increase in the fitted interpulse spacing by 5 ns. The maximum signal intensity is also clearly dependent on the interpulse spacing, with longer spacings yielding smaller overall FID intensities. This can likely be attributed to the T_2^* ($= T_2$ for the exchange

narrowed line of BDPA) decay of the processing spins. T_2^* is estimated to be ~ 30 ns from the linewidth of the resonance, which is consistent with the substantial decrease in signal observed when the interpulse spacing was increased from 30 to 55 ns.

6.3.3 Modulating the Relative Phase with Dielectric Materials

The effect of the relative phase of the two pulses was investigated by modulating the phase of one of the pulses by changing the length of the beam paths. By inserting a material with a higher index of refraction, we can change the phase acquired in the path. For this purpose, a high resistivity silicon wafer (index of refraction $n = 3.42$) of thickness $191 \mu\text{m}$ was chosen. The phase acquired across a material is given by $\phi_{mat} = \frac{n_{mat}\omega d \cos(\theta_r)}{c}$, where n_{mat} is the material's index of refraction, ω is the angular frequency of the FEL pulse, d is the thickness of the material, c is the speed of light, and θ_r gives the angle of propagation in the material as given from Snell's law for a given incident angle (θ_i). When we account for the different phase acquired passing through a $191 \mu\text{m}$ thick silicon wafer rather than through air (i.e. $\phi_{Air} - \phi_{Si}$), the phase change should be 134° at normal incidence. Further, the phase change should range from 134° to 166° as the angle of incidence is changed from 0° to 75° , allowing for some tunability.

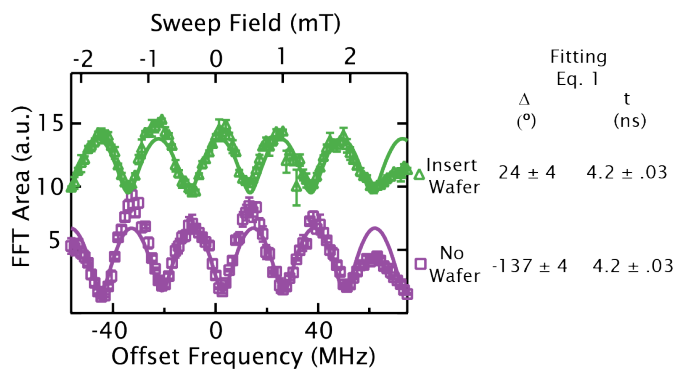


Figure 6.8: Effect of Silicon Wafers on FELEPR Phase. The phase of the oscillation is shown to shift due to the change in path length upon insertion of a dielectric material. The oscillations can be well described with fits to Eq. 6.5, and show a phase shift of $\sim 140^\circ$ as expected based on the thickness and dielectric constant of the silicon wafers.

The dielectric induced phase shift was observed experimentally, as can be seen in Fig. 6.7 (from “No Wafer” to “Insert Wafer”), with the insertion of a wafer at an incidence of $\theta_i \sim 27^\circ$, which is expected to induce a phase shift of $\sim 137^\circ$ based on calculations. Fitting with Eq. 6.5, while again forcing $\beta = 16^\circ$ and $\sigma = 9^\circ$, shows that the traces are consistent with having the same frequency (or pulse separation), but show a shift in phase of $\Delta = 140^\circ$, which is consistent with the calculated shift. Further, if the wafer is then removed from the beam path, the phase returns to a similar value as in the “No Wafer” trace. A small phase difference is found ($\sim 20^\circ$) between the two traces without wafers. It is likely that this small difference in the phase results from the errors in calculating the Larmor frequency from the magnetic field. Given that the oscillations observed are ~ 25 MHz, a magnetic field drift of only a fraction of one Gauss (~ 3 MHz, well within reason for a superconducting magnet) could account for such a small phase shift.

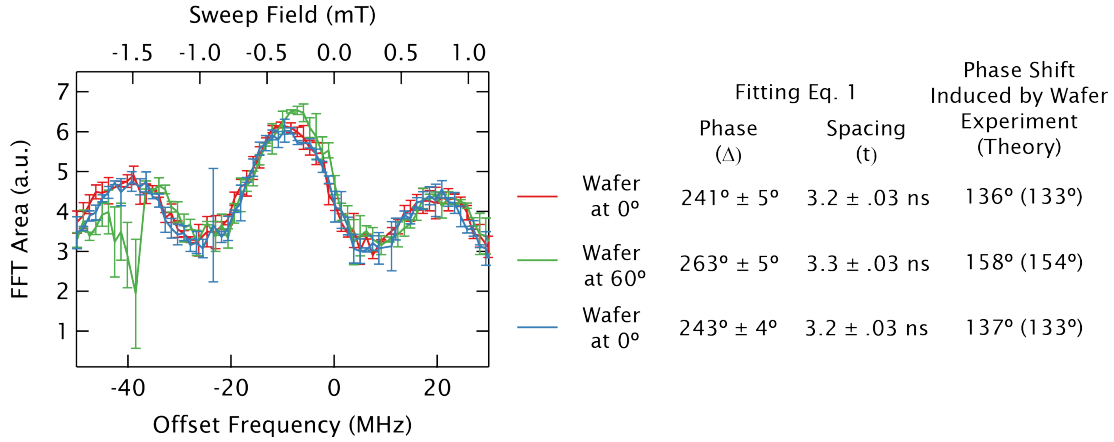


Figure 6.9: Effect of Wafer Incident Angle on Phase Shift. The insertion of a silicon wafer into the beam-path of one of the FEL pulses generates a significant shift in the relative phase of the two pulses, as can be observed in the oscillations in the signal magnitude. When we carefully change the angle of incidence of the wafer, we find the resulting phase shifts are well described by the expected phase shift discussed in the text. The shift is found to be reproducible (upon careful measurement of the Larmor frequency at each field).

A more careful set of measurements, where the resonance frequency was recorded at each point, was undertaken to examine the effects of the angle of incidence on acquired phase and is shown in Fig. 6.9. For these measurements the incidence angle was changed from $\theta_i \sim 0^\circ$ to $\theta_i \sim 60^\circ$, which should display phase shifts of $\Delta = 133^\circ$ and $\Delta = 154^\circ$, respectively. These measurements show the acquired phase agrees well with the calculations and reproducibly allowed the phase shift to be tuned by $\sim 25^\circ$ by changing the angle of incidence of the silicon wafer, though a consistent $\sim 3^\circ$ systematic deviation is observed between the measured and expected phase shift.

As the dielectric wafers serve to alter the path length of one of the pulses, an alternative approach to vary the relative phase between the two pulses is to

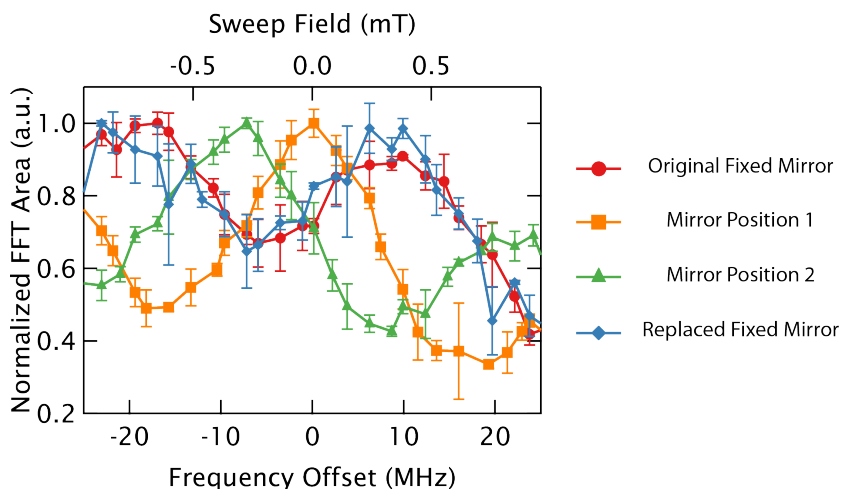


Figure 6.10: Effect of Mirror Position on Two Pulse Phase. The relative phase of the two FEL pulses can be shifted by small modifications to the beam-path of one of the pulses, as is seen in the changes in the observed oscillations. The change in the location of a mirror dramatically shifts the phase, allowing us to achieve a maximum perfectly on resonance (in orange), indicating the two pulses are in phase. However, the movement of the mirror was done crudely, and led to a drop in the intensity of the maximum signal due to misalignment of the quasi-optics.

physically modify the path length of one pulse. This can be accomplished by a very slight change to the location of a mirror in the pulse slicer. Given the short wavelength, only changes less than 1.25 mm are necessary to appreciably modify the phase. Small shifts in the path of one of the pulses is shown capable of tuning the relative phase of the two pulses, and the relative path lengths can be adjusted such that phases of the two pulses are identical (as shown for several mirror positions in Fig. 6.10). However, the movement of the quasi-optics was done crudely, and caused a drop in the intensity of the measured FID due to misalignment.

6.3.4 Impact of Relative Phases in Two Pulse EPR

The ability to measure the relative phases of the two pulses through the oscillations in signal strength as a function of offset frequency showed that the relative phase of the two pulses is (at least over the course of multiple scans taking several hours) stable. With this now understood, the opportunity exists to set the relative phase of the two pulses to a desired value, which can be achieved in one of two ways. The most direct approach would be design and installation of a precision mount to change the location of a mirror and 'stretch' one beam path. However, such an approach would require an additional mechanism to correct the alignment of the beam through the pulse slicer as the beam path is changed. Further, it disrupts the design principle of the quasi-optics, which is built to precisely image beam waists at horn mouths, and at switches to maximize coupling. A preferable alternative is the use of dielectric materials of varying thickness and incident angles to cover the range of necessary phase shifts. This chapter demonstrates that silicon wafers offer $\sim 25^\circ$ of tunability from changing the incident angle, and so a library of wafers of different thickness could be used to cover the full range of phases. Alternatively, Terahertz lenses are often made from polymers (e.g., polymethylpentene (TPX), polyethylene (PE), polypropylene (PP), and polytetrafluoroethylene (PTFE)), which are highly transmissive, easily machined, and have a lower dielectric constant than silicon, making them suitable for use as thicker phase shifters. For instance, TPX has a dielectric constant of 1.46 at 240

GHz, so that a 4 mm thick wafer induces a phase change of 535° at a 10° incidence, and 895° at 70° incidence, easily covering a full 360° . Some beam-offset occurs during passage through a wafer, and for these proposed thicker wafers this problem would have to be accounted for. However, this should be possible by using pairs of wafers to compensate for the displacement (for instance, a pair of 2 mm TPX pieces mounted at opposite incident angles).

While the mechanical tuning of path lengths is suitable for calibrating the relative phase of the two pulses, another goal is the capability to reproducibly and rapidly change the relative phase of the pulses by fixed amounts during the experiment (i.e., to cycle the phases). For this purpose, tuning of a wafer's incidence angle is too slow. However, the insertion of a suitable dielectric material into the path induces a large and discrete phase shift. Given the FEL repetition rate is currently ~ 1 Hz (and even with forthcoming improvements will not exceed 10 Hz), a wafer can easily be inserted and removed in a chopper-like setup, which can be synchronized to the FEL firing. In this way, using dielectric materials with tuned thicknesses (for instance, TPX as mentioned above), the phase can be cycled by different increments (for instance, 90° , or truly 180°). Combinations of the dielectric materials can then be used to achieve more complex phase cycles—for instance, combining three 90° shifters in a 4-step cycle to achieve 0° , 90° , 180° , and 270° . Notice that this approach could include, but does not necessarily require, tuning the relative phase of the two pulses to a precise value as discussed

above. In many phase-cycling approaches when using two pulses, the absolute phase of the second pulse is unimportant, so long as it can be modulated by a fixed amount relative to the first pulse. An example is using a 2-pulse phase cycling for inversion recovery measurements (180° -T- 90° -measurement), where the relative phase of the two pulses should be flipped by 180° .¹⁹⁸ This allows the effects of imperfect pulses flip angles (for both pulses) to be screened out, ensuring that only the signal inverted and then excited is measured. This capability is necessary to permit measuring T_1 with high accuracy through the use of phase-cycling that eliminates the effects of imperfect pulses, and could be expanded to include more advanced, 4-pulse phase cycling as well.¹⁹⁹

6.4 Impact of Phase Cycling for FELEPR

In concluding, we find that the problem of phase stability of an FEL (or other) source can be addressed through retrospective measurement of the pulse phase and correction of the signal phase. This allows the full sensitivity of phase-sensitive detection to be utilized through coherent averaging, and in cases where the phase of the source varies randomly (as is the case for the FEL), it provides an effective phase cycling to eliminate artifacts. For FEL-EPR, where two pulses follow different physical paths, the relative phase of the two pulses can be tuned and abruptly changed through the use of dielectric materials to modify the relative path lengths. In combination, these approaches allow us to apply phase cycling

routines which require modification of the relative phase of the two pulses, calibration of the phase of the two pulses, and coherent detection of a particular phase of the signal. Phase cycling greatly expands the versatility of pulse sequences, such as to greatly increase the sensitivity, accuracy, and robustness of seemingly simple EPR sequences, which has now been shown to be applicable using the FEL source.

Chapter 7

Conclusion

The work presented in this dissertation covers a wide range of topics including both applications and development of high-field EPR. The central thread which ties this work together is the goal of expanding the capabilities of high-field EPR as it is applied to biological systems. This dissertation has described the ability to probe interspin distances (and particularly probe clustering) by using the high-fields to silence the electron spin bath. This techniques are found to be applicable, to even longer distances in new spin probes, based on Gd^{3+} that show sensitivity out to extremely long interspin distances, though further theoretical and experimental work is necessary to finish this development. However, the more exciting application of these Gd^{3+} probes is to directly probe long interspin distances by utilizing cw-distance measurements, which can applied in at higher temperatures than is possible using pulsed distance techniques. Indeed, it is also shown that Gd^{3+} makes a suitable probe for DEER in studying membrane protein oligomerization. Finally, the development of a high-field EPR spectrometer using

the UCSB Free Electron Laser as a source has eliminated the ceiling for high-field EPR that once existed as a result of the limited power of sources. Introduction of phase control greatly expands the capabilities of the spectrometer and leads towards more advanced measurements. Together, these efforts follow the separate (but equally important) paths of uncovering new high-field EPR methodologies, and pushing (and moving) the boundaries of the state of the art in instrumentation in an effort to advance the capabilities of high-field EPR more generally.

It had been said, colloquially, that justifying the acquisition or development of high-field EPR equipment is akin to requesting a multi-story ladder. That is, one should not attempt to use a 30 foot ladder to wash the first floor windows, and a high-field EPR spectrometer should only be utilized for situations where it is necessary. While such justifications are sensible considering the technological challenge and expense of high-field EPR, it seems that the time has finally come when technique and technology have developed to the point where the advantages of working at high-field can be generally applied. Low-field EPR remains a potent spectroscopic tool, and will remain so into the foreseeable future. However, it is the hope that finally the use of high-field EPR can begin to expand and become a more common approach for non-specialists. Such a goal requires both maturation of the technique (to which this thesis, I hope, contributes), but also the “introduction” of the technique to a wider audience, which requires demonstrations on “relevant” problems. The majority of that work in this dissertation has now stepped into

the realm of practical application. For instance, the studies of ruler molecules with spin bath quenching are critical as models for biological systems, cw EPR measurements of Gd^{3+} labeled Proteorhodopsin and Chemotaxis proteins are in the fledgling stage, and efforts are being made to identify suitable systems for application using the FELEPR. As the FELEPR is the only spectrometer of its kind at the moment, it is our hope that by encouraging collaboration with other spectroscopists we can emphasize the potential uses of FELEPR, identify new directions to take the technological capabilities, and help in providing a road-map for the continued development of high-field EPR. Finally, in contrast to the “ladder” analogy above, it has been my experience that many of the most interesting components of the work in this thesis was not (specifically) part of the original vision of the project. Instead, it seems as if, once we purchased a large ladder for cleaning the second story windows, we began to discover new things on the roof that we could not see from the ground. As such, in addition to the outlook provided here, it seems most likely that many new, exciting applications for high-field EPR will emerge now that the technology has become available. Thus, the biological applications for high-field EPR (those presented here, and elsewhere) beyond offering an exquisite method for targeted studies of structure and dynamics in support of other techniques, hopefully provide a framework for the road forward in EPR generally, which lies towards high fields.

Appendix A

Experiments and Methods

A.1 EPR Spectrometers

The majority of measurements in this dissertation were done at 240 GHz using either a low-powered, cw/pulsed EPR spectrometer, or an “advanced” version of the same spectrometer where the Free Electron Laser is used as a high-power source. The details of operation of the FELEPR is covered in Chapter 5. Because the low-powered spectrometer, while home built, has been employed elsewhere, it’s setup is discussed below. The DEER measurements carried out in Chapter 4 utilized spectrometers in the Goldfarb group at the Weizmann Institute of Science and are briefly outlined below.

A.1.1 Home Built 240 GHz EPR Spectrometer

Further details of the spectrometer operation for low-powered EPR can be found in the spectrometer manual available from the Sherwin Group at UCSB.

The spectrometer is a dual, pulsed and cw EPR spectrometer operating at 240 GHz, using a low power solid state source, developed to operate as the staging instrument for a Free Electron Laser-powered EPR spectrometer⁸⁸. It is similar in operation to spectrometers described elsewhere⁸⁷. It utilizes a frequency multiplier source (Virginia Diodes Inc) which multiplies a 15 GHz source 16x to achieve a frequency of 240 GHz with cw power of order 30 mW. The system utilizes a quasi-optical bridge and induction mode detection²⁰⁰. Super-heterodyne detection is employed using a Schottky subharmonic mixer (Virginia Diodes Inc) and a home built IF stage at 10 GHz, which is then mixed down to baseband for detection. The detector system has a noise temperature of 1300 K, and the overall spin sensitivity at room temperature is measured to be 10^{10} spins/mT in cw operation⁸⁸. The radiation is passed to the samples which sit at the end of a 1.25 meter long overmoded waveguide (Thomas Keating Inc). The waveguide is placed with the sample at the field center of a sweepable, passively shielded, 12.5 T magnet (Oxford Instruments plc). The magnet is outfitted with a continuous flow cryostat (Janis Research Company LLC) mounted in the room temperature bore of the magnet, allowing continuous operation between 2.3 and 300 K and down to 1.5 K in batch mode.

The sample temperature is recorded with a Cernox temperature sensor (Lake-shore Cryogenics Inc), mounted at the end of the waveguide just above the sample. A second sensor, attached to the cryostat and near the heater was used to control

the temperature with a PID feedback optimized temperature controller (Model 335 Lakeshore Cryogenics Inc) to minimize oscillations. For temperatures down to 4.2 K, the cryostat can be run under vacuum or atmospheric pressure. To reach temperatures from 2.3-4.2K requires pumping on the sample space, which was done with a rotary vane pump. From 1.5-2.3 K the cryostat is run in batch mode, where the transfer valve's needle valve is fully opened and the cryostat is pumped on for 30 minutes to collect helium in the cryostat. The needle valve is then closed and low pressure generated can cool the sample to 1.5K for 1 hour. It is not uncommon to see substantial phase jitter in this mode, likely as a result from pumping on the liquid He.

A.1.2 95 GHz and 10 GHz Spectrometers

W-Band (95 GHz) pulse measurements on the Gd³⁺ labeled protein were carried out a homebuilt spectrometer described previously⁷⁰ using 0.84 o.d , 0.6 i.d quartz capillaries with EPR active volume of 2-3 μL . X-Band pulse EPR (9.5 MHz GHz) measurements were done on a Bruker ELEXSYS E580 spectrometer (9.5 GHz) using an ER4118X-MS-5 probe head with a split ring resonator (5 mm sample access) on 50-60 μL samples.

A.1.3 cw 10 GHz Spectrometer

Measurements of Fig. 1.3 in the introduction were done on the commercial cw EPR spectrometer operating at 10 GHz in UCSB's MRL.

A.2 Samples

A variety of samples were made and used in this dissertation, and they are described below, divided into the chapters of the text.

A.2.1 Chapter 1

4-Amino-TEMPO was purchased from Acros Organics and glycerol were purchased from Sigma Aldrich. The Amino Tempo was dissolved into H₂O/glycerol (0.4:0.6, v:v) solution by weight to reach the desired concentration.

A.2.2 Chapter 2

DOTAP (1,2-dioleoyl-3-trimethylammonium-propane (chloride salt)), PC-TEMPO (1,2-dioleoyl-sn-glycero-3-phospho(TEMPO)choline), and DOPC (1,2-dioleoyl-sn-glycero-3-phosphocholine) were obtained from Avanti Polar Lipids. D₂O and glycerol were purchased from Sigma Aldrich. Deuterated glycerol was purchased from Cambridge Isotope Labs. 4-Amino-TEMPO was purchased from Acros Organics, and deuterated-4-Amino-TEMPO was purchased from Isotec.

All were used as purchased without further purification. Free-in-solution samples were made by dissolving the spin label (4-Amino-TEMPO or deuterated-4-Amino-TEMPO) in D₂O/d-glycerol (0.4:0.6, v:v).

Vesicles were prepared following a rapid extrusion procedure¹⁰⁶, and the details of their constituency is given in Table 2.2. Vesicle samples were prepared in a D₂O/d-glycerol (0.7:0.3, v:v) solution. The average inter-electron distance in vesicles was calculated by determining the approximate number of PC-TEMPO lipids on the surface of the 200 nm vesicle using an estimate of the headgroup area of the DOTAP and DOPC lipids of $\sim 70 \text{ \AA}^2$ ²⁰¹. Once the number of PC-TEMPO probes was determined, this was converted to an average inter-electron spin angular separation²⁰² that was used to estimate inter-electron spin distances.

TOTAPOL (1-(TEMPO-4-oxy)-3-(TEMPO-4-amino)propan-2-ol)¹³³ was purchased commercially from DyNuPol. GdCl₃6H₂O (Gadolinium chloride hexahydrate) was purchased from Sigma Aldrich, and Gd595, C2-Gd595, and C3-Gd595 were synthesized following established procedures.^{131,134-136}. All compounds were dissolved in D₂O/d-glycerol (0.4:0.6, v:v).

The compound 4MMDPA was purchased from Cedarlanes. 4MMDPA solutions were also prepared in D₂O/d-glycerol (0.7:0.3, v:v), to which a 1:1 molar ratio of GdCl₃6H₂O (in 0.7:0.3 v:v D₂O/d-glycerol) was added. For PR synthesis and labeling with 4MMDPA see the information on sample preparation for

chapter 4 below. In this case, a 1:1 molar ratio of $\text{GdCl}_3 \cdot 6\text{H}_2\text{O}$ (in 0.7:0.3 v:v $\text{D}_2\text{O}/\text{d-glycerol}$) was used.

The samples were between 5 and 10 μL and placed in a Teflon sample cup that had a ~ 2 mm inner diameter and was ~ 5 mm in height. The samples were frozen in liquid nitrogen before being mounted on a silver mirror at the end of the waveguide.

A.2.3 Chapter 3

The compound 4MMDPA was purchased from Cedarlanes. Gd595 and C2-Gd595 were synthesized following established procedures.^{131,134–136} $\text{GdCl}_3 \cdot 6\text{H}_2\text{O}$ (Gadolinium chloride hexahydrate), D_2O and d-glycerol were purchased from Sigma Aldrich. Deuterated glycerol was purchased from Cambridge Isotope labs. All chemicals were used as purchased without further purification. GdCl_3 samples were made by dissolving $\text{GdCl}_3 \cdot 6\text{H}_2\text{O}$ in a solution of $\text{D}_2\text{O}/\text{d-glycerol}$ (0.4:0.6, v:v). Both Gd-595 and C2-Gd-595 samples were prepared in solutions of $\text{D}_2\text{O}/\text{d-glycerol}$ (0.4:0.6, v:v). 4MMDPA solutions were also prepared in $\text{D}_2\text{O}/\text{d-glycerol}$ (0.4:0.6, v:v), to which a 1:1 molar ratio of $\text{GdCl}_3 \cdot 6\text{H}_2\text{O}$ was added.

The samples were between 3 and 15 μL (with smaller volumes used for higher concentrations) and placed in one of two Teflon sample cups. The larger cup is roughly ~ 4 mm inner diameter and 6 mm in height, the smaller was ~ 2 mm

inner diameter and ~ 5 mm in height. The samples were frozen in liquid nitrogen before being mounted on a silver mirror at the end of the waveguide.

A.2.4 Chapter 4

The purification and expression of PR followed methods in literature.^{203,204} A gene (provided by Gregg Whited from Genencore, Palo Alto, CA) for green Proteorhodopsin with 6x histidine tags at the C-terminus, and the naturally occurring cysteines (residues 107, 156, 175) replaced with serines, was subcloned into a pTricHis2 plasmid. The cysteine mutations have been shown to not affect overall function.^{41,205} Further mutagenesis on the plasmid modified the glytamic acid at residue 108 to a glutamine which extends the M-intermediate state of the photocycle by eliminating a proton acceptor site.^{206,207} Single cysteine mutations were introduced in the proteins at residues W58C, and K177C. Precise descriptions of the preparation of single cysteine mutants from the plasmid, and expression of the protein can be found in Stone et al.⁴¹

Purification of the protein similarly followed Stone et al, and for the PR labeled with nitroxide radicals the spin-labeling the process was identical. For labeling using Gd^{3+} , 4-Mercaptomethyl-dipicolinic acid (4MMDPA) was used (unmodified from Cedarlane, Burlington NC) following previous literature.¹²⁹ After the protein was bound with a His-tag affinity resin and free protein washed away, the bound PR was reacted with a 30-fold excess of 5,5'-Dithiobis-(2-Nitrobenzoic

Acid) (DTNB) in a tris buffer and allowed to set. Free DTNB and TNB were then washed before A 4-fold excess of 4MMDPA was added and again allowed to set. The labeled protein was eluted in a tris buffer containing DETAILS.

Both MTSL labeled PR and Gd^{3+} labeled PR were further purified upon being removed from the column using size-exclusion chromatography with a Sephadex 200 column on an FPLC instrument (Akta; GE Healthcare, Wauwatosa, WI). For these experiments, only the fraction previously found to be the hexamer was used.⁴¹ The solvent was exchanged to D_2O using centrifugal filters. Gd^{3+} is bound to the 4MMDPA tags through addition of $GdCl_3$ in deuterated buffer following buffer exchange. Spin diluted oligomers (where some fraction of the total PR is labeled) were generated for both the 4MMDPA- and MTSL-labeled samples. MTSL dilutions were prepared by mixing unlabeled PR (with no cysteine mutations) while the labeled protein remained on the affinity column (before undergoing FPLC). Alternatively, Gd^{3+} dilutions were prepared by simply varying the amount of $GdCl_3$ introduced into the system. The maximum nominal Gd^{3+} -loading level utilized was 80% in order to avoid any chance of free Gd^{3+} in solution.¹⁵⁷ The samples (both MTSL and 4MMDPA) were diluted to 30:70 d-glycerol: D_2O to ensure formation of a good glass. The estimated spin-concentration (as opposed to the protein concentration) was maintained between 100-300 μM for all samples for the PDS measurements. At W-Band $\sim 3 \mu L$ was used, while at X-Band $\sim 50 \mu L$ of sample was necessary.

A.2.5 Chapter 5

The samples of 1:1 crystalline α - γ -bisdiphenylene- β -phenylallyl (BDPA) with Benzene were purchase from Sigma Aldrich and used without modification. Both nitroxide and GdCl_3 samples were prepared as in the sample preparations for Chapter 2, only using $\sim 8 \mu\text{L}$ of sample in a sample cup ~ 4 mm inner diameter and ~ 6 mm in height.

A.2.6 Chapter 6

The samples of 1:1 crystalline α - γ -bisdiphenylene- β -phenylallyl (BDPA) with Benzene were purchase from Sigma Aldrich and used without modification. For all measurements, a single grain was selected from the bottle and placed in the center of a 7 mm silver mirror positioned at the end of the waveguide. A single, undiluted grain was used to achieve a high spin concentration sufficient to induce exchange narrowing of the EPR line, thus leading to long free induction decays. The cw EPR peak-to-peak linewidth of these grains is typically measured to be approximately 0.3 mT. Although there is well known sample-to-sample variation for BDPA samples purchased commercially,²⁰⁸[38] for the purposes of this work these variations did not impact the results, as the only requirement was to have a single, strong, and narrow EPR resonance.

A.3 Measurement and Calculation Details

A.3.1 Chapter 1

The cw EPR concentration series was performed at 10 GHz at a temperature < 200 K. The modulation amplitude was set to $< 1G$, and a wide (30 mT) sweep with was used to get good background for the signal. The fitting of the spectra was done using a program kindly provided from the Hubbel group at UCLA.

A.3.2 Chapter 2

The echo decays and echo-detected spectrum for nitroxides was measured using a 650 ns- τ -750 ns- τ spin-echo pulse sequence using the maximum available power of the solid state source (~ 30 mW). For measurements of Gd^{3+} a 175 ns- τ -275 ns- τ spin-echo pulse sequence was used. The area under the echo signal was recorded using an oscilloscope (Lecroy Corporation DDA-120), measuring the signal magnitude. A superconducting sweep coil, separate from the main coil of the superconducting magnet was used to irradiate at the maxima of the nitroxide spectra. Errors for measurements of TM were determined from the error estimates during fitting to the stretched exponential.

A.3.3 Chapter 3

CW measurements were carried out using field modulation at 20 kHz with modulation amplitude between 0.05 and 0.2 mT-to keep modulation $<1/5$ of the linewidth that typically was between .45 and 2.0 mT-and measured in quadrature using lock-in amplifiers (Stanford Research Instruments Inc. SR830). The incident power was highly attenuated with a wiregrid polarizer, and was on the order of μ Watts at the sample. The spectra were rephased in post-processing procedures to determine the derivative lineshape by equalizing the positive and negative peaks of the derivative shape. A superconducting sweep coil, separate from the main coil of the superconducting magnet, capable of sweeping the field up to ± 60 mT was used to carry out cw measurements. For measuring the full width of the Gd^{3+} spectra, as presented in Fig.1, the field was swept using the main coil of the magnet. The echo-detected spectrum was measured using a $175 \text{ ns}-\tau-275 \text{ ns}-\tau$ (with $\tau = 1 \mu\text{s}$) spin-echo pulse sequence using the maximum available power of the solid state source ($\sim 30 \text{ mW}$) and the integral of the echo signal area was measured using an oscilloscope (Lecroy Corporation DDA-120).

Calculations of both the dipolar broadening (Sec: 3.3) and the refractive broadening (Appendix D) were carried out in Matlab (Mathworks 2011a).

A.3.4 Chapter 4

The “deadtime free”, 4-pulse DEER sequence as shown in Fig. 1.4, $\frac{\pi}{2}(\nu_{obs}) - \tau_1 - \pi(\nu_{obs}) - t - \pi(\nu_{pump}) - (\tau_1 + \tau_2 - t) - \pi(\nu_{obs}) - \tau_2 - \text{echo}$, was used for distance measurements.⁵² In the case of the W-Band measurements, the pump pulse was centered on the maximum of the Gd^{3+} spectrum, which was also centered at center of the cavity frequency, and the observer pulse was applied at a spacing of ~ 75 MHz. The pump π -pulse length was 15 ns and the $\frac{\pi}{2}$, π observer pulses were 15 and 30 ns, respectively. Other parameters were ; $\tau_1=400$ ns and repetition time 500 μs . Similarly, in the X-Band measurements, the maximum of the nitroxide spectrum was placed at the center of the cavity bandwidth, and used for the pump pulse, while the observer pulse was spaced by 65 MHz. The pump π -pulse length was 16 ns and the $\frac{\pi}{2}$, π observer pulses were both 32 ns, and $\tau_1=300$ ns and repetition time 2.5 μs . Measurements were carried out at 20 K at W-Band and at 50 K at X-Band. Phase memory times and echo detected EPR spectra were measured using the spin echo sequence. The raw DEER data was processed using DEERAnalysis⁶¹ following established procedures.¹¹² Though the Gd^{3+} spin is $S = \frac{7}{2}$ (as opposed to the typical $S = \frac{1}{2}$ for nitroxides), the approximation of analyzing the Gd^{3+} DEER data using an $S = \frac{1}{2}$ formalize has been discussed and justified.^{111,112,131}

A.3.5 Chapter 5

Rabi Oscillation Measurements

For these experiments a BDPA grain was used as a sample and the magnetic field centered at the BDPA resonance (~ 8.58 T) (except where specific mention is made of moving off resonance). The resonance is determined by observing the FEL frequency, and overlapping the Larmor frequency with it (which neglects the fact that the pulse length affects the Larmor frequency). The time domain trace is taken in a single-pulse setup, as described in Section 5.2.4. This allows the pulse length to be adjusted over the entire length of the FEL pulse (up to several μs), by electronically changing the delay between the laser pulses. The Cavity Dump Coupler (CDC) was fired to shutoff the FEL and prevent leaked or scattered light from reaching the detector during the measurement, and the pulse is contained in this amplified region. The strong signal from the BDPA sample necessitated attenuation of the signal (ranging from 30 dB) at the 10 GHz stage to prevent saturation of the mixers.

For Sec. 5.3 only the magnitude area of the FID was collected for each pulse length, but to identify the Larmor frequency shift in Sec. 5.4, the entire traces were saved in order to examine the frequency changes through post-processing in Igor Pro (Wavemetrics).

Echo Measurements

When the pulse slicer is used to generate two pulses, the pulses were generated using the lasers as described in for two pulses in Section 5.2.4. Each pulse was ~ 10 ns, and the separation was changed by modifying the firing of the two lasers. The CDC was again used to help reduce the deadtime, and little attenuation was used (as the signal was rather small). No effort was made to optimize the pulse lengths due to the difficulty of aligning the delay line properly.

A.3.6 Chapter 6

One Pulse Measurements

Experimental Details can be found in Sec. 6.2.

Two Pulse Measurements

Some details of the two pulse measurement. The first pulse was ~ 12 ns in total length, with a roughly 4 ns rise and fall time, and the second pulse was nearly square and roughly 9 ns long. The magnetic field was swept through the center of the BDPA resonance (~ 8.58 T) and the free induction decay (FID) at each field value was measured after applying a simple pulse sequence consisting of two $< 45^\circ$, 240 GHz pulses. As the BDPA grain is highly concentrated, the exchange narrowing results in a homogeneous EPR line, and there is no refocused echo. The two pulses were spaced by a coarsely calibrated delay in the firing of two lasers,

which nominally ranges from 30 ns to 60 ns. The calibration of the delay time was done visually on an oscilloscope, and the scattered 240 GHz radiation generated during the activation of the switches makes it difficult to precisely determine the interpulse spacing in this way. The Cavity Dump Coupler (CDC) was fired during the second pulse (boosting its power by $\sim 3x$) to shutoff the FEL and prevent leaked or scattered light from reaching the detector during the measurement. To place the measured FID safely beyond the deadtime of the spectrometer in these experiments, the detector switch was activated ~ 80 ns following the end of the second pulse. A schematic of the pulse slicer and a simplified timing diagram is shown in Fig. 5.4B. The strong signal from the BDPA sample necessitated the use of a ~ 30 dB attenuation of the signal at the 10 GHz stage to prevent saturation of the mixers. In order to measure the total transverse magnetization, the area under the signal peak in the magnitude Fast Fourier Transform (FFT) of the FID was recorded as a function of the magnetic field. During one of the field sweeps, the Larmor frequency at each magnetic field was also recorded.

Here some details are provided of the measurements of the transverse magnetization as a function of offset frequency. It covers the use of the Cavity Dump Coupler (CDC), the data collection and processing, and the determination of Larmor frequency from field. The CDC was used as a Q-switch to suddenly lower the quality factor of the FEL cavity at the same time that the second sliced pulse was ended.¹ This prevents lasing after the end of the second pulse in order to eliminate

scattered light and leakage from appearing during the FID. An additional, though in this case unnecessary, result is that the CDC offers a roughly two-fold increase in B_1 amplitude for the second pulse. As the magnetic field was stepped, the sweep coil was allowed to briefly settle before the magnitude of the Fast Fourier Transform (FFT) of the FID was recorded. As the resonance moves when the magnet field is swept, the area was always measured in a window of roughly +/- 100 MHz about the center frequency of 500 MHz (the IF frequency) to ensure the entire signal was included at every field point. 3 scans were taken at each field to determine an average value and standard deviation for each field/frequency point. Occasional misfires of the FEL cause missed pulses, where the FEL does not lase. This caused large disruptions to the data, and so a filter was applied to eliminate scans where no FID was visible above the noise. This filter acted during data collection, and so did not change the number of scans for each point (if a result was discarded, another scan was taken). This filtering acted only to screen out the clear cases when the FEL failed to fire as the cutoff criterion was always far smaller than the weakest measured FID, ensuring it did not skew the results.

The measurement of field from the superconducting magnet is based on a calibration of the applied current, and shows appreciable drift over days. During one field sweep each FID was saved (in addition to the integrated, magnitude FFT area) and later processed to create an accurate map from the measured magnetic field to the Larmor frequency of the BDPA sample. This map was created using a

linear fit, and the variation in Larmor frequency due to the sample magnetization was ignored as it was small (examples can be found in the ESI of¹⁹³). The Larmor frequency as a function of the swept field, which was used for this calibration shows the small deviations from linearity mentioned above. For subsequent scans only the integrated FFT area was recorded, and the measured magnetic field was used to determine the Larmor frequency based on the previously generated map. Although this was sufficient to observe clear oscillations, there were some fluctuations that likely emerged from small field drifts.

Appendix B

Increased Rabi Frequency in Gd^{3+}

Following the rules for evaluating matrix elements of the operators \hat{S}_{\pm} found in any quantum mechanics text (for instance Sakurai's text²¹)

$$\hat{S}_{\pm}|j, m\rangle = \hbar\sqrt{(j \mp m)(j \pm m + 1)}|j, m \pm 1\rangle \quad (\text{B.1})$$

Using this, we can easily construct the $S_X = \frac{1}{2}(S_+ + S_-)$ and $S_Y = \frac{1}{2i}(S_+ - S_-)$ for the $S = \frac{7}{2}$ ion.

$$S_X^{\frac{7}{2}} = \frac{\hbar}{2} \begin{pmatrix} 0 & \sqrt{7} & 0 & 0 & 0 & 0 & 0 & 0 \\ \sqrt{7} & 0 & 2\sqrt{3} & 0 & 0 & 0 & 0 & 0 \\ 0 & 2\sqrt{3} & 0 & \sqrt{15} & 0 & 0 & 0 & 0 \\ 0 & 0 & \sqrt{15} & 0 & 4 & 0 & 0 & 0 \\ 0 & 0 & 0 & 4 & 0 & \sqrt{15} & 0 & 0 \\ 0 & 0 & 0 & 0 & \sqrt{15} & 0 & 2\sqrt{3} & 0 \\ 0 & 0 & 0 & 0 & 0 & 2\sqrt{3} & 0 & \sqrt{7} \\ 0 & 0 & 0 & 0 & 0 & 0 & \sqrt{7} & 0 \end{pmatrix} \quad (\text{B.2})$$

$$S_Y^{\frac{7}{2}} = \frac{i\hbar}{2} \begin{pmatrix} 0 & \sqrt{7} & 0 & 0 & 0 & 0 & 0 & 0 \\ -\sqrt{7} & 0 & 2\sqrt{3} & 0 & 0 & 0 & 0 & 0 \\ 0 & -2\sqrt{3} & 0 & \sqrt{15} & 0 & 0 & 0 & 0 \\ 0 & 0 & -\sqrt{15} & 0 & 4 & 0 & 0 & 0 \\ 0 & 0 & 0 & -4 & 0 & \sqrt{15} & 0 & 0 \\ 0 & 0 & 0 & 0 & -\sqrt{15} & 0 & 2\sqrt{3} & 0 \\ 0 & 0 & 0 & 0 & 0 & -2\sqrt{3} & 0 & \sqrt{7} \\ 0 & 0 & 0 & 0 & 0 & 0 & -\sqrt{7} & 0 \end{pmatrix} \quad (\text{B.3})$$

The transition strength for the EPR transitions can then be written as $P_m^{\frac{7}{2}} = \langle m_Z | S_X^{\frac{7}{2}} | m_Z \pm 1 \rangle$, with the limitation that $-\frac{7}{2} \leq m_Z \leq \frac{7}{2}$ and $-\frac{7}{2} \leq m_Z \pm 1 \leq \frac{7}{2}$ (i.e. that the transitions we look at are between existing energy levels. For our work, the most interesting transition is the narrow, central transition ($|- \frac{1}{2}\rangle \leftrightarrow |\frac{1}{2}\rangle$))

and we find $P_{\frac{1}{2}}^{\frac{7}{2}} = \langle \frac{1}{2} | S_X | -\frac{1}{2} \rangle = 2\hbar$. By comparison, for an $S = \frac{1}{2}$ spin we can write, based on the Pauli matrices

$$S_X^{\frac{1}{2}} = \frac{\hbar}{2} \begin{pmatrix} 0 & 1 \\ 1 & 0 \end{pmatrix} \quad (\text{B.4})$$

$$S_Y^{\frac{1}{2}} = \frac{i\hbar}{2} \begin{pmatrix} 0 & -1 \\ 1 & 0 \end{pmatrix} \quad (\text{B.5})$$

$$(\text{B.6})$$

then we calculate simply $P_{\frac{1}{2}}^{\frac{1}{2}} = \langle \frac{1}{2} | S_X^{\frac{1}{2}} | -\frac{1}{2} \rangle = \frac{\hbar}{2}$. Thus we see that the transition strength of the central transition is 4x stronger for an $S = \frac{7}{2}$ spin than for an $S = \frac{1}{2}$, and therefore given an identical pulse amplitude, the pulse length can be reduced by a factor of 4.

Appendix C

Evaluating the Gd^{3+} Hamiltonian with Perturbation Theory

We start with the Hamiltonian:

$$\mathcal{H} = g\beta B_0 S_Z + D(S_{Z_C}^2 - \frac{1}{3}S(S+1)) + E(S_{X_C}^2 - S_{Y_C}^2)$$

(identical to Eq. 3.1) For us, S_X , S_Y , and S_Z are the spin operators in the laboratory frame, while S_{X_C} , S_{Y_C} , and S_{Z_C} are the spin operators in the molecular, or crystal frame. We first must express the operators in the crystal field frame in terms of the laboratory frame. To do this, we introduce a new variable θ , which represents the orientation of the molecule z-axis with respect to the magnetic field. We neglect a second angle ϕ as the phase in the x/y plane is arbitrary, and we simply assume $\phi = 0$

So then following some algebra and grouping we wind up with.

$$\begin{aligned}
S_{Z_C} &= S_Z \cos(\theta) + S_X \sin(\theta) \\
S_{X_C} &= S_X \cos(\theta) - S_Z \sin(\theta) \\
S_{Y_C} &= S_Y
\end{aligned} \tag{C.1}$$

Grouping by the spin operators helps us moving forward, so we write:

$$\begin{aligned}
\mathcal{H} &= g\beta B_0 S_Z - \frac{D}{3}(S(S+1)) + S_Z^2(D \cos^2(\theta) + E \sin^2(\theta)) \\
&\quad + (S_X S_Z + S_Z S_X) \cos(\theta) \sin(\theta) (D - E) \\
&\quad + S_X^2(D \sin^2(\theta) + E \cos^2(\theta)) - S_Y^2 E
\end{aligned} \tag{C.2}$$

Because we are dealing with an $S = \frac{7}{2}$ ion, $\frac{D}{3}(S(S+1)) = \frac{\frac{7}{2}(\frac{8}{2})}{3}D = \frac{21}{4}D$ is just a constant. Similarly we know $S_Z|m\rangle = m\hbar|m\rangle$, and similarly $S_Z^2|m\rangle = \hbar^2 m^2|m\rangle$. We have the spin operators S_X , and S_Y , in Eqs. B.2 and B.3, and we can write out S_Z

$$S_Z = \frac{\hbar}{2} \begin{pmatrix} 7 & 0 & 0 & 0 & 0 & 0 & 0 & 0 \\ 0 & 5 & 0 & 0 & 0 & 0 & 0 & 0 \\ 0 & 0 & 3 & 0 & 0 & 0 & 0 & 0 \\ 0 & 0 & 0 & 1 & 0 & 0 & 0 & 0 \\ 0 & 0 & 0 & 0 & -1 & 0 & 0 & 0 \\ 0 & 0 & 0 & 0 & 0 & -3 & 0 & 0 \\ 0 & 0 & 0 & 0 & 0 & 0 & -5 & 0 \\ 0 & 0 & 0 & 0 & 0 & 0 & 0 & -7 \end{pmatrix} \quad (\text{C.3})$$

At this point, it is useful to emphasize that zero-field interactions (characterized by D and E) are small relative to the Zeeman term, so we will address the zero-field terms through perturbation theory. To do so, we first wish to look at the matrices that are present for the relevant terms. Namely, these are S_Z^2 , S_X^2 , S_Y^2 , $S_X S_Z$ and $S_Z S_X$. It is easiest to simply calculate these matrices (in Mathematica for instance).

The first important realization is that for first order perturbation theory we are interested in the diagonal elements of the matrix operators.²¹ Therefore, to first order in perturbation theory we can drop the $S_X S_Z$ and $S_Z S_X$ terms, and then we are only worried about a perturbation Hamiltonian of the form.

$$\begin{aligned}
\mathcal{H} &= g\beta B_0 S_Z - \frac{21}{4}D + S_Z^2(D \cos^2(\theta) + E \sin^2(\theta)) \\
&\quad + S_X^2(D \sin^2(\theta) + E \cos^2(\theta)) - S_Y^2 E \\
\mathcal{H} &= H_0 + V
\end{aligned} \tag{C.4}$$

where $H_0 = g\beta B_0 S_Z$ and

$$V = -\frac{21}{4}D + S_Z^2(D \cos^2(\theta) + E \sin^2(\theta)) + S_X^2(D \sin^2(\theta) + E \cos^2(\theta)) - S_Y^2 E \tag{C.5}$$

Notice that this matrix form of V is complete ONLY along the diagonal, as we've neglected the terms that have the form $S_Z S_X$ and similar terms. To complete the perturbation matrix to higher orders, we must include the terms, which I choose to call $V_1 = (S_X S_Z + S_Z S_X) \cos(\theta) \sin(\theta) (D - E)$, which we had initially dropped. Carrying out work to higher orders in perturbation theory would allow direct calculation of the transition frequency for the central line (which we will in a moment see is unaffected to first order). However, for this work we do not carry out this calculation, although we briefly discuss the *form* of the next leading term at the end of this appendix.

Following standard perturbation theory we can write $\Delta_n^1 = \langle n|V|n\rangle$, where Δ_n^1 is the first order energy correction of the state $|n\rangle$, and the states $|n\rangle$ are the eigenstates of the unperturbed Hamiltonian (i.e. in our case the Zeeman states). Thus, the energy shifts of each state $|m_Z\rangle$ is given by the diagonal elements of the

perturbation matrix V , i.e. $\Delta_{-\frac{7}{2}} = \langle \frac{-7}{2} | V | \frac{-7}{2} \rangle = V_{1,1}$, $\Delta_{-\frac{5}{2}} = \langle \frac{-5}{2} | V | \frac{-5}{2} \rangle = V_{2,2}$ etc. It is somewhat similar to calculate these diagonal elements if we rewrite the operators in a different form using the following results.

$$S_Z^2 |m_Z\rangle = \frac{\hbar^2}{4} m_z^2 \quad (\text{C.6})$$

$$\begin{aligned} S_X^2 &= \left(\frac{1}{2}(S_+ + S_-)\right)^2 = \frac{1}{4}(S_+^2 + S_-^2 + S_+S_- + S_-S_+) \\ S_Y^2 &= \left(\frac{1}{2i}(S_+ - S_-)\right)^2 = -\frac{1}{4}(S_+^2 + S_-^2 - S_+S_- - S_-S_+) \end{aligned} \quad (\text{C.7})$$

In looking at our expressions for S_X^2 and S_Y^2 we see immediately that the diagonal elements are given simply by the S_+S_- and S_-S_+ terms (the others give rise to the off-diagonal terms in V). But we can write

$$\begin{aligned} S_+S_-|m_Z\rangle &= \hbar^2\sqrt{(J-m+1)(J+m)}\sqrt{(J+m)(J-m+1)}|m_Z\rangle \\ &= \hbar^2(J+m)(J-m+1)|m_Z\rangle \\ &= \hbar^2\left(\frac{63}{4} + m - m^2\right)|m_Z\rangle \\ S_-S_+|m_Z\rangle &= \hbar^2\sqrt{(J+m+1)(J-m)}\sqrt{(J-m)(J+m+1)}|m_Z\rangle \\ &= \hbar^2(J+m+1)(J-m)|m_Z\rangle \\ &= \hbar^2\left(\frac{63}{4} - m - m^2\right)|m_Z\rangle \end{aligned} \quad (\text{C.8})$$

Therefore,

$$\begin{aligned}
S_X^2|m_Z\rangle &= \frac{\hbar^2}{4}\left(\left(\frac{63}{4} - m - m^2\right) + \left(\frac{63}{4} + m - m^2\right)\right)|m_Z\rangle \\
&= \frac{\hbar^2}{4}\left(\frac{63}{2} - 2m_Z^2\right)|m_Z\rangle \\
S_Y^2|m_Z\rangle &= -\frac{\hbar^2}{4}\left(-\left(\frac{63}{4} - m - m^2\right) - \left(\frac{63}{4} + m - m^2\right)\right)|m_Z\rangle \\
&= \frac{\hbar^2}{4}\left(\frac{63}{2} - 2m_Z^2\right)|m_Z\rangle
\end{aligned} \tag{C.9}$$

Thus, we can rewrite the diagonal elements of V using these results

$$\begin{aligned}
\langle m_Z|V|m_Z\rangle &= -\frac{21}{4}D + S_Z^2(D \cos^2(\theta) + E \sin^2(\theta)) \\
&+ S_X^2(D \sin^2(\theta) + E \cos^2(\theta)) - S_Y^2E \\
&= -\frac{21}{4}D + \frac{\hbar^2}{4}(D \cos^2(\theta) + E \sin^2(\theta))m_Z^2 \\
&+ (D \sin^2(\theta) + E \cos^2(\theta) + E)\frac{\hbar^2}{4}\left(\frac{63}{2} - 2m_Z^2\right) \\
&= \frac{21}{4}D + \frac{\hbar^2}{4}\left[\frac{63}{2}(D \sin^2(\theta) + E \cos^2(\theta) + E) \right. \\
&\quad \left. - m_Z^2(D \cos^2(\theta) + E \sin^2(\theta))\right]
\end{aligned} \tag{C.10}$$

The first two terms are independent of the spin state, and so represent a constant energy shift of all the states. As such, it does not affect the frequency of the EPR transitions (which depend on the energy difference between the different states). Thus, we can take only the 3rd term to calculate the shift of the EPR transition frequencies, and thus simplify affect of the energy of each state as

$$E_{m_Z} = \hbar\omega m_Z - m_Z^2(D \cos^2(\theta) + E \sin^2(\theta)) \tag{C.11}$$

We can write the EPR transition energy as the energy difference between $|m_Z\rangle$ and $|m_Z + 1\rangle$ yielding:

$$\Delta E = E_{m_Z+1} - E_{m_Z} = \hbar\omega - (2m_Z + 1)(D \cos^2(\theta) + E \sin^2(\theta)) \quad (\text{C.12})$$

We notice, immediately, the result proposed in the text. Namely that for $m_Z = \frac{1}{2}$ (corresponding to the $|\frac{1}{2}\rangle \leftrightarrow |-\frac{1}{2}\rangle$ transition), the shift caused by the ZFS vanishes. For all other values of m_Z , this does not vanish, and indeed will depend on both the strength of D and the relative orientation of the ZFS frame.

Thus, 1st order perturbation theory is sufficient to identify the effect of the ZFS on all transitions except the central transition. However, we must carry out perturbation theory to higher order in the case that we wish to identify the broadening of the central transition. However, this calculation, while possible using the matrices presented here, is not substantially illustrative. Instead, we use a simple scaling of the transition to demonstrate the key result that the width of the central transition due to ZFS broadening is reduced as the applied field is increased. To do so we first operate under the assumption that $E \ll D$, which is generally true in the Gd^{3+} complexes studied in this dissertation. In this case, the full perturbation matrix can be written as

$$V + V_1 \propto D \quad (\text{C.13})$$

And therefore

$$(V + V_1)^2 \propto D^2 \tag{C.14}$$

and therefore, the second order shifts of the central line (which is the leading term as the first order term is zero) is $\propto \frac{D^2}{\hbar\omega} \propto \frac{D^2}{B_0}$

Appendix D

Calculation of Refractive Broadening for Gd^{3+} Lineshapes

This section of the supplement describes the background and methodology of extracting the dipolar-broadened linewidth of a resonance at high concentrations, where the measured lineshapes are affected by refractive broadening. This accounts for the same effect known as the “propagation effect” which the authors found treated similarly in literature following submission.¹⁵⁹ Refractive broadening emerges in samples where the high concentration, large polarization and narrow linewidth cooperate to cause an extremely large change in sample susceptibility on resonance. This dramatic change in susceptibility alters the dielectric properties of the sample appreciably. When this occurs, the reflections from the sample are no longer simply proportional to the field-dependent susceptibility response as is the case at lower concentrations. As the 240 GHz EPR spectrometer measures the reflection from the sample (backed by a mirror), this means that when this occurs our measured signal is no longer identical to the field-dependent

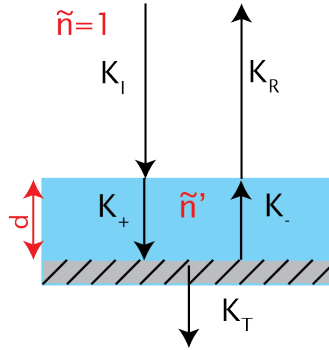


Figure D.1: Reflection Sample Geometry. Shows the simplified geometry used for the calculation for a sample of thickness d . This three media setup shows wavevectors K_I and K_R of the incident and reflected fields in the waveguide (with index $\tilde{n} = 1$). K_+ and K_- are the wavevectors of forward and backward moving waves within the sample, which has a complex, frequency (/field) dependent index of refraction (\tilde{n}'). Finally, K_T is the transmitted wave, which is assumed have zero amplitude as the sample is backed with a metallic mirror. Note the interfaces of the sample holder are ignored.

susceptibility response that we wish to measure. Therefore, we examine a method of determining the susceptibility response by explicitly calculating the reflection with the Fresnel equations. This allows us to approximate the shape of the susceptibility response that generated the measured reflection and use that to estimate the true dipolar-broadened linewidth.

D.0.7 Calculation of Reflection from a Paramagnetic Sample

We begin by examining the physical arrangement of our sample as shown in Fig. D.1. We approximate a flat sample of thickness d on top of a mirror. This ignores the sample holder, which is made from Teflon, and thus should not have

any response to the modulated field. This also ignores any asymmetry in sample geometry or meniscus formed in the sample. We expect that, while both effects may be present, this is still a sufficient approximation to develop an understanding of our spectra. The problem is then reduced to a two interface problem where we must satisfy two boundary conditions. The first interface is between air and the sample for the incident and reflected waves (given by wavevectors K_I and K_R) and the two waves propagating within the sample (wavevectors K_+ and K_-). Additionally, the interface between the sample and mirror requires the transmitted wave (with wave vector K_T) be zero. It is then a straightforward calculation to express the reflection from this sample setup as a function of the samples permeability and permittivity.

$$\begin{aligned}
R &= \frac{E_R}{E_I} = X + iY \\
&= \left[\frac{\exp(2i\phi)(\sqrt{\epsilon_R\mu_{Air}} + \sqrt{\epsilon_{Air}\mu_R}) + (\sqrt{\epsilon_R\mu_{Air}} - \sqrt{\epsilon_{Air}\mu_R})}{\exp(2i\phi)(\sqrt{\epsilon_R\mu_{Air}} - \sqrt{\epsilon_{Air}\mu_R}) + (\sqrt{\epsilon_R\mu_{Air}} + \sqrt{\epsilon_{Air}\mu_R})} \right] \\
&\approx \left[\frac{\exp(2i\phi)(\sqrt{\epsilon_R} + \sqrt{\mu_R}) + (\sqrt{\epsilon_R} - \sqrt{\mu_R})}{\exp(2i\phi)(\sqrt{\epsilon_R} - \sqrt{\mu_R}) + (\sqrt{\epsilon_R} + \sqrt{\mu_R})} \right] \tag{D.1}
\end{aligned}$$

is the reflected signal calculated from the Fresnel Equations⁶⁶ and is a complex number containing the in- and out-of-phase response of the spins as X and Y respectively. E_R and E_I are the electric field strengths of the reflected and incident radiation respectively, ϕ is the phase acquired by millimeter-wave radiation when passing through the sample, ϵ_{Air} and ϵ_R are the permittivity of air and the sample respectively, and μ_{Air} and μ_R are the permeability of air and the sample

respectively. We can express the phase acquired in terms of the known parameters by $\phi = \frac{\omega d}{c} \sqrt{\epsilon_R \mu_R}$, where d is the sample thickness, and c is the speed of light. We make the (accurate) approximation that $\mu_{Air} \approx \epsilon_{Air} \approx 1$. To determine the reflections we write $\mu_R = 1 + \chi$ where $\chi = \chi' + i\chi''$ is the complex susceptibility, and we take $\epsilon_R \approx 3.2$ from the permittivity of frozen ice.²⁰⁹ We approximate the susceptibility response as a simple Lorentzian for simplicity and so can write⁴²⁷

$$\begin{aligned}\chi' &= \frac{\chi_0 \omega_L}{2} \frac{\omega_L - \omega}{(\omega - \omega_L)^2 + (\frac{1}{T_2})^2} \\ \chi'' &= \frac{\chi_0 \omega_L}{2T_2} \frac{1}{(\omega - \omega_L)^2 + (\frac{1}{T_2})^2}\end{aligned}\tag{D.2}$$

where χ_0 is the DC susceptibility of the spins, ω_L is the electron Larmor frequency, ω is the irradiation frequency, and T_2 is the width of the resonance. We emphasize here that T_2 is only a manner of characterizing the resonance width of the susceptibility in our approximation of a homogeneous, Lorentzian lineshape and does not reflect the phase memory time in our samples. By calculating the expected susceptibility response as a function of ω_L (which is given by the swept magnetic field) this yields ϕ and μ_R (also as a function of ω_L). Then the expected signal (real and imaginary parts) can be calculated as a function of ω_L through Eq. D.1, giving us a calculated spectrum to compare to those measured in experiment.

Our input parameters for these calculations are ω_L , ω , T_2 , χ_0 and d . It is clear that ω is fixed by our irradiation frequency (2240 GHz) and ω_L is fixed by the

external magnetic field, which is swept around 8.6 T. χ_0 is fixed by the spin species ($S = \frac{7}{2}$ for Gd^{3+}), concentration, temperature and magnetic field as follows²⁷

$$\chi_0 = \frac{N}{V} \frac{\mu_\beta (g_J J)^2}{kT} \left(\frac{1}{4J^2} \text{csch}^2 \left(\frac{g_J \mu_\beta B}{2kT} \right) \right) - \frac{(2J+1)^2}{2J^2} \text{csch}^2 \left(\frac{(2J+1)g_J \mu_\beta B}{2kT} \right) \quad (\text{D.3})$$

where $\frac{N}{V}$ is the spin concentration, J is the spin quantum number, g_j is the effective g-value of the spins ($g_j = 1.992$ for Gd^{3+}), μ_β is the Bohr Magneton, μ_0 is the vacuum permeability, k is Boltzmann's constant, and T is temperature.

D.0.8 Evaluating Calculated Spectra for $\bar{r} = 1.78$ nm Samples

Estimation of parameters based on calculations are only carried out for the $\bar{r} = 1.8$ nm (50 mM) samples, as mentioned in the manuscript. Although we find sample geometry affects the lineshape of the $\bar{r} = 2.4$ nm (20 mM) and the $\bar{r} = 3.0$ nm (10 mM) samples, it proved difficult to decisively determine estimates of the exact broadening parameter through comparison with calculation. Spectra that demonstrate notable deviations from a typical derivative lineshape are much easier to characterize. At lower concentrations the distinction between refractive broadening and true linewidth broadening becomes subtle. Thus, we recognize that refractive broadening is slightly broadening some spectra at $\bar{r} = 2.41$ nm (20 mM) and $\bar{r} = 3.05$ nm (10 mM), where some variability of lineshapes is still observed, but make no attempt to quantify the correct linewidth in these samples.

Nominally, we have only 2 variable parameters, the sample thickness (d) and the resonance width (T_2). However, the measurement of the magnetic field is done through calibration of the current in a superconducting sweep coil. Thus, the field calibration is not precise enough to be used without modification, and so we must introduce a shifting parameter to maximize overlap of the simulated to experimental spectrum. Finally, although the detection is done in quadrature, the absolute phase is not precisely defined and depends on sample temperature, room temperature and other parameters. Therefore, a 4th parameter is necessary to match the phase shift of the collected data. In practice, the experimental spectra are first shifted by hand in post-processing to roughly display a pure absorption and dispersion lineshape by optimizing the symmetry of the spectra. Later, when calculated spectra are generated, their phase and field offsets are varied to achieve maximum overlap with the experimental spectra (as determined by the minimizing the difference between calculated and experimental spectra with the Error discussed below).

As the phase and field shift are not meaningful parameters for this work, we seek only to optimize them at each value of (T_2, d) , giving us a 2D parameter space to investigate. We adopt the brute force method of generating a series of spectra spanning the reasonable values of these two parameters and determining the error from the magnitude of the difference in real and imaginary parts, i.e.

$$\text{Error} = \frac{\sum_n \sqrt{(X_{Exp} - X_{Calc})^2 + (Y_{Exp} - Y_{Calc})^2}}{N_{Pts}}$$

where X and Y represent the in phase and out of phase components, the subscripts “Exp” and “Calc” referring to experimentally taken spectrum, and spectrum generated from the calculation outlined above. The summation symbol indicates summation over all the points in the spectrum and N_{Pts} is the number of data points. As the wings of the experimental lineshapes are not well described by Lorentzians, the error was only calculated for the center of the spectra, defined by edges just outside the extrema of the spectra. All the spectra (real and imaginary) are normalized by intensity before they are compared.

We generated error landscapes for a range of parameters which reasonably covered the experimentally possible configurations. Specifically, sample thicknesses out to ~ 3 mm were generally considered. However, no reasonable points were found beyond ~ 1.5 mm, which is consistent with our expectations from sample volumes and holders. The sample thickness, calculated based on the volumes assuming perfect, cylindrical packing were between 250 μm to 1.25 mm in the larger sample holder (~ 4 mm inner diameter) and was ~ 2.5 mm for the small holder (~ 2 mm inner diameter). For the small sample holder (sample 4), the calculated sample thickness was $\sim 10\times$ smaller than 2.5 mm, suggesting this estimation is inaccurate for this sample setup. However, for the other samples (all measured in the larger sample holder), we find in general that larger volumes lead to larger calculated thicknesses. However, the trend is neither perfect, nor do the absolute thicknesses match, which can likely be explained by the fact that the approxima-

tion of a flat sample is poorly realized given the high sample viscosity encountered before freezing (resulting in a significant meniscus). While signal intensity does generally increase with increasing volume, effects due to sample geometry and the short wavelength compared to sample thickness (particularly for larger volumes) results in a nonlinear relationship between signal strength and volume, and some variability is encountered based on the quality of the loading.

As a general principle, we wished to investigate the local minima with values near to that of the global minimum to determine if local minima provided better parameters estimates than the global minimum, and to gauge the degree of confidence in our parameter estimates. We restricted our investigation of minima to error values within 250% of the global minimum, to screen only local minima which provide good agreement with the experimental lines. Thus, much of the parameter space shown in forthcoming figures is yellow indicating a comparatively high error value. In all cases, excepting one, the global minimum was retained after reviewing the qualifying local minima. The evaluations of all five experiments are presented below with a brief discussion in each case evaluating the reasonableness of the parameters. In all cases, the parameters cited in the manuscript are those for the minima which are boxed and have a blue arrow. These parameters are then used to determine the linewidth of the susceptibility response, which is then the linewidth cited in the manuscript.

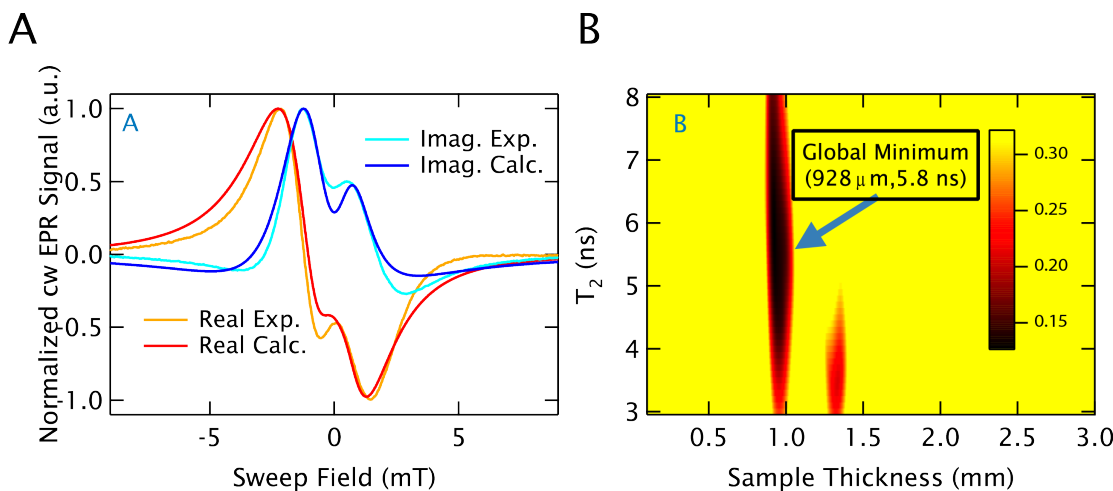


Figure D.2: Sample 1 Error Plots. **A.** The real and imaginary parts of the experimental spectrum ($Real_{Exp.}$ and $Imag_{Exp.}$, respectively) are plotted for sample 1 ($\bar{r} = 1.8$ nm (50 mM)) along with the spectrum calculated from the best fit parameters shown in **B** ($Real_{Calc.}$ and $Imag_{Calc.}$, respectively). **B.** The error landscape for the experimental spectrum shown in **A** is plotted. The unusual lineshapes provide a simple landscape with one clear, robust global minimum, which described the spectral features better than the visible local minimum. The values of the minimum are shown in the boxed inset text with blue arrow, which provides the parameters for the calculated spectrum shown in **A**.

Sample 1

The first sample (shown in Fig. D.2A) has a spectrum showing substantial deviation from a single line, which generated an error landscape with a clear minimum value as shown in Fig. D.2B. Although another local minimum exists (located at $d \sim 1.3$ mm, $T_2 \sim 3.5$ ns), the error value was more than 50% higher than the chosen global minimum, and only the global minimum reproduced the oscillations in the experimental lineshape well. Calculations with parameters near this local minimum resulted in spectra with broader features, which smoothed out the oscillations substantially. Thus, the robust global minimum located at $d = 928$

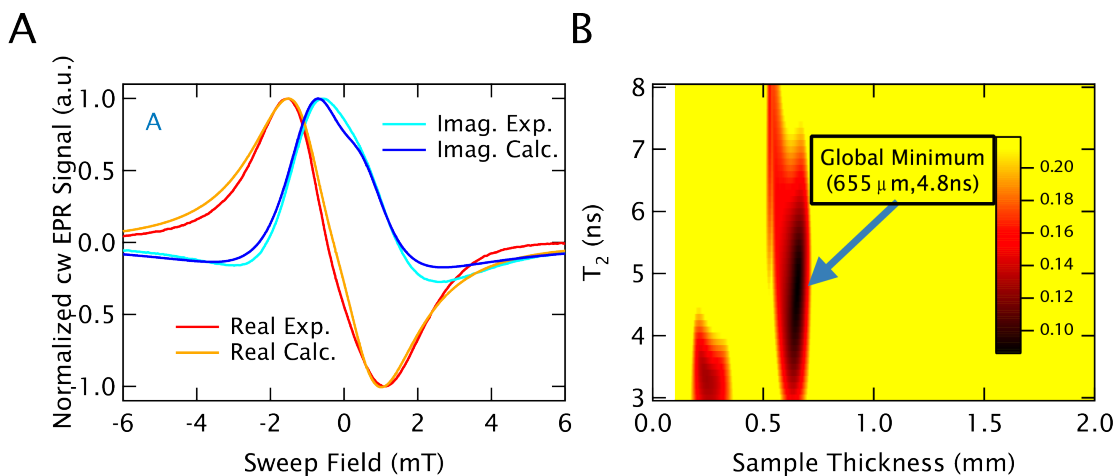


Figure D.3: Sample 2 Error Plots. **A.** The real and imaginary parts of the experimental spectrum ($Real_{Exp.}$ and $Imag_{Exp.}$, respectively) are plotted for sample 2 ($\bar{r} = 1.8$ nm (50 mM)) along with the spectrum calculated from the best fit parameters shown in **B** ($Real_{Calc.}$ and $Imag_{Calc.}$, respectively). **B.** The error landscape for the experimental spectrum shown in **A** is plotted, with a nearby local minimum with a value within 50% of the global minimum (in the lower left of the error landscape). However, as described further in the text, the global minimum better described the spectrum and so was used. The values of the minimum are shown in the boxed inset text with blue arrow, and provide the parameters for the calculated spectrum shown in **A**.

μ m and $T_2 = 4.8$ ns was used, and the resulting calculated spectrum is shown in Fig. D.2A.

Sample 2

The experimental spectrum for sample 2 is shown in Fig. D.3A and does not display substantial deviations from a single line as was the case for sample 1, but rather is broadened by the effects from refractive broadening. Fig. D.3B shows an error landscape with both a global and local minimum. Again, as expected from the error plots, we found that the local minimum offered a less reliable fit,

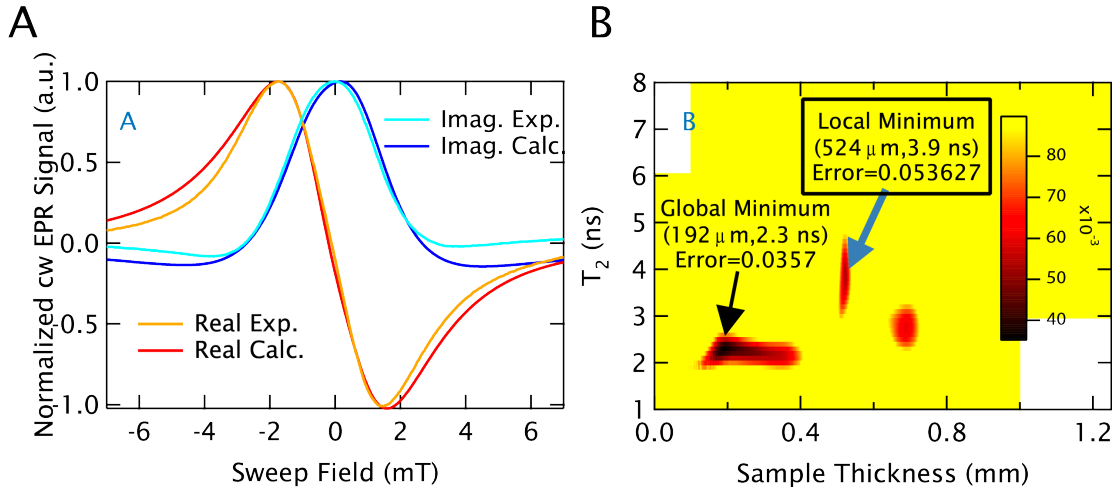


Figure D.4: Sample 3 Error Plots. **A.** The real and imaginary parts of the experimental spectrum ($Real_{Exp.}$ and $Imag_{Exp.}$, respectively) are plotted for sample 3 ($\bar{r} = 1.8 \text{ nm}$ (50 mM)) along with the spectrum calculated from the best fit parameters shown in **B** ($Real_{Calc.}$ and $Imag_{Calc.}$, respectively). **B.** The error landscape for the experimental spectrum shown in **A** is plotted. The error landscape is more complicated than the previous two, with a two local minima which generate spectra similar to that of the global minimum. Although unequivocally justifying one set of parameters was not possible, the local minimum at $d = 524 \mu\text{m}$ and $T_2 = 3.9 \text{ ns}$ is reasoned in the text to be most consistent with previous results and so was chosen. The values of this minimum are shown in the boxed inset text with blue arrow, and provide the parameters for the calculated spectrum shown in **A**.

especially in the wings of the spectrum, where it was substantially broader. Thus, the global minimum located at $d = 928 \mu\text{m}$ and $T_2 = 4.8 \text{ ns}$ was used, and the resulting calculated spectrum is shown in Fig. D.3A. However, the differences in lineshape between the local and global minimum are not as drastic as in the previous case, where obvious features were missing/obscured.

Sample 3

The spectrum of the third sample is presented in Fig. D.4A and leads to a complicated error landscape. Fig. D.3B shows the error landscape with two different local minima in addition to the global minimum. Although the local minimum at $d = 524 \mu\text{m}$ and $T_2 = 3.9 \text{ ns}$ produces a lineshape with a higher error in the central part of the spectrum (compared to the global minimum), it agrees slightly better in the wings. However, the two local minima and the global minimum generate spectra which look largely similar; there are no distinguishing features (such as oscillations) to help in discriminating between them. This helps demonstrate the subtlety of the problem in the case of moderate effects from refractive broadening, where the effect causes some broadening of the line, but no dramatic change in the features. Essentially, the broadness of the line can then result either from refractive broadening (which depend strongly on sample thickness), or from dipolar broadening (which affects T_2). Given that our experimental lines are already non-Lorentzian, we cannot distinguish well the best possible parameters easily. However, we note that the volume for this sample was roughly 50% of that employed in sample 1 (Fig. D.2A), using the same sample holder, making $d \sim 500 \mu\text{m}$ a more reasonable physical estimate of the thickness. Thus, facing the inability to clearly distinguish the quality of parameters purely from the spectral comparison we reason that that the local minimum at $d = 524 \mu\text{m}$ and $T_2 = 3.9 \text{ ns}$ gives a result which is consistent in terms of thickness and has comparable T_2

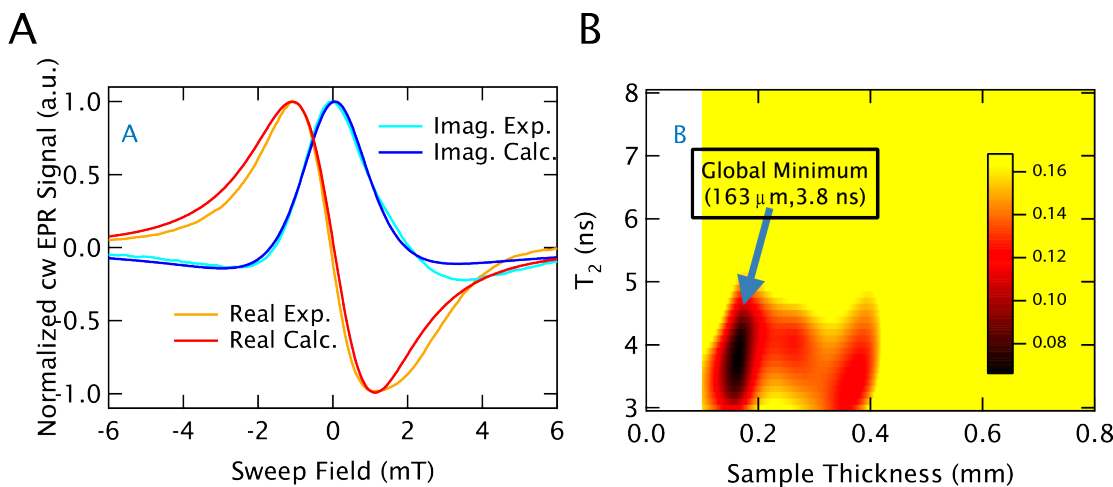


Figure D.5: Sample 4 Error Plots. **A.** The real and imaginary parts of the experimental spectrum ($Real_{Exp.}$ and $Imag_{Exp.}$, respectively) are plotted for sample 4 ($\bar{r} = 1.8 \text{ nm}$ (50 mM)) along with the spectrum calculated from the best fit parameters shown in **B** ($Real_{Calc.}$ and $Imag_{Calc.}$, respectively). **B.** The error landscape for the experimental spectrum shown in **A** is plotted. This error landscape offers a clear global minimum which describes the lineshape well, while the local minima present errors more than 50% above that of the global minimum. The values of the minimum are shown in the boxed inset text with blue arrow, and provide the parameters for the calculated spectrum shown in **A**.

values with previous results. Therefore is used as the most reasonable parameter values as shown Fig. D.4A.

Sample 4

The spectrum of the 4th sample is shown in Fig. D.5A. Although there are no dramatic deviations from a single line, the error landscape in Fig. D.5B offers a clear global minimum that describes the lineshape well. The nearby local minima offer the correct qualitative lineshape, but produce error values more than 50% great than the global minimum. In the absence of clear distinguishing features

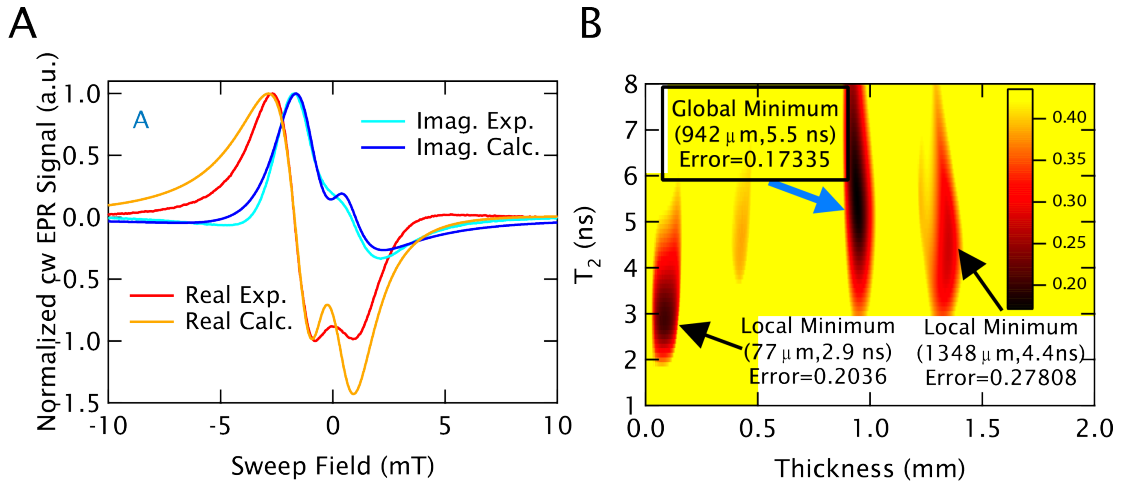


Figure D.6: Sample 5 Error Plots. **A.** The real and imaginary parts of the experimental spectrum ($Real_{Exp.}$ and $Imag_{Exp.}$, respectively) are plotted for sample 5 ($\bar{r} = 1.8$ nm (50 mM)) along with the spectrum calculated from the best fit parameters shown in B ($Real_{Calc.}$ and $Imag_{Calc.}$, respectively). **B.** The error landscape for the experimental spectrum shown in A is plotted. This error landscape offers a distinct global minimum and two local minima. Although the local minima both provide reasonable error values, neither describes the lineshape features properly, and so the global minimum is used. The values of the minimum are shown in the boxed inset text with blue arrow, and provide the parameters for the calculated spectrum shown in **A**.

of the experimental spectrum (such as oscillations), it is difficult to determine the best spectrum by eye, and so we selected the global minimum at $d = 163$ μm and $T_2 = 3.8$ ns. Further, these local minima do not have substantially different T_2 values than the global minimum, and so would not dramatically alter the estimated linewidth.

Sample 5

The 5th spectrum shows substantial deviations from a simple line as shown in Fig. D.6A. However, the error landscape, shown in Fig. D.5B shows a deep global

minimum, but two local minima which also offer reasonable error values (at ~ 0.1 mm and 1.3 mm). However, local minimum $d \sim 0.1$ mm does not produce any of the oscillations observed in the experimental spectra. Alternately, the local minimum at $d \sim 1.3$ mm does present some oscillations, but they do not agree well with those observed in experiments. Thus, the global minimum at $d = 942$ μm and $T_2 = 5.5$ ns was used to determine the true linewidth in the presence of refractive broadening, as it describes the experimental spectrum well.

Bibliography

- [1] F. Bloch, W. W. Hansen, and M. Packard. The nuclear induction experiment. *Physical Review*, 70(7-8):474–485, 1946. PR.
- [2] E. M. Purcell, H. C. Torrey, and R. V. Pound. Resonance absorption by nuclear magnetic moments in a solid. *Physical Review*, 69(1-2):37–38, 1946. PR.
- [3] Research Collaboratory for Structural Bioinformatics. Pdb current holdings breakdown, 2013.
- [4] R. C. deCharms. Applications of real-time fmri. *Nat Rev Neurosci*, 9(9):720–729, 2008. 10.1038/nrn2414.
- [5] E. K. Zavoisky. The paramagnetic absorption of a solution in parallel fields. *J. Phys. USSR*, 8:377–380, 1944.
- [6] E. K. Zavoisky. *Paramagnetic Absorption in Orthogonal and Parallel Fields for Salts, Solutions and Metals*. PhD thesis, 1944.

- [7] G. R. Eaton, S. S. Eaton, and K. M. Salikhov. *Foundations of Modern EPR*. World Scientific Publishing Company, 1998.
- [8] D. Rugar, R. Budakian, H. J. Mamin, and B. W. Chui. Single spin detection by magnetic resonance force microscopy. *Nature*, 430(6997):329–332, 2004. 10.1038/nature02658.
- [9] V. I. Krinichnyi. *High-Field ESR Spectroscopy of Conductive Polymers*, pages 307–338. John Wiley & Sons, Inc., 2006.
- [10] W. Lubitz, K. Mobius, and K-P. Dinse. High-field epr in biology, chemistry and physics, 2005.
- [11] A. Savitsky and K. Mbius. High-field epr. *Photosynthesis Research*, 102(2-3):311–333, 2009.
- [12] O. Grinberg and L. J. Berliner. *Very High Frequency (VHF) ESR/EPR*, volume 22 of *Biological Magnetic Resonance*. Springer, 2004.
- [13] P. C. Riedi. *Progress in High-Field EPR of Inorganic Materials*, volume 20, chapter 9, pages 338–373. Royal Society of Chemistry Publishing, 2007.
- [14] S. K. Misra. *Multifrequency Electron Paramagnetic Resonance: Theory and Applications*. Wiley-VCH, 2011.
- [15] A. Abragam. *The Principles of Nuclear Magnetism*. The International Series of Monographs on Physics. Oxford University Press, London, 1961.

- [16] C. P. Slichter. *Principles of Magnetic Resonance*. Springer, 1990.
- [17] P. Callaghan. *Principles of Nuclear Magnetic Resonance Microscopy*. Clarendon Press, 1993.
- [18] J. A. Weil and J. R. Bolton. *Electron Paramagnetic Resonance: Elementary Theory and Practical Applications*. Wiley, 2007.
- [19] C.P. Poole. *Electron Spin Resonance: A Comprehensive Treatise on Experimental Techniques*. Dover Publications, Incorporated, 1983.
- [20] A. Schweiger and G. Jeschke. *Principles of pulse electron paramagnetic resonance spectroscopy*. Oxford University Press, Incorporated, 2001.
- [21] J. J. Sakurai. *Modern Quantum Mechanics (Revised Edition)*. Addison Wesley, 1993.
- [22] A. Abragam and B. Bleaney. *Electron Paramagnetic Resonance of Transition Ions*. Oxford University Press, 1970.
- [23] J. P. Hornak and J. H. Freed. Spectral rotation in pulsed esr spectroscopy. *Journal of Magnetic Resonance (1969)*, 67(3):501–518, 1986.
- [24] E. L. Hahn. Spin echoes. *Physical Review*, 80(4):580–594, 1950. PR.
- [25] B. R. McGarvey. The isotropic hyperfine interaction. *The Journal of Physical Chemistry*, 71(1):51–66, 1967.

- [26] A. I. Smirnov, A. Ruuge, V. A. Reznikov, M. A. Voinov, and I. A. Grigor'ev. Site-directed electrostatic measurements with a thiol-specific pH-sensitive nitroxide: differentiating local pK and polarity effects by high-field EPR. *Journal of the American Chemical Society*, 126(29):8872–8873, 2004.
- [27] J. Solyom. *Fundamental of the Physics of Solids*, volume 1 Structure and Dynamics. Springer, 2007.
- [28] T. A. Miller, R. N. Adams, and P. M. Richards. Quantitative observation of slow and fast exchange in EPR spectra of organic free radicals. *The Journal of Chemical Physics*, 44(10):4022–4024, 1966.
- [29] M. J.N. Junk. *Assessing the functional structure of molecular transporters by EPR spectroscopy*. Springer, 2012.
- [30] L. J. Berliner, S. S. Eaton, and G. R. Eaton. *Distance Measurements in Biological Systems by EPR*, volume 19 of *Biological Magnetic Resonance*. Springer, 2000.
- [31] V. W. Cornish, D. R. Benson, C. A. Altenbach, K. Hideg, W. L. Hubbell, and P. G. Schultz. Site-specific incorporation of biophysical probes into proteins. *Proceedings of the National Academy of Sciences*, 91(8):2910–2914, 1994.
- [32] J. Braman. *In vitro mutagenesis protocols*, volume 182. Springer, 2004.

- [33] C. Altenbach, S. L. Flitsch, H. G. Khorana, and W. L. Hubbell. Structural studies on transmembrane proteins. 2. spin labeling of bacteriorhodopsin mutants at unique cysteines. *Biochemistry*, 28(19):7806–7812, 1989.
- [34] C. Altenbach, T. Marti, H. G. Khorana, and W. L. Hubbell. Transmembrane protein structure: Spin labeling of bacteriorhodopsin mutants. *Science*, 248(4959):1088–1092, 1990.
- [35] G. L. Millhauser. Selective placement of electron spin resonance spin labels: new structural methods for peptides and proteins. *Trends in Biochemical Sciences*, 17(11):448–452, 1992.
- [36] O. Schiemann, N. Piton, J. Plackmeyer, B. E. Bode, T. F. Prisner, and J. W. Engels. Spin labeling of oligonucleotides with the nitroxide tpa and use of peldor, a pulse epr method, to measure intramolecular distances. *Nat. Protocols*, 2(4):904–923, 2007. 10.1038/nprot.2007.97.
- [37] W. L. Hubbell, D. S. Cafiso, and C. Altenbach. Identifying conformational changes with site-directed spin labeling. *Nat Struct Mol Biol*, 7(9):735–739, 2000. 10.1038/78956.
- [38] G. Jeschke and Y. Polyhach. Distance measurements on spin-labelled biomacromolecules by pulsed electron paramagnetic resonance. *Physical Chemistry Chemical Physics*, 9(16):1895–1910, 2007.

- [39] G. Jeschke. Deer distance measurements on proteins. *Annual Review of Physical Chemistry*, 63(1):419–446, 2012.
- [40] W. L. Hubbell and C. Altenbach. Investigation of structure and dynamics in membrane proteins using site-directed spin labeling. *Current Opinion in Structural Biology*, 4(4):566–573, 1994.
- [41] K.M Stone, J. Voska, M. Kinnebrew, A. Pavlova, M.J. N. Junk, and S. Han. Structural insight into proteorhodopsin oligomers. *Biophysical Journal*, 104(2):472–481, 2013.
- [42] S. S. Eaton and G. R. Eaton. *Distance Measurements by CW and Pulsed EPR*, volume 19 of *Biological Magnetic Resonance*, chapter 1, pages 1–27. Springer US, 2002.
- [43] H. J. Steinhoff, N. Radzwill, W. Thevis, V. Lenz, D. Brandenburg, A. Antson, G. Dodson, and A. Wollmer. Determination of interspin distances between spin labels attached to insulin: comparison of electron paramagnetic resonance data with the x-ray structure. *Biophysical Journal*, 73(6):3287–3298, 1997.
- [44] G. Jeschke. Determination of the nanostructure of polymer materials by electron paramagnetic resonance spectroscopy. *Macromolecular Rapid Communications*, 23(4):227–246, 2002.

- [45] G. E. Pake. Nuclear resonance absorption in hydrated crystals: Fine structure of the proton line. *The Journal of Chemical Physics*, 16(4):327–336, 1948.
- [46] J. E. Banham, C. M. Baker, S. Ceola, I. J. Day, G. H. Grant, E. J. J. Groenen, C. T. Rodgers, G. Jeschke, and C. R. Timmel. Distance measurements in the borderline region of applicability of cw epr and deer: A model study on a homologous series of spin-labelled peptides. *Journal of Magnetic Resonance*, 191(2):202–218, 2008. doi: 10.1016/j.jmr.2007.11.023.
- [47] M. D. Rabenstein and Y. K. Shin. Determination of the distance between two spin labels attached to a macromolecule. *Proceedings of the National Academy of Sciences*, 92(18):8239–8243, 1995.
- [48] H. W. Spiess. Addendum to the paper dead-time free measurement of dipole-dipole interactions between electron spins by m. pannier, s. veit, a. godt, g. jeschke, and h.w. spiess [j. magn. reson. 142 (2000) 331340]. *Journal of Magnetic Resonance*, 213(2):326–328, 2011.
- [49] A. D. Milov, K. M. Salikhov, and M. D. Shirov. Application of eldor in electron-spin echo for paramagnetic center space distribution in solids. *Fiz. Tverd. Tela*, 23:975–982, 1981.
- [50] A. D. Milov, A. B. Ponomarev, and Yu. D. Tsvetkov. Electron-electron double resonance in electron spin echo: Model biradical systems and the

- sensitized photolysis of decalin. *Chemical Physics Letters*, 110(1):67–72, 1984. doi: 10.1016/0009-2614(84)80148-7.
- [51] V. Pfannebecker, H. Klos, M. Hubrich, T. Volkmer, A. Heuer, U. Wiesner, and H. W. Spiess. Determination of end-to-end distances in oligomers by pulsed epr. *The Journal of Physical Chemistry*, 100(32):13428–13432, 1996.
- [52] M. Pannier, S. Veit, A. Godt, G. Jeschke, and H. W. Spiess. Dead-time free measurement of dipole-dipole interactions between electron spins. *Journal of Magnetic Resonance*, 142(2):331–340, 2000. doi: 10.1006/jmre.1999.1944.
- [53] G. Sicoli, G. Mathis, O. Delalande, Y. Boulard, D. Gasparutto, and S. Gambarelli. Double electronelectron resonance (deer): A convenient method to probe dna conformational changes. *Angewandte Chemie*, 120(4):747–749, 2008.
- [54] R. Ward, D. J. Keeble, H. El-Mkami, and D. G. Norman. Distance determination in heterogeneous dna model systems by pulsed epr. *ChemBioChem*, 8(16):1957–1964, 2007.
- [55] G. Jeschke, A. Bender, H. Paulsen, H. Zimmermann, and A. Godt. Sensitivity enhancement in pulse epr distance measurements. *Journal of Magnetic Resonance*, 169(1):1–12, 2004.
- [56] G. Jeschke. Distance measurements in the nanometer range by pulse epr. *ChemPhysChem*, 3(11):927–932, 2002.

- [57] G. W. Reginsson and O. Schiemann. Pulsed electron-electron double resonance: beyond nanometre distance measurements on biomacromolecules. *Biochemical Journal*, 434(3):353–363, 2011.
- [58] O. Schiemann and T. F. Prisner. Long-range distance determinations in biomacromolecules by epr spectroscopy. *Quarterly Reviews of Biophysics*, 40(01):1–53, 2007.
- [59] Y. D. Tsvetkov, A. D. Milov, and A. G. Maryasov. Pulsed electron-electron double resonance (peldor) as epr spectroscopy in nanometre range. *Russian Chemical Reviews*, 77(6):487, 2008.
- [60] P. P. Borbat, E. R. Georgieva, and J. H. Freed. Improved sensitivity for long-distance measurements in biomolecules: Five-pulse double electron-electron resonance. *The Journal of Physical Chemistry Letters*, 4(1):170–175, 2012.
- [61] G. Jeschke, V. Chechik, P. Ionita, A. Godt, H. Zimmermann, J. Banham, C. R. Timmel, D. Hilger, and H. Jung. Deeranalysis2006a comprehensive software package for analyzing pulsed eldor data. *Applied Magnetic Resonance*, 30(3-4):473–498, 2006.
- [62] G. Jeschke, A. Koch, U. Jonas, and A. Godt. Direct conversion of epr dipolar time evolution data to distance distributions. *Journal of Magnetic Resonance*, 155(1):72–82, 2002.

- [63] G. Jeschke, G. Panek, A. Godt, A. Bender, and H. Paulsen. Data analysis procedures for pulse epr measurements of broad distance distributions. *Applied Magnetic Resonance*, 26(1):223–244, 2004.
- [64] G. Jeschke. Deeranalysis 2013 user manual, 2013.
- [65] E. R. Georgieva, T. F. Ramlall, P. P. Borbat, J. H. Freed, and D. Eliezer. Membrane-bound α -synuclein forms an extended helix: Long-distance pulsed esr measurements using vesicles, bicelles, and rodlike micelles. *Journal of the American Chemical Society*, 130(39):12856–12857, 2008.
- [66] J. Jackson. *Classical Electrodynamics Third Edition*. Wiley, 1998.
- [67] G. A. Rinard, R. W. Quine, J. R. Harbridge, R. Song, G. R. Eaton, and S. S. Eaton. Frequency dependence of epr signal-to-noise. *Journal of Magnetic Resonance*, 140(1):218–227, 1999.
- [68] T. F. Prisner, M. Rohrer, and K. Mbius. Pulsed 95 ghz high-field epr heterodyne spectrometer with high spectral and time resolution. *Applied Magnetic Resonance*, 7(2-3):167–183, 1994.
- [69] W. Hofbauer, K. A. Earle, C. R. Dunnam, J. K. Moscicki, and J. H. Freed. High-power 95 ghz pulsed electron spin resonance spectrometer. *Review of Scientific Instruments*, 75(5):1194–1208, 2004.

- [70] D. Goldfarb, Y. Lipkin, A. Potapov, Y. Gorodetsky, B. Epel, A. M. Rait-simring, M. Radoul, and I. Kaminker. Hyscore and deer with an upgraded 95 ghz pulse epr spectrometer. *Journal of Magnetic Resonance*, 194(1):8–15, 2008.
- [71] P. A. S. Cruickshank, D. R. Bolton, D. A. Robertson, R. I. Hunter, R. J. Wyld, and G. M. Smith. A kilowatt pulsed 94 ghz electron paramagnetic resonance spectrometer with high concentration sensitivity, high instantaneous bandwidth, and low dead time. *Review of Scientific Instruments*, 80(10):103102–15, 2009.
- [72] H. Ghimire, R. M. McCarrick, D. E. Budil, and G. A. Lorigan. Significantly improved sensitivity of q-band peldor/deer experiments relative to x-band is observed in measuring the intercoil distance of a leucine zipper motif peptide (gcn4-lz). *Biochemistry*, 48(25):5782–5784, 2009.
- [73] Y. Polyhach, E. Bordignon, R. Tschaggelar, S. Gandra, A. Godt, and G. Jeschke. High sensitivity and versatility of the deer experiment on nitroxide radical pairs at q-band frequencies. *Physical Chemistry Chemical Physics*, 14(30):10762–10773, 2012.
- [74] E. J. Reijerse. High-frequency epr instrumentation. *Applied Magnetic Resonance*, 37(1-4):795–818, 2010.

- [75] K. Mbius and A. Savitsky. *High-field EPR spectroscopy on proteins and their model systems : characterization of transient paramagnetic states*. Royal Society of Chemistry, Cambridge, UK, 2009. (Great Britain).
- [76] Ya. S. Lebedev. Very-high-field epr and its applications. *Applied Magnetic Resonance*, 7(2-3):339–362, 1994.
- [77] A. A. Galkin, O. Ya. Grinberg, A. A. Dubinskii, N. N. Kabdin, V. N. Krymov, V. I. Kurochkin, Ya. S. Lebedev, L. G. Oranskii, and V. F. Shuvalov. Epr spectrometer in 2-mm range for chemical research. *Instrum. Exp. Tech*, 20(4):1229–1233, 1977.
- [78] W. B. Lynch, K. A. Earle, and J. H. Freed. 1-mm wave esr spectrometer. *Review of Scientific Instruments*, 59(8):1345–1351, 1988.
- [79] R. T. Weber, J. A. J. M. Disselhorst, L. J. Prevo, J. Schmidt, and W. T. H. Wenckebach. Electron spin-echo spectroscopy at 95 ghz. *Journal of Magnetic Resonance (1969)*, 81(1):129–144, 1989.
- [80] P Hofer, A. Kamlowksi, G.G. Maresch, D. Schmalbein, and R. T. Weber. The bruker elexsys e600/680 w-band spectrometer series. *Very High-Frequency (VHF) ESR/EPR*, 22:401–429, 2004.
- [81] I. Gromov, V. Krymov, P. Manikandan, D. Arieli, and D. Goldfarb. A w-band pulsed endor spectrometer: Setup and application to transition metal centers. *Journal of Magnetic Resonance*, 139(1):8–17, 1999.

- [82] P. Dorlet, S. A. Seibold, G. T. Babcock, G. J. Gerfen, W. L. Smith, A.-l. Tsai, and S. Un. High-field epr study of tyrosyl radicals in prostaglandin h2 synthase-1. *Biochemistry*, 41(19):6107–6114, 2002.
- [83] K. V. Lakshmi, M. J. Reifler, G. W. Brudvig, O. G. Poluektov, A. M. Wagner, and M. C. Thurnauer. High-field epr study of carotenoid and chlorophyll cation radicals in photosystem ii. *The Journal of Physical Chemistry B*, 104(45):10445–10448, 2000.
- [84] C. Sirtori. Applied physics: Bridge for the terahertz gap. *Nature*, 417(6885):132–133, 2002. 10.1038/417132b.
- [85] P. H. Siegel. Terahertz technology. *Microwave Theory and Techniques, IEEE Transactions on*, 50(3):910–928, 2002.
- [86] P. W. Gwyn. Filling the thz gaphigh power sources and applications. *Reports on Progress in Physics*, 69(2):301, 2006.
- [87] J. van Tol, L.-C. Brunel, and R. J. Wylde. A quasioptical transient electron spin resonance spectrometer operating at 120 and 240 ghz. *Review of Scientific Instruments*, 76(7):074101–8, 2005.
- [88] S. Takahashi, L.-C. Brunel, D. T. Edwards, J. van Tol, G. Ramian, S. Han, and M. S. Sherwin. Free-electron laser-powered electron paramagnetic resonance spectroscopy. *Nature*, 2012.

- [89] X. Haiyong, G. S. Schoenthal, J. L. Hesler, T. W. Crowe, and R. M. Weikle. Nonohmic contact planar varactor frequency upconverters for terahertz applications. *Microwave Theory and Techniques, IEEE Transactions on*, 55(4):648–655, 2007.
- [90] G. W. Morley, D. R. McCamey, H. A. Seipel, L. C. Brunel, J. van Tol, and C. Boehme. Long-lived spin coherence in silicon with an electrical spin trap readout. *Physical Review Letters*, 101(20):207602, 2008. PRL.
- [91] E. J. Hustedt and A. H. Beth. Nitroxide spin-spin interactions: Applications to protein structure and dynamics. *Annual Review of Biophysics and Biomolecular Structure*, 28(1):129–153, 1999.
- [92] D. T. Edwards, S. Takahashi, M. S. Sherwin, and S. Han. Distance measurements across randomly distributed nitroxide probes from the temperature dependence of the electron spin phase memory time at 240 ghz. *Journal of Magnetic Resonance*, 223(0):198–206, 2012.
- [93] R. Ward, A. Bowman, E. Sozudogru, H. El-Mkami, T. Owen-Hughes, and D. G. Norman. Epr distance measurements in deuterated proteins. *Journal of Magnetic Resonance*, 207(1):164–167, 2010. doi: 10.1016/j.jmr.2010.08.002.
- [94] S. Takahashi, R. Hanson, J. van Tol, M. S. Sherwin, and D. D. Awschalom. Quenching spin decoherence in diamond through spin bath polarization.

- Physical Review Letters*, 101(4):047601, 2008. PRL.
- [95] S. Takahashi, I. S. Tupitsyn, J. van Tol, C. C. Beedle, D. N. Hendrickson, and P. C. E. Stamp. Decoherence in crystals of quantum molecular magnets. *Nature*, 476(7358):76–79, 2011. 10.1038/nature10314.
- [96] S. Takahashi, J. van Tol, C. C. Beedle, D. N. Hendrickson, L.-C. Brunel, and M. S. Sherwin. Coherent manipulation and decoherence of $s=10$ single-molecule magnets. *Physical Review Letters*, 102(8):087603, 2009. Copyright (C) 2010 The American Physical Society Please report any problems to prola@aps.org PRL.
- [97] C. Kutter, H. P. Moll, J. van Tol, H. Zuckermann, J. C. Maan, and P. Wyder. Electron-spin echoes at 604 ghz using far infrared lasers. *Physical Review Letters*, 74(15):2925–2928, 1995. PRL.
- [98] S. Chandrasekhar. Stochastic problems in physics and astronomy. *Reviews of Modern Physics*, 15(1):1–89, 1943. RMP.
- [99] I. M. Brown. *Electron spin-echo studies of relaxation processes in molecular solids*, pages 195–229. Wiley-Interscience, Toronto, Canada, 1979.
- [100] K. M. Salikhov and Y. D. Tsvetkov. *Electron spin-echo studies of relaxation processes in molecular solids*, pages 231–277. Wiley-Interscience, Toronto, Canada, 1979.

- [101] M. Romanelli and L. Kevan. Evaluation and interpretation of electron spin-echo decay part i: Rigid samples. *Concepts in Magnetic Resonance*, 9(6):403–430, 1997.
- [102] A. Zecevic, G. R. Eaton, S. S. Eaton, and M. Lindgren. Dephasing of electron spin echoes for nitroxyl radicals in glassy solvents by non-methyl and methyl protons. *Molecular Physics*, 95(6):1255–1263, 1998.
- [103] A. Barbon, M. Brustolon, A. Lisa Maniero, M. Romanelli, and L.-C. Brunel. Dynamics and spin relaxation of tempone in a host crystal. an endor, high field epr and electron spin echo study. *Physical Chemistry Chemical Physics*, 1(17):4015–4023, 1999.
- [104] M. N. Berberan-Santos, E. N. Bodunov, and B. Valeur. Mathematical functions for the analysis of luminescence decays with underlying distributions 1. kohlrausch decay function (stretched exponential). *Chemical Physics*, 315(1-2):171–182, 2005. doi: DOI: 10.1016/j.chemphys.2005.04.006.
- [105] A. D. Milov, Salikhov K. M., and Yu. D. Tsvetkov. Phase relaxation of hydrogen atoms stabilized in an amorphous matrix. *Soviet Physics Solid State*, 15(4):802–806, 1973.
- [106] M. J. Hope, M. B. Bally, G. Webb, and P. R. Cullis. Production of large unilamellar vesicles by a rapid extrusion procedure. characterization of size distribution, trapped volume and ability to maintain a membrane potential.

- Biochimica et Biophysica Acta (BBA) - Biomembranes*, 812(1):55–65, 1985.
doi: 10.1016/0005-2736(85)90521-8.
- [107] Y. Zhou, B. E. Bowler, G. R. Eaton, and S. S. Eaton. Electron spinlattice relaxation rates for high-spin fe(iii) complexes in glassy solvents at temperatures between 6 and 298 k. *Journal of Magnetic Resonance*, 144(1):115–122, 2000.
- [108] Y. Zhou, B. E. Bowler, K. Lynch, S. S. Eaton, and G. R. Eaton. Interspin distances in spin-labeled metmyoglobin variants determined by saturation recovery epr. *Biophysical Journal*, 79(2):1039–1052, 2000.
- [109] P. Lueders, G. Jeschke, and M. Yulikov. Double electronelectron resonance measured between gd3+ ions and nitroxide radicals. *The Journal of Physical Chemistry Letters*, 2(6):604–609, 2011.
- [110] I. Kaminker, H. Yagi, T. Huber, A. Feintuch, G. Otting, and D. Goldfarb. Spectroscopic selection of distance measurements in a protein dimer with mixed nitroxide and gd3+ spin labels. *Physical Chemistry Chemical Physics*, 14(13):4355–4358, 2012.
- [111] A. Potapov, H. Yagi, T. Huber, S. Jergic, N. E. Dixon, G. Otting, and D. Goldfarb. Nanometer-scale distance measurements in proteins using gd3+ spin labeling. *Journal of the American Chemical Society*, 132(26):9040–9048, 2010. doi: 10.1021/ja1015662.

- [112] A. M. Raitsimring, C. Gunanathan, A. Potapov, I. Efremenko, J. M. L. Martin, D. Milstein, and D. Goldfarb. Gd³⁺ complexes as potential spin labels for high field pulsed epr distance measurements. *Journal of the American Chemical Society*, 129(46):14138–14139, 2007. doi: 10.1021/ja075544g.
- [113] A. Pavlova, E. R. McCarney, D. W. Peterson, F. W. Dahlquist, J. Lew, and S. Han. Site-specific dynamic nuclear polarization of hydration water as a generally applicable approach to monitor protein aggregation. *Physical Chemistry Chemical Physics*, 11(31):6833–6839, 2009.
- [114] E. D. Walter, K. B. Sebby, R. J. Usselman, D. J. Singel, and M. J. Cloninger. Characterization of heterogeneously functionalized dendrimers by mass spectrometry and epr spectroscopy. *The Journal of Physical Chemistry B*, 109(46):21532–21538, 2005.
- [115] . Tth, L.r Helm, and A. E. Merbach. *Relaxivity of MRI Contrast Agents*, volume 221 of *Topics in Current Chemistry*, chapter 3, pages 61–101. Springer Berlin Heidelberg, 2002.
- [116] P. Caravan, J. J. Ellison, T. J. McMurry, and R. B. Lauffer. Gadolinium(iii) chelates as mri contrast agents: structure, dynamics, and applications. *Chemical Reviews*, 99(9):2293–2352, 1999.
- [117] J. G. Penfield and R. F. Reilly. What nephrologists need to know about gadolinium. *Nat Clin Pract Neph*, 3(12):654–668, 2007. 10.1038/ncp-

neph0660.

- [118] A. J. Spencer, S. A. Wilson, J. Batchelor, A. Reid, J. Pees, and E. Harpur. Gadolinium chloride toxicity in the rat. *Toxicologic Pathology*, 25(3):245–255, 1997.
- [119] S. Laurent, L. V. Elst, and R. N. Muller. Comparative study of the physico-chemical properties of six clinical low molecular weight gadolinium contrast agents. *Contrast Media & Molecular Imaging*, 1(3):128–137, 2006.
- [120] P. Caravan. Strategies for increasing the sensitivity of gadolinium based mri contrast agents. *Chemical Society Reviews*, 35(6):512–523, 2006.
- [121] J. Reuben. Gadolinium(iii) as a paramagnetic probe for proton relaxation studies of biological macromolecules. binding to bovine serum albumin. *Biochemistry*, 10(15):2834–2838, 1971.
- [122] M. R. Jensen, G. Petersen, C. Lauritzen, J. Pedersen, and J. J. Led. Metal binding sites in proteins: identification and characterization by paramagnetic nmr relaxation. *Biochemistry*, 44(33):11014–11023, 2005.
- [123] C. D. Barry, A. C. T. North, J. A. Glasel, R. J. P. Williams, and A. V. Xavier. Quantitative determination of mononucleotide conformations in solution using lanthanide ion shift and broadening nmr probes. *Nature*, 232(5308):236–245, 1971. 10.1038/232236a0.

- [124] G. Pintacuda, M. John, X.-C. Su, and G. Otting. Nmr structure determination of proteinligand complexes by lanthanide labeling. *Accounts of Chemical Research*, 40(3):206–212, 2007.
- [125] G. Otting. Prospects for lanthanides in structural biology by nmr. *Journal of Biomolecular NMR*, 42(1):1–9, 2008.
- [126] G. Pintacuda, A. Moshref, A. Leonchiks, A. Sharipo, and G. Otting. Site-specific labelling with a metal chelator for protein-structure refinement. *Journal of Biomolecular NMR*, 29(3):351–361, 2004.
- [127] B. Graham, C. T. Loh, J. D. Swarbrick, P. Ung, J. Shin, H. Yagi, X. Jia, S. Chhabra, N. Barlow, G. Pintacuda, T. Huber, and G. Otting. DOTA-amide lanthanide tag for reliable generation of pseudocontact shifts in protein nmr spectra. *Bioconjugate Chemistry*, 22(10):2118–2125, 2011.
- [128] S. Ahlgren, A. Orlova, D. Rosik, M. Sandström, A. Sjöberg, B. Baastrup, O. Widmark, G. Fant, J. Feldwisch, and V. Tolmachev. Evaluation of maleimide derivative of DOTA for site-specific labeling of recombinant antibody molecules. *Bioconjugate Chemistry*, 19(1):235–243, 2007.
- [129] X.-C. Su, B. Man, S. Beeren, H. Liang, S. Simonsen, C. Schmitz, T. Huber, B. A. Messerle, and G. Otting. A dipicolinic acid tag for rigid lanthanide tagging of proteins and paramagnetic nmr spectroscopy. *Journal of the American Chemical Society*, 130(32):10486–10487, 2008. doi: 10.1021/ja803741f.

- [130] B. J. Tucker. *EPR of Powers, Crystals, and Clay of MRI Contrast Agents: Zero Field Splitting and Proton Relaxation*. PhD thesis, 2010.
- [131] A. Potapov, Y. Song, T. J. Meade, D. Goldfarb, A. V. Astashkin, and A. Raitsimring. Distance measurements in model bis-gd(iii) complexes with flexible "bridge". emulation of biological molecules having flexible structure with gd(iii) labels attached. *Journal of Magnetic Resonance*, 205(1):38–49, 2010. doi: DOI: 10.1016/j.jmr.2010.03.019.
- [132] O. Bj, L. Aravind, E. V. Koonin, M. T. Suzuki, A. Hadd, L. P. Nguyen, S. B. Jovanovich, C. M. Gates, R. A. Feldman, J. L. Spudich, E. N. Spudich, and E. F. DeLong. Bacterial rhodopsin: Evidence for a new type of phototrophy in the sea. *Science*, 289(5486):1902–1906, 2000.
- [133] C. Song, K.-N. Hu, C.-G. Joo, T. M. Swager, and R. G. Griffin. Totapol: A biradical polarizing agent for dynamic nuclear polarization experiments in aqueous media. *Journal of the American Chemical Society*, 128(35):11385–11390, 2006.
- [134] Y. Song, E. K. Kohlmeir, and T. J. Meade. Synthesis of multimeric mr contrast agents for cellular imaging. *Journal of the American Chemical Society*, 130(21):6662–6663, 2008. doi: 10.1021/ja0777990.
- [135] R. F. H. Viguier and A. N. Hulme. A sensitized europium complex generated by micromolar concentrations of copper(i): toward the detection of copper(i)

- in biology. *Journal of the American Chemical Society*, 128(35):11370–11371, 2006.
- [136] Jr. D. E. Prasuhn, R. M. Yeh, A. Obenaus, M. Manchester, and M. G. Finn. Viral mri contrast agents: coordination of gd by native virions and attachment of gd complexes by azide-alkyne cycloaddition. *Chemical Communications*, (12):1269–1271, 2007.
- [137] A. Raitsimring, A. Astashkin, J. Enemark, A. Blank, Y. Twig, Y. Song, and T. Meade. Dielectric resonator for ka-band pulsed epr measurements at cryogenic temperatures: Probehead construction and applications. *Applied Magnetic Resonance*, 42(4):441–452, 2012.
- [138] D. T. Edwards, Z. Ma, T. J. Meade, D. Goldfarb, S. Han, and M. S. Sherwin. Extending the distance range accessed with continuous wave epr with gd³⁺ spin probes at high magnetic fields. *Physical Chemistry Chemical Physics*, 15(27):11313–11326, 2013.
- [139] P P. Borbat and J. H. Freed. *Double-Quantum ESR and Distance Measurements*, volume 19 of *Biological Magnetic Resonance*, pages 383–459. Springer US, 2000.
- [140] P. P. Borbat and J. H. Freed. *Measuring Distances by Pulsed Dipolar ESR Spectroscopy: SpinLabeled Histidine Kinases*, volume Volume 423, pages 52–116. Academic Press, 2007.

- [141] Z. Yang, Y. Liu, P. P. Borbat, J. L. Zweier, J. H. Freed, and W. L. Hubbell. Pulsed esr dipolar spectroscopy for distance measurements in immobilized spin labeled proteins in liquid solution. *Journal of the American Chemical Society*, 134(24):9950–9952, 2012.
- [142] R. Dastvan, B. E. Bode, M. P. R. Karuppiah, A. Marko, S. Lyubenova, H. Schwalbe, and T. F. Prisner. Optimization of transversal relaxation of nitroxides for pulsed electron-electron double resonance spectroscopy in phospholipid membranes. *The Journal of Physical Chemistry B*, 114(42):13507–13516, 2010.
- [143] M. M. Teeter, A. Yamano, B. Stec, and U. Mohanty. On the nature of a glassy state of matter in a hydrated protein: Relation to protein function. *Proceedings of the National Academy of Sciences*, 98(20):11242–11247, 2001.
- [144] D. Ringe and G. A. Petsko. The glass transition in protein dynamics: what it is, why it occurs, and how to exploit it. *Biophysical Chemistry*, 105(23):667–680, 2003.
- [145] A. L. Tournier, J. Xu, and J. C. Smith. Translational hydration water dynamics drives the protein glass transition. *Biophysical Journal*, 85(3):1871–1875, 2003.
- [146] A. Raitsimring, A. Astashkin, O. Poluektov, and P. Caravan. High-field pulsed epr and endor of gd3+ complexes in glassy solutions. *Applied Mag-*

- netic Resonance*, 28(3):281–295, 2005.
- [147] M. Benmelouka, J. Van Tol, A. Borel, M. Port, L. Helm, L.-C. Brunel, and A. E. Merbach. A high-frequency epr study of frozen solutions of gd(iii) complexes: Straightforward determination of the zero-field splitting parameters and simulation of the nmrd profiles. *Journal of the American Chemical Society*, 128(24):7807–7816, 2006. doi: 10.1021/ja0583261.
- [148] J. S. Hyde and T. Sarna. Magnetic interactions between nitroxide free radicals and lanthanides or cu²⁺ in liquids. *The Journal of Chemical Physics*, 68(10):4439–4447, 1978.
- [149] L. B. Lane. Freezing points of glycerol and its aqueous solutions. *Industrial & Engineering Chemistry*, 17(9):924–924, 1925.
- [150] J. A. Trejo Gonzalez, M. P. Longinotti, and H. R. Corti. The viscosity of glycerolwater mixtures including the supercooled region. *Journal of Chemical & Engineering Data*, 56(4):1397–1406, 2011.
- [151] H. S. McHaourab, K. J. Oh, C. J. Fang, and W. L. Hubbell. Conformation of t4 lysozyme in solution. hinge-bending motion and the substrate-induced conformational transition studied by site-directed spin labeling. *Biochemistry*, 36(2):307–316, 1997.
- [152] J. S. Jr. Leigh. Esr rigid-lattice line shape in a system of two interacting spins. *The Journal of Chemical Physics*, 52(5):2608–2612, 1970.

- [153] J. Voss, L. Salwiski, H. R. Kaback, and W. L. Hubbell. A method for distance determination in proteins using a designed metal ion binding site and site-directed spin labeling: evaluation with t4 lysozyme. *Proceedings of the National Academy of Sciences*, 92(26):12295–12299, 1995.
- [154] G. Gonzalez, D. H. Powell, V. Tissieres, and A. E. Merbach. Water-exchange, electronic relaxation, and rotational dynamics of the mri contrast agent $[gd(dtpa-bma)(h_2o)]$ in aqueous solution: a variable pressure, temperature, and magnetic field oxygen-17 nmr study. *The Journal of Physical Chemistry*, 98(1):53–59, 1994.
- [155] D. H. Powell, O. M. Ni Dhubhghaill, D. Pubanz, L. Helm, Y. S. Lebedev, W. Schlaepfer, and A. E. Merbach. Structural and dynamic parameters obtained from ^{17}o nmr, epr, and nmrd studies of monomeric and dimeric gd^{3+} complexes of interest in magnetic resonance imaging: an integrated and theoretically self-consistent approach¹. *Journal of the American Chemical Society*, 118(39):9333–9346, 1996.
- [156] C. Altenbach, K.-J. Oh, R. J. Trabanino, K. Hideg, and W. L. Hubbell. Estimation of inter-residue distances in spin labeled proteins at physiological temperatures: experimental strategies and practical limitations. *Biochemistry*, 40(51):15471–15482, 2001.

- [157] M. Gordon-Grossman, I. Kaminker, Y. Gofman, Y. Shai, and D. Goldfarb. W-band pulse epr distance measurements in peptides using gd³⁺-dipicolinic acid derivatives as spin labels. *Physical Chemistry Chemical Physics*, 13(22):10771–10780, 2011.
- [158] H. Yagi, D. Banerjee, B. Graham, T. Huber, D. Goldfarb, and G. Otting. Gadolinium tagging for high-precision measurements of 6 nm distances in protein assemblies by epr. *Journal of the American Chemical Society*, 133(27):10418–10421, 2011. doi: 10.1021/ja204415w.
- [159] D. Friselli, C.A. Massa, M. Martinelli, L. Pardi, and I. Ricci. Simulation of the propagation effects in the hf-epr spectra of non-diluted magnetic materials. *Inorganica Chimica Acta*, 361(1415):4164–4166, 2008.
- [160] Ye Polyhach, A. Godt, C. Bauer, and G. Jeschke. Spin pair geometry revealed by high-field deer in the presence of conformational distributions. *Journal of Magnetic Resonance*, 185(1):118–129, 2007.
- [161] A. Marko, D. Margraf, H. Yu, Y. Mu, G. Stock, and T. Prisner. Molecular orientation studies by pulsed electron-electron double resonance experiments. *The Journal of Chemical Physics*, 130(6):064102–9, 2009.
- [162] J. E. Lovett, A. M. Bowen, C. R. Timmel, M. W. Jones, J. R. Dilworth, D. Caprotti, S. G. Bell, L. L. Wong, and J. Harmer. Structural informa-

- tion from orientationally selective deer spectroscopy. *Physical Chemistry Chemical Physics*, 11(31):6840–6848, 2009.
- [163] Y. Song, T. J. Meade, A. V. Astashkin, E. L. Klein, J. H. Enemark, and A. Raitsimring. Pulsed dipolar spectroscopy distance measurements in biomacromolecules labeled with gd(iii) markers. *Journal of Magnetic Resonance*, 210(1):59–68, 2011.
- [164] G. Jeschke, M. Sajid, M. Schulte, and A. Godt. Three-spin correlations in double electron-electron resonance. *Physical Chemistry Chemical Physics*, 11(31):6580–6591, 2009.
- [165] M. J. N. Junk, H. W. Spiess, and D. Hinderberger. Deer in biological multispin-systems: A case study on the fatty acid binding to human serum albumin. *Journal of Magnetic Resonance*, 210(2):210–217, 2011.
- [166] T. von Hagens, Y. Polyhach, M. Sajid, A. Godt, and G. Jeschke. Suppression of ghost distances in multiple-spin double electron-electron resonance. *Physical Chemistry Chemical Physics*, 15(16):5854–5866, 2013.
- [167] M. H. Ali and B. Imperiali. Protein oligomerization: How and why. *Bioorganic & Medicinal Chemistry*, 13(17):5013–5020, 2005.
- [168] S. Ferr and R. Franco. Oligomerization of g-protein-coupled receptors: A reality. *Current Opinion in Pharmacology*, 10(1):1–5, 2010.

- [169] O Beja, E N. Spudich, J. L. Spudich, M. Leclerc, and E. F. DeLong. Proteorhodopsin phototrophy in the ocean. *Nature*, 411(6839):786–789, 2001. 10.1038/35081051.
- [170] J. Hoffmann, L. Aslimovska, C. Bamann, C. Glaubitz, E. Bamberg, and B. Brutschy. Studying the stoichiometries of membrane proteins by mass spectrometry: microbial rhodopsins and a potassium ion channel. *Physical Chemistry Chemical Physics*, 12(14):3480–3485, 2010.
- [171] A. L. Klyszejko, S. Shastri, S. A. Mari, H. Grubmiller, D. J. Muller, and C. Glaubitz. Folding and assembly of proteorhodopsin. *Journal of Molecular Biology*, 376(1):35–41, 2008.
- [172] S. Hussain, J. M. Franck, and S. Han. Transmembrane protein activation refined by site-specific hydration dynamics. *Angewandte Chemie International Edition*, 52(7):1953–1958, 2013.
- [173] S. Reckel, D. Gottstein, J. Stehle, F. Lhr, M.-K. Verhoefen, M. Takeda, R. Silvers, M. Kainosho, C. Glaubitz, J. Wachtveitl, F. Bernhard, H. Schwalbe, P. Gntert, and V. Dtsch. Solution nmr structure of proteorhodopsin. *Angewandte Chemie International Edition*, 50(50):11942–11946, 2011.
- [174] B. E. Sturgeon and R. D. Britt. Sensitive pulsed epr spectrometer with an 8–18 ghz frequency range. *Review of Scientific Instruments*, 63(4):2187–2192,

1992.

- [175] T. F. Prisner, S. Un, and R. G. Griffin. Pulsed esr at 140 ghz. *Israel Journal of Chemistry*, 32(2-3):357–363, 1992.
- [176] B. D. Armstrong, D. T. Edwards, R. J. Wylde, S. A. Walker, and S. Han. A 200 ghz dynamic nuclear polarization spectrometer. *Physical Chemistry Chemical Physics*, 12(22):5920–5926, 2010.
- [177] G. W. Morley, L.-C. Brunel, and J. van Tol. A multifrequency high-field pulsed electron paramagnetic resonance/electron-nuclear double resonance spectrometer. *Review of Scientific Instruments*, 79(6):064703, 2008.
- [178] P. G. O’Shea and H. P. Freund. Free-electron lasers: Status and applications. *Science*, 292(5523):1853–1858, 2001.
- [179] G. Ramian. The new ucsb free-electron lasers. *Nuclear Instruments and Methods in Physics Research Section A: Accelerators, Spectrometers, Detectors and Associated Equipment*, 318(13):225–229, 1992.
- [180] S. Takahashi, G. Ramian, M. S. Sherwin, L. C. Brunel, and H. Van Tol. Submegahertz linewidth at 240 ghz from an injection-locked free-electron laser. *Applied Physics Letters*, 91(17):174102, 2007.

- [181] S. Takahashi, G. Ramian, and M. S. Sherwin. Cavity dumping of an injection-locked free-electron laser. *Applied Physics Letters*, 95(23):234102, 2009.
- [182] S. Takahashi, D. G. Allen, J. Seifter, G. Ramian, M. S. Sherwin, L.-C. Brunel, and J. van Tol. Pulsed epr spectrometer with injection-locked ucsb free-electron laser. *Infrared Physics & Technology*, 51(5):426–428, 2008.
- [183] P. F. Goldsmith. Quasioptical system: Gaussian beam quasioptical propagation and applications. *IEEE Press, New York, NY*, 21:221–282, 1998.
- [184] D. Oepts, A. F. G. van der Meer, and P. W. van Amersfoort. The free-electron-laser user facility felix. *Infrared Physics & Technology*, 36(1):297–308, 1995.
- [185] F. A. Hegmann and M. S. Sherwin. Generation of picosecond far-infrared pulses using laser-activated semiconductor reflection switches. *Proc. SPIE*, 2842:90–105, 1996.
- [186] M. F. Doty, B. E. Cole, B. T. King, and M. S. Sherwin. Wavelength-specific laser-activated switches for improved contrast ratio in generation of short thz pulses. *Review of Scientific Instruments*, 75(9):2921–2925, 2004.
- [187] P. A. S. Cruickshank, D. R. Bolton, D. A. Robertson, R. J. Wylde, and G. M. Smith. Reducing standing waves in quasi-optical systems by optimal feed-

- horn design. In *Infrared and Millimeter Waves, 2007 and the 2007 15th International Conference on Terahertz Electronics. IRMMW-THz. Joint 32nd International Conference on*, pages 941–942.
- [188] D. H. Martin and R. J. Wylde. Wideband circulators for use at frequencies above 100 ghz to beyond 350 ghz. *Microwave Theory and Techniques, IEEE Transactions on*, 57(1):99–108, 2009.
- [189] Y. B. Band. *Light and matter: electromagnetism, optics, spectroscopy and lasers*, volume 1. Wiley, 2006.
- [190] M. H. Levitt. Demagnetization field effects in two-dimensional solution nmr. *Concepts in Magnetic Resonance*, 8(2):77–103, 1996.
- [191] J. A. Osborn. Demagnetizing factors of the general ellipsoid. *Physical Review*, 67(11-12):351–357, 1945. PR.
- [192] Y.-Y. Lin, N. Lisitza, S. Ahn, and W. S. Warren. Resurrection of crushed magnetization and chaotic dynamics in solution nmr spectroscopy. *Science*, 290(5489):118–121, 2000.
- [193] D. T. Edwards, Y. Zhang, S. J. Glaser, S. Han, and M. S. Sherwin. Phase cycling with a 240 ghz, free electron laser-powered electron paramagnetic resonance spectrometer. *Physical Chemistry Chemical Physics*, 15(15):5707–5719, 2013.

- [194] J. Keeler. *Understanding NMR spectroscopy*. Wiley, 2011.
- [195] R. R. Ernst, G. Bodenhausen, and A. Wokaun. *Principles of nuclear magnetic resonance in one and two dimensions*. Clarendon Press Oxford, 1987.
- [196] D. Reichert and G. Hempel. Receiver imperfections and cyclops: An alternative description. *Concepts in Magnetic Resonance*, 14(2):130–139, 2002.
- [197] M. D. Bruch. Multidimensional nmr spectroscopy of liquids. *Practical Spectroscopy Series*, 21:145–238, 1996.
- [198] D. E. Demco, P. Van Hecke, and J. S. Waugh. Phase-shifted pulse sequence for measurement of spin-lattice relaxation in complex systems. *Journal of Magnetic Resonance (1969)*, 16(3):467–470, 1974.
- [199] R. R. Vold and G. Bodenhausen. Phase-shifted pulse sequence for measurement of spin-lattice relaxation in complex spin systems: An improvement. *Journal of Magnetic Resonance (1969)*, 39(2):363–366, 1980.
- [200] G. M. Smith, J. C. G. Lesurf, R. H. Mitchell, and P. C. Riedi. Quasi-optical cw mm-wave electron spin resonance spectrometer. *Review of Scientific Instruments*, 69(11):3924–3937, 1998.
- [201] A. J. Lin, N. L. Slack, A. Ahmad, C. X. George, C. E. Samuel, and C. R. Safinya. Three-dimensional imaging of lipid gene-carriers: Membrane

- charge density controls universal transfection behavior in lamellar cationic liposome-dna complexes. *Biophysical Journal*, 84(5):3307–3316, 2003.
- [202] D. Scott and C. A. Tout. Nearest neighbour analysis of random distributions on a sphere. *Royal Astronomical Society, Monthly Notices*, 241:109–117, 1989.
- [203] R. A. Krebs, A. M. DeVita, R. Parthasarathy, U. Alexiev, D. Dunmire, and M. S. Braiman. Purification and spectroscopic studies of proteorhodopsin. *Biophys. J*, 82:224A–224A, 2002.
- [204] R. D. Parthasarathy, T. Caterino, and M. S. Braiman. Site-directed mutagenesis of proteorhodopsin; study of light activated proton transfer.’. *Biophysical Journal*, 82(1):226A–227A, 2002.
- [205] J. R. Hillebrecht, J. Galan, R. Rangarajan, L. Ramos, K. McCleary, D. E. Ward, J. A. Stuart, and R. R. Birge. Structure, function, and wavelength selection in blue-absorbing proteorhodopsin. *Biochemistry*, 45(6):1579–1590, 2006.
- [206] B. Xi, W. C. Tetley, D. L. Marcy, C. Zhong, G. Whited, R. R. Birge, and J. A. Stuart. Evaluation of blue and green absorbing proteorhodopsins as holographic materials. *The Journal of Physical Chemistry B*, 112(8):2524–2532, 2008.

- [207] A. K. Dioumaev, J. M. Wang, Z. Blint, G. Vr, and J. K. Lanyi. Proton transport by proteorhodopsin requires that the retinal schiff base counterion asp-97 be anionic. *Biochemistry*, 42(21):6582–6587, 2003.
- [208] D. G. Mitchell, R. W. Quine, M. Tseitlin, R. T. Weber, V. Meyer, A. Avery, S. S. Eaton, and G. R. Eaton. Electron spin relaxation and heterogeneity of the 1:1 , -bisdiphenylene--phenylallyl (bdpa)/benzene complex. *The Journal of Physical Chemistry B*, 115(24):7986–7990, 2011.
- [209] J. H. Jiang and D. L. Wu. Ice and water permittivities for millimeter and sub-millimeter remote sensing applications. *Atmospheric Science Letters*, 5(7):146–151, 2004.